FROM HIGHER BANDS TO HIGHER SPINS: ULTRACOLD FERMIONS IN NOVEL REGIMES

Dissertation
zur Erlangung des Doktorgrades
des Departments Physik
der Universität Hamburg

vorgelegt von
Jannes Heinze
aus Leer

Hamburg
2013

Gutachter der Dissertation: Prof. Dr. Klaus Sengstock
Prof. Dr. Ludwig Mathey
Prof. Dr. Joseph H. Thywissen

Gutachter der Disputation: Prof. Dr. Klaus Sengstock
Prof. Dr. Andreas Hemmerich

Datum der Disputation: 06.08.2013

Vorsitzender des Prüfungsausschusses: Prof. Dr. Peter Schmelcher

Vorsitzender des Promotionsausschusses: Prof. Dr. Peter H. Hauschildt

Dekan der Fakultät für Mathematik,
Informatik und Naturwissenschaften: Prof. Dr. Heinrich Graener

ZUSAMMENFASSUNG

Seit der ersten Realisierung von quantenentarteten Bose- und Fermi-Gasen in verdünnten atomaren Systemen haben diese zur Beobachtung einer langen Reihe von faszinierenden und teilweise unerwarteten Entdeckungen geführt. Ein weites Feld ist hierbei die Simulation von Effekten aus der Festkörpertheorie, wobei insbesondere ultrakalte Fermi-Gase, die die gleiche Quantenstatistik wie Elektronen haben, eine besondere Rolle spielen. Die beispiellose Kontrolle über alle experimentellen Parameter in Quantengasen erlaubt darüber hinaus die Untersuchung von völlig neuartigen Quantensystemen. Dazu gehören Ensembles mit hohem internen Spin, sowie Mischungen von bosonischen und fermionischen Teilchen.

Im Rahmen dieser Arbeit präsentiere ich Experimente, die zum ersten Mal umfassend die Physik von fermionischen Atomen in höheren Bändern eines optischen Gitters beleuchten, sowie die erste Untersuchung von Spin-Anregungen in Fermi-Gasen mit hohem Spin. In Verbindung mit beiden Systemen existiert eine Vielzahl weiterer theoretischer Vorschläge zur Erzeugung und Erforschung ungewöhnlicher Quantenphasen und neuartiger Nichtgleichgewichtsphysik. Daher sind die präsentierten Studien wegweisend und die Resultate legen eine bedeutende Grundlage für nachfolgende Experimente, die noch viele ungeklärte Fragen zu beantworten haben.

Im speziellen wurde in dieser Arbeit eine Methode zur Spektroskopie von ultrakalten Fermionen in optischen Gittern entwickelt. Diese Methode nutzt Übergänge zu angeregten Bändern und wurde verwendet um die ersten voll impulsaufgelösten Messungen der Bandstruktur von quantendegenerierten Fermi-Gasen zu erzielen. Darüber hinaus wurden attraktiv wechselwirkende Bose-Fermi-Mischungen untersucht, in welchen zum ersten Mal auf direktem Wege eine wechselwirkungsinduzierte Lokalisierung der Fermionen nachgewiesen wurde. Die Lokalisierung resultiert aus einer Kopplung benachbarter Gitterplätze über Wechselwirkungsprozesse, was im Rahmen eines erweiterten Hubbard Modells erklärt werden kann.

Bei der Anregung von Atomen in höhere Bänder entstehen ebenso Löcher im untersten Band des Gitters. Dies resultiert aus dem fermionischen Charakter der untersuchten Teilchen. Die erste ausführliche Untersuchung beider Anregungen in ultrakalten Atomen wird im Rahmen dieser Arbeit präsentiert. Die untersuchten Prozesse weisen eine große Ähnlichkeit zur Photoleitung in herkömmlichen Isolatoren auf, wodurch sich eine neuartige Analogie zwischen der Festkörperpysik und ultrakalten Atomen ergibt.

Im weiteren wurden neuartige Fermi-Gase mit hohem internen Spin untersucht, welche in den letzten Jahren ein wachsendes Interesse erfahren. Es wurden hier zum ersten Mal die fundamentalen spinabhängigen Anregungen solcher Systeme untersucht. Dies wurde sowohl für harmonisch gefangene Vielteilchensysteme, als auch für Atompaare auf isolierten Gitterplätzen durchgeführt. Beide Systeme zeigen ein deutlich unterschiedliches Verhalten, jedes für sich stimmt jedoch mit den Resultaten theoretischer Modelle überein. Im Rahmen dieser Untersuchungen wurden die ersten kohärenten spin-ändernden Stöße zwischen ultrakalten Fermionen beobachtet, wobei zum ersten Mal überhaupt vielzahliger wechselwirkungsinduzierter Spin-Überträg nachgewiesen werden konnte.

Das mikroskopische Verständnis von Wechselwirkungsprozessen legt den Grundstein für die Untersuchung von Vielteilcheneffekten, die in Hochspin-Systemen zu völlig neuartigen Phänomenen führen. Die Untersuchungen an harmonisch gefangenen Gasen erlauben einen ersten Einblick in dieses faszinierende Forschungsfeld. Hierbei wurde der Einfluss des hohen Spins auf kollektive Spin-Wellen Anregungen untersucht, was die erste Beobachtung von kohärenter Vielteilchen-Dynamik in solchen fermionischen Hochspin-Systemen darstellt.

ABSTRACT

Since the first realization of quantum degenerate Bose and Fermi gases in dilute atomic vapor, these systems led to a large number of fascinating and sometimes unexpected discoveries. A broad field in this context is the simulation of solid state theories, where especially fermionic systems play a major role, since they have the same quantum statistics as electrons. Beyond that, the unprecedented control over all experimental parameters using ultracold atoms allows for the realization of completely novel quantum systems. These include particles with high internal spins and mixtures of bosonic and fermionic particles.

In the frame of this thesis, I present experiments that thoroughly study the physics of fermionic atoms in excited bands of an optical lattices for the first time. In addition, the first investigation of spin-excitations in Fermi gases with a high spin larger than $1/2$ is reported. In connection with these systems, a wealth of further proposals exists for the realization and study of unconventional quantum phases and novel nonequilibrium behavior. Therefore, the presented results pave the way towards further studies of these fascinating regimes, where many open questions are still to be answered.

In detail, a novel spectroscopy method for ultracold Fermi gases in optical lattices has been developed during this thesis. This technique employs transitions to excited bands and has been used for the first fully momentum-resolved measurement of the band structure for a fermionic quantum gas. Beyond that, it has been applied to attractively interacting Bose-Fermi mixtures, where a direct observation of an interaction induced localization of the fermionic atoms has been possible for the first time. This localization is produced by an offsite interaction, which can be described in an extended Hubbard model.

As the atoms are excited to the higher bands, they leave holes in the lowest energy band. This is a result of the fermionic character of the particles. The first comprehensive investigation of these particle and the hole excitations in the framework of ultracold atoms is presented in this thesis. The relevant processes prove to be in close analogy photoconductivity in conventional insulating solids, which results in a novel analogy between solid state physics and ultracold atoms.

Moreover, novel Fermi gases with high spin are studied, which are subject to an increasing interest in recent years. In this thesis, the fundamental spin excitations of such systems have been investigated for the first time. This has been done for harmonically trapped many-body systems, as well as for atom pairs on isolated lattice sites. Both systems show a clearly different behavior, whereas the results are in good agreement with the respective theoretical models. In the frame of these studies, the first coherent spin-changing collisions of ultracold fermions have been observed. This also led to the generally first observation of higher-order spin-exchange interactions.

The microscopic understanding of interaction processes is of high importance for the investigation of many-body phenomena, which introduce completely novel effects in high-spin systems. The investigation of the harmonically trapped high-spin gases allowed here for first insights into this fascinating field. Thereby, the influence of the high spin on collective spin-wave excitations has been investigated. This constitutes the first observation of coherent many-body dynamics in such fermionic high-spin systems.

Publikationen

Im Rahmen der vorliegenden Arbeit sind die folgenden wissenschaftlichen Veröffentlichungen entstanden.

Publications

The following research articles have been published in the course of this thesis.

[1] J. S. Krauser, U. Ebling, N. Fläschner, J. Heinze, K. Sengstock, M. Lewenstein, A. Eckardt, and C. Becker, *Giant Spin Oscillations in an Ultracold Fermi Sea*, Science, **343**, 157-160 (2014)

[2] O. Jürgensen, J. Heinze, and D.-S. Lühmann, *Large-Amplitude Superexchange of High-Spin Fermions in Optical Lattices*, New J. Phys. **15**, 113017 (2013)

[3] J. Heinze, J. S. Krauser, N. Fläschner, K. Sengstock, C. Becker, U. Ebling, A. Eckardt, and M. Lewenstein, *Engineering Spin Waves in a High-Spin Ultracold Fermi Gas*, Phys. Rev. Lett. **110**, 250402 (2013)

[4] J. Heinze, J. S. Krauser, N. Fläschner, B. Hundt, S. Götze, A. P. Itin, L. Mathey, K. Sengstock, and C. Becker, *Intrinsic Photoconductivity of Ultracold Fermions in Optical Lattices*, Phys. Rev. Lett. **110**, 085302 (2013)

[5] J. S. Krauser, J. Heinze, N. Fläschner, S. Götze, O. Jürgensen, D.-S. Lühmann, C. Becker, and K. Sengstock, *Coherent multi-flavour spin dynamics in a fermionic quantum gas*, Nat. Phys. **8**, 813-818 (2012)

[6] J. Heinze, S. Götze, J. S. Krauser, B. Hundt, N. Fläschner, D.-S. Lühmann, C. Becker, and K. Sengstock, *Multiband Spectroscopy of Ultracold Fermions: Observation of Reduced Tunneling in Attractive Bose-Fermi Mixtures*, Phys. Rev. Lett. **107**, 135303 (2011)

[7] U. Bissbort, S. Götze, Y. Li, J. Heinze, J. S. Krauser, M. Weinberg, C. Becker, K. Sengstock, and W. Hofstetter, *Detecting the Amplitude Mode of Strongly Interacting Lattice Bosons by Bragg Scattering*, Phys. Rev. Lett. **106**, 205303 (2011)

CONTENTS

LIST OF FIGURES

LIST OF TABLES

CHAPTER 1

INTRODUCTION

In everyday life, at typical temperatures of about 300 K, atoms and molecules in dilute gases essentially behave as classical particles and their physical state can be described by a Maxwell-Boltzmann distribution [8]. At temperatures near zero Kelvin, the quantum mechanical properties of the individual particles become important. There are two fundamentally different kinds of particles, which are distinguished in this regime, namely bosons and fermions. They have different quantum statistics and, in direct connection, different internal spins, which are integer valued for bosons and half-integer valued for fermions [9]. If the quantum statistics dominate the thermal state of the gas, the system is usually said to be quantum degenerate, which leads to a fundamentally different behavior of bosons and fermions [10].

Bosonic particles undergo a phase transition to the quantum degenerate regime, where they form a Bose-Einstein condensate (BEC), which has been demonstrated for the first time in a dilute gas of atoms in 1995 [11–13], and was awarded with the Nobel price in 2001. This discovery started the research field of quantum degenerate gases, and soon after, the first quantum degenerate Fermi gas has been demonstrated in 1999 [14].

Following these seminal experiments, a steadily growing research community developed over the years, where many different phenomena have been investigated using ultracold atoms [15, 16]. A big advantage of ultracold atom systems is the high control over most external parameters, such as the geometry, the dimensionality, the interaction strength, and the internal state of the atoms. Since the gases are also well isolated from the environment, being trapped only by magnetic fields or far offresonant laser beams, they have very long coherence times and preserve their pure quantum state for a long time. Typical timescales for dynamics in ultracold atom systems are in the order of milliseconds, much slower than processes in solids or molecules, such that quantum degenerate gases are also ideally suited for the study of coherent quantum dynamics.

A particularly rich field of research are quantum phases and phase transitions. Apart from the BEC transition itself, the crossover from a BEC of molecules to Cooper pairs in strongly interacting Fermi gases has been observed [17–20], as well as the strongly correlated Mott insulator phase in optical lattices [21–29] and other even more exotic phases [30–32].

Many of these observations rely on the controlled preparation of ultracold ensembles in optical lattices; a topic, which have gained a lot of attention in the past years [33–44]. These periodic potentials are provided by interfering laser beams, which create a so-called *crystal of light*. The resulting many-body systems are in strong analogy to real crystals and realize the same many-body Hamiltonians as used to describe electrons in solids [15]. This similarity allows for the simulation of solid state phenomena using ultracold atoms [45], but also yields

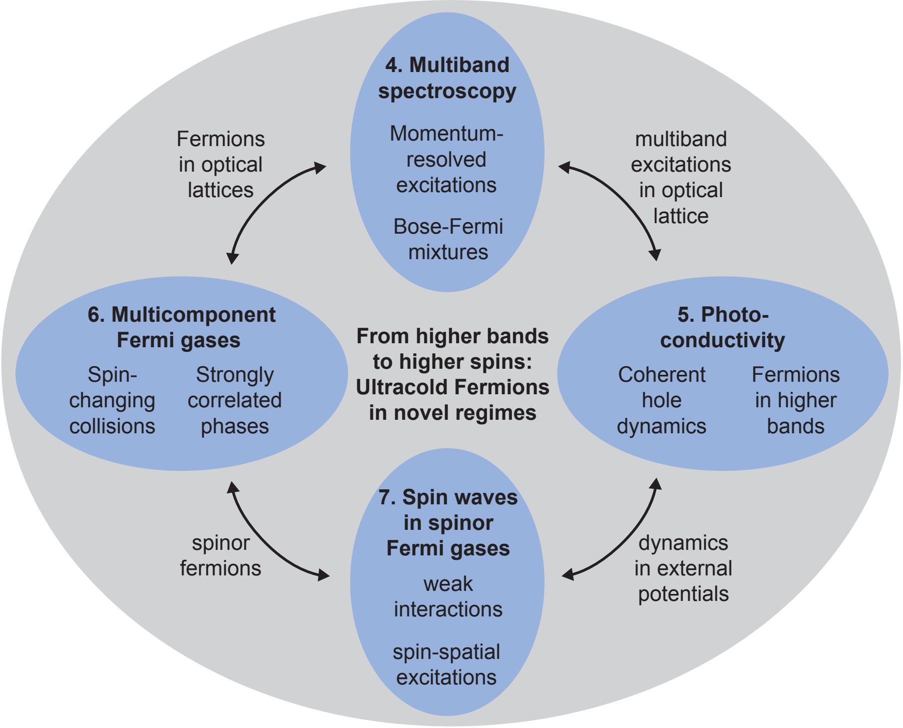

Figure 1.1: Connection between all topics presented in this thesis. The ellipses depict the different chapters 4 to 7 and the main effects investigated therein. The arrows show the direct overlap between the different chapters.

---

the possibility to adapt methods from solid state physics to ultracold atoms, in order to control or probe the quantum degenerate gases themselves. Of great interest in this context are ultracold fermions. Since they share the same quantum statistics, fermions resemble electrons in solids more closely than bosons do [46]. Therefore, a major effort is directed towards the realization of fermionic lattice systems [25, 26, 33, 46–54]. While the reported experiments are mainly restricted to the ground state properties in the lattice, a growing theoretical interest is directed on the realization of fermions in higher energy bands [55–65].

Another important field are multicomponent gases [50, 66–74]. These allow for the mixture of bosonic and fermionic particles, which constitute a completely novel class of many-body systems [68–71, 75]. In such mixtures, unexpected and highly debated results have been obtained. A shift of the bosonic Mott insulator transition was observed in the presence of fermions with attractive interspecies interactions [23, 24, 76], which was the direct opposite of the behavior expected from theory at that time [77–81]. In an ongoing discussion different approaches have been proposed to explain this shift, where the correct description is still debated [56, 82–85].

Multicomponent systems can also be realized with multiple hyperfine states of the same atomic species. Such mixtures can form spinor many-body systems, where the internal states provide novel degrees of freedom accessible only in ultracold matter [86–88]. In these systems, interactions allow for novel spin-exchange processes, which influence the system properties dramatically. While ultracold bosons with internal degrees of freedom have been studied extensively over the last years [67, 89–97], quantum degenerate high-spin Fermi gases with more than two internal spin states have only been realized recently [50, 73, 74]. Despite the small, but growing, number of experimental realizations, there are many theoretical proposals for the realization of novel phases and other unexplored regimes using such fermionic high-spin systems [2, 51, 98–101, 101–113].

The results presented in this thesis combine many of the research fields mentioned above. Figure 1.1 depicts the connections and overlap between all investigated topics. The main results can be summarized as follows.

The study of multiband excitations of ultracold Fermi gases in optical lattices is presented. This allowed for the first momentum-resolved spectroscopy of ultracold fermions in optical lattices and for first the direct observation of an interaction induced tunneling reduction in attractively interacting Bose-Fermi mixtures (see chapter 4). Further, the study of multiband excitations led to a new connection between ultracold atoms and solid state physics, realizing an analog to photoconductivity with ultracold atoms, as discussed in chapter 5. In chapter 6, interacting high-spin fermions in optical lattices are studied, where the first realization of spin-changing collisions with fermionic atoms is reported. Finally, multicomponent Fermi gases at weak interactions are investigated in chapter 7, which constitutes the first observation of coherent many-body dynamics with high-spin fermions.

These results are of high relevance for further studies of ultracold fermions, pioneering especially two topics that gained much interest in recent years, namely high-spin Fermi gases and fermions in excited lattice bands. The study of multiband effects in fermionic quantum gases is of high importance for the realization of novel quantum phases in higher bands, including time-reversal symmetry breaking ground states. The identification of the microscopical interaction properties of high-spin Fermi gases paves the way towards the investigation of novel magnetic properties and involved quantum phases. A more detailed introduction for each topic can be found at the beginning of each chapter.
The structure of the thesis is as follows.

- In chapter 2, I describe the most relevant experimental concepts for the realization of quantum degenerate Fermi gases. I concentrate in particular on the features implemented during this work. This includes the preparation of interacting multicomponent Fermi gases, a new optical dipole trap setup, and a new optical lattice setup.

- The basic properties of ultracold fermions and Bose-Fermi mixtures in optical lattices are discussed in chapter 3. Here, I concentrate on the influence of the harmonic confinement, which is of high relevance for the correct description and understanding of the ground state properties of these quantum gases.

- In chapter 4, a novel multiband spectroscopy technique is presented. This method allows for the first momentum-resolved detection of the full band structure for ultracold fermions, resulting in textbook-like pictures of the reduced and extended zone scheme of the lattice potential. The chapter contains a detailed description of the experimental realization of the spectroscopy. A thorough experimental characterization of its properties is given, using ideal noninteracting fermions. Beyond that, the method is applied to attractively interacting Bose-Fermi mixtures, analyzing the tunneling properties of the mixture. The results have been partly published in [6].

- Chapter 5 shows the first realization of an analog to photoconductivity in ultracold quantum gases. In this context, the first comprehensive investigation of the dynamical properties of ultracold fermions excited to higher bands of an optical lattice is reported. Moreover, coherent dynamics of holes in momentum space, imprinted on an initially band insulating ground state in the optical lattice, are realized for the first time. I compare the experimental results to two different theoretical approaches, using a semiclassical analysis, obtained by Alexander Itin and Ludwig Mathey, and a fully numerical approach, mainly conceived by myself. Finally, I discuss the influence of interactions on the excitations properties. The results presented in this chapter have been partly published in [4].

- In chapter 6, the physics of multicomponent Fermi gases in optical lattices are discussed. I give the first detailed description of the full spin-dependent interaction properties of ^{40}K. Presenting proof-of-principle experiments, I compare the theoretical and experimental results quantitatively. The results constitute the first demonstration of coherent spin-changing collisions with ultracold fermions. Beyond that, I present a spin-resolved determination of double occupancy in ultracold Fermi gases, which is of high relevance for the detection of novel multicomponent phases in the optical lattice. Finally, I propose a possible realization of a novel phase crossover between two strongly correlated states in an open quantum system without particle conservation, using a Feshbach resonance in ^{40}K with strong inelastic collisions. While each of the states has been realized independently [25, 26, 31, 54], I discuss the novel possibilities introduced by a tunable system. For the determination of the scattering properties of ^{40}K and the parameters of the novel Feshbach resonance, numerical data from molecular coupled channel calculations has been kindly provided by T. Hanna and L. Cook. The results on the spin-changing collisions have been partly published in [5]. An in-depth discussion of these experiments, including more experimental details and results, can be found in the thesis of Jasper S. Krauser [114].

- In the final chapter 7, weakly interacting high-spin Fermi gases in optical dipole traps are studied. The fundamental excitations in this regime are spin waves, which are driven by exchange interactions between indistinguishable particles. A thorough experimental study of spin-wave excitations is presented for a $f = 3/2$ Fermi gas, constituting the simplest realization of a high-spin system with fermions. I discuss the underlying theoretical concepts relevant for the understanding of spin-wave excitations and compare the experimental results to numerical calculations using a semiclassical mean-field theory. This description has been worked out and the results are kindly provided by Ulrich Ebling, supervised by Andre Eckardt and Maciej Lewenstein. An intuitive description of the novel properties, induced by the high spin of $f = 3/2$, is obtained using a suitable basis of irreducible spherical tensors. The results of this chapter are partly published in [3].

During this work, I also participated in several other studies on ultracold atoms, which are not presented in this thesis. This includes the detection of the amplitude mode in a strongly interacting Bose gas using Bragg spectroscopy [7, 115], the measurement of several new Feshbach resonances in ^{40}K [114, 116], the investigation of spin-changing collisions in ultracold bulk Fermi gases [1], and the theoretical description of spinor fermions in optical lattices [2].

CHAPTER 2

EXPERIMENTAL SETUP AND METHODS

In this chapter, I introduce the basic experimental concepts and methods used in this work to prepare, manipulate, and detect the ultracold atomic gases investigated throughout this thesis. All experiments reported have been performed at the Bose-Fermi mixture (BFM) setup in the group of Prof. Dr. Klaus Sengstock at the *Institut für Laser-Physik* of the *Universität Hamburg*. While a detailed description of the setup can be found in [117, 118], several modifications have been implemented during this work. New dipole trap and lattice setups have been designed and installed and various experimental methods have been implemented. In particular, the first interacting mixtures of ultracold fermionic atoms in Hamburg have been prepared and studied during this work.

All experimental data presented in this chapter was taken and analyzed together with Jasper S. Krauser, Sören Götze and Nick Fläschner. The numerical calculations were performed mainly by myself. To my knowledge, also the analytical results (2.10) and (2.11) have not been introduced before.

The telescope for the elliptical dipole trap was assembled and characterized in the course of the diploma thesis by Nick Fläschner at the BFM setup, which was co-supervised by me. The optical lattice telescopes were assembled and characterized in the course of the diploma thesis by Malte Weinberg at the BFM setup, which was also co-supervised by me.

2.1 PRODUCTION OF ULTRACOLD BOSE AND FERMI GASES

The BFM setup was originally designed for the simultaneous production of ultracold mixtures of spin-polarized fermionic ^{40}K and bosonic ^{87}Rb [117, 118]. While one part of the experiments reported here was performed in this configuration, another part was performed with multicomponent Fermi gases consisting of two or more hyperfine states of ^{40}K. The realization of both systems is described in the following.

2.1.1 GENERAL SETUP

The core of the setup consists of a combined 2D and 3D magneto-optical trap (MOT) setup which has been described in great detail in [117, 118]. The MOTs for both species are overlapped and operate simultaneously. To reduce losses due to light-assisted collisions, the MOT for ^{40}K uses a Dark-SPOT configuration [117–119]. After cooling the ^{40}K and ^{87}Rb atoms in the two-stage MOT, the atoms are further cooled in an optical molasses. Using an σ^+-polarized optical pumping beam, all atoms are subsequently transferred to the maximally polarized and

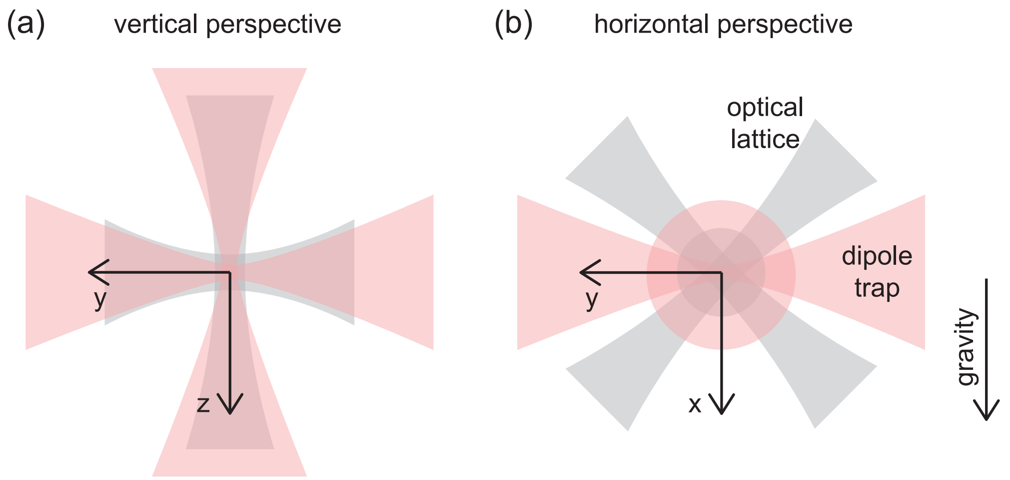

Figure 2.1: Sketch of the dipole trap and optical lattice beams in the BFM setup. The red shadings depict the dipole trap beams along the horizontal y- and z-direction. The gray shadings represent the optical lattice beams, where one beam is overlapped with the optical lattice in the z-direction, using a dichroitic mirror and the other two beams are aligned in $45°$ with respect to the vertical x-direction within the xy-plane. For comparison, the weak trapping of the magnetic trap is along the z-direction, where also a strong gradient field can be applied using an anti-Helmholtz configuration of the MOT magnetic coils [117, 118].

---

magnetically trapped hyperfine states with $f = 2$, $m = 2$ and $f = 9/2$, $m = 9/2$, before being loaded into the magnetic trap. This optical pumping increases the number of atoms transferred to the magnetic trap by a factor of up to 5 for rubidium and up to 10 for potassium. During the transfer the trapping frequencies of the magnetic trap are set to about $2\pi\times 11\,\mathrm{Hz}$ in all three directions, to allow for a good mode-match between the magnetic trap and the MOTs [117, 118]. Afterwards, the trap is compressed within $1.5\,\mathrm{s}$ to trapping frequencies of about $2\pi\times(214, 214, 11)\,\mathrm{Hz}$ for rubidium and a factor of $\sqrt{87/40}$ larger for potassium, which corresponds to the mass ratio of both species [118]. In the magnetic trap the mixture is cooled to quantum degeneracy, where the fermionic potassium atoms are sympathetically cooled by the rubidium atoms [120].

For all presented experiments, the atoms are subsequently transferred to an optical dipole trap, operated at about $808-812\,\mathrm{nm}$ (see section 2.3), where additional evaporative cooling is performed if necessary. Overlapped with the dipole trap, there is a three-dimensional cubic optical lattice operated at $1030\,\mathrm{nm}$ consisting of three retro-reflected rectangular oriented laser beams (see section 2.4). After the experiments, performed either in the pure dipole trap or in the optical lattice potential, the atoms are detected using resonant absorption imaging. There are two imaging systems in the horizontal plane, one along the z-direction, and another along the y-direction. The pictures are taken by CCD cameras (Pixelfly PCO). The detection systems allow magnifications of 0.5, 1 and 2. All data presented in this thesis is taken along the y-direction, which especially allows for an independent detection of different spin components, as discussed in section 2.2 in more detail. A sketch of all optical potentials, clarifying the coordinate system used, is shown in Fig. 2.1.

Additional tools are the radio-frequency and two different microwave antennas, allowing the creation of radiation in the range of $0-200\,\mathrm{MHz}$, near $1.3\,\mathrm{GHz}$, and near $6.8\,\mathrm{GHz}$. These are used for evaporative cooling in the magnetic trap and state preparation in the dipole trap.

2.1.2 BOSE-FERMI MIXTURES AND SINGLE-COMPONENT FERMIONS

To create mixtures of bosonic ^{87}Rb atoms and fermionic ^{40}K atoms, first the K-MOT is loaded alone for a variable time between 3 s and 30 s. Then the Rb-MOT is switched on for typically 1.5 s to 5 s, such that both MOTs are operated simultaneously. The reason for this procedure are collisions between rubidium and potassium atoms in the overlapping MOT leading to losses [117, 118]. These are especially severe for the K-MOT, which is loading less efficiently compared to the Rb-MOT. Hence, the K-MOT is loaded in advance to trap enough atoms before the Rb-MOT is switched on. Loading the Rb-MOT as efficient as possible is necessary if large potassium atom numbers are desired. The maximal MOT particle numbers in the BFM setup are up to 1×10^{10} atoms in the ^{87}Rb 3D MOT and up 1.5×10^{8} in the ^{40}K 3D MOT, and one order of magnitude lower in the mixtures [117, 118]. The typical MOT particle numbers versus loading time can be found in [117].

In the magnetic trap the atomic mixture is evaporatively cooled to quantum degeneracy [121]. This is done by an exponential radio-frequency sweep from 40 MHz down to about 1 MHz for up to 30 s. In this process the hottest rubidium atoms are removed from the magnetic trap and a simultaneous thermalization leads to an effective cooling of the gas [122]. Thereby, the ^{40}K atoms are sympathetically cooled by the ^{87}Rb atoms [71, 120]. Note, that the sympathetic cooling of potassium is indeed very important, since the spin-polarized fermionic ^{40}K atoms do not interact with themselves at very low temperatures, due to Pauli blocking [14, 123]. Only the interactions with the bosonic ^{87}Rb atoms lead to a thermalization of the fermionic atom cloud and allow for cooling to quantum degeneracy. The evaporation is stopped at a frequency slightly above the transition frequency for ^{87}Rb at the magnetic trap center. The final state in the magnetic trap is a mixture of ultracold rubidium atoms, forming a BEC with up to 5×10^{6} atoms and an ultracold Fermi gas with typically up to 2×10^{6} atoms and temperatures down to a tenth of the Fermi temperature ($T\approx 0.1\,T_{\mathrm{F}}$; see [10, 124] and appendix A.2 for the Fermi temperature in harmonically trapped gases). The exact values depend strongly on the initial atom number in the magnetic trap and therefore on the MOT loading times for potassium and rubidium. The numbers given above are typical values for nearly pure single-species systems. Typical mixtures with similar particle numbers contain about 2×10^{6} rubidium and 4×10^{5} potassium atoms.

From the magnetic trap, the mixture is transferred to an optical dipole trap. For this, the trap laser beams are first switched on at large intensities of about 300 mW, to capture as many atoms as possible. The magnetic gradient field and the dipole trap power are slowly reduced at the same time using exponential ramps up to 1s, until the magnetic gradient field is zero and the dipole trap saturates at a final value of typically about 100 mW. The trapping frequencies at this point are $2\pi\times(46, 50, 50)$ Hz. The corresponding trap depths are $(2.5, 170, 170)\,h$kHz. Note, that the vertical depth strongly depends on the laser power in this regime. The given parameters correspond to dipole trap setup 1 (see section 2.3), which was mostly used to investigate Bose-Fermi mixtures and single-component fermions. In this procedure, the dipole trap serves as a dimple potential [125], while the magnetic field is lowered. The bosons condense in the dimple potential, which is simultaneously filled with fermionic atoms. All atoms not trapped in the dimple dipole trap are lost when the magnetic field is reduced to zero. The resulting mixture contains typically up to 4×10^{5} rubidium and 2×10^{5} potassium atoms, which can be tuned by the two MOT loading times and the final dipole trap depth. To create a non-interacting, spin-polarized Fermi gas, the ^{87}Rb atoms are removed at this point with a short 1 ms pulse of laser light resonant with the D2 transition line of ^{87}Rb at approximately 780.24 nm [126]. Since the two species are only weakly interacting at this point, this removal does not perturb the ^{40}K

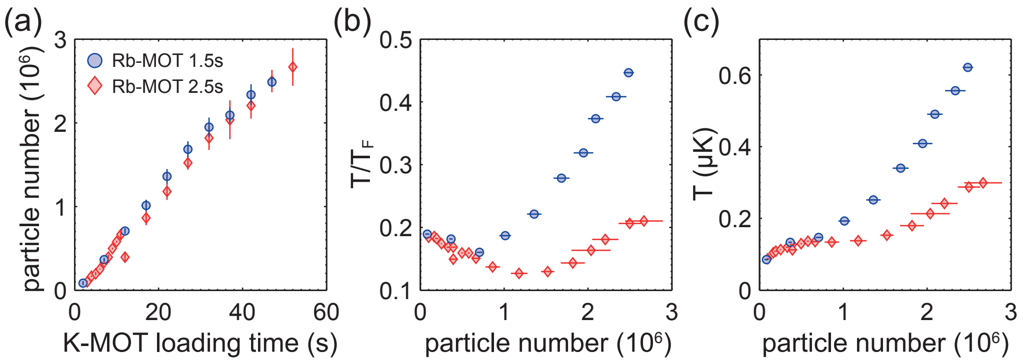

Figure 2.2: ^{40}K particle number and temperature in the magnetic trap. (a) shows the ^{40}K particle number in the magnetic trap after the evaporation in dependence on the MOT loading time for two different ^{87}Rb MOT loading times. The small drop in the particle number at short loading times results from a disruption of the measurement. (b) Relative temperature T/T_{F} of the fermionic atoms. (c) Absolute temperatures of the Fermi cloud.

---

atoms significantly.

2.1.3 FERMI-FERMI MIXTURES

The production of interacting Fermi-Fermi mixtures follows the same route as the production of Bose-Fermi mixtures. The main difference is that this preparation requires a second evaporative cooling stage in the optical dipole trap. To acquire large particle numbers for this step, an optimization of the full procedure is needed.

A measurement of the ^{40}K particle number and temperature in dependence on the MOT loading time is shown for two different Rb-MOT loading times in Fig. 2.2. The reported parameters are measured after the evaporation in the magnetic trap. In this case, all ^{87}Rb atoms are removed by the magnetic trap evaporation creating a pure spin-polarized sample of ^{40}K atoms.

As depicted in Fig. 2.2(a) the total particle number rises nearly proportional to the loading time and is about the same for both measurements. This shows, that a stable particle number can be produced, independent of the exact performance of the Rb-MOT. In contrast, the temperature of the Fermi gas strongly depends on the Rb-MOT loading time. The data in Fig. 2.2(b) reveals that only a certain amount of ^{40}K atoms can be efficiently cooled by the rubidium atoms and longer Rb-MOT loading times are necessary to achieve large and cool potassium samples. Especially the sharp increase of the temperature at particle numbers above 1×10^6 shows that the 1.5 s Rb-MOT loading is not suitable for the production of large quantum degenerate Fermi gases with high densities, as required for the production of interacting Fermi-Fermi mixtures.

From these measurements, MOT loading times of 30 s for potassium alone and about $2-3$ s for rubidium were chosen as a starting point for the experimental realization of interacting ^{40}K gases. This results in a particle number of $1.5-2\times10^6$ particles at about $0.15\,T_{\mathrm{F}}$.

The non-interacting single-component ^{40}K ensemble is transferred to the optical dipole trap. Therefore, the trap lasers are initially switched on at large intensities of about $300\,$mW, such that all potassium atoms from the magnetic trap can be captured. The corresponding trapping frequencies are about $2\pi\times(50, 100, 200)$ Hz. The trap depths are in the order of $200\,h$kHz (vertical) to $300\,h$kHz (horizontally). The given parameters correspond to dipole trap setup 2 (see section 2.3), which was used for most of the experiments on interacting Fermi gases.

Then the magnetic gradient field is reduced slowly with an exponentially decreasing ramp over about $1\,\mathrm{s}$, at a constant dipole trap power. After the pure optical dipole trap is reached a series of radio-frequency pulses and sweeps is used to create the desired mixture of hyperfine states, as described in section 2.2. This is typically done at a magnetic offset field of about $45\,\mathrm{G}$. Due to a finite magnetic field gradient, the different atomic spin states decohere quickly which allows for mutual interactions between the particles, necessary for thermalization in the evaporative cooling. The latter is performed by reducing the dipole trap laser intensity in an exponential ramp of $2\,\mathrm{s}$ to about $100\,\mathrm{mW}$, depending on the particular experimental parameters. In this process, the trapping depth is reduced and thus the hottest atoms are continuously lost from the trap, while the slow ramp ensures a proper thermalization. The final trapping depths in the vertical direction typically range between 2 and $5\,h\mathrm{kHz}$, depending on the desired particle numbers. The final mixture has typically temperatures of about 0.1 to $0.3\,T_\mathrm{F}$ with $0.5-2.5\times10^5$ atoms per spin state, depending on the chosen parameters.

2.2 STATE PREPARATION AND DETECTION

In this section, I introduce the internal structure of ^{40}K and ^{87}Rb and discuss shortly the state preparation using radio-frequency (rf) and microwave (mw) radiation [127, 128], which is the basis for many results presented in this thesis. I present measurements that demonstrate the feasibility of these methods for ^{40}K. Subsequently, I give a short account of the different imaging procedures used throughout this thesis, in particular two different methods to separately image different hyperfine states.

A more detailed analysis of the state preparation of ^{40}K will be given in [114].

2.2.1 INTERNAL STRUCTURE OF ^{87}RB AND ^{40}K

As rubidium and potassium are both alkali atoms with one unpaired electron on the outer s-shell, they possess a hyperfine structure in the electronic ground state. The complete shell spin of the ground state is $J=1/2$, which consists of $l=0$ for the spatial s-shell wave function, and $s=1/2$, corresponding to the internal spin of the single unpaired electron. The total spin f is composed of $J=1/2$ and the spin of the atomic core which is $I_\mathrm{Rb}=3/2$ for ^{87}Rb and $I_\mathrm{K}=4$ for ^{40}K, leading to hyperfine-manifolds with $f_\mathrm{Rb}=\{1,2\}$ and $f_\mathrm{K}=\{9/2,7/2\}$.

If the atoms are subject to a magnetic field, the different hyperfine levels split energetically due to the Zeeman effect. For alkali atoms as ^{40}K, the full magnetic field dependence of the Zeeman energy can be calculated analytically using the Breit-Rabi formula [130]

$$E_\mathrm{BR}(m,B) = -\frac{\Delta E_\mathrm{hfs}}{2(2I+1)} + g_I\mu_\mathrm{B}B(m_\mathrm{I}\pm1/2) \pm \frac{\Delta E_\mathrm{hfs}}{2}\sqrt{1+\frac{4x(m_\mathrm{I}\pm1/2)}{2I+1}+x^2}\,, \quad (2.1)$$

with the hyperfine splitting $\Delta E_\mathrm{hfs} = (I+1/2)A_\mathrm{hfs}$ of the two hyperfine manifolds. The abbreviation $x=(g_\mathrm{J}-g_\mathrm{I})\mu_\mathrm{B}B/\Delta E_\mathrm{hfs}$ contains the Bohr magneton μ_B and Landé factors g_J and g_I. The ± sign accounts for the spin configurations $m_\mathrm{J}=\pm1/2$. Note here, that ^{40}K has an inverted hyperfine structure, where the manifold with the larger spin $f=9/2$ has the lower energy.

For low fields, this splitting between neighboring states of the same manifold depends approximately linear on the magnetic field. This is the Zeeman regime, where the hyperfine spin f and the corresponding magnetization m are good quantum numbers [129]. In the following, a spin state in the Zeeman regime is written as $|f,m\rangle$ or simply $|m\rangle$ if the total spin f is fixed.

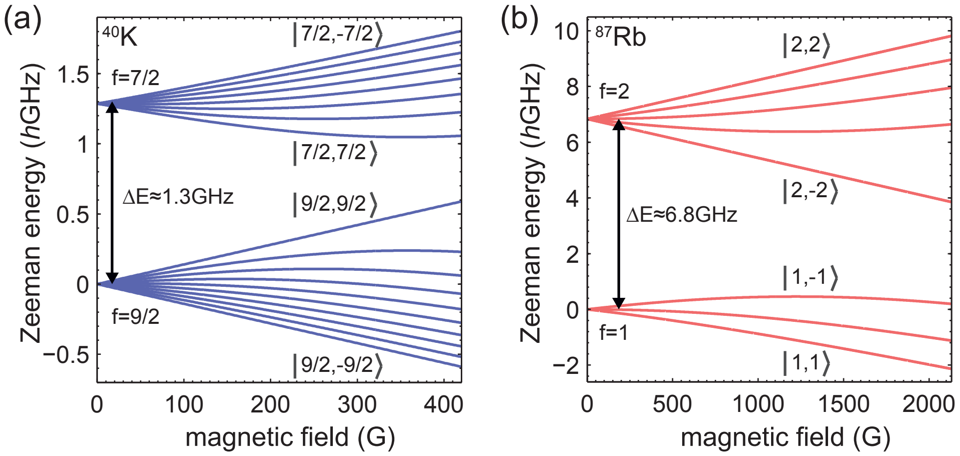

Figure 2.3: Magnetic field dependence of the Zeeman energy for (a) ^{40}K and (b) ^{87}Rb for both hyperfine ground state manifolds, calculated using (2.1). At low magnetic fields, the Zeeman energy changes approximately linearly, corresponding to the Zeeman regime, where the total spin f of the atoms is well defined. In this regime, the energy difference between two adjacent states is nearly equal for all pairs of states. At large magnetic fields, the energy changes nonlinearly and the energy difference of different pairs of states becomes different. At very large fields, the atoms eventually reach the Paschen-Back regime, where only the magnetization of the individual spin states is a good quantum number [129].

For larger magnetic fields, nonlinear contributions lead to deviations from the linear behavior until eventually only the magnetizations of electron and core are good quantum numbers. This is called the Paschen-Back regime [129]. The full magnetic field dependence of the hyperfine energies of ^{40}K and ^{87}Rb using (2.1) is shown in Fig. 2.3 and the magnetic field dependent splitting in more detail for the $f = 9/2$ manifold of ^{40}K in Fig. 2.4.

2.2.2 INTERNAL STATE CONTROL USING RADIO FREQUENCY AND MICROWAVE FIELDS

A population transfer between different hyperfine states can be induced by a radio-frequency or microwave fields, resonant with a hyperfine transition. The field couples the respective states, which can be used either to induce a Landau-Zener transition or a Rabi oscillation between them [127, 128].

To induce Rabi oscillation, the rf radiation is switched on instantaneously in resonance with the desired transition between two states of the same hyperfine manifold [127, 128]. The energy difference between the coupled states is determined by the magnetic field as shown in Fig. 2.3. The sudden creation of a coupling between both states leads to oscillatory occupation dynamics. A total transfer between both state is possible at resonant coupling, which is typically referred to as a Rabi resonance [129]. Since the transfer strongly depends on the rf-pulse frequency, a full transfer is usually hard to achieve. However, a nearly perfect transfer is possible for typical experimental parameters, as shown below. If the Rabi oscillation is stopped in between, mixtures of two states with arbitrary relative particle numbers can be created. This process is less sensitive on the exact resonance position and can be achieved experimentally. Thus, the resonant coupling between two hyperfine states allows for a versatile state preparation. The same can be achieved by using mw radiation between the two ground state hyperfine manifolds. Note, that for both, rf and mw coupling, only states with $\Delta m = \{0, \pm 1\}$ can be coupled directly, using the linear and circular polarizations of the field, respectively.

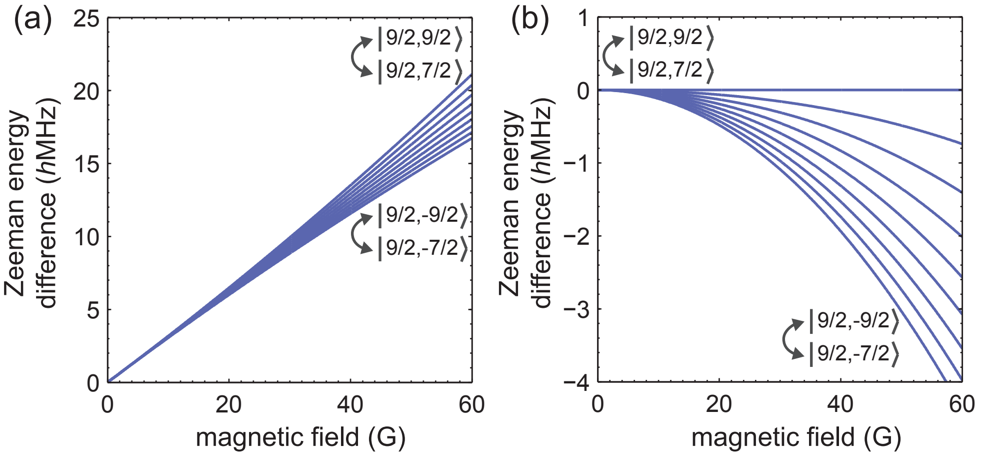

Figure 2.4: Typical Zeeman splittings within the $f = 9/2$ hyperfine manifold of ^{40}K, calculated using (2.1). (a) shows the absolute splitting for all pairs with $\Delta m = 1$. The pair $|9/2,9/2\rangle|9/2,7/2\rangle$ has the largest splitting, continuously reduced for lower magnetizations. (b) shows the splitting normalized to the $|9/2,9/2\rangle|9/2,7/2\rangle$ pair, which highlights the absolute differences of the splittings more clearly. Since the linear contribution of the Zeeman energy leads to equal splittings, the splitting difference changes dominantly quadratically with the magnetic field. This behavior is discussed in detail in section 6.2.

An alternative approach for the preparation of spin states are Landau-Zener sweeps [131], which are created by slowly ramping the rf or mw frequency across the transition [127, 128]. As usual in a two level system, a slow ramp leads to an adiabatic transfer of the atoms from one state to the other, allowing especially for a robust transfer of all atoms, in contrast to the Rabi oscillation method, where a full transfer can only be achieved exactly at resonance. Using faster sweeps, or finishing the sweep near a resonance, leads to a mixture of the two coupled states. However, while the full sweep is very stable, the preparation of mixtures shows large fluctuations and Rabi oscillations are preferable.

Note here, that the coupling in both situations leads to a coherent transfer between the different states. The resulting wave function of each atom is therefore a coherent superposition of the two coupled hyperfine states.

In ^{40}K and ^{87}Rb the situation is generally more complicated than for the simple two-level system. Due to the higher spins, there are at least 2 transitions for $f_{\mathrm{Rb}} = 1$ and up to 9 transitions for $f_{\mathrm{K}} = 9/2$. In Fig. 2.4, typical energy splittings versus the magnetic field are shown within the $f = 9/2$ manifold of ^{40}K. If the resonances between different states are separated strongly enough, each of the transitions can be addressed separately and all hyperfine states can be populated independently.

For mw transitions, the differences are very large and two-level systems are easily accessible. For rf transitions, the differences are very small such that fields of about 45 G are typically used in the experiment to separate the different transitions.

A measurement of population transfer between two coupled hyperfine states of ^{40}K is shown in Fig. 2.5(a), demonstrating the possibility of a nearly full transfer using Rabi oscillations. Figure 2.5(b) shows the transfer of spin states using the Landau-Zener transitions, which demonstrates a perfect transfer between all states of the $f = 9/2$ manifold of ^{40}K. Using these two methods, any desired spin mixture can be prepared in the hyperfine ground states of ^{40}K. With a subsequent evaporative cooling, this allows to produce variable interacting two-

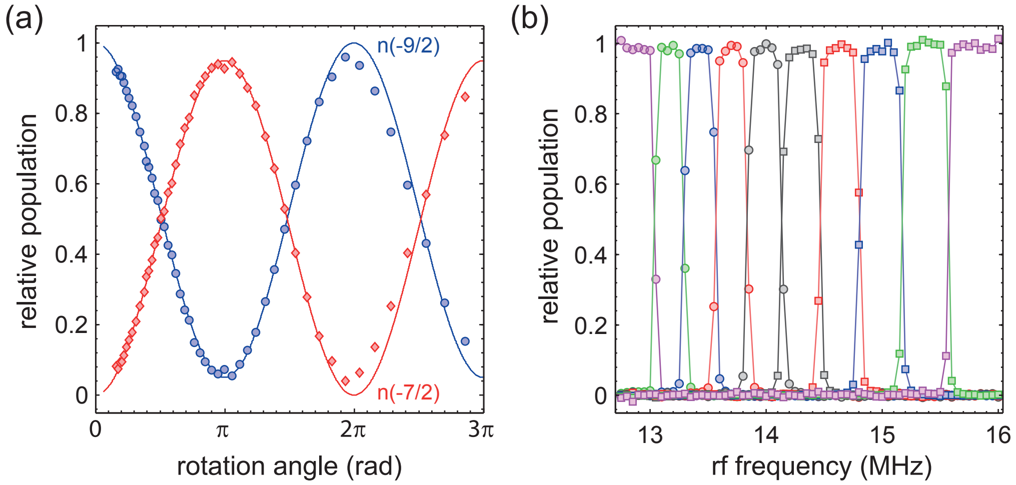

Figure 2.5: State preparation in the $f = 9/2$ hyperfine manifold of ^{40}K at large fields. (a) shows a measurement of a resonant transfer between the hyperfine states $|9/2, -9/2\rangle$ and $|9/2, -7/2\rangle$ in dependence on the coupling strength for a $50\,\mu$s rf pulse. A nearly full transfer between both states is demonstrated. The solid lines serve as guides to the eye. (b) Shows a 20 ms Landau-Zener transfer starting from 16.5 MHz in the state $|9/2, 9/2\rangle$ to lower frequencies, reaching pure samples of all spin states in the $f = 9/2$ manifold. The magnetization states $|\pm 1/2\rangle$ are shown in black, $|\pm 3/2\rangle$ in red, $|\pm 5/2\rangle$ in blue, $|\pm 7/2\rangle$ in green and $|\pm 9/2\rangle$ in purple. All positive magnetizations are depicted as squares and all negative as circles. The different data is connected by solid lines as guides to the eye. Both measurements were performed at a magnetic field of about 45 G.

---

component spin mixtures as used throughout this thesis. This procedures are the basis for many studies presented in the following.

If the magnetic field is very low, the energy differences of all transitions within one hyperfine manifold are very small. In this regime, the Rabi resonance method allows for another spin preparation scheme, where all hyperfine states are coupled simultaneously as already demonstrated for bosonic atoms (see, e.g., [90, 92, 127]). To my knowledge, this method has not been applied to fermionic atoms so far.

To achieve the multicomponent coupling, a very short rf pulse is used with a pulse width broader than the typical splitting differences of the different transitions. This leads to multicomponent Rabi oscillations that can be described as rotations on a generalized Bloch sphere [127]. Using $f_{\mathrm{K}} = 9/2$, up to 10 states are involved in this preparation scheme, depending on the rotation angle. Figure 2.6 shows measurement for the case used in this thesis, starting from an interacting two-component mixture of the states $|9/2, 1/2\rangle$ and $|9/2, -1/2\rangle$.

The preparation of coherent spinor states allows in combination with the high spin of ^{40}K for the investigation of novel regimes of spinor physics with fermionic gases. At low pulse intensities, four-component system can be prepared, which constitute pseudo-spin $3/2$ Fermi gases. This is the most fundamental fermionic high-spin system with effects beyond conventional electron-like $s = 1/2$ systems and serves as a model system for all higher spins. For higher pulse intensities, even larger effective spins can be realized. This demonstrates the variable and versatile preparation techniques, implemented during this thesis together with Jasper S. Krauser, which allowed for the first studies of fermionic spinor physics as presented in this thesis.

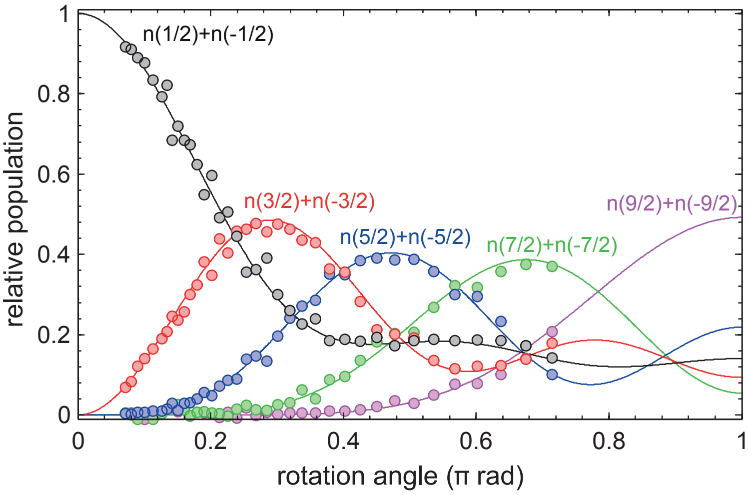

Figure 2.6: Multicomponent spin transfer using rf coupling. A measurement of the relative populations of spin states in an ultracold ^{40}K cloud with $f = 9/2$, starting from an incoherent evaporated superposition of $|9/2, 1/2\rangle$ and $|9/2, -1/2\rangle$ is shown. The atoms are subject to a $20\,\mu$s rf pulse with varying intensity. The magnetic field is $B = 169$ mG, corresponding to an absolute resonance frequency of 53 kHz and a maximal frequency difference between two single transitions of 0.034 kHz. In comparison, the width of the rf pulse is in the order of 50 kHz, not resolving the different transitions. Since all spins are populated symmetrically, $n(m) = n(-m)$, for clarity only the symmetric addition is shown. The solid line depicts a numerical single-particle calculation, detailed in appendix A.3. The absolute rotation angle is fitted between experiment and calculation. A rotation angle of 2π corresponds to a full rotation back to the initial state.

2.2.3 DETECTION OF COLD ATOMIC ENSEMBLES

For the detection of the ultracold atomic ensembles, resonant absorption imaging was employed in all presented experiments [122]. It is a standard procedure in ultracold atom experiments and in the following I concentrate mainly on its different applications during this work and explain the advantages and disadvantages.

One application of absorption imaging used in this thesis is direct *in situ* imaging of the trapped sample, which directly reveals the density distribution of the atoms [122]. However, *in situ* imaging has two fundamental limitations. First, since the atomic cloud in the trap is typically very small, a high resolution is required. Second, the small sample size leads to a high density in the trap, resulting in saturated images, where structures in the density distribution are not discernible anymore. Both limitations are especially severe for bosonic atoms, where direct *in situ* absorption imaging is usually not applicable. For fermionic atoms, however, the density is limited by Pauli blocking, which also increases the total size of the cloud. Therefore, *in situ* absorption imaging can be employed for fermions at typical system parameters without saturation effects.

The other application of absorption imaging is to measure the atomic distribution after a long time-of-flight (TOF), which allows for the measurement of the momentum distribution of the atoms [122]. This circumvents the limitations of *in situ* imaging in the following way: Instead of imaging the atomic distribution in the trap, the latter is switched off allowing for a free expansion of the atoms. Due to gravity, the center-of-mass of the atoms is accelerated whereas the cloud expands according to its initial momentum distribution. In the far field limit of this expansion, the resulting density distribution is the Fourier transform of the spatial distribution in the trap. Thus, the detected distribution after TOF is close to the momentum distribution of the atoms in the trap. The expansion during TOF leads to a strongly increased extension of the cloud and therefore a strong reduction of the density, such that the shadow in the absorption imaging is no longer saturated, compared to *in situ* imaging. In addition, fine regular structures in the density profile in the trap transform to large structures in the momentum distribution and can be detected with an imaging system with much coarser resolution.

Naturally, also the TOF procedure has limitations. First, the information on the original density distribution are lost for all non-regular structures, such as smooth density variations. Second, the transformation from the spatial to the momentum distribution is only perfect at infinite expansion times. Therefore a finite TOF can lead to a mixture of both momentum and position space. In particular with an increasing size of the atomic cloud in the trap an increased TOF is necessary to achieve a reasonable transformation to the momentum distribution. The expansion time is limited by the size of the science chamber due to the gravitational acceleration and by the specifications of the imaging system, if the full atomic distribution needs to be detected.

As discussed above, both atomic species, ^{40}K and ^{87}Rb, have an internal structure with different hyperfine states. An independent detection of these states is crucial for many of the presented experiments. Indeed, both detection procedures allow for the detection of the individual hyperfine states.

The standard procedure is a Stern-Gerlach setup, where a magnetic field gradient is applied during the TOF [127, 128]. Due to the different magnetic moments of the different states, the resulting horizontal forces lead to a separation of the spin components. As the Stern-Gerlach separation considerably increases the area of interest, the above mentioned limitations of the TOF due to the detection system are important, often not allowing for a full transformation to the momentum distribution.

An alternative procedure allows for the *in situ* detection of the individual spin components. For this, all spin states except one are transferred to the $f = 1$ or $f = 7/2$ hyperfine manifold for ^{87}Rb or ^{40}K, respectively, using mw pulses of about $50\,\mu$s. These states are offresonant for the detection light and thus do not influence the absorption pictures. Since the mw pulses are much shorter than all atomic timescales in the experiment, this method can also be used to observe dynamical phenomena, like spin-dependent spatial dynamics. Note here, that a finite time (≤ 1 ms) prior to the absorption detection all potentials must be switched off to avoid any line shifts either magnetically or light induced such that a short evolution of the atomic cloud is inevitable. This is the limiting timescale for the investigation of dynamical phenomena. In the *in situ* procedure an independent image must be taken for each spin component, which increases the experimental effort considerably. Therefore, in most measurements in this thesis the Stern-Gerlach procedure is used to distinguish the different spin components.

2.3 OPTICAL DIPOLE TRAP

The dipole trap in the BFM setup has been redesigned throughout this thesis. Therefore, I discuss in detail the relevant physical aspects and their influence on the dipole trap design before I present the new implemented dipole trap designs.

2.3.1 DIPOLE POTENTIAL AND SPONTANEOUS SCATTERING

Optical traps take advantage of the coupling between light and atoms via the atomic polarizability α. The light induces a dipole moment in the atoms and thus changes their internal energy

[132]. A spatially varying intensity $I(r)$ of the light field consequently leads to a spatially varying total energy of the atoms and thus to a conservative dipole potential [133]

$$U_\mathrm{D}(\vec{r},P) = -\frac{\Re(\alpha)}{2\epsilon_0 c} I(\vec{r},P) = -\pi c^2 \sum_\mathrm{i} \frac{c_\mathrm{i}}{\omega_\mathrm{i}^3} \left(\frac{\Gamma_\mathrm{i}}{\omega_\mathrm{i}-\omega_\mathrm{d}} + \frac{\Gamma_\mathrm{i}}{\omega_\mathrm{i}+\omega_\mathrm{d}} \right) I(\vec{r},P)\,, \tag{2.2}$$

where P is the absolute power of the light field. The potential exactly resembles the form of the light intensity. Its global strength depends on the detuning $\Delta = \omega_\mathrm{i} - \omega_\mathrm{d}$ between the laser with frequency $\omega_\mathrm{d} = 2\pi c/\lambda_\mathrm{d}$ and all transition lines of the atoms with frequencies ω_i, as well as on the width of these transitions Γ_i. The strengths of the transitions c_i can be calculated from the corresponding Glebsch-Gordan coefficients. For lists of all relevant properties of ^{87}Rb and ^{40}K, see [126] and [134] and the references therein. Using a red detuned laser ($\omega_\mathrm{d} < \omega_\mathrm{i}$), the potential energy becomes negative, while for blue detuning ($\omega_\mathrm{d} > \omega_\mathrm{i}$) it becomes positive. Therefore, red detuned lasers allow for trapping atoms in their intensity maximum, while blue detuned lasers provide the possibility to create barriers inside an atomic cloud [13] or to trap atoms by external walls [135]. Only red detuned dipole traps were employed in the presented experiments and are discussed in the following.

In (2.2) only the real part of the polarizability $\Re(\alpha)$ contributes to the dipole potential. The imaginary part $\Im(\alpha)$ leads to spontaneous scattering of photons. This is exploited in laser cooling applications, but also leads to heating and losses for an optically trapped atom cloud [132]. The scattering rate is given by

$$\Gamma_\mathrm{S}(\vec{r},P) = -\frac{\pi c^2 \omega_\mathrm{d}^3}{\hbar^2} \sum_\mathrm{i} \frac{c_\mathrm{i}}{\omega_\mathrm{i}^6} \left(\frac{\Gamma_\mathrm{i}}{\omega_\mathrm{i}-\omega_\mathrm{d}} + \frac{\Gamma_\mathrm{i}}{\omega_\mathrm{i}+\omega_\mathrm{d}} \right)^2 I(\vec{r},P)\,, \tag{2.3}$$

which has the same intensity dependence as the trapping potential. The scattering decreases quadratically, while the dipole potential (2.2) only decreases linear with the detuning Δ. Therefore, a far detuned dipole trap reduces the heating due to spontaneous scattering, but requires an increased total laser power.

2.3.2 GAUSSIAN BEAMS AND THE GRAVITATIONAL FORCE

Red detuned dipole traps are typically realized with Gaussian laser beams [133]. The intensity profile of a Gaussian beam in the z-direction with laser power P is given by [136]

$$I(\vec{r},P) = \frac{2P}{\pi w_\mathrm{x}(z) w_\mathrm{y}(z)} \mathrm{e}^{-2\left(\frac{x^2}{w_\mathrm{x}^2(z)} + \frac{y^2}{w_\mathrm{y}^2(z)} \right)}\,, \tag{2.4}$$

with the radius $w_\mathrm{i}(z) = w_\mathrm{0,i}\sqrt{1 + z/z_\mathrm{R,i}}$ of the beam in the direction $i = x, y$. The Rayleigh range is defined by $z_\mathrm{R,i} = \pi w_\mathrm{0,i}^2/\lambda_\mathrm{d}$ with the radius $w_\mathrm{0,i}$ at the beam focus in the respective direction i. Since atoms are attracted to the maximum intensity, the trapped ensemble usually stays inside the focus along the z-direction and in the center of the beam in the other two directions. While the total potential has a Gaussian shape, it can be approximated around the center to second order as a harmonic potential

$$U_\mathrm{D}(\vec{r}) \approx \frac{1}{2} m \omega_\mathrm{x}^2 x^2 + \frac{1}{2} m \omega_\mathrm{y}^2 y^2 + \frac{1}{2} m \omega_\mathrm{z}^2 z^2\,, \tag{2.5}$$

where the harmonic trapping frequencies are given by [128]

$$\omega_{\mathrm{x_i}} = \sqrt{\frac{1}{m} \frac{d^2}{dx_\mathrm{i}^2} U_\mathrm{D}(\vec{r})}\,, \tag{2.6}$$

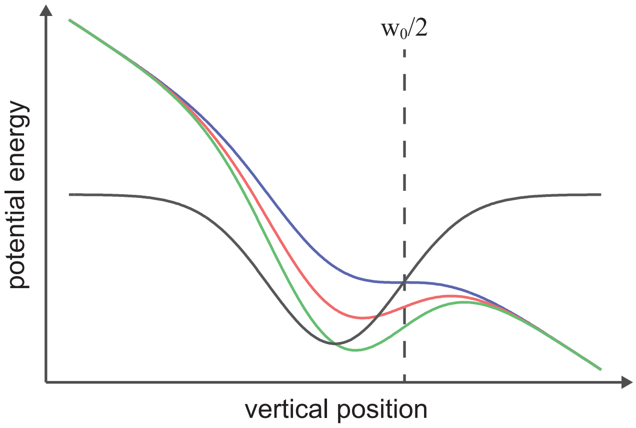

Figure 2.7: Sketch of the trapping potential with and without gravity. A Gaussian potential without gravitation is depicted in black, as realized in (2.2). The trapping volume is given solely by the intensity and thus by the depth of the Gaussian beam, with the point of maximal force at half the waist $w_0/2$. Combinations of Gaussian potentials of different strengths and the linear gravitational force are shown with decreasing intensity in green, red and blue, calculated with (2.8). The potential is no longer symmetric and the trapping volume is given by the heights of the tunneling barrier, which emerges at the bottom of the trap. In addition, the position of the trap center changes depending on the dipole trap strength. For a certain dipole trap power P_0 a saddle-point develops in the potential (blue potential curve). It appears exactly at $w_0/2$ away from the beam center, when the gravitational force and the maximal force of the trap exactly cancel each other. For lower trap strengths no atoms are trapped anymore.

evaluated at $\{x, y, z\}$=0.

The radial trapping frequencies of a single beam in the z-direction are of the form [128]

$$\omega_\mathrm{x} = \sqrt{\frac{8P}{m w_{0,\mathrm{y}} w_{0,\mathrm{x}}^3} \frac{\Re(\alpha)}{2\epsilon_0 c}} \quad \text{and} \quad \omega_\mathrm{y} = \sqrt{\frac{8P}{m w_{0,\mathrm{x}} w_{0,\mathrm{y}}^3} \frac{\Re(\alpha)}{2\epsilon_0 c}}\,. \tag{2.7}$$

The intensity variation along the beam direction is given by the Rayleigh range z_R, which is much larger than the perpendicular waist $w_{0,\mathrm{i}}$. Therefore, the corresponding trapping frequency is very small ($\omega_\mathrm{x}, \omega_\mathrm{y} \gg \omega_\mathrm{z}$), and in the experiment usually a second perpendicular beam is overlapped with the first one, leading to a stronger trapping in this direction. In the BFM setup, such a crossed dipole trap is used with one beam in the z-direction and another in the y-direction. Consequently, both beams lead to a strong trapping potential in the x-direction. In the harmonic approximation, the two corresponding trapping frequencies simply add up quadratically as $\omega_\mathrm{x} = \sqrt{\omega_{\mathrm{x,Y}}^2 + \omega_{\mathrm{x,Z}}^2}$, where the subscripts Y and Z denote the propagation direction of the beams. In the other two directions, the contributions of the Rayleigh-range trapping can typically be neglected for crossed dipole traps, such that the trapping frequencies are given simply by the single beam contributions $\omega_\mathrm{y} = \omega_{\mathrm{y,Z}}$ and $\omega_\mathrm{x} = \omega_{\mathrm{x,Y}}$.

The second important contribution to the total potential is the gravitational force [117, 128]. It leads to a constant force mg in the vertical direction, corresponding to a potential energy of $-mg\vec{x}$. Note, that the x-axis is pointed along the gravitational direction in the used coordinate system, leading to the negative sign of the potential energy. The full potential including the

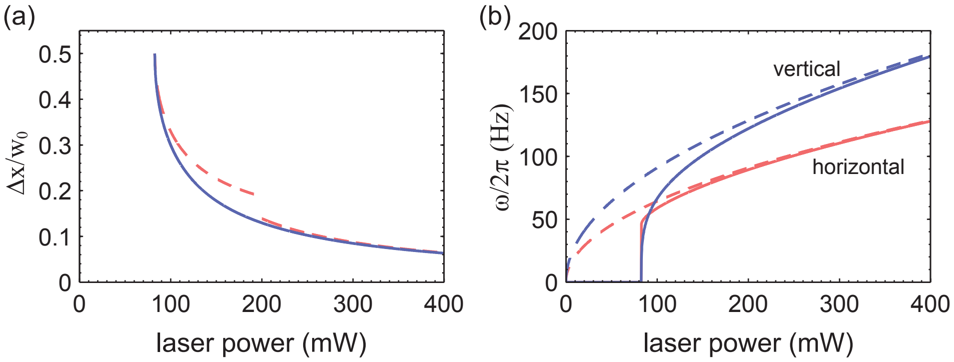

Figure 2.8: Gravitational sag Δx and trapping frequencies ω versus the trap power for a crossed circular dipole trap with equal beam waists $w_0 = 120\,\mu$m and equal powers P at 811 μm for ^{40}K, corresponding to setup 1 as introduced below. (a) The solid line shows the gravitational sag over the trap power, calculated using (2.8). The dashed lines show the limiting results from (2.9) and (2.10). (b) Trapping frequencies for same parameters as (a), calculated using (2.8). The dashed lines show the results for $g \equiv 0$ from (2.7). For the crossed beam configuration without gravitation, the trapping frequency in the x-direction is always $\sqrt{2}$ larger than in the other two directions, due to the quadratic addition of trapping frequencies. Including gravitation, the trapping frequency in the vertical x-direction reduces to zero at P_0, while the horizontal trapping stays approximately the same as before. Therefore, the trap ratio inverts below a certain power, where the trap is completely spherical.

---

gravitational force and two laser beams at the same wavelength λ_d is given by

$$U_\mathrm{tot}(\vec{r},P) = -\pi c^2 \sum_\mathrm{i} \frac{c_\mathrm{i}}{\omega_\mathrm{i}^3} \left(\frac{\Gamma_\mathrm{i}}{\omega_\mathrm{i} - \omega_\mathrm{d}} + \frac{\Gamma_\mathrm{i}}{\omega_\mathrm{i} + \omega_\mathrm{d}} \right) \Big(I_\mathrm{LA}(\vec{r},P) + I_\mathrm{HD}(\vec{r},P) \Big) - mg\vec{x}\,. \tag{2.8}$$

Typical forms of this potential are shown in Fig. 2.7 for different trap intensities. The gravitational contribution has a strong impact on the potential: First, it reduces the trap depth in the vertical direction, limiting the number of atoms that can be trapped. Second, it introduces a gravitational sag Δx, shifting the trap minimum away from the center of the dipole trap laser beam. The value of Δx increases with decreasing power of the dipole trap. With increasing sag, the Gaussian form of the potential becomes important. The atoms can only be trapped, if the maximal force at some point of the beam is larger or equal to the gravitational force. The largest force is created at the point of maximal slope of the Gaussian beam at $x = w_{0,\mathrm{x}}/2$. As shown in Fig. 2.7, this point marks the maximal gravitational sag. It is reached at the minimal beam power P_0, where the gravitational force and the maximal trap forces become equal. The trapping frequency becomes zero at P_0, strongly deviating from the results without the gravitational contribution (2.7). A calculation of the sag and the corresponding trapping frequencies for realistic parameters is shown in Fig. 2.8.

In the limiting case of small gravitational sags $\Delta x \ll w_{0,\mathrm{x}}/2$, the potential can be assumed to be harmonic with the unperturbed trapping frequencies (2.7) and the sag can be calculated to be approximately [117]

$$\Delta x = \frac{g}{\omega_\mathrm{x}^2}\,. \tag{2.9}$$

This is valid for strong laser beams, where the atoms are close to the center of the beam. Reaching the minimal trapping intensity P_0, the sag becomes $\Delta x = w_{0,\mathrm{x}}/2$, independent of any other parameter. Near this point, small increases of the laser intensity lead to a gravitational sag of

$$\Delta x(P) = \frac{w_{0,\mathrm{x}}}{2} - \frac{w_{0,\mathrm{x}}}{6^{1/2}} \left(1 - \frac{g m w_{0,\mathrm{x}}/2}{U_\mathrm{D}(w_{0,\mathrm{x}}/2, 0, 0, P)}\right)^{1/2}, \tag{2.10}$$

calculated by a Taylor expansion of the potential around $w_{0,\mathrm{x}}/2$.

2.3.3 MAGIC DIPOLE TRAP

The BFM setup was originally designed to produce and investigate mixtures of bosonic ^{87}Rb and fermionic ^{40}K [117, 118]. This leads to the complication, that a different gravitational force acts on both atomic species, proportional to the respective mass. Therefore, the total trap potential becomes deformed differently for the two species and, in particular, the gravitational sag is not equal. This can lead to a complete separation of the different species. The solution employed in the BFM setup is, to use a dipole trap at a magic wavelength, where both species experience different potentials that lead, however, to the same trapping frequencies, assuring an equal gravitational sag as can be seen in equation (2.9). The properties of the magic dipole trap have been originally discussed in [117].

At the magic wavelength the different gravitational forces and the difference in the dipole force due to the different detuning for both species exactly cancel [117]. Using the complete potentials for both species the magic wavelength can be calculated to be 806.6 nm. A measurement of the dipole trap oscillations of both species is shown in Fig. 2.9(a). The wavelength where both species show the same oscillation frequency is determined to be 808 nm, using a fit to the data. The slight difference to the theoretical result can be explained as follows. For a perfect harmonic trap, the oscillation frequencies of a quantum degenerate gas directly reproduces the trap frequency. In a Gaussian trap, as realized in the experiment, this is no longer exactly true. Especially for fermionic atoms the oscillation frequencies are typically slightly lower than the trapping frequency [137], which results in a shift in the observed direction.

Figures 2.9(b) and (c) show a full calculation of the differential gravitational sag for ^{87}Rb and ^{40}K for the dipole trap setup 1, as discussed below, comparing different wavelengths. The calculations reveal, that the differential gravitational sag becomes especially large for small beam powers near P_0, where most experiments are performed. Thus, using a trap at the magic wavelength is necessary to obtain a good overlap between both species.

2.3.4 EXPERIMENTAL REALIZATION: CIRCULAR AND ELLIPTICAL TRAPS

I now turn to the actual experimental realization of the dipole trap. The design of the new dipole trap followed two major goals. First, the dipole trap was designed for the magic wavelength to ensure a good overlap between ^{87}Rb and ^{40}K. Second, low trapping frequencies are desired, to create atomic samples with relatively homogeneous density distributions and small site occupation if overlapped with the optical lattice.

Two different setups have been designed and implemented during this work. I first discuss the circular beam setup that was used mainly in the optical lattice experiments presented in chapters 4 and 5 of this thesis. The properties and disadvantages of this trap are discussed, which lead to the development of the second elliptical beam setup that was used in all experiments presented in chapters 6 and 7.

The laser light for both setups is provided by a Ti:sapphire laser (MBR110, Coherent), which is laser pumped with a frequency-doubled, diode-pumped Nd:YAG laser at 532 nm (Verdi V18, Coherent, 18 W). The Ti:sapphire laser is typically operated at $\lambda_\mathrm{d} = 808 - 812$ nm, close to the magic wavelength. The typical output power at this wavelength is up to 5 W.

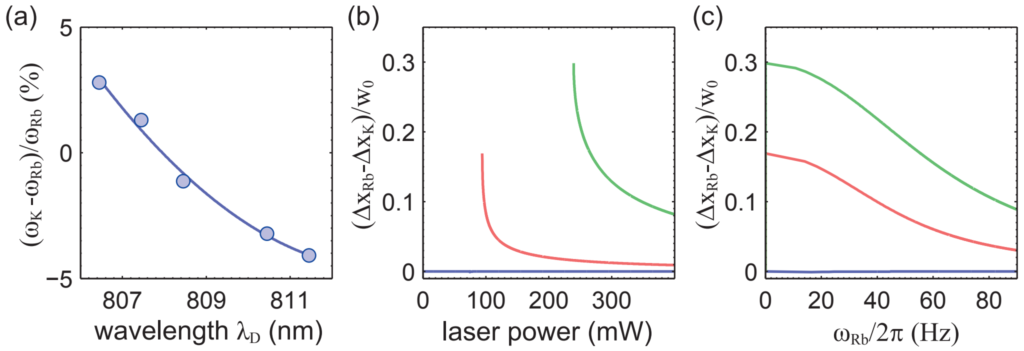

Figure 2.9: Magic wavelength and the differential gravitational sag. (a) Ratio of the trap frequency of both species measured in the gravitational direction at different wavelengths using dipole oscillations. The solid line is a quadratic fit of the data ($\omega_K/\omega_{Rb} = a + b\lambda + c\lambda^2$), used to determine the magic wavelength, where $\omega_{Rb}/\omega_K = 1$, and yields 808 nm. (b) Calculation of the differential gravitational sag $\Delta x_{Rb} - \Delta x_K$ over trap power for a crossed circular dipole trap with $w_0 = 120\,\mu$m, using (2.8). At the magic wavelength (806.6 nm from theoretical calculations, depicted in blue), the sag vanishes for all trap strength. For larger wavelengths (shown are 811 nm depicted in red, and 850 nm depicted in green), rubidium has a weaker trap at equal laser power, and is lost from the trap earlier. Near the minimal trapping power for rubidium, the differential gravitational sag shows the strongest deviation. (c) Same results as in (b), where the abscissa is rescaled onto the trapping frequency for ^{87}Rb in the vertical direction. The results show, that already a small change in the wavelength leads to a strong shift of the center of the atomic clouds.

The light is separated in two arms, producing the trap power for the two telescopes of the crossed dipole trap. Up to 1 W per arm is sufficient for loading and evaporation of the cold atomic samples as I discuss in the following. In each arm, the laser passes through an 80 MHz accusto-optical modulator (AOM 3080-122, Crystal Technology) once. By this, the beams are detuned by about 150 MHz. Afterwards the light is coupled into two non-polarization maintaining single-mode fibers with about 5 μm mode-field diameter (780-HP, Nufern). At the end of each fiber, the light is collimated, polarization-cleaned by a polarizing beam splitter, and focused onto the atoms, using self-assembled telescopes, as described below. About 4 % of the light is deflected onto a fast photodiode (PDA 55, Thorlabs) and is used to control and stabilize the output power after the fiber, using self-built PI-controllers and the AOMs in front of the fiber as feedback elements. The two dipole trap setups mainly differ concerning the design of the telescopes as discussed in the following.

FIRST DESIGN: CROSSED CIRCULAR DIPOLE TRAP

The dipole trap setup 1 consists of two circular beams, which have a focus beam waist of approximately $w_0 = 120\,\mu$m. The beams are created using telescopes consisting of four lenses as sketched in Fig. 2.10. The first one collimates the beam, followed by a beam expander consisting of two lenses and a final lens to focus the beam onto the atoms. The dipole trap beams are pointed in the horizontal y and z-directions and are usually operated with equal powers leading to a spherical trap in the yz-plane and a trapping frequency in the vertical x-direction, which is up to $\sqrt{2}$ larger.

Figure 2.11 shows calculations of the trapping frequencies, gravitational sags, the maximal particle numbers, the size of the atomic clouds, and the spontaneous scattering rate for both species and two different wavelengths. The diameter and cloud sizes are calculated assuming

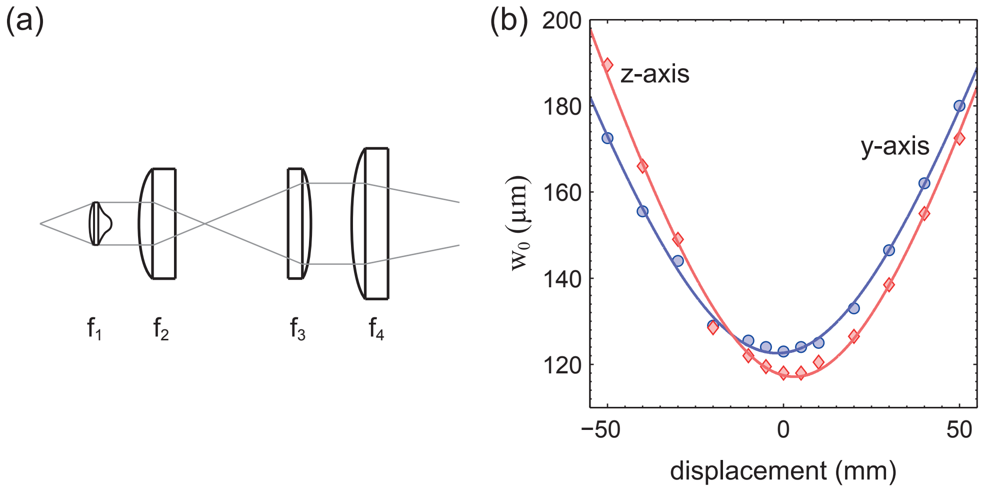

Figure 2.10: Sketch of dipole trap setup 1 and corresponding waist measurements. (a) shows the optical elements included in the telescope. After the light is emitted from the end of the optical fiber, an aspheric lens with focus length of $f_1 = 4.51\,\mathrm{mm}$ (C230 TME-B, Thorlabs) collimates the beam, which is then expanded by a two-lens telescope, consisting of two achromatic lenses with $f_2 = 19\,\mathrm{mm}$ (AC127-019-B, Thorlabs) and $f_3 = 40\,\mathrm{mm}$ (AC257-040-B, Thorlabs), leading to a beam expansion by a factor of approximately 2. With a final achromatic lens ($f_4 = 400\,\mathrm{mm}$, AC508-400-B, Thorlabs), the light is focused onto the atoms. In between the first and second lens, the light is polarization filtered by a polarizing beam splitter (G335743000, Linos, not shown) and before the final focusing lens, about 4% of the light is deflected for intensity stabilization using a glass plate (not shown). The same design has been used for both telescopes. In (b) a measurement of the beam focus is shown for both implemented telescopes, resulting in focus waists of about $w_0 = 122.6 \pm 1\,\mu\mathrm{m}$ for the telescope in y-direction and $w_0 = 117.6 \pm 2\,\mu\mathrm{m}$ for the z-direction.

Thomas-Fermi distributions at $T = 0$ for both species [10, 118]. The differential gravitational sag vanishes at the magic wavelength of $806.6\,\mathrm{nm}$ and the trap volume for both species is equal. However, the maximal particle number for the fermionic potassium atoms is much smaller than the corresponding rubidium number. This is due to the different statistics of both species, allowing for more rubidium atoms within the same trap volume. The very small potassium atom numbers at reasonable rubidium atom numbers have also been observed in the experiment. It was found that no approximately equal particle numbers could be achieved in the mixtures using a dipole trap at the magic wavelength. For this reason, a slightly larger wavelength of $811\,\mathrm{nm}$ has been used typically, where the relative atom numbers can be tuned in a broad range. In this case, the potassium atoms have a smaller gravitational sag and an effectively stronger trap at the same beam power. Consequently, the maximal particle number for the fermions increases relative to the bosons [see Fig. 2.11(d)]. In particular, the rubidium atoms are lost completely from the trap at higher trap powers at this non-magic wavelength. The potassium atoms are still well confined in the trap. Thus large potassium numbers can be achieved for varying rubidium numbers. Note, that due to the large size of the fermionic ^{40}K cloud, the two species still overlap strongly for all trap powers as shown in Fig. 2.11(e). The typical operation point is slightly below the completely circular point, with trapping frequencies of $\omega_\mathrm{x} \approx 2\pi \times 46\,\mathrm{Hz}$ in the vertical direction and about $\omega_\mathrm{y} \approx \omega_\mathrm{z} \approx 2\pi \times 50\,\mathrm{Hz}$ in the horizontal directions, where potassium numbers up to 2×10^5 and rubidium numbers up to 4×10^5 atoms have been achieved. Typical trap depths in this regime are around $2.5\,h\mathrm{kHz}$ in the vertical

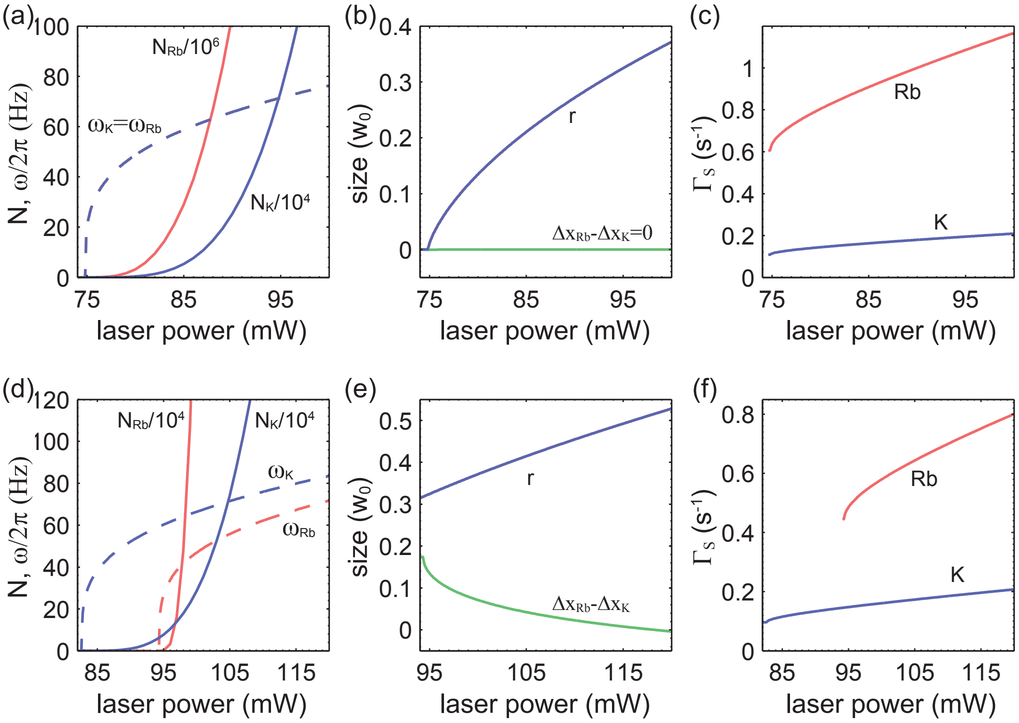

Figure 2.11: Calculation of the characteristic parameters of dipole trap setup 1 as a function of the beam power as discussed in the text. (a)-(c) show the parameters at 806.6 nm. In (a), the trapping frequencies (dashed lines) and particle numbers (solid lines) for both species are shown in dependence on the laser power. The trapping frequencies for both species are equal. Note the different scaling of the particle numbers, showing that much more ^{87}Rb atoms can be stored in the trap at a fixed power. (b) shows the differential gravitational sag, which is zero in this case, and the typical cloud radius r. In (c) the spontaneous scattering rate with the trap photons is shown. Figures (d)-(f) show the same data for an operation at 811 nm. Note especially, that mixtures with equal particle numbers are possible, and that the differential gravitational sag near this point is typically smaller than the radius of the cloud. Therefore, there is still a good overlap between both species.

---

direction and 170 hkHz in the horizontal directions, where the vertical depth strongly depends on the laser power in this regime.

Since the magic wavelength leads to a small detuning, in particular for the ^{87}Rb D1 (794.98 nm) and D2 (780.24 nm) transition lines [126], spontaneous scattering of photons as described by (2.3) cannot be neglected. Figures 2.11(c) and (f) show that the spontaneous scattering rate for rubidium is in the order of 1 Hz in the present setup. Near the minimal trapping intensity P_0, the trap depth in the vertical direction is much lower than the energy gained by an atom via the absorption of one single photon, which is about 3.5 hkHz for rubidium at 811 nm. Therefore, each atom is immediately lost, if it absorbs a single photon and the loss rate from the trap is a direct measure of the spontaneous scattering rate. In this regime, an atom loss rate of 0.7 Hz has been measured at a dipole trap wavelength of 808 nm, which is in good agreement with the calculated scattering rate (see Fig. 2.11(c)). For larger trap depths, the larger scattering rates lead to a severe heating of the atomic cloud that prohibits an efficient evaporative cooling in the dipole trap and also limits the maximal timescale for experiments in the dipole trap. Since the scattering rate decreases with the light intensity, the minimal

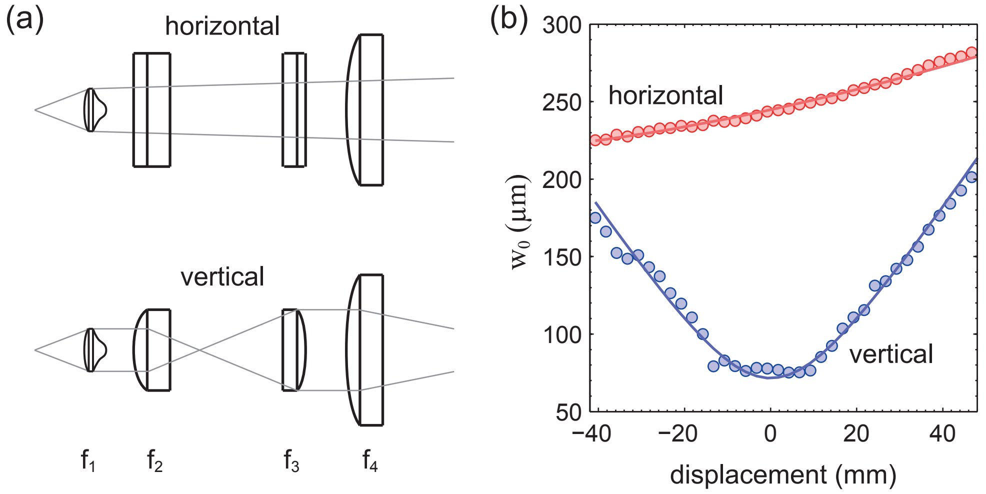

Figure 2.12: Sketch of dipole trap setup 2 and corresponding waist measurements. (a) shows the optical elements included in the telescope. After the light is emitted from the end of the optical fiber, an aspheric lens with focus length of $f_1 = 4\,\text{mm}$ (C610TME-B, Thorlabs) collimates the beam, which is then expanded in the vertical direction only by a two-lens telescope, consisting of cylindrical lenses with $f_2 = 10\,\text{mm}$ (G318302000, Linos) and $f_3 = 40\,\text{mm}$ (G318314000, Linos). With a final achromatic lens ($f_4 = 400\,\text{mm}$, AC508-400-B, Thorlabs), the light is focused onto the atoms. In between the first and second lens, the light is polarization filtered by a polarizing beam splitter (G335743000, Linos, not shown) and before the final focusing lens, about 4% of the light is deflected for intensity stabilization using a glass plate (not shown). In (b) a measurement of the beam focus is shown for both implemented telescopes, resulting in a focus waist of about $w_0 = 71.5{\pm}1\,\mu\text{m}$ in the vertical and a beam waist of $w_0 = 245{\pm}1\,\mu\text{m}$ at the same position in the horizontal direction. The telescope for setup 2 was assembled in the course of the diploma thesis by Nick Fläschner, which was co-supervised by me.

---

heating for a given trap geometry is set by the minimal trapping power P_0. This is given by the equation $mgw_{0,\text{x}}/2 = U_\text{D}(w_{0,\text{x}}/2, 0, 0, P_0)$, which depends on the beam waist $w_{0,\text{x}}$ in the vertical direction.

Reducing the beam waist reduces the heating, since the trap effectively holds the atoms at lower powers. Directly at P_0, a straightforward calculation leads to a linear dependence of the scattering rate on the vertical beam-waist

$$\Gamma_\text{S}(P_0) = \frac{\Gamma_\text{S}(w_{0,\text{x}}, 0, 0, P_0)}{U_\text{D}(w_{0,\text{x}}, 0, 0, P_0)} \frac{mg}{2} w_{0,\text{x}} \,. \tag{2.11}$$

Consequently, to reduce the scattering rates, the vertical beam waist must be reduced. This also increases the trapping frequency in this direction and decreases the absolute gravitational sag, which provides a better overlap of the clouds, if the trap is not operated directly at the magic wavelength. However, the increased trapping frequency contradicts the main design consideration to obtain low trapping frequencies. This can be resolved by using an elliptical trap with a small waist along the vertical direction and a large waist in the horizontal yz-plane. By this, the trapping frequencies are significantly decreased in the horizontal direction, while the scattering rate remains low. This approach was used in the second dipole trap setup as discussed in the following.

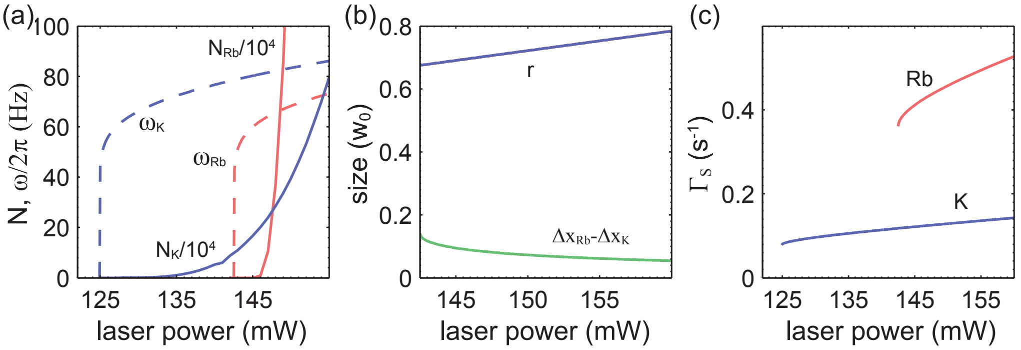

Figure 2.13: Calculation of the characteristic parameters of dipole trap setup 2 versus the beam power. Shown are the same parameters as in Fig. 2.11. Only results for an operation at 811 nm are shown, using a disk-shaped configuration with fixed relative beam powers $P_Y/P_Z = 4.46$. (a) shows the mean trapping frequencies and the particle numbers for both species, (b) the differential gravitational sag and the typical cloud size. (c) shows the inelastic scattering rates for both species versus the trap power. Due to the smaller beam waist, the heating is reduced compared to setup 1.

SECOND DESIGN: ELLIPTICAL DIPOLE TRAP

In setup 2, the circular beam in the y-direction is exchanged by a elliptical telescope with an aspect ratio of about $1:3.5$. The waists are about $71.5\,\mu$m in the vertical x-direction and about $245\,\mu$m in the horizontal z-direction as shown in Fig. 2.12. The design consists again of four lenses, two of them being cylindrical in this case. The latter two replace the beam expander, which does now only influence the vertical direction and is designed for an aspect ratio of 4. This leads to different beam diameter for the vertical and horizontal direction at the last focusing lens, and hence to an elliptical beam waist at the focus. The observed aspect ratio of 3.5 is slightly different than the expected value of 4. This might be a result from the cylindrical lenses, which do not have the same quality as the aspheric or achromatic lenses and possibly introduce wavefront errors and distort the originally Gaussian beam profile. Note, that the beam does not have a focus in the horizontal direction after the focusing lens, which is a result of Gaussian optics. This is not important for the trapping, however, since the position of the atoms along the beam is still defined by the focus in the vertical direction for a single-beam trap, and completely defined by the perpendicular beam for the crossed dipole trap setup.

All relevant parameters for the combined elliptical and circular trapping beam are shown in Fig. 2.13. The calculations show, that the scattering rate is further reduced in the new setup, while the mean trapping frequencies are comparable to the first setup. As for setup 1, this was verified using a rubidium gas near the minimal trap power, which resulted in a reduced loss rate for rubidium of 0.34 Hz for $\lambda_d = 811$ nm. This is again in good agreement with the calculated value shown in Fig. 2.13. By tuning the relative intensity in both beams, the shape of the trap can be tuned in this configuration. Typical configurations are either disk-shaped or elongated. The disk-shaped configuration, where the elliptical beam is stronger, is typical used at trapping frequencies of about $\omega_{x,y,z} = 2\pi \times (125, 42, 31)$ Hz, with trap depths of about $25\,h$kHz in the vertical direction and $100\,h$kHz in the horizontal directions. The elongated configuration, with trapping frequencies of about $2\pi \times (70, 74, 12)$ Hz, has trap depths of about $6\,h$kHz in the vertical direction and $90\,h$kHz in the horizontal directions. Both configurations have been used throughout the measurements presented in this thesis.

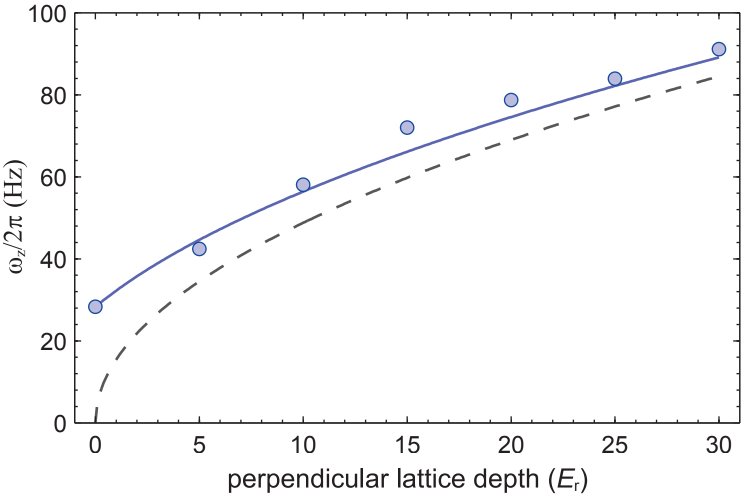

Figure 2.14: Influence of the optical lattice on the trapping frequency. The data shows the center-of-mass oscillation frequency of the atomic cloud in the tube configuration in dependence on the perpendicular lattice depth, being a direct measure for the trap frequency. The solid line shows a calculation of the combined harmonic trapping frequency from the trap and the lattice. For the calculations, the experimentally measured oscillation frequency at $V_0 = 0$ is used as the bare trap frequency. The dashed line shows the theoretically calculated trapping frequency induced by the lattice beams only.

2.4 OPTICAL LATTICE SETUP

A major part of the experiments presented in this thesis were performed using ultracold atoms in optical lattices. In the course of this thesis, a new lattice setup has been implemented in the BFM setup. It was designed, such that the increase of the trapping frequency is as small as possible, while large lattice depths can be achieved with the maximum laser power.

CUBIC OPTICAL LATTICE

The interference of two or more laser beams leads to a modulated intensity pattern on the scale of the laser wavelength. If the frequencies of all beams are equal and the relative phases are constant, a time average over the fast oscillations of the light field leads to an effectively stationary intensity pattern for the atoms. Such a periodic intensity pattern constitutes a potential for the atoms that is called an optical lattice in the following [133, 138–140]. The simplest case of an optical lattice is a retro-reflected laser beam with a wavelength λ_L, which results in a periodic sinusoidal optical potential [10]

$$V_\mathrm{L} = V_0 \sin^2(k_\mathrm{L} z)\,, \tag{2.12}$$

where the potential strength V_0 is determined by the laser intensity and the lattice vector is $k_\mathrm{L} = 2\pi/\lambda_\mathrm{L}$. The lattice has a spacing of $d = \lambda_\mathrm{L}/2$ between to adjacent sites.

In the BFM setup, three rectangular oriented, retro-reflected lattice beams of the form (2.12) are installed [22, 117, 118]. The light is produced by an Yb:YAG thin disk laser at $\lambda_\mathrm{L} = 1030\,\mathrm{nm}$ (VersaDisk, ELS), stabilized to an external cavity. The laser-setup is described in detail in [118]. The three beams are focused onto the atoms using telescopes of the same principle design as the dipole trap setup 1. They have been assembled by Malte Weinberg, whose diploma thesis was performed at the BFM setup and was co-supervised by me. The design and the waist measurements are detailed in [141]. The measured beam waists are $205{\pm}1\,\mu$m, $194.5{\pm}1\,\mu$m and $188.5{\pm}1\,\mu$m for the telescopes installed in the z-direction and the two diagonals xy and yx as sketched in Fig. 2.1. The three axes do not interfere, since they are orthogonally polarized to each other and off-resonant by a few tens of MHz [118]. Thus, the total potential is a three-dimensional, simple cubic lattice [142]. By using only one or two beams of the lattice, it is also possible to create one- or two-dimensional arrays of pancake-shaped or tube-shaped systems.

Using the existing laser setup, the new telescope design allows for the realization of optical lattice depths corresponding to up to $V_0 = 40\,E_\mathrm{r}$ for the fermionic atoms, where $E_\mathrm{r} = h^2/2m\lambda_\mathrm{L}^2$ is the energy gained by one potassium atom, if it absorbs a single photon from the lattice. The maximum depth corresponds to roughly 1 W beam power per lattice beam.

INFLUENCE ON THE TRAPPING POTENTIAL

A measurement of the influence of the optical lattice beams on the trapping frequencies is shown in Fig. 2.14 for a two-dimensional lattice of tubes. The trapping frequencies along the tubes have been determined by measuring center-of-mass oscillations of the atomic cloud along this direction. The influence of the lattice beams on the trapping frequency is still very strong, especially at large lattice depths. The trapping frequencies for different beams are added quadratically, as discussed for the crossed dipole trap above. Thus, for weak lattice potentials (small V_0), the trapping frequency is mainly determined by the external harmonic trap. For strong lattices, however, the trapping frequency is fully determined by the lattice. A comparison with the theoretically expected influence shows, that the implemented telescopes reproduce very well the aspired behavior. Reducing the additional trapping by the laser beams would require even larger beam diameters, which is not practical in the current setup due to the maximum reachable lattice depths, which are already limited in the current design. A completely different approach to circumvent the problem of large trapping frequencies at high lattice depths would be a blue detuned lattice, which reduces the trapping frequency directly [133].

CHAPTER 3

QUANTUM GASES IN OPTICAL LATTICES

In this chapter, I discuss the fundamental properties of ultracold atoms in optical lattices, relevant for the experimental results presented in the following chapters.

All experimental data was taken and analyzed together with Jasper S. Krauser and Sören Götze. The numerical calculations were performed mainly by myself. The experimental results have also been presented in the diploma thesis of Bastian Hundt, performed at the BFM setup and co-supervised by me.

3.1 SINGLE-PARTICLE DESCRIPTION: BAND STRUCTURE AND TIGHT BINDING

In this section, I review the basic theoretical description of single particles in optical lattices [10]. First, I discuss the derivation of the Bloch states and the corresponding energy spectrum, i.e. the band structure. Then I proceed to the influence of the harmonic confinement on the single-particle spectrum and end with a short description of the tight-binding approximation in the lowest energy band of the lattice.

3.1.1 SINGLE-PARTICLE BAND STRUCTURE

As described in section 2.4, the optical lattice in the BFM setup has a three-dimensional simple cubic geometry operated at $\lambda_\mathrm{L} = 1030\,\mathrm{nm}$ [22, 118]. Since all three lattice axes are separable, the excitation spectrum can be calculated for each dimension independently and the total spectrum is simply the sum of the individual contributions. Using the optical lattice potential (2.12), the single-particle Hamiltonian in one dimension of the lattice is given by [10]

$$H_\mathrm{L} = \frac{p^2}{2m} + sE_\mathrm{r}\sin^2(k_\mathrm{L}z)\,, \tag{3.1}$$

where I use the standard representation of the lattice potential strength $V_0 = sE_\mathrm{r}$ with the lattice depth s and the atomic recoil energy in the optical lattice $E_\mathrm{r} = \hbar^2k_\mathrm{L}^2/2m$ with $k_\mathrm{L} = 2\pi/\lambda_\mathrm{L}$. The eigensolution of this Hamiltonian is well known and is based on the Bloch theorem [10, 129], according to which the eigenstates of (3.1), called Bloch states, have the same periodicity as the potential $d = \lambda_\mathrm{L}/2$. They can be written as a discrete series expansion of plane waves around

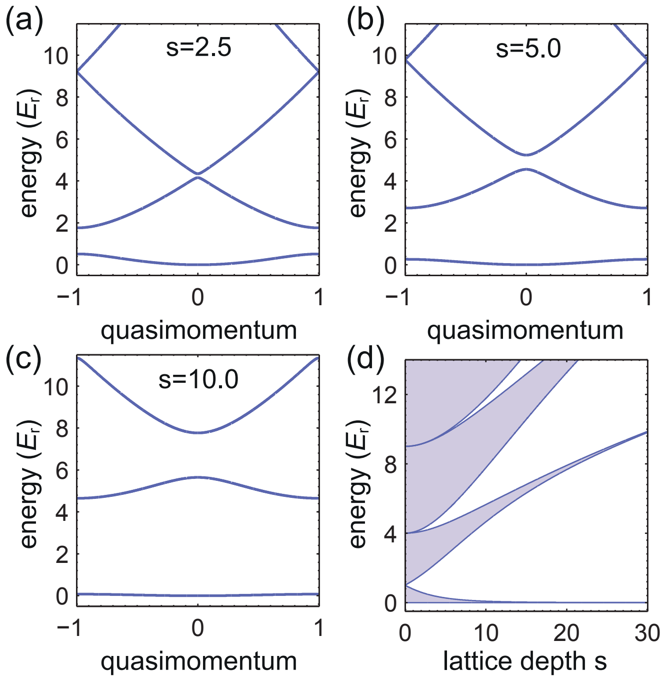

Figure 3.1: Typical band structures in a one-dimensional optical lattice, calculated with (3.3). (a)-(c) Momentum resolved band structure for three different lattice depths s as indicated in the figure. (d) Energy bands and gaps over the lattice depth. The opening of the band gaps and the decrease of the band widths are clearly visible in all figures.

---

a fixed momentum q, called the quasimomentum, which is defined dimensionless in the range $-1 < q \leq 1$ in units of k_{L}:

$$|\psi(q,n)\rangle = \mathrm{e}^{-\mathrm{i}qk_{\mathrm{L}}z} \sum_{\mathrm{k}=-\infty}^{\infty} c^{\mathrm{n}}_{\mathrm{q,k}} \mathrm{e}^{-\mathrm{i}2kk_{\mathrm{L}}z} \,. \tag{3.2}$$

The $c^{\mathrm{n}}_{\mathrm{q,k}}$ are generally real numbers in this representation. The index $n = 0, 1, 2, \ldots$ labels different solutions for the same q with increasing energy.

Inserting this expansion into the eigenvalue equation for the Hamiltonian (3.1) results in a matrix equation for the coefficients $c^{\mathrm{n}}_{\mathrm{q,k}}$, separately for each individual q

$$4(q+2k)^2 c^{\mathrm{n}}_{\mathrm{q,k}} - \frac{s}{4} c^{\mathrm{n}}_{\mathrm{q,k-1}} - \frac{s}{4} c^{\mathrm{n}}_{\mathrm{q,k+1}} = \frac{E^{\mathrm{n}}_{\mathrm{q}}}{E_{\mathrm{r}}} c^{\mathrm{n}}_{\mathrm{q,k}} \,, \tag{3.3}$$

with the energy $E^{\mathrm{n}}_{\mathrm{q}}$ of the state $|\psi(q,n)\rangle = |n,q\rangle$. The solutions for all q with equal n can be grouped into energy bands with gaps in between. The resulting eigenspectrum is uniquely defined by the parameter s, independent of the particular atomic or lattice parameters, if the spectrum is normalized to the atomic recoil energy E_{r}, as on the right hand side of (3.3).

Typical energy spectra for different s are shown in Fig. 3.1. The different energy bands and gaps in between are clearly visible. The gaps increase with the lattice depth and at the same time, the band widths decrease exponentially [see Fig. 3.1(d)]. The representation of the band structure in Fig. 3.1 is called the reduced zone scheme. An alternative representation can be obtained in the reciprocal lattice space, as shown in Fig. 3.2. Here, various Brillouin zones can be defined, corresponding to the different bands in the reduced zone scheme [142].

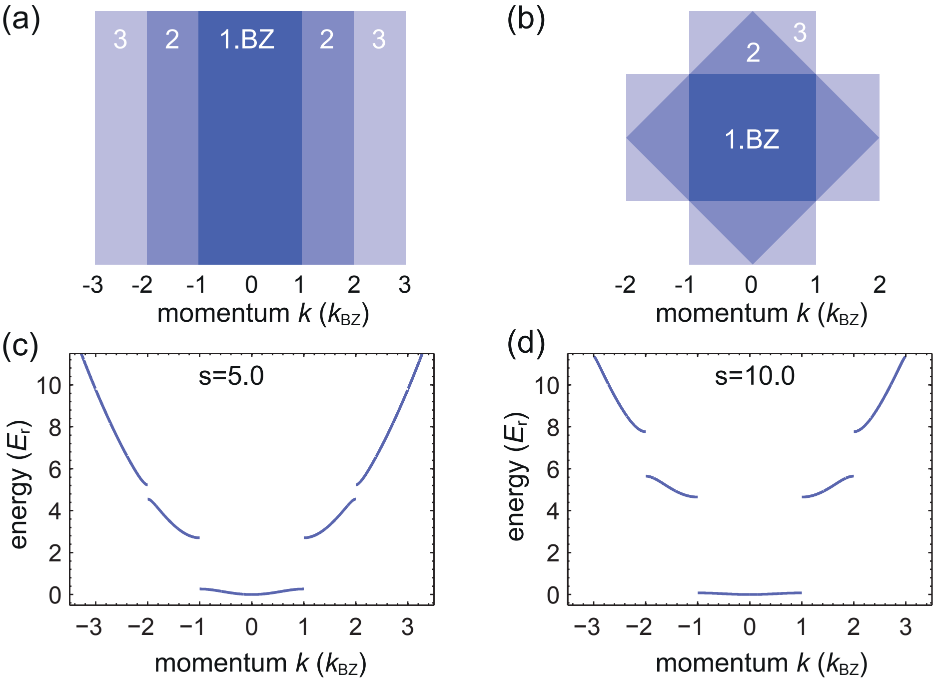

Figure 3.2: Brillouin zones and the extended zone scheme. (a) Sketch of the Brillouin zones of a one-dimensional lattice. The first Brillouin zone is between $-k_{\mathrm{BZ}}$ and k_{BZ}. The higher Brillouin zones are split to both sides at larger momenta. (b) Sketch of the Brillouin zones of a cubic lattice in two dimensions. The system consists of two perpendicular one-dimensional lattices. (c),(d) Extended zone schemes for a one-dimensional lattice at two different lattice depths s.

Expanding the different bands onto these Brillouin zones, leads to the extended zone scheme, shown in Fig. 3.2. This representation motivates the notion of the Brillouin zone momentum k_{BZ}, representing the width of the Brillouin zones. In the notation used throughout this thesis, it equals the lattice momentum $k_{\mathrm{L}} \equiv k_{\mathrm{BZ}}$. Both representations are used throughout this thesis.

3.1.2 BAND STRUCTURE WITH HARMONIC CONFINEMENT

In typical quantum gas experiments the atoms are subject to an external confinement in addition to the optical lattice, which is created by the dipole trap and the lattice beams themselves, as discussed in section 2.4. In the harmonic approximation, the trapping potential is separable in all three directions such that a one-dimensional description is possible, equivalent to the pure lattice potential [10]

$$H_{\mathrm{LT}} = \frac{p^2}{2m} + sE_{\mathrm{r}} \sin^2(k_{\mathrm{L}} z) + \frac{1}{2} m\omega^2 z^2 \,. \tag{3.4}$$

Since the trapping potential is not periodic as the lattice potential, the Bloch theorem does not apply anymore and the eigenstates cannot be expanded as in (3.2). For certain lattice depths and trapping frequencies, however, the properties of the resulting spectrum can be described similar to the bare lattice states. Note here, that the harmonic potential always rises to infinity, and thus can never be regarded as small, if large position differences are important. This is an artificial problem for the case of optically trapped atoms, resulting from the harmonic approximation, since the real potential is actually Gaussian and therefore bounded. Further, the atomic cloud has only a finite extension, leading to a second natural cutoff for the influence

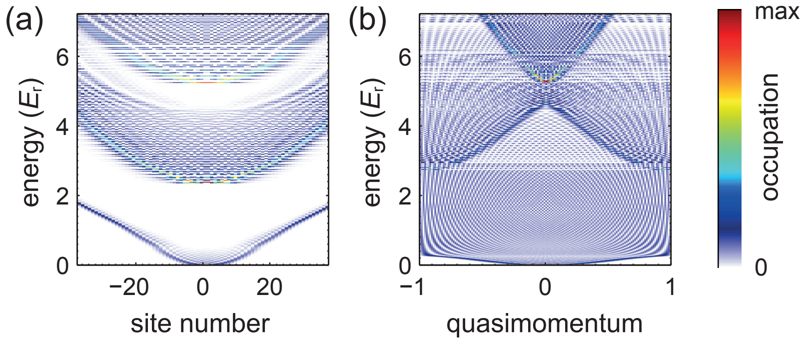

Figure 3.3: Eigenstates of a combined optical lattice and trapping potential, using (3.4). (a) Displayed is the site-resolved distribution of the eigenstates for $s = 5$ and $\omega = 2\pi \times 100\,\mathrm{Hz}$. Inspecting especially the lowest band shows, that states in the original band gap appear, which are localized far away from the center of the trap. (b) shows the corresponding momentum distribution. In this representation the band gaps vanish in the trapped system. However, the individual bands are still clearly visible (compare to Fig. 3.1). Comparing both representations clearly shows, that the states in the former band gap are delocalized in the quasimomentum, as expected for localized states.

---

of long-distance effects. Therefore, it is possible to consider a given trapping potential as small under appropriate circumstances.

If the maximum energy difference $\Delta\varepsilon$ between two neighboring lattice sites due to the trapping potential is much smaller than the band gaps of the optical lattice potential, the potential can locally be regarded as periodic at an approximately constant background energy, leading to a local band structure. Typical lattice depths in the experiment range from $2\,E_\mathrm{r}$ to $30\,E_\mathrm{r}$. The corresponding band gap between the lowest and the first excited band ranges thereby from approximately $4.5\,h$kHz to $45\,h$kHz for ^{40}K. The maximal potential difference between two lattice sites is given by the largest potential gradient in the Gaussian potential. For the elliptical dipole trap implemented in the BFM setup, this leads to maximal values of $0.2\,h$kHz to $0.5\,h$kHz for $\Delta\varepsilon$ at the typical working point without a lattice. It increases up to $0.5\,h$kHz to $2\,h$kHz for an additional lattice of $30\,E_\mathrm{r}$. Hence, for all experiments presented in this thesis, a local band structure can be defined, where the different bands are well separated.

A calculation of the band structure for the combined lattice and dipole trap is shown in Fig. 3.3. The local band structure is clearly visibly. Note, that the states at the edge of the system are strongly localized and therefore have a flat momentum distribution. Therefore, the momentum resolved energy spectrum has no gaps anymore, in contrast to the purely periodic potential. However, if only local processes are considered, the described situation is very similar to the homogeneous case with respect to interband properties. The global vanishing of the band gap has no relevant influence.

On the contrary, the main influence of the trap in the considered parameter regime is the coupling of Bloch states with different quasimomenta q within the individual bands. A typical situation for the lowest energy band is shown in Fig. 3.4. The calculation shows two different types of states. States that are energetically located within the original band width ΔE are well localized at a given quasimomentum and delocalized in real space. They resemble the Bloch states of the homogeneous optical lattice. The other class of states are the localized states. They have no significant contribution in the trap center and are localized spatially in the outer part of the trap, while their momentum distribution is completely delocalized [33]. These localized states have no analog in the homogeneous optical lattice, but are similar to

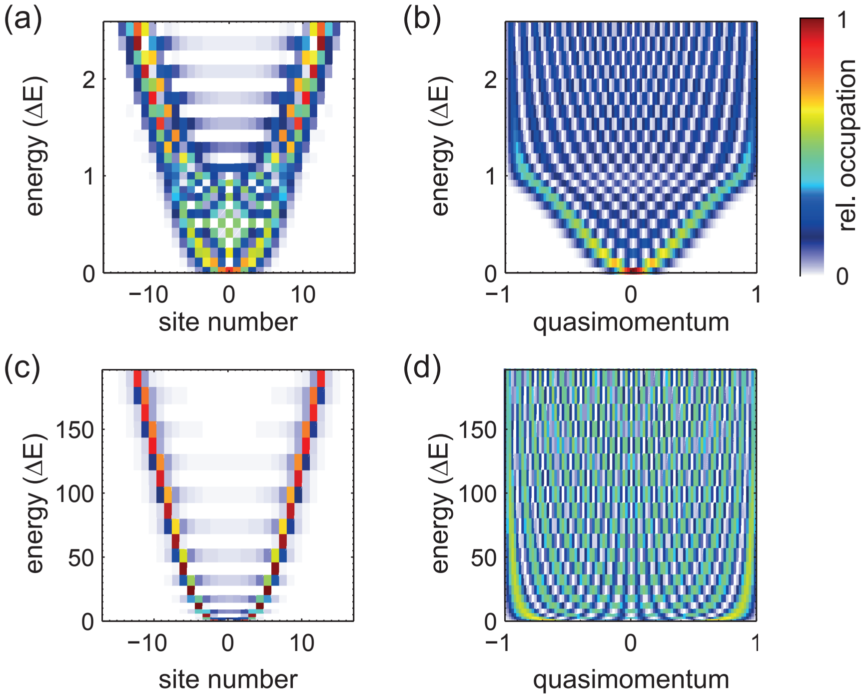

Figure 3.4: Eigenstates of a lowest energy band of the combined optical lattice and trapping potential for calculated using (3.4). (a) and (b) show the spatial and momentum distribution of the first 25 eigenstates of the lowest energy band for $\omega = 2\pi \times 100\,\mathrm{Hz}$ and $s = 10$. The energy is given relative to the bandwidth ΔE of the lowest energy band, which is $\Delta E/h \approx 361\,\mathrm{Hz}$. For energies smaller than ΔE, the states are delocalized in the center of the trap. For larger energies, the states become localized in the wings of the system. (c) and (d) show the same as (a) and (b) for $\omega = 2\pi \times 150\,\mathrm{Hz}$ and $s = 30$. Here, $\Delta E/h \approx 5\,\mathrm{Hz}$, and practically the all states are localized due to the lattice potential.

---

the eigenstates in Wannier-Stark ladders, where a strong linear potential induces localization in periodic potentials [143].

The size of the delocalized part in the center strongly depends on the exact lattice and trap parameters and generally increases with the ratio $\Delta E/\omega^2$. If the trap-induced energy difference between the central and its neighboring site, given by

$$\Delta\varepsilon_0 = \frac{1}{2} m\omega^2 \left(\frac{\lambda_\mathrm{L}}{2}\right)^2 , \tag{3.5}$$

is larger than the bandwidth ΔE, the delocalized region in the trap center becomes vanishingly small. The transition point to this regime in dependence on the trapping frequency and the lattice depth is shown in Fig. 3.5. For comparison, the typical experimental regime for ^{40}K in the the BFM setup is depicted. The results show, that the fully localized regime is reached in the experimentally accessible parameter range.

For this regime, a description in the basis set of delocalized Bloch state is not sensible anymore. Figure 3.5 shows the transition point to a totally localized system in dependence on the lattice depth and the trapping frequency. A comparison with the typical experimental parameters shows, that this regime is reached for deep lattices in the BFM setup and is therefore relevant for the interpretation of the experimental results. This holds especially for the ground state properties of fermionic atoms in the trapped lattice system as discussed in section 3.2.

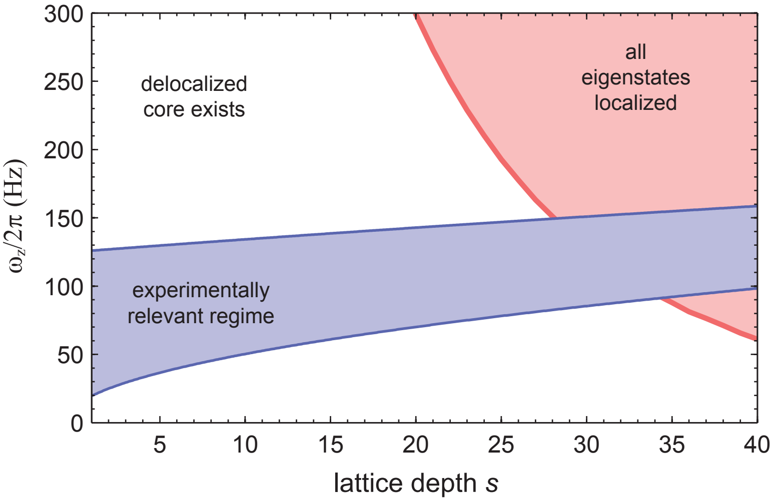

Figure 3.5: Regimes of harmonically trapped lattice systems. The red curve depicts the trapping frequency, where the width of the lowest energy band of the lattice is equal to the energy difference between the central lattice state and its neighbor. For larger trapping frequencies, all eigenstates of the system are completely localized already due to the harmonic potential. The blue shaded area shows the experimentally relevant regime for the BFM setup, assuming bare trapping frequencies between $2\pi\times 12\,\mathrm{Hz}$ and $2\pi\times 125\,\mathrm{Hz}$. The calculations take into account the increase of the trapping frequency due to the lattice beams (see Fig. 2.14).

3.1.3 TIGHT-BINDING APPROXIMATION

As the Bloch function basis set is not suitable for the regime of exclusively localized eigenstates, it is desirable to obtain an alternative representation, which appropriately describes the localized case. The most common alternative approach is the tight-binding approximation [142, 144, 145], which uses the so-called Wannier functions [21, 146] as a basis set. This description has also advantages, when dealing with interacting lattice systems, where a localization can occur at strong interactions [15].

For simplicity, I restrict the following discussion of the tight-binding approximation to the lowest band of the optical lattice, while in principle it can also be applied to excited bands. Wannier functions constitute the maximally localized states that can be constructed exclusively from the Bloch functions of the discussed energy band. For the lowest energy band they are given by [145]

$$w_{\mathrm{i}}(z) = \int dq \mathrm{e}^{\mathbb{i} z_{\mathrm{i}} q} |0, q\rangle \,, \tag{3.6}$$

forming an equivalent basis set to the Bloch functions $|0, q\rangle$. Note, that the description is again separable in all three dimensions, if the potential is separable. A particle in a given Wannier function w_{i} can be interpreted as occupying the corresponding lattice site i [21]. Starting from the Wannier functions the matrix elements of the Hamiltonian (3.1) for all pairs of lattice sites

$$J_{\mathrm{i,j}} = \int dz w_{\mathrm{i}}(z) H_{\mathrm{L}} w_{\mathrm{j}}(z) \tag{3.7}$$

describe the tunneling from site i to site j in the lattice potential.

The tight-binding approximation assumes, that the matrix elements $J_{\mathrm{i,j}}$ are negligibly small for $|j - i| > 1$, that is, for beyond nearest-neighbor tunneling (see Fig. 3.6). In this regime, the

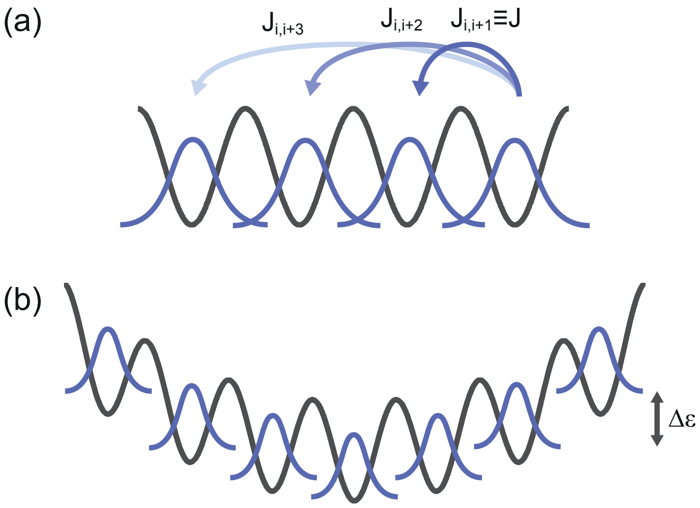

Figure 3.6: Lowest band Wannier functions and corresponding tunneling processes. (a) Sketch of the Wannier function in a homogeneous lattice. The overlap between Wannier functions at adjacent lattice sites is largest, while it becomes negligible for larger distances. (b) Sketch of the system including the harmonic confinement. If the offset energy difference $\Delta\varepsilon$ between two adjacent sites becomes larger than the typical tunneling energy, the tunneling becomes offresonant and the particles localized.

---

lattice Hamiltonian can consequently be approximated as

$$H_{\mathrm{L}}^{0} = -J \sum_{\langle \mathrm{ij} \rangle} a_{\mathrm{i}}^{\dagger} a_{\mathrm{j}} \,, \tag{3.8}$$

where $J \equiv J_{\mathrm{i,i+1}}$, the brackets in the sum index indicate a sum only over indices with $|j-i| = 1$ and the operators $a_{\mathrm{i}}^{(\dagger)}$ are the usual annihilation (creation) operators which obey the fermionic or bosonic anti-commutation or commutation relations, respectively. The energy spectrum of this Hamiltonian can be calculated analytically as

$$E_{\mathrm{q}}^{0} = -2J\cos(\pi q) \,. \tag{3.9}$$

Numerical calculations show, that (3.9) approximates the results for the full optical lattice potential very good for $s \gtrsim 3$. Note, that this result connects the width of the lowest energy band with the tunneling amplitude between two neighboring lattice sites. This means, that the amount of energy that a particle can gain by delocalizing over the full lattice is limited by the tunneling amplitude.

The harmonic confinement can be included in the tight-binding description by calculating the corresponding matrix elements

$$\varepsilon_{\mathrm{i}} = \int dz w_{\mathrm{i}}(z) \frac{1}{2} m\omega^2 z^2 w_{\mathrm{i}}(z) \,. \tag{3.10}$$

This leads to an additional term in the Hamiltonian as (see Fig. 3.6)

$$H_{\mathrm{LT}} = -J \sum_{\langle \mathrm{ij} \rangle} a_{\mathrm{i}}^{\dagger} a_{\mathrm{j}} + \sum_{\mathrm{i}} \varepsilon_{\mathrm{i}} a_{\mathrm{i}}^{\dagger} a_{\mathrm{i}} \,. \tag{3.11}$$

The Hamiltonian (3.11) allows to directly compare the energy offset $\Delta\varepsilon$ between neighboring sites induced by the harmonic confinement to the tunneling energy. If the offset exceeds

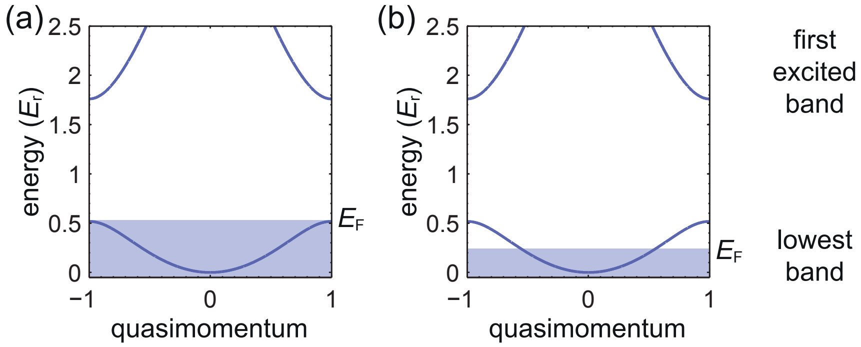

Figure 3.7: Ground state of a homogeneous ideal Fermi gas. (a) shows a band insulator, where the lowest band is completely filled and the Fermi energy E_F lies above the band. The excitation spectrum has a gap, given by the distance to the next band. (b) shows a metallic state, where E_F lies within the band. The corresponding excitation spectrum is gapless for an infinite system.

---

the tunneling energy between two sites, the tunneling becomes offresonant and is suppressed, leading to the emergence of the localized states. This clarifies the emergence of the localized states observed in the numerical results above, since the band width is directly connected to the tunneling energy.

3.2 ULTRACOLD FERMIONS IN OPTICAL LATTICES

I now turn to the many-body properties of quantum gases in optical lattices. I start here with the description of fermionic systems and proceed in the following section with a short introduction of Bose-Fermi mixtures in optical lattices.

3.2.1 SINGLE-COMPONENT FERMIONS

At ultralow temperatures, indistinguishable fermions atoms in the same internal hyperfine state do not interact. The reason for this is, that an energy barrier prevents interactions involving a finite relative angular momentum of the two atoms [147]. Therefore, only s-wave scattering is possible at these temperatures. However, Pauli blocking prevents s-wave collisions between identical fermions. As a result, an ultracold gas of spin-polarized fermions constitutes an ideal Fermi gas [10]. At $T = 0$, the only free parameter in the description of this system is the Fermi energy E_F.

For the case of a one-dimensional system in a periodic potential the many-body Hamiltonian for N fermions reads [148]

$$H = \sum_{\mathrm{k}=1}^{\mathrm{N}} \frac{p_\mathrm{k}^2}{2m} + sE_\mathrm{r}\sin^2(k_\mathrm{L} z_\mathrm{k}) \, , \tag{3.12}$$

where the index k denotes the different particles. The eigenstates are given by different combinations of occupations of Bloch states, where each state can only be occupied once due to the Pauli exclusion principle. The ground state is given by the occupation of the lowest energy states only, where the Fermi energy is the energy of the highest occupied state. Note, that the ground state in ultracold atom experiments usually contains only particles in the lowest energy band [46]. Thus, I refer exclusively to this situation in the following.

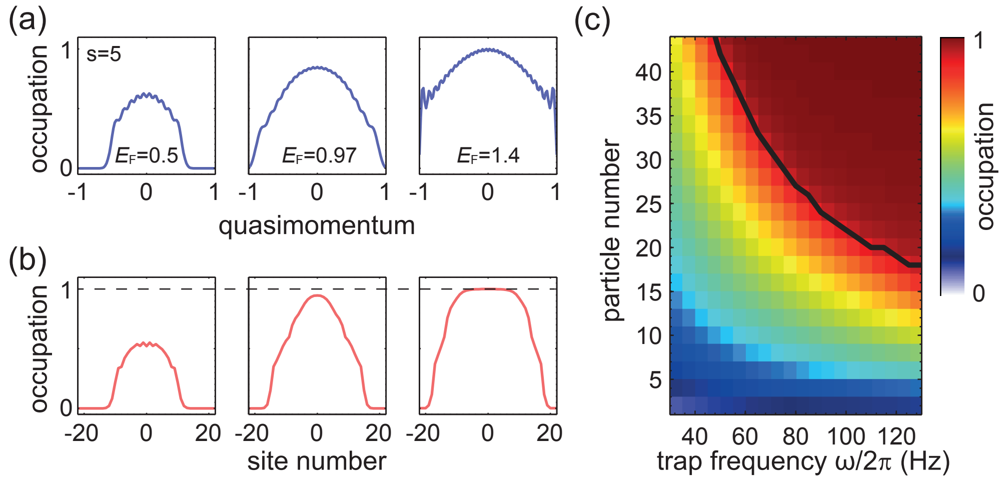

Figure 3.8: Ground state of a trapped ideal Fermi gas at zero temperature. (a) Momentum distribution of a one-dimensional system for different Fermi energies E_{F} at a lattice depth of $s = 5$ and a trapping frequency of $\omega = 2\pi \times 100\,\mathrm{Hz}$. The Fermi energies are given in units of the band width ΔE of the lowest energy band. The filling varies from a metallic state with a partly filled Brillouin zone to a band insulator, where the whole Brillouin zone is filled. When the Fermi energy coincides with the band width, the system reaches an approximate unity occupation in the center, becoming insulating for all larger Fermi energies. (b) Density distributions for the same parameters as in (a). The metallic and insulating phases can be clearly distinguished due to the core with unity filling in the latter case. The eigenstates have been calculated using (3.4). (c) Filling of the central lattice site in dependence on the number of particles and the trapping frequency. The solid line shows the particle number, at which the Fermi energy coincides with the band width ΔE for the different trapping frequencies.

In general, two distinct classes of ground states can be found for the ideal Fermi gas in an optical lattice, as sketched in Fig. 3.7. First, if all states of the lowest band are populated the only possible excitations are transitions to the first excited band. These excitations have a large energy gap and cannot be induced by small perturbations to the system. Therefore, this state is incompressible and insulating and is called a band insulator. The second class of states are characterized by a Fermi energy within the lowest band, such that excitations can be created within the band. This allows for compression of and conduction in the state, which is therefore called metallic.

The above considerations rely on the particular properties of the gapped band structure of the homogeneous system. In trapped systems, as usual for ultracold atom experiments, the gapped structure does no longer exist globally, and therefore a generalization of the band insulating state must be defined.

A numerical calculation of the momentum and site occupation is shown in Fig. 3.8 for a one-dimensional system. It is clearly visible, that a unity occupation in the center of the trap emerges at $E_{\mathrm{F}} = \Delta E$, which extends for larger Fermi energies. At the same time, the Brillouin zone becomes completely filled similar to the band insulator transition in the homogeneous system. In contrast, for $E_{\mathrm{F}} < \Delta E$ only the central momenta within the first Brillouin zone contribute to the many-body ground state and the local number of particles is below one for each lattice site. These properties resemble the metallic state from the homogeneous case very well.

These numerical results imply a generalization of the band insulator by choosing the same criterion as for the homogeneous system, i.e., that the Fermi energy reaches the largest energy of the lowest energy band $E_\mathrm{F} = \Delta E$ [26, 46]. In addition to the emerging unity filling in the trap center, this energy coincides with the change of the single-particle eigenstate properties, from delocalized to localized as shown in Fig. 3.4. Hence, a tunneling blockade arises in two different ways. First, a unity filling in the center blockades any flow due to Pauli blocking. Second, the localized states at the edge are intrinsically insulating, such that the system becomes insulating for $E_\mathrm{F} \geq \Delta E$.

In the case of ultracold atoms, it is possible to choose the dimensionality of the lattice potential freely. The above discussion covers a real one-dimensional system, which can be realized by using two deep and one shallow lattice direction, such that tunneling in the two strong directions is completely suppressed. The discussion is also valid for two-dimensional systems, where only one lattice is very strong, and for a three-dimensional systems where all lattice directions are equally strong. If the Fermi energy lies within the band gap of all shallow lattice directions, the system is band insulating in all cases. It is also possible to create systems with lattice potentials only in one or two dimensions and the remaining directions being only harmonically trapped. This constitutes a coupled array of pancake shaped Fermi gases or a coupled square lattice of tubes as discussed in section 2.4. In this case, however, it is also possible to tune the lattice potential, such that the Fermi energy is in between two bands of one of the lattice directions. The above considerations do not directly apply in this case, since each pancake or tube has many occupied states and a band insulator is not directly formed. It turns out, however, that the system still becomes insulating regarding transport in the lattice directions. This is a direct consequence of the localized states, which hinder any transport into or out of the inner region due to Pauli blocking [47]. If a particular physical effect does only rely on the state occupation or transport properties in a certain direction of the optical lattice, the real band insulator and the lower-dimensional lattice cases are completely equivalent.

3.2.2 BAND MAPPING

In order to detect the above mentioned band insulator, it is necessary to accurately measure both, the momentum distribution within the band and the absolute band occupation of the different bands. This can be achieved by the band-mapping method [149, 150]. For this purpose, the optical lattice potential is reduced slowly compared to the band gap, such that there is not enough energy to create band transitions at any time. In the homogeneous lattice, also the different quasimomentum states are uncoupled, such that each state in the lattice is unambiguously mapped onto one single real momentum state. Thereby, the lowest energy band is mapped onto the first Brillouin zone, the first excited band is mapped onto the second Brillouin zone and so on. A good mapping can be obtained with ramping times in the order of a few ms, avoiding excitations to higher bands. As the size of the band gaps decreases exponentially with the lattice depth, the best band mapping ramp is also an exponential ramp being fast at high lattice depths and slow at small lattice depths.

For trapped systems, the external potential couples Bloch states with different quasimomenta. To avoid a redistribution of the quasimomentum states during the band mapping itself, the mapping time must be much shorter than the typical dynamical timescale in the trap, given by the harmonic oscillation period $P = 2\pi/\omega$. In a real system this prevents a perfect band mapping. The band mapping is especially sensitive at the band edges. If the band-mapping ramp is too fast, transitions between different bands are possible and the absolute band occupation is imperfectly mapped, while the quasimomentum distribution is correctly mapped [150]. If the band-mapping time is too long, the lattice states are not mapped onto free momenta, but on the eigenstates of the external trap. This averages out any information about the quasimo-

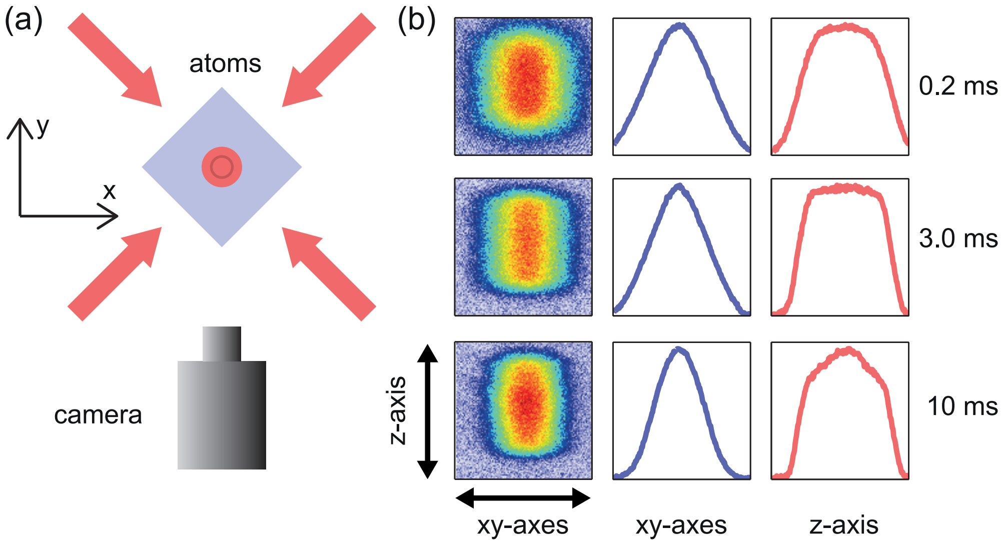

Figure 3.9: Band mapping in the experiment. (a) Sketch of the lattice geometry in the y-direction. The lattice beams in the xy-plane are diagonal to the camera while the beam in the z-direction is perpendicular. Thus, the lattice is oriented in a $45°$ angle to the camera in the y-direction in the xy-plane, leading to a triangular density profile. In the z-axis it is oriented perpendicular, leading to a rectangular profile. (b) shows experimental band mapping results for various band mapping times, starting from an initial band insulating state at $s = 12$ with trapping frequencies of about $2\pi \times (100, 31, 31)$ Hz before the lattice is ramped up. The particle number is about 1.8×10^5 and the temperature $0.1\,T_{\mathrm{F}}$. For short band mapping times (0.2 ms), the distribution becomes smooth at the wings because of transitions of particles to higher bands during the band mapping procedure. At intermediate ramping times (3 ms), the density profile well resembles the expected triangular shape and the plateau from th two different directions. For very long ramping times (10 ms), the atoms are influenced by the trap, which leads to a distortion of the density profile, which no longer maps out the quasimomentum. For longer ramping times, the system would eventually occupy the ground state of the harmonic potential.

mentum distribution. A band-mapping measurement for different ramping times is shown in Fig. 3.9, demonstrating this behavior for a gas deep in the band insulator regime.

3.2.3 INTERACTING FERMI-FERMI MIXTURES

Interactions are suppressed in a single-component Fermi gas due to Pauli blocking, which does not allow for two fermions to be in the same single-particle quantum state simultaneously. Including an additional internal degree of freedom circumvents this restriction. If two fermions occupy different internal states, they can occupy the same spatial quantum state and thus interact via s-wave scattering [14]. S-wave interactions can be described in the pseudo-potential approach as a local δ-function for the relative particle position, with an interaction strength that is defined by a single effective hard-sphere scattering radius a, called the scattering length [151]. For ^{40}K its value is about $a \approx 170\,a_{\mathrm{B}}$ [152], which is discussed in more detail in chapter 6 (a_{B} is the Bohr radius). For later use, the interaction strength is usually abbreviated by $g = 4\pi\hbar^2 a/m$. Note here, that the positive value of the scattering length means, that the particles interact repulsively.

To describe a system with two internal states $\sigma = \pm$, the single-component Hamiltonian

(3.12) must be extended by an interaction term as [16]

$$H = \sum_{\sigma}\Big[\sum_{\mathrm{k}_\sigma=1}^{\mathrm{N}_\sigma}\frac{\vec{p}_{\mathrm{k}_\sigma}^{\,2}}{2m}+\sum_{\alpha}s_\alpha E_{\mathrm{r}}\sin^2(k_{\mathrm{L}}r_{\mathrm{k}_\sigma,\alpha})\Big]+g\sum_{\mathrm{k}_+,\mathrm{k}_-}\delta(\vec{r}_{\mathrm{k}_+}-\vec{r}_{\mathrm{k}_-})\,. \tag{3.13}$$

Due to the interaction term, the Hamiltonian (3.13) does no longer separate for the different directions and cannot be solved in general. Therefore, it is common to use an approximated Hamiltonian, called the Fermi-Hubbard model [15, 144, 153]. This model is based on the tight-binding description introduced in section 3.1.3. In addition to the nearest-neighbor tunneling term (3.8), the interaction is taken into account only on-site, described by the interaction matrix element

$$U = \frac{4\pi\hbar^2}{m}a\int dx|w(x)|^4\int dy|w(y)|^4\int dz|w(z)|^4\,, \tag{3.14}$$

using the Wannier functions w on each lattice site. I assume in (3.14) a three-dimensional cubic lattice with equal lattice depths s in all directions.

The full Fermi-Hubbard Hamiltonian is [153]

$$H_{\mathrm{FH}} = -J\sum_{\sigma}\sum_{\langle \mathrm{ij}\rangle}a^\dagger_{\mathrm{i},\sigma}a_{\mathrm{j},\sigma}+U\sum_{\mathrm{i}}a^\dagger_{\mathrm{i},+}a^\dagger_{\mathrm{i},-}a_{\mathrm{i},-}a_{\mathrm{i},+}\,, \tag{3.15}$$

where the indices i, j represent different lattice sites. This Hamiltonian is very well realized for ultracold atoms in optical lattices in the tight-binding regime and with scattering lengths much smaller than the intersite distance $a \ll \lambda_{\mathrm{L}}/2$.

At small interactions $U \ll J$, the ground state of the system is either a band insulator or a metal, depending on the Fermi energy, as in the noninteracting case. Note, however, that in the band insulator all sites are filled by two fermions in this case, one of each species.

If the repulsive interaction is large and dominates the system ($U \gg J$), the system becomes Mott insulating [25, 26]. In this regime, tunneling to an already occupied site is prohibited also, if the particles are of different spin states, since the increase in interaction energy exceeds the gain in energy due to the tunneling. Therefore, the ground state has only singly-occupied sites and strongly reduced particle number fluctuations on individual lattice sites The excitation spectrum becomes gapped with a gap energy of U, even though the lattice is only half filled. The gap excitation corresponds to the excitation of a single particle to an already occupied site [25]. This creates an empty site and a doubly occupied site, which is energetically suppressed. Therefore, tunneling is inhibited and the state becomes incompressible [26] and insulating.

For inhomogeneous systems as realized in the experiment, a shell structure is possible with a band insulator in the center and a Mott insulator shell around it. In between and in the wings, the system shows a metallic behavior [154].

3.3 ULTRACOLD BOSE-FERMI MIXTURES IN OPTICAL LATTICES

This section provides a short introduction of the description of Bose-Fermi mixtures in optical lattices and especially some features regarding the BFM setup . I start with the Hamiltonian of a single-component Bose gas in an optical lattice, given by [10]

$$H = \sum_{\mathrm{k}=1}^{\mathrm{N}}\Big(\frac{\vec{p}_{\mathrm{k}}^{\,2}}{2m}+\sum_{\alpha}s_\alpha E_{\mathrm{r}}\sin^2(k_{\mathrm{L}}r_{\mathrm{k},\alpha})\Big)+g\sum_{\mathrm{k}\neq\mathrm{l}}\delta(\vec{r}_{\mathrm{k}}-\vec{r}_{\mathrm{l}})\,. \tag{3.16}$$

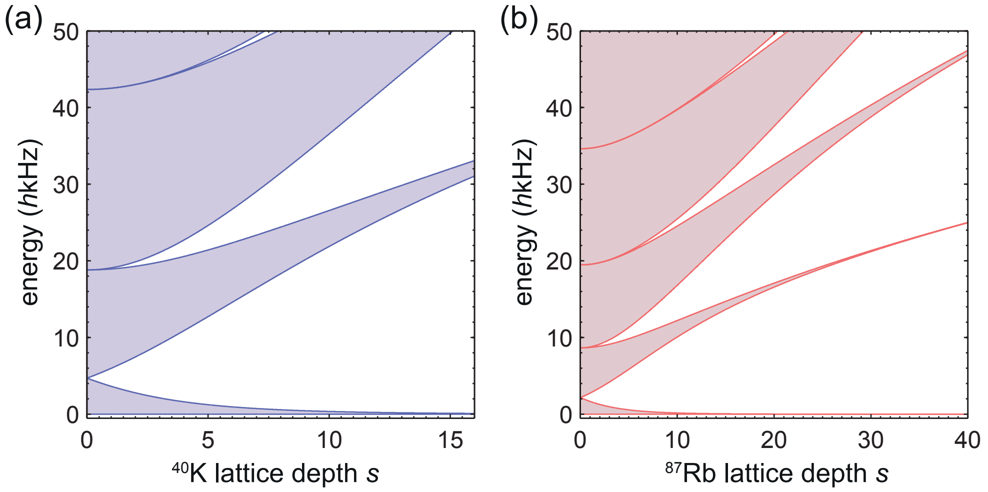

Figure 3.10: Comparison of the band structure of (a) ^{40}K and (b) ^{87}Rb in the $1030\,\mathrm{nm}$ optical lattice of the BFM setup, calculated using (3.3). The plotted regions correspond to the same lattice intensities, where the effective lattice depth for ^{87}Rb is approximately a factor of 2.5 larger than for ^{40}K.

Since bosons are not subject to Pauli blocking, they can interact also at very low temperatures via s-wave scattering. For ^{87}Rb the scattering length is about $a \approx 100\,a_\mathrm{B}$ [155]. For small interactions the bosons form a superfluid state with strong number fluctuations, in contrast to the metallic state of the fermions. As for the fermions, the repulsive interaction leads to a Mott insulating state at large interactions [21, 22]. Since multiple identical bosons can occupy a single site, the Mott insulator for the bosonic atoms can consist of different shells with equal integer filling of $n = 1, 2, 3, \ldots$ [156, 157].

Combining bosons and fermions in an optical lattice leads to an additional interaction term between them. The total Hamiltonian of the Bose-Fermi mixture in an optical lattice is given by [158]

$$\begin{aligned} H_\mathrm{bf} = & \underbrace{\sum_{\mathrm{k}=1}^{\mathrm{N_f}} \left(\frac{\vec{p}_\mathrm{k}^{\,2}}{2m_\mathrm{f}} + \sum_\alpha s_\alpha^\mathrm{f} E_\mathrm{r}^\mathrm{f} \sin^2(k_\mathrm{L} r_{\mathrm{k},\alpha}) \right)}_{\mathrm{H_f}} \\ & + \underbrace{\sum_{\mathrm{l}=1}^{\mathrm{N_b}} \left(\frac{\vec{p}_\mathrm{k}^{\,2}}{2m_\mathrm{b}} + \sum_\alpha s_\alpha^\mathrm{b} E_\mathrm{r}^\mathrm{b} \sin^2(k_\mathrm{L} r_{\mathrm{k},\alpha}) \right) + g \sum_{\mathrm{k}\neq\mathrm{l}} \delta(\vec{r}_\mathrm{k} - \vec{r}_\mathrm{l})}_{\mathrm{H_b}} \\ & + \underbrace{g_\mathrm{bf} \sum_{\mathrm{k,l}} \delta(\vec{r}_\mathrm{k} - \vec{r}_\mathrm{l})}_{\mathrm{H_{bfi}}} \,, \end{aligned} \tag{3.17}$$

where the indices b and f indicate the different parameters for bosons and fermions. The Hamiltonian (3.17) is the sum of the single component bosonic and fermionic Hamiltonians (3.12) and (3.16), and an additional contribution, given by the interspecies interaction H_bfi. This additional term has a scattering strength $g_\mathrm{bf} = 2\pi\hbar^2 a_\mathrm{bf}/\mu$, where the reduced mass of the interacting bosons and fermions is given by $\mu = m_\mathrm{f} m_\mathrm{b}/(m_\mathrm{f} + m_\mathrm{b})$. The interspecies scattering length for mixtures of ^{40}K and ^{87}Rb is $a_\mathrm{bf} = -\,185\,a_\mathrm{B}$ [159, 160]. This interaction is attractive in contrast to the repulsive intraspecies interaction of ^{87}Rb. The attractive nature of the interaction is expected to induce many fascinating effects, thoroughly discussed in the literature [23, 56, 77–85, 161, 162].

At the BFM setup an optical lattice is implemented, which is far detuned with respect to both species ^{40}K and ^{87}Rb. Therefore, they experience approximately the same lattice potential $V_0 = s^{\mathrm{f}} E_{\mathrm{r}}^{\mathrm{f}} \approx s^{\mathrm{b}} E_{\mathrm{r}}^{\mathrm{b}}$. Since the mass ratio of $m_{\mathrm{b}}/m_{\mathrm{f}} \approx 2$ leads to different recoil energies $E_{\mathrm{r}}^{\mathrm{b/f}}$, both species experience different lattice depths $s^{\mathrm{b/f}}$ at the same lattice intensity. Including carefully all experimental parameters, in particular the slightly different detuning for both species, the absolute lattice-depth ratio can be calculated as $s^{\mathrm{b}}/s^{\mathrm{f}} \approx 2.5$. The resulting band structure of both species for equal laser intensity is compared in Fig. 3.10, highlighting that the rubidium atoms experience a much deeper lattice than the potassium atoms. This indicates, that the tunneling amplitude is much smaller for rubidium than for potassium in the mixture. It is therefore possible to create a mixture with bosons deep in the Mott insulating phase, while the fermions still have a large tunneling amplitude.

CHAPTER 4

MULTIBAND SPECTROSCOPY OF ULTRACOLD FERMIONS

The excitation spectrum of a given quantum system allows for the determination of many of its fundamental properties. The development of novel spectroscopy and probing techniques is therefore very important to characterize, understand and control novel quantum systems. Since the advent of ultracold quantum gases, several spectroscopy techniques have been developed. In particular, a full momentum resolution allows for the measurement of the dispersion relation of the system, which carries practically all information on the underlying quantum state. Examples for momentum-resolved spectroscopy techniques in ultracold gases are optical Bragg spectroscopy, where a moving lattice is superimposed with the system [7, 35–37, 163–167], and rf-spectroscopy, typically applied to strongly interacting bulk Fermi gases [168]. An especially elegant spectroscopy method, however, lacking momentum resolution thus far, is lattice amplitude modulation [169–171], which requires no additional setup components. It has been used to measure the gapped excitation spectrum of strongly interacting bosonic and fermionic systems [25, 34], as well as to perform pump and probe experiments involving higher bands [172].

In this chapter, I describe a newly developed, momentum-resolved spectroscopy method for ultracold fermionic atoms in optical lattices. It allows for the determination of the full band structure with very high accuracy, similar to ARPES in solid state physics [173]. From the band structure, the tunneling energy can be directly inferred as a function of the lattice depth (see section 3.1.1). The presented spectroscopy is based on lattice amplitude modulation, using excitations to higher spatial bands. Combining the excitation with a quasimomentum-resolved detection, provided by the band-mapping technique, allows for the full momentum resolution as discussed below.

Beyond the demonstration and evaluation of the multiband spectroscopy, the method was employed to investigate the behavior of attractively interacting Bose-Fermi mixtures [23, 24, 71]. These constitute a prominent example for novel quantum systems only realizable in ultracold matter. Pioneering experiments detected a shift of the bosonic Mott insulator transition in the presence of fermions [23, 24, 76]. This observation initialized a strong debate about the origin of this shift [56, 82–85, 161]. One of the explanations attributes this effect to an interspecies interaction induced self-trapping with effective tunneling and interaction parameters [56, 76], while other theoretical studies attribute it to adiabatic heating in the attractive mixture [82, 84], or to offsite interaction induced tunneling [83, 85]. Measurements of the interaction energies in the mixture are consistent with the effective parameter description [162]. However,

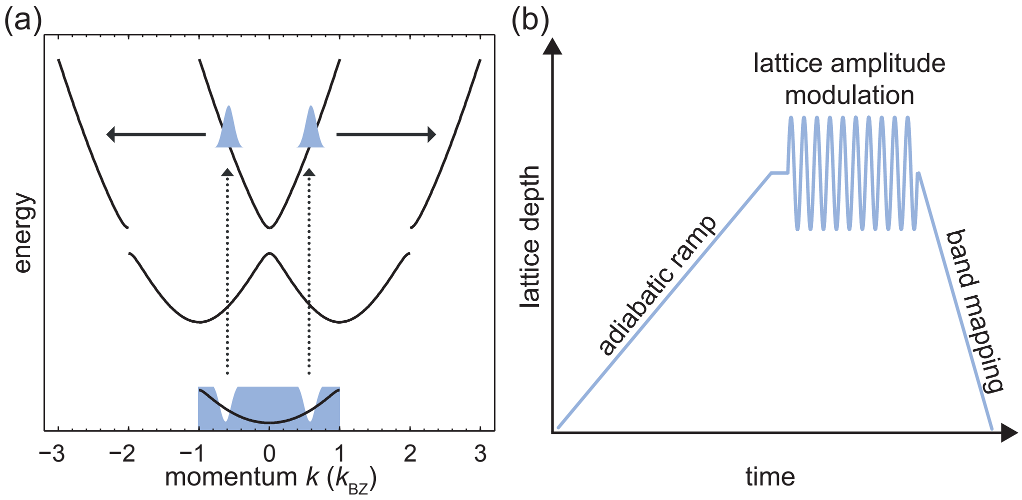

Figure 4.1: Sketches of the multiband spectroscopy procedure. (a) Sketch of the excitation (dotted line) and detection (solid line) processes in momentum space, as detailed in the text. (b) Sketch of the lattice depth over time. First the lattice depth is adiabatically increased within 100 ms from zero to the final value, followed by a 1 ms lattice amplitude modulation pulse that excites atoms to the second excited band. Finally the momentum distribution is mapped out via a band-mapping procedure.

so far it has not been possible to directly observe the reduced tunneling, which is the main origin of the transition shift in this theoretical approach.

As presented in this chapter, the novel multiband spectroscopy has been used in this thesis to investigate the shift of the fermionic tunneling in the presence of a bosonic cloud. In these measurements, a reduction of the tunneling amplitude is observed, directly confirming a change of the single-particle tunneling properties due to the interspecies interaction.

All experimental data presented this chapter was taken and analyzed together with Jasper S. Krauser and Sören Götze. The numerical and analytical calculations were performed mainly by myself. The results of this chapter have been partly published in [6]. The spectroscopy technique has also been discussed in the diploma thesis of Bastian Hundt [174], performed at the BFM setup, which was co-supervised by me.

4.1 PRINCIPLES OF THE MULTIBAND SPECTROSCOPY

In this section I present the experimental implementation of the newly developed multiband spectroscopy. The general idea of the multiband spectroscopy is as follows [see Fig. 4.1(a)]. The fermionic atoms are prepared in a band-insulating state, where all quasimomenta in the lowest band are occupied. Using lattice amplitude modulation, they are transferred to an excited band, not changing the quasimomentum in this process. Thereby, the modulation frequency determines the energy at which atoms are excited [171]. Since the lowest and the excited energy bands have different curvatures, each quasimomentum has a different excitation energy. Therefore, the excited momentum can be effectively tuned by changing the lattice modulation frequency. The resulting quasimomentum distribution can be detected fully momentum resolved using the band mapping technique. Repeating this procedure for different modulation frequencies results in a fully energy- and momentum-resolved spectrum.

4.1.1 EXPERIMENTAL REALIZATION

In the experiment the spectroscopy is performed in the following way. First an ultracold gas of spin-polarized fermionic atoms is produced as described in section 2.1. Therefore, an ultracold Bose-Fermi mixture is prepared in the magnetic trap and is subsequently transferred to the dipole trap. The rubidium atoms are then removed from the dipole trap by a resonant light pulse. Typical atom numbers for the fermionic particles are about 1×10^5 at temperatures of about $0.2\,T_\mathrm{F}$. The typical mean trap frequencies $(\omega_\mathrm{x}\omega_\mathrm{y}\omega_\mathrm{z})^{1/3}$ are about $2\pi\times50\,\mathrm{Hz}$.

At this point, a three-dimensional optical lattice is adiabatically ramped up linearly over $100\,\mathrm{ms}$ to a variable lattice depth between $2.5\,E_\mathrm{r}$ and $10\,E_\mathrm{r}$ [see Fig. 4.1(b)]. After a short waiting time of typically 1 ms, the lattice depth is modulated for 1 ms with a variable frequency ν, typically ranging between 0 and $50\,\mathrm{kHz}$, and a peak-to-peak modulation amplitude of typically $10-20\,\%$. This constitutes the lattice amplitude modulation, which creates excitations in the excited band. Directly thereafter, the lattice depth is reduced to zero in a $200\,\mu\mathrm{s}$ linear intensity ramp, which results in the band-mapping process. Using a TOF of $15-20\,\mathrm{ms}$ prior to the absorption imaging leads to a mapping onto the momentum distribution of the system. Together with the band mapping procedure, this allows for the direct measurement of the quasimomentum distribution and the band index of the excited particles.

The excitation process has several important features, which eventually lead to the momentum resolution of the spectroscopy. To begin with, in the case of noninteracting particles, as discussed here, the excitation spectrum is fully determined by the external potential consisting of the optical lattice and the harmonic confinement. Similar to the band mapping, the amplitude modulation time is chosen to be much shorter than the typical timescales of the harmonic confinement. Therefore, the created excitation procedure averages over the harmonic confinement and the excitations are basically determined by the periodic lattice potential. Consequently, the created excitations have a well defined quasimomentum. Their energy is given solely by the band structure of the lattice potential, which only depends on the lattice depth s. For longer excitation times, the redistribution of the excited atoms because of the trap can lead to errors in the momentum determination. Further, the excitation Hamiltonian has the same periodicity as the lattice potential itself. Therefore, it conserves the quasimomentum q during the excitation process. The lattice amplitude modulation can also be regarded as a two-photon process similar to Bragg spectroscopy. In this case, the lattice itself, instead of any external Bragg beams [36, 163], provides the photons, which induce exactly two lattice momenta k_L, corresponding to a quasimomentum transfer of $\Delta q=0$ in the reduced zone scheme [7]. Finally, the lattice amplitude modulation only couples states that have an energy difference identical to the modulation frequency ν [171].

Combining all these properties results in the quasimomentum resolution of the spectroscopy as follows. In the band structure, all bands have a different curvature. Therefore, the transition energy is slightly different at every quasimomentum, such that for each modulation frequency ν only a single quasimomentum $q(\nu)$ is resonantly excited. If all momentum states in the lowest energy band are occupied, as realized in a band insulating state, this leads to an energy and momentum-resolved signal $q(\nu)$ with a unique dispersion for each lattice depth s. This shows, that a full momentum resolution in the optical lattice can be obtained very elegantly by using interband excitations with $\Delta q=0$.

The whole excitation process is sketched in momentum space in Fig. 4.1(a), using the reduced and extended zone schemes for the lattice amplitude modulation and the band-mapping process, respectively. Note, that the method always induces symmetric excitations at positive and negative quasimomenta with equal absolute value, since the band structure is symmetric

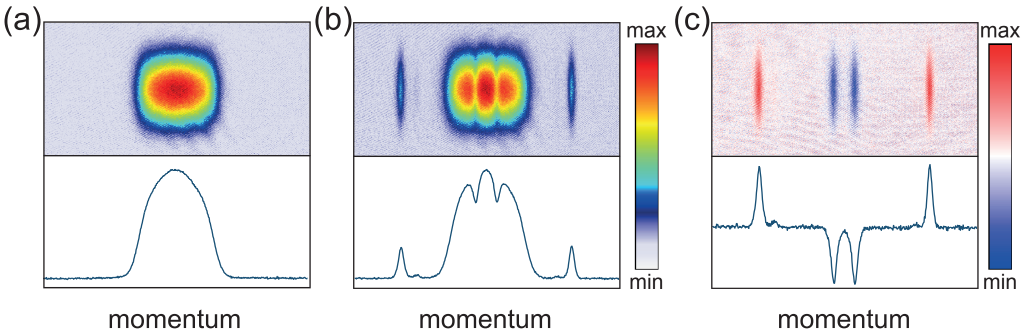

Figure 4.2: Typical experimental multiband spectroscopy momentum distributions. (a) Offresonant modulation: Absorption picture (top) and column density (bottom). No excitations are generated at off-resonant modulation. (b) Resonant modulation: Absorption picture (top) and column density (bottom). The hole and particle excitations are clearly visible in the data as gaps in the filled first Brillouin zones and peaks in the third Brillouin zone. (c) Contrast picture, where (a) is subtracted from (b). The particle excitations are positively valued and the hole excitations are negatively valued. Both can be treated equally as peaks in this representation.

---

around $q = 0$.

I want to stress here, that the momentum resolution in this method requires a completely filled first band, as realized for a fermionic band insulator. In contrast, for bosonic atoms, the superfluid ground state occupies only a small momentum class around $q = 0$ [22]. This precludes the momentum resolution in comparable experiments with bosonic atoms [172]. In a strongly interacting Bose gas, all quasimomenta are occupied, if the system is in the Mott insulating state [22]. Thereby, the momentum resolution is established also for bosons [175], which has been observed using Bragg spectroscopy. In this case, however, the excitation spectrum is dominated by interactions [37]. This is in contrast to the fermionic system, where a full momentum resolution is ensured for all interaction strengths, resulting in a much more versatile spectroscopy scheme.

Typical experimental TOF pictures for offresonant and resonant lattice amplitude modulation are shown in Fig. 4.2. For offresonant modulation, no excitations are induced, and the momentum distribution is identical to the non-modulated case. The atoms occupy the ground state in the lattice which is a band insulator in the case of Fig. 4.2. Therefore, the momentum distribution covers the whole first Brillouin zone after the band mapping. The wings of the distribution are distorted due to the very short band-mapping time of 200 μs, especially chosen to minimize dynamical redistribution during the band mapping because of the trap. As discussed in section 3.2, a short band-mapping time does not reduce the quasimomentum resolution but leads only to the observed softening at the zone boundaries [150].

At a resonant modulation frequency ν, the corresponding momentum class $q(\nu)$ is excited to a higher band. The excited particles are mapped to the corresponding Brillouin zone. In the case of Fig. 4.2, the second excited band is populated by the excitation process, leading to a band mapping to the third Brillouin zone. Apart from the excited atoms in the third Brillouin zone, the holes, where particles are missing in the first Brillouin zone, are clearly visible.

To treat the hole excitations on an equal footing as the particle excitations, one additional processing step is required. The TOF distribution of the nonexcited system must be subtracted from the excited system, which leads to a contrast picture as shown in Fig. 4.2(c), where both excitations are clearly visible and can be evaluated in the same way. For this, both distributions must be carefully normalized to the same particle number to avoid any offsets.

4.1.2 CHARACTERIZATION OF THE EXCITATION PROCESS

As described above, the lattice amplitude modulation to higher bands is intrinsically momentum resolved. However, it is not clear, whether all excited bands and quasimomenta can be populated, or if any selection rules apply. This issue is addressed in the following, using a linear response analysis of the excitation process in time-dependent perturbation theory [129], which has been worked out in this thesis[1]. The results are compared to experimental data for different lattice depths.

I assume the unperturbed Hamiltonian of the system to be the pure lattice Hamiltonian [compare (3.1)]

$$H_0 = \frac{p^2}{2m} + sE_\mathrm{r}\sin^2(k_\mathrm{L}z)\,, \tag{4.1}$$

and neglect any effects of the external trapping potential. The eigenstates of the system are given by the Bloch states

$$|n,q\rangle = \mathrm{e}^{-\mathrm{i}qk_\mathrm{L}z}\sum_{\mathrm{k}=-\infty}^{\infty} c^{\mathrm{n}}_{\mathrm{q,k}}\mathrm{e}^{-\mathrm{i}2kk_\mathrm{L}z}\,, \tag{4.2}$$

defined by the band index n and the quasimomentum q. I further assume a band insulator as the initial state, where all states of the lowest energy band are occupied. Therefore, any perturbation can to first order only create excitations to higher bands with $n > 0$. The lattice amplitude modulation perturbs H_0 by the additional contribution

$$V(t) = V\sin(2\pi\nu t) = \frac{\epsilon}{2}sE_\mathrm{r}\sin^2(k_\mathrm{L}z)\sin(2\pi\nu t)\,, \tag{4.3}$$

where ϵ is the peak-to-peak amplitude relative to the lattice depth s. The first order excitation probability for such a system is given by Fermis golden rule as [129]

$$P^{\mathrm{n}}_{\mathrm{q',q}} \propto \delta\left(E^{\mathrm{n}}_{\mathrm{q'}} - E^{0}_{\mathrm{q}} - h\nu\right)|\langle n,q'|V|0,q\rangle|^2\,, \tag{4.4}$$

where an infinite excitation time is assumed, resulting in the δ-function in energy space, which corresponds to the above mentioned energy conservation in the excitation process.

The matrix element $\langle n,q|V|0,q\rangle$ contains all other information about the momentum dependence or spatial symmetries restrictions. It can be calculated using a simply trick: the perturbation V can be written as

$$V = \frac{\epsilon}{2}\left(H_0 - \frac{p^2}{2m}\right)\,. \tag{4.5}$$

Inserting (4.5) into Fermis golden rule (4.4) and assuming a resonant excitation frequency $h\nu = E^{\mathrm{n}}_{\mathrm{q'}} - E^{0}_{\mathrm{q}}$ leads to

$$P^{\mathrm{n}}_{\mathrm{q',q}} \propto |\underbrace{\langle n,q'|H_0|0,q\rangle}_{=0} - \langle n,q'|p^2|0,q\rangle/2m|^2\,, \tag{4.6}$$

---

[1] During the publication of this manuscript, I became aware that a similar calculation has also been performed in [171], where losses due to excitations via lattice amplitude modulation have been investigated.

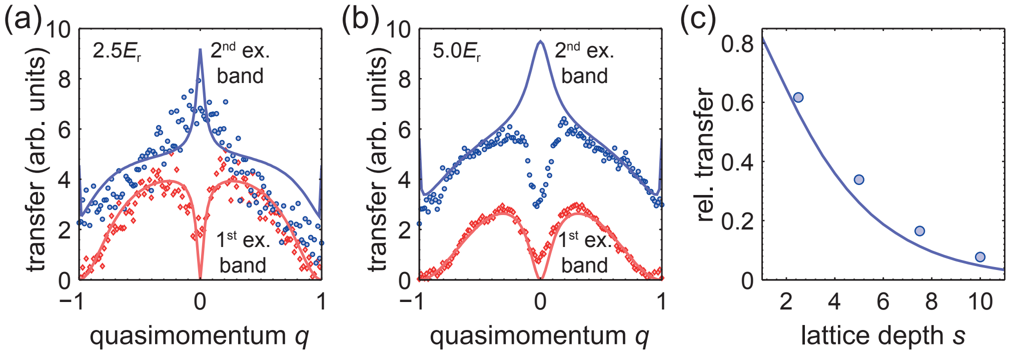

Figure 4.3: Momentum-dependent transfer amplitudes of the lattice amplitude modulation. Shown is the measured momentum-dependent transfer amplitudes to the excited bands with $n=1$ and $n=2$ in comparison to the theoretical prediction from (4.8), depicted as solid lines. (a) shows the results for $s=2.5$ and (b) for $s=5.0$. The absolute transfer amplitude was fitted between theory and experiment. (c) Ratio of the integrated excitation amplitudes for $n=1$ over $n=2$, in dependence on the lattice depth s. Solid line is the theoretical prediction.

---

where the first term vanishes for $n>0$, since the Bloch states $|n,q\rangle$ are eigenstates of H_0. The remaining matrix elements can be calculated in the spatial basis using (4.2) and the representation of the momentum operator $p=-\mathrm{i}\hbar\partial_\mathrm{z}$. Inserting both into (4.6) results in

$$\begin{aligned} P^\mathrm{n}_{\mathrm{q}',\mathrm{q}} &\propto \left|\sum_{\mathrm{k},\mathrm{k}'} c^0_{\mathrm{q},\mathrm{k}} c^\mathrm{n}_{\mathrm{q}',\mathrm{k}'} \int \mathrm{e}^{-\mathrm{i}qk_\mathrm{L}z}\mathrm{e}^{-\mathrm{i}kk_\mathrm{L}z}\partial^2_\mathrm{z}\mathrm{e}^{\mathrm{i}q'k_\mathrm{L}z}\mathrm{e}^{\mathrm{i}2k'k_\mathrm{L}z}dz\right|^2 \\ &\propto \left|\sum_{\mathrm{k},\mathrm{k}'} c^0_{\mathrm{q},\mathrm{k}} c^\mathrm{n}_{\mathrm{q}',\mathrm{k}'} k^2_\mathrm{L}(q'+2k')^2 \int \underbrace{\mathrm{e}^{\mathrm{i}(q'-q)k_\mathrm{L}z}}_{\delta(q'-q)}\underbrace{\mathrm{e}^{\mathrm{i}2(k'-k)k_\mathrm{L}z}}_{\delta(k'-k)}dz\right|^2 . \end{aligned} \tag{4.7}$$

Note, that the δ-functions can only be satisfied in this combination, since $-k_\mathrm{L}<q\leq k_\mathrm{L}$ and k is integer valued $(k=0,\pm1,\pm2,\dots)$. The δ-functions in (4.7) represent the momentum conservation of the excitation; in particular $\delta(q'-q)$ leads to the conservation of the quasimomentum. In total, the transition probability simplifies to

$$P^\mathrm{n}_\mathrm{q} \propto \left|\sum_\mathrm{k} c^0_{\mathrm{q},\mathrm{k}} c^\mathrm{n}_{\mathrm{q},\mathrm{k}}(q+2k)^2\right|^2 , \tag{4.8}$$

which can be directly calculated from the Bloch functions.

Figures 4.3(a) and (b) show the results of (4.8) for two different lattice depths and the first two excited bands, while Fig. 4.3(c) depicts the relative excitation strength to the first and second excited band in dependence on the lattice depth. The theoretical transition amplitudes to the second excited band $(n=2)$ are stronger for all quasimomenta, and the transitions to the first excited band $(n=1)$ are suppressed especially at larger lattice depths. This behavior is the same for all even $(n=2,4,\dots)$ and odd $(n=1,3,\dots)$ bands. Transitions to even bands are generally stronger, while the excitations to odd bands are especially suppressed at large lattice depths relative to the even bands. Further, no transitions occur for $q=0$ and $q=\pm1$ to the odd bands, while all other quasimomenta can be populated.

The latter can be explained as follows. At the direct band gap, where two bands have the lowest energy difference, the bands couple strongest. This leads to an avoided crossing similar to a coupled two-level system, leading to the band gap. Such an avoided crossing usually leads

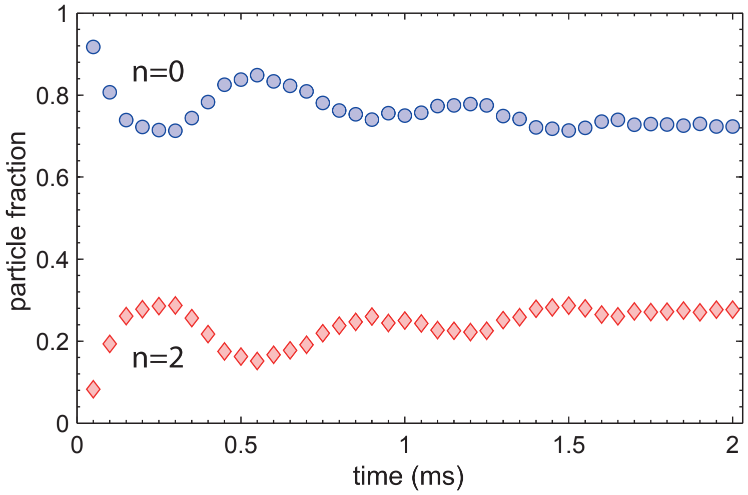

Figure 4.4: Rabi oscillations in the lattice amplitude modulation process at a modulation amplitude of $40\,\%$. Shown is the fraction of atoms in the lowest ($n = 0$, circles) and the second excited ($n = 2$, diamonds) energy band. The oscillatory exchange between the populations shows the coherent nature of the lattice amplitude modulation excitation process.

---

to one even and one odd parity state under exchange of the two levels. In an optical lattice the even parity state is always in the even excited bands. The lowest band is also even ($n = 0$) and therefore has the same parity as the even excited bands and a different parity than the odd bands. Since the lattice amplitude modulation operator is an even operator, the matrix elements of the form $\langle \text{odd}|\text{even}|\text{even}\rangle$ vanish. This manifests in (4.8) in the way, that the sign of $c^{\text{odd}}_{0,\text{k}}$ is the same as of k, while the sign of $c^{\text{even}}_{0,\text{k}}$ is always positive. Therefore, the contributions of k and $-k$ cancel out in the sum and $P^{\text{odd}}_0 = 0$. For all other q, the parity of the Bloch states is in general mixed, since the degenerate states with q and $-q$ can form states with both spatial symmetries. Therefore, an excitation to any band is possible for $q \neq 0, \pm 1$.

The behavior at large lattice depths is directly connected with the above parity argument. For deep lattices with $s > 30$ the contribution of q in (3.3) becomes negligible and the eigenvalue equation becomes identical to the $q = 0$ case for all q. Therefore, all states acquire the same parity-properties asymptotically for $s \to \infty$, and the transfer to odd bands is suppressed. This can also be understood by approximating the different sites of the lattice as harmonic oscillators, which is a good approximation for lattice depths $s > 30$. In this case, the local eigenstates of each site have an alternating parity and the symmetric modulation operator cannot couple states of different parity as discussed above.

Figure 4.3 shows also measurements of the quasimomentum-resolved band excitation probability in direct comparison with the theoretical predictions. First, the relative excitation amplitude, shown in Fig. 4.3(c), is in very good agreement with the theoretical predictions. Further, the momentum-resolved excitation amplitude in experiment and theory agrees well, and the parity-induced suppression of excitations to the first excited band is clearly visible. A notable difference between the theoretical and experimental results is the reduction of excitations at $q = 0$ also for even bands at higher lattice depths, where a maximum is expected from the theoretical model. This effect also explains the small but systematic excess of the experimental data in the total excitation amplitude.

Two possible reasons for the missing excitation amplitude are the short modulation time,

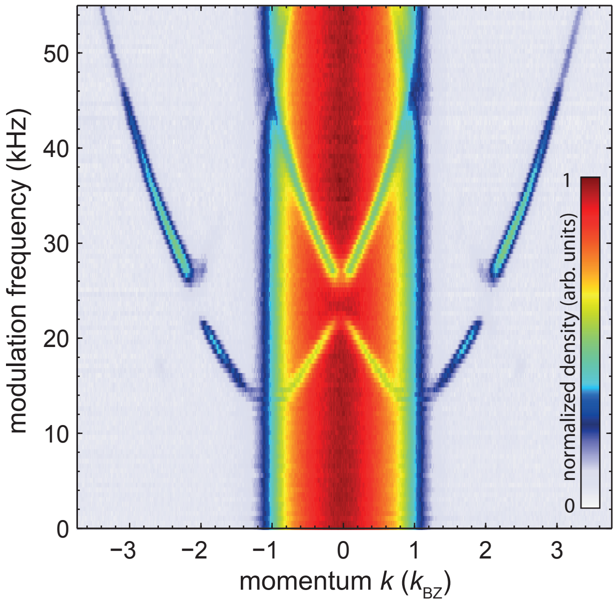

Figure 4.5: Experimental spectrum recorded by multiband spectroscopy. Shown are the column densities for different modulation frequencies at a modulation amplitude of $20\,\%$ for a non-interacting Fermi gas of $2{\times}10^5$ particles at $0.2\,T_{\mathrm{F}}$ in a three-dimensional lattice of $5\,E_{\mathrm{r}}$. The atoms in the lowest energy band are mapped to the first Brillouin zone. The hole excitations correspond to the reduced zone scheme. The excited atoms are mapped to their corresponding Brillouin zones and represent the extended zone scheme. The gaps between the different bands are clearly visible.

---

which does not satisfy the linear response approximation from the calculation, or the external harmonic confinement. The latter was excluded using numerical calculations including the harmonic confinement as discussed in section 3.1.1. The results show, that the confinement does not induce strong changes of the excitation probability in the linear response limit, leaving the finite modulation time as a possible explanation.

To estimate the influence of the short excitation time in more detail, an experiment was performed with a very large modulation amplitude of $40\,\%$. The variation of the excitation amplitude with the modulation time is shown in Fig. 4.4. A clear oscillation of the number of excited atoms is observable, which has a slowly decaying amplitude and saturates for long times. This measurement shows, that the lattice amplitude modulation process with short excitation times is a coherent transfer between the different bands. This is in strong contrast to the linear response assumption in the preceding calculation, supporting the short modulation time as a possible explanation for the difference of the experimental and theoretical transfer amplitude at small q [see Fig. 4.3(b)]. It demonstrates also, that the excitation is a coherent state and therefore the amplitude modulation can also be used for state preparation. This feature is employed in chapter 5, where the dynamics of particle and hole excitations are investigated.

4.2 BAND STRUCTURE OF FERMIONIC GASES

As illustrated above, the presented multiband spectroscopy allows for a momentum- and energy-resolved excitation of fermionic atoms to higher bands of the optical lattice. Figure 4.5 shows a typical energy- and momentum-resolved spectrum, recorded with the multiband spectroscopy, for a pure spin-polarized Fermi gas in an initially insulating ground state.

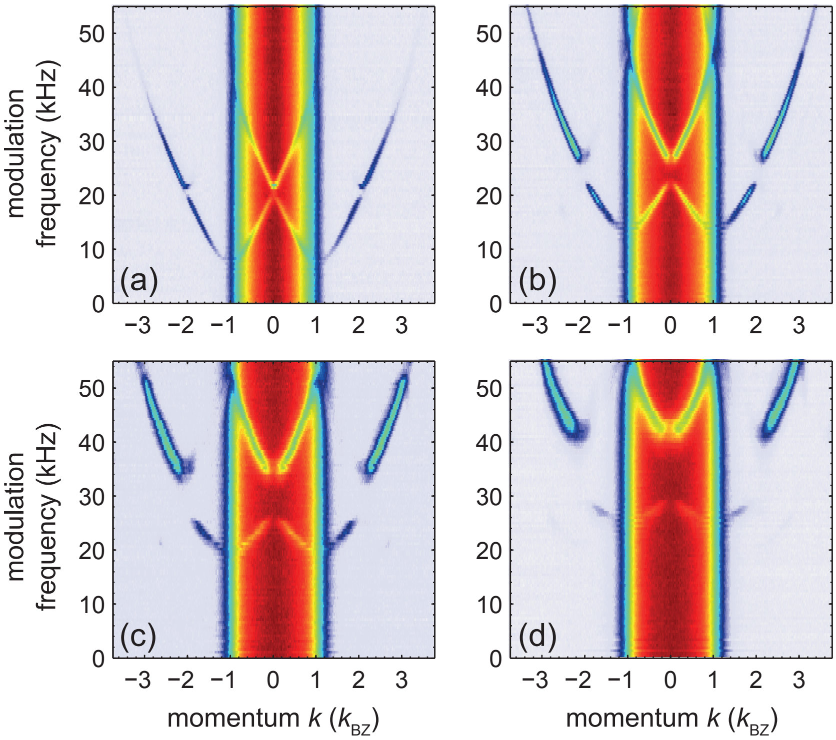

Figure 4.6: Momentum-resolved spectra for different lattice depths at a modulation amplitude of $20\,\%$. The lattice depths are calibrated in the experiment to (a) $2.5\,E_{\mathrm{r}}$, (b) $5\,E_{\mathrm{r}}$ (coincides with the data from Fig. 4.5), (c) $7.5\,E_{\mathrm{r}}$, and (d) $10\,E_{\mathrm{r}}$.

At small modulation frequencies ν no excitations are created, since ν is located in the band gap between the lowest and the first excited band. For frequencies above the bang gap, atoms are transferred to the first excited band and are mapped to the second Brillouin zone. The missing atoms are also visible as holes in the first Brillouin zone. The excitations are created fully energy and momentum-resolved for the complete band, until the next bang gap is reached, where again no atoms are excited. When the modulation frequency becomes resonant with the second excited band, new excitations are created, where the excited particles are mapped onto the third Brillouin zone this time, and so on. Band gaps to higher bands cannot be resolved in the presented experiments that have an energy resolution of $500\,h$Hz.

Note, that the lowest energy band is not directly visible in the spectrum, since only the energy differences between the lowest and the excited bands are measured. Nevertheless, I refer to the spectrum as the band structure in the following, since it contains the same information. In this analogy, the particle and hole excitations correspond to the extended and reduced zone scheme, respectively.

Figure 4.6 shows experimentally recorded spectra for different lattice depths. The increase of the band gaps and the narrowing of the band widths for increasing lattice depths is clearly visible. The unique spectrum for each lattice depth allows for a clear determination of the corresponding lattice depth. The increase of the excitation width in momentum space with increasing s is a combined result of the constant absolute Fourier broadening in energy space because of the finite modulation time and the decreasing band width.

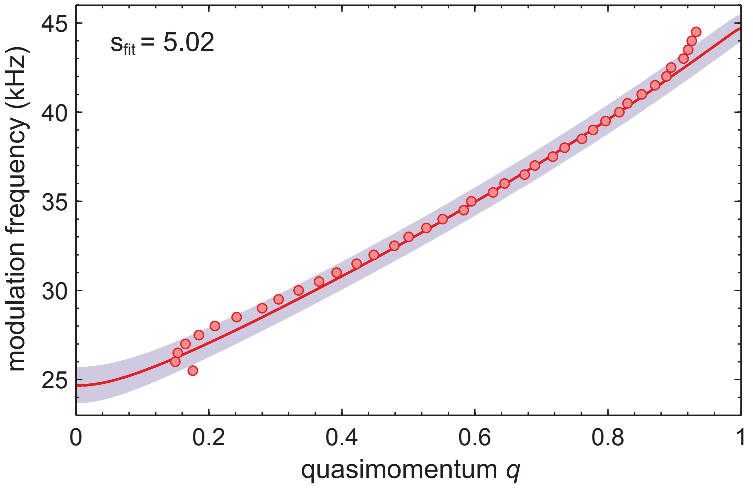

Figure 4.7: Energy-momentum dispersion for the second excited band using the COM-momentum approach. The data shows the COM momentum excited from the lowest to the second excited band for different modulation frequencies. The solid line shows a fit to the data, using the energy difference $E_{\mathrm{q}}^2 - E_{\mathrm{q}}^0$ from a single-particle band structure calculation employing (3.3). The fit yields a lattice depth of $5.02 \pm 0.02\, E_{\mathrm{r}}$. The shaded area depicts a $10\,\%$ deviation from the fitted value. The fitted momenta are restricted to the range of $0.55 < q < 0.85$.

4.2.1 MOMENTUM-RESOLVED EVALUATION OF THE PARTICLE EXCITATIONS

To connect the momentum-resolved multiband spectra with the tunneling properties of the atoms, it is necessary to extract the lattice depth quantitatively. A first approach is to extract the center-of-mass (COM) quasimomentum for each excitation frequency. While the modulation frequency ν is given by the experimental parameters, the momentum must be extracted from the data. For the excited particles the center-of-mass position is determined from the column sums for each modulation frequency ν, with respect to the center of the atomic cloud. The corresponding momentum p is calculated by the relation

$$\mathrm{COM} = \frac{p}{m}\frac{M}{l}T\,, \tag{4.9}$$

where m is the mass of the particles, M is the magnification, l is the diameter of a pixel on the CCD camera and T is the duration of the TOF. To be insensitive to total displacements, the positive and negative momenta $p_{\pm}$ are detected independently and their difference is used as $p = (p_+ - p_-)/2$, eliminating any offsets in (4.9). From this, the quasimomentum is calculated via

$$q = \frac{p}{\hbar k_{\mathrm{L}}} - n\,, \tag{4.10}$$

where $n = 0, 1, 2, \ldots$ is the usual band index.

This approach is most reliably performed for the second excited band, since it has the largest excitation strength and no overlapping atoms from the first band because of the imperfect band mapping, which is a problem for the evaluation of the first excited band. The resulting energy-momentum dispersion $q(\nu)$ is shown in Fig. 4.7. It corresponds to the energy difference $E_{\mathrm{q}}^2 - E_{\mathrm{q}}^0$ between the bands with $n = 2$ and $n = 0$. A fit of the theoretical single-particle band structure reveals a lattice depth of $5.02 \pm 0.02\, E_{\mathrm{r}}$. This corresponds to a tunneling amplitude of

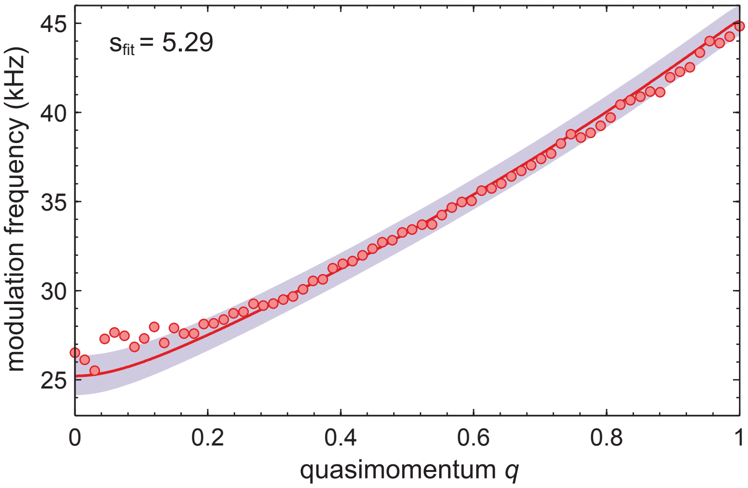

Figure 4.8: Energy-momentum dispersion for the second excited band using the COM-energy approach. The data shows the extracted excitation energy from the lowest to the second excited band for all quasimomenta. The solid line is a fit to the data, using the energy difference $E^2_\mathrm{q} - E^0_\mathrm{q}$ from a single-particle band structure calculation employing (3.3). The fit yields a lattice depth of $5.29 \pm 0.07\,E_\mathrm{r}$. The shaded area depicts a $10\,\%$ deviation from the fitted value. The fitted momenta are restricted to the range of $0.15 < q < 0.85$.

$J/h = 309$ Hz in the lowest energy band, which can be evaluated from (3.7) by using the fitted lattice depth to calculate the Wannier functions w_i.

Note the deviation of the extracted data from the single-particle dispersion especially at large and small quasimomenta. This is a combined result of the external trapping potential and the COM determination. As shown in section 3.1.2, the confinement leads to states within the band gap, which can also be weakly excited by the lattice amplitude modulation. As visible in the false color images in Fig. 4.5 and 4.6, the excited fraction at frequencies below the band gap is very small, corresponding to the above mentioned trap-induced states (see the band structure of a harmonically trapped lattice system in Fig.3.3). At frequencies above the second excited band, a trap-induced coupling to the third excited band, deforming the spectrum, cannot be excluded. The influence of the trapping potential is inherent in the system and cannot be fully eliminated. Therefore, the corresponding regions are not included in the band structure fit, which is only performed in the range of $0.55 < q < 0.85$.

The influence of the COM determination is a technical aspect and can be circumvented. The band mapping procedure divides the second Brillouin zone into two parts, with a cut at $q = 0$ (see Fig. 3.2). Taking the COM along the momentum direction leads to the effect, that a particle distribution with small absolute momentum is separated between both parts. The COM in each of the parts does not coincide with the central momentum of the full peak but is larger than the real value. Especially a distribution with a finite momentum width and a central momentum of $q = 0$ is never correctly evaluated by this method.

To avoid the problems of the COM-momentum approach, it is desirable not to evaluate the momentum $q(\nu)$ in dependence on the frequency, but rather the frequency $\nu(q)$ in dependence on the momentum. This has the advantages, that the splitting of the Brillouin zone does not interfere with the COM determination and that a single energy value is assigned to each momentum, instead of two momenta for each energy as in the COM-momentum approach. The

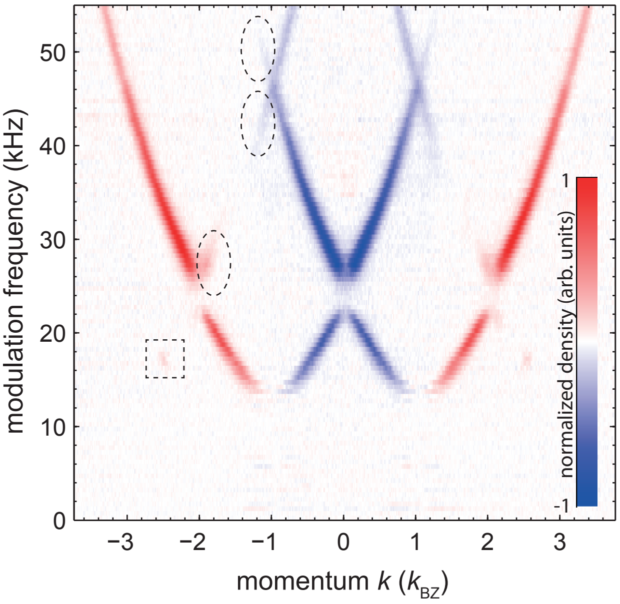

Figure 4.9: Contrast spectrum recorded by multiband spectroscopy for the same data as in Fig. 4.5, from which an average of the data between 0 kHz and 10 kHz is subtracted. This removes the background population in the lowest energy band and depicts the hole excitations as negative peaks, fully equivalent to the positive particle excitations. The circular marked regions show failures of the band mapping procedure. The square shows particles, that were excited to the second excited band via higher order processes in the lattice amplitude modulation.

---

drawback is, that the COM-energy is not determined from a single experimental realization anymore, but from the full energy and momentum resolved spectrum, requiring a high resolution in energy space. Additionally, all measured momentum distributions must be normalized to the same total particle number. The COM is taken along the energy axis for every single pixel, corresponding to a given quasimomentum in the second excited band via (4.9) and (4.10).

The resulting energy-momentum dispersion $\nu(q)$ is shown in Fig. 4.8 for the same data as in Fig. 4.7, using this COM-energy approach . A fit of the theoretical single-particle band structure reveals a lattice depth of $5.29 \pm 0.07\, E_{\mathrm{r}}$, slightly differing from the COM-momentum result. The COM-energy approach leads to much closer resemblance between the experimental data and the single-particle band structure, especially at $q = 0$, where the curvature is reproduced adequately and no bending to lower energies is observed.

4.2.2 MOMENTUM-RESOLVED EVALUATION OF THE HOLE EXCITATIONS

In addition to the particle excitations, the hole excitations carry exactly the same information about the energy-momentum relation. However, using the hole excitations has a systematic advantage for measuring the excited momentum. Since the excitations are eigenstates of the lattice potential alone, they perform oscillatory dynamics in the harmonic trapping potential after the excitation. Due to the lower curvature of the lowest energy band, the hole dynamics are much slower than the particle dynamics. While the particle dynamics can already be relevant on the timescale of the excitation procedure, the hole dynamics only change the quasimomentum after much longer times and can be neglected during the excitation procedure. Therefore, the systematic errors for the energy-momentum relation are reduced, when using hole excitations

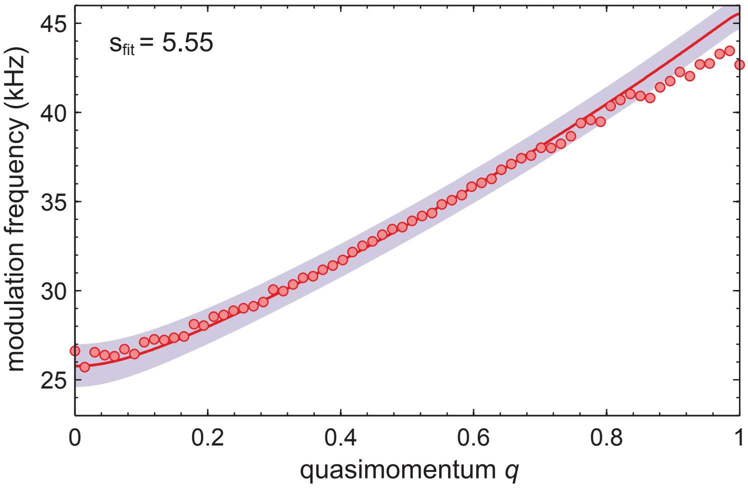

Figure 4.10: Energy-momentum dispersion for the second excited band using the COM-energy approach for hole excitations. The data shows the extracted excitation energy from the lowest to the second excited band for all quasimomenta, using the hole excitations evaluated from the contrast spectrum shown in Fig. 4.9. The solid line is a fit to the data, using the energy difference $E_{\mathrm{q}}^{2} - E_{\mathrm{q}}^{0}$ from a single-particle band structure calculation employing (3.3). The fit yields a lattice depth of $5.55 \pm 0.05\, E_{\mathrm{r}}$. The shaded area depicts a $10\,\%$ deviation from the fitted value. The fitted momenta are restricted to the range of $0.15 < q < 0.8$. The upper cutoff is needed in the COM-energy approach for holes, since the third excited band starts right above the second excited band, leading to similar cutoff mistakes as in the COM-momentum approach for the excitations.

instead of particle excitations. The dynamics of the particle and hole excitations are discussed in chapter 5, where the above mentioned processes are worked out in more detail.

In order to utilize the hole excitations, it is necessary to create a contrast image of the experimental spectrum, similar to Fig. 4.2(c), where the hole excitations are represented as negative peaks, fully equivalent to the particle excitations represented as positive peaks. Such a contrast spectrum is depicted in Fig. 4.9.

For the holes, I only present the COM-energy approach, which minimizes the influence of the evaluation procedure compared to the COM-momentum approach, as discussed for the particle excitations. Since the hole excitations are arranged in the reduced zone scheme, where all bands are represented within the same momentum interval between $-k_{\mathrm{BZ}}$ and $+k_{\mathrm{BZ}}$, one has to be careful to use a properly chosen energy range for the evaluation, such that no contributions from other bands disturb the spectrum. Therefore, energies near the unresolved band gap from the second to the third excited band must be excluded from the fit when using this method. A determination of the band structure for the same data as in Fig. 4.7 and Fig. 4.8 is shown in Fig. 4.10. The features of the COM-energy approach are as clear as for the particle excitations. However, the resulting lattice depth of $s = 5.55 \pm 0.05$ deviates from the particle result. Taking into account the stronger dynamical evolution of the particle excitations, the deviation between the hole and the particle results is an indication for systematical errors in the particle result.

An additional check of the fitting performance can be made, comparing the experimental results for the different lattice depths to the calibrated lattice-depth behavior. Figure 4.11 shows the results of all three evaluation methods for four different measurements in relation to the experimentally calibrated lattice depth. On one hand, all methods show a strong disagreement with the calibrated lattice depth, questioning the validity of the calibration. On the other hand,

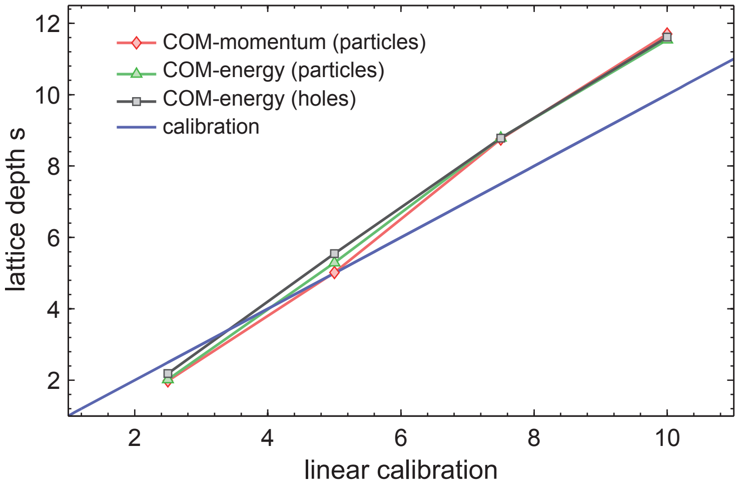

Figure 4.11: Measured versus calibrated lattice depths for different evaluation methods. Shown are the measured lattice depths from all three presented evaluation methods for the four different measurements presented in Fig. 4.6, in comparison to the calibrated lattice depth from the experiment. For this, the lattice depth was determined at one single beam intensity using the linear power over voltage regime of a photodiode. The lattice depth was then extrapolated under the assumption, that a vanishing photodiode voltage gives a vanishing lattice depth, and that the lattice depth depends linearly on the photodiode voltage.

the results of all three approaches are very similar overall, while the most linear performance is shown by the COM-energy approach for the hole excitations. Especially at larger lattice depths ($s > 5$), all methods agree with each other. In this regime, the form of the bands becomes less important and the total energy gap between the bands becomes the most relevant information, which is reproduced independent of any momentum dynamics. In conclusion, all methods can be used for the determination of the lattice depth, especially at large lattice depths. However, a careful check of calibration is necessary, since the presented data shows a strong deviation from the assumed linearity of the photodiode (see Fig. 4.11).

4.3 REDUCED TUNNELING IN ATTRACTIVE BOSE-FERMI MIXTURES

The novel multiband spectroscopy presented above allows for an intuitive visualization and easy-to-use characterization of the band structure of non-interacting fermions in an optical lattice. Even moderate interactions can change the excitation spectrum strongly, however.

4.3.1 THE EFFECTIVE POTENTIAL

A prominent example for an effective interaction-induced change of the single-particle excitation spectrum is the above mentioned attractively interacting mixture of bosonic and fermionic particles, where the effective tunneling amplitude is expected to be reduced considerably [56, 76]. This can be explained as an interaction induced localization in the following way.[2]

---

[2] The following discussion is based on the general idea presented in [56], but does not include the self-consistent change of the on-site wave function due to the attractive interactions. This contribution is, however, most important for large bosonic filling factors $\langle n_\mathrm{b} \rangle > 3$, which are not realized in the presented experiments.

Consider the Hamiltonian (3.17) for the Bose-Fermi mixture in the optical lattice. Since the bosons experience a much deeper lattice than the fermions, their density distribution can be regarded as fixed in a homogeneous Mott insulator. The remaining Hamiltonian for the fermionic particles with a fixed bosonic background density $n_{\mathrm{b}}(\vec{r})$ is

$$H_{\mathrm{bf}}^{f} \approx \sum_{\mathrm{k}=1}^{\mathrm{N_F}} \frac{\vec{p}_{\mathrm{k}}^{\,2}}{2m_{\mathrm{f}}} + \sum_{\alpha}^{\mathrm{x,y,z}} s_{\alpha}^{\mathrm{f}} E_{\mathrm{r}}^{\mathrm{f}} \sin^2(k_{\mathrm{L}} r_{\mathrm{k},\alpha}) + g_{\mathrm{bf}} n_{\mathrm{b}}(\vec{r}_{\mathrm{k}})\,. \tag{4.11}$$

The bosonic density acquires the form of a potential in this approximation. For sufficiently deep lattices, the density distribution on each site is given by the Wannier functions (3.6) in each direction, such that the ground state density can be written as

$$n_{\mathrm{b}}(\vec{r}) = \langle n_{\mathrm{b}} \rangle \sum_{\mathrm{ijk}} \big(w_{\mathrm{b,i}}(x) w_{\mathrm{b,j}}(y) w_{\mathrm{b,k}}(z)\big)^2\,, \tag{4.12}$$

where i, j, k denote the lattice sites in the directions x, y, z and $\langle n_{\mathrm{b}} \rangle$ is the mean occupation per lattice site.

Note here, that the ground state of the Bose gas has the same periodicity as the lattice potential. Therefore, its contribution to (4.11) can be regarded as an effective additional lattice potential. While the bosonic potential is not separable in principle, its effective strength regarding the tunneling in a given direction can be approximated by an integration of the two remaining directions, such that the total effective lattice potential can be written as

$$V_{\mathrm{eff}}^{\mathrm{x}} = \underbrace{s_{\mathrm{x}}^{\mathrm{f}} E_{\mathrm{r}}^{\mathrm{f}} \sin^2(k_{\mathrm{L}} x)}_{V_{\mathrm{L}}} + g_{\mathrm{bf}} \langle n_{\mathrm{b}} \rangle \underbrace{\sum_{\mathrm{i}} w_{\mathrm{b,i}}^2(x) \int dy \big(w_{\mathrm{b}}(y) w_{\mathrm{f}}(y)\big)^2 \int dz \big(w_{\mathrm{b}}(z) w_{\mathrm{f}}(z)\big)^2}_{\rho_{\mathrm{b}}^{\mathrm{1d}}} \tag{4.13}$$

(here exemplary shown for the x-direction), which is in short notation $V_{\mathrm{eff}} = V_{\mathrm{L}} + g_{\mathrm{bf}} \langle n_{\mathrm{b}} \rangle \rho_{\mathrm{b}}^{\mathrm{1d}}$. For attractive interactions, where $g_{\mathrm{bf}} < 0$, the potential (4.13) leads to an increased lattice depth for the fermions in the presence of bosons.

The additional lattice depth is proportional to the mean bosonic site occupation $\langle n_{\mathrm{b}} \rangle$ and to the scattering length a_{bf}. A sketch of the effective potential is shown in Figs. 4.12(a) and (b). Since the additional potential due to the interaction has the form of the bosonic Wannier functions, this leads not only to a deeper, but also to a slightly deformed lattice potential and therefore in principle to a slightly deformed band structure compared to a similarly deeper lattice depth s for the pure Fermi gas. Figure 4.12(c) shows the excitation spectra for different bosonic filling factors; A best fit with a pure fermionic band structure is shown in comparison, revealing that the deformation of the band structure is hardly detectable with the current experimental resolution and can be neglected for the data analysis.

The increased lattice depth in the mixture is intrinsically connected to a reduced tunneling of the atoms, which leads to a different point of view on the effective potential. If an attractive boson is placed into a lattice site in addition to a fermionic atom, the total energy of the pair is reduced. If one of the atoms tunnels to an adjacent site, the on-site energy increases, due to the vanishing interaction energy. This hinders the tunneling process, and thus reduces the tunneling amplitude J. Naturally, this argument holds equally valid for the bosonic tunneling in the presence of the fermions and is the driving force for the observed shift of Mott insulator transition in the effective parameter approach [56, 76].

An alternative description for the tunneling properties of Bose-Fermi mixtures has been recently developed [83, 85], which attributes the reduced tunneling to a offsite interactions, the

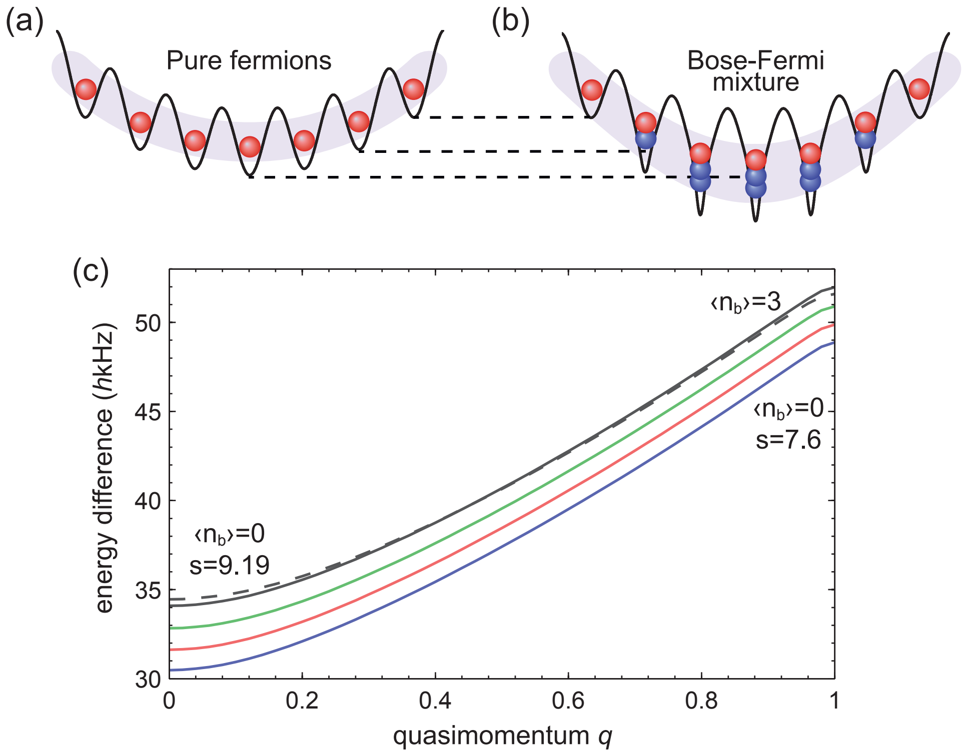

Figure 4.12: Sketch and calculation of the effective potential in an attractive Bose-Fermi mixture. (a) Pure fermionic cloud in a trapped lattice system. (b) Bose-Fermi mixture with a wedding cake structure in the bosonic Mott insulator. The additional well depth depends on the number of bosons per site. To highlight this dependence, the dashed lines compare the lattice depth with and without bosons at different filling factors. (c) Solid lines show the calculated spectrum for excitations to the second excited band. A pure fermionic gas (blue) in a three-dimensional lattice with $s = 7.6$ has a tunneling energy of $J/h = 160\,\mathrm{Hz}$. For comparison, the effective excitation spectra in the presence of bosonic Mott insulators with $\langle n_\mathrm{b} \rangle = 1$ (red) and $\langle n_\mathrm{b} \rangle = 2$ (green), and $\langle n_\mathrm{b} \rangle = 3$ (black) are shown. The dashed line shows exemplarily a fit of the effective band structure for $\langle n_\mathrm{b} \rangle = 3$ with a bare band structure of a pure lattice potential without bosons. The fitted values for the three boson occupations are $s = 8.12$, 8.65, and 9.19, leading to reduced tunneling energies of $J/h = 141$, 124, and $109\,\mathrm{Hz}$.

---

so-called bond-charge interactions [176]. These interactions have been originally discussed in solid state physics in the context of superconductivity and ferromagnetism [177, 178] and constitute an extension of the pure Hubbard model. In this context, the tunneling energy of the fermionic atoms is reduced due to the interaction of the particle with the bosonic particle on the neighboring site, representing a density induced tunneling. It can be shown, that this effect is is practically equivalent to the effective potential as in (4.13) [85], while both methods take into account slightly different orders of the interaction effects in the calculation.

Using bond-charge interactions, the effective tunneling for the fermionic atoms in the lowest band approximation for the parameters of Fig. 4.12 yields a reduced fermionic tunneling energy per boson of 20 Hz [179]. This leads to a total tunneling of 140, 120, and 100 Hz for $\langle n_\mathrm{b} \rangle = 1, 2, 3$. Comparing these values to the effective potential approach (see Fig. 4.12) shows a very good agreement for a single boson and similar values for the higher boson numbers, as expected form the close relation between both approaches.

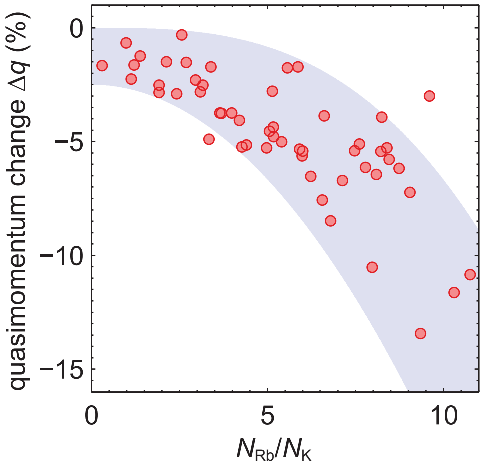

Figure 4.13: Shift of the excited momentum in an attractive Bose-Fermi mixture in dependence on the relative particle number. The lattice depths in all three directions are $s^{\mathrm{f}} = 5$ for the fermions, and $s^{\mathrm{b}} = 12.5$ for the bosons. The modulation amplitude is $20\,\%$ and the modulation frequency is $34\,\mathrm{kHz}$, leading to a transfer of atoms to the second excited band. The relative particle number was tuned by varying the MOT-loading times of ^{40}K and ^{87}Rb. The shaded area is a guide to the eye.

4.3.2 EXPERIMENTAL RESULTS

As outlined previously, the bosonic atoms in the ^{40}K and ^{87}Rb mixture act as an additional periodic potential, leading to an effective lattice depth. Therefore, the multiband spectroscopy presented in the current chapter is suited to measure the resulting change in the excitation spectrum, corresponding to a reduced tunneling amplitude. To maximize the signal-to-noise ratio, the measurements are restricted to the second excited band, where the excitation amplitude is the highest. Figure 4.13 shows measurements performed in different mixtures in the optical lattice. For this, the ^{87}Rb atoms have not been removed in the dipole trap and the relative particle numbers have been varied by changing the relative MOT loading times for rubidium and potassium. Shown is the dependence of the excited momentum on the relative particle number in the mixture at a fixed modulation frequency. The measurements reveal a decreasing excitation momentum with increasing particle number ratios, that is, an increasing mean occupation $\langle n_{\mathrm{b}} \rangle$. The decrease in momentum corresponds to an increase of the band gap and therefore an increase of the lattice depth, as predicted by the effective potential approach discussed above. Thus, the observed particle number shift of the spectroscopy signal directly confirms the predicted increase in lattice depth due to the attractive interspecies interaction. The nonlinear slope in Fig. 4.13 indicates an enhanced localization of the particles at higher particle numbers. This might be because of an effective self trapping [56] or enhanced correlation effects with increasing occupations [85, 176]. Both effects are neglected in the above discussion of the effective potential, where the bosonic density is assumed to be fixed. To describe these effects, a more involved treatment is required, which is beyond the scope of this work.

For a quantitative comparison of the experiment with the numerical results a second set of experiments has been performed, where the full momentum-resolved spectrum of the second excited band was investigated for a three-dimensional lattice with a depth of $7.6\,E_{\mathrm{r}}$, corresponding to a bosonic lattice depth of $19\,E_{\mathrm{r}}$. Therefore, the bosons are deep in the Mott insulating regime in these measurements.

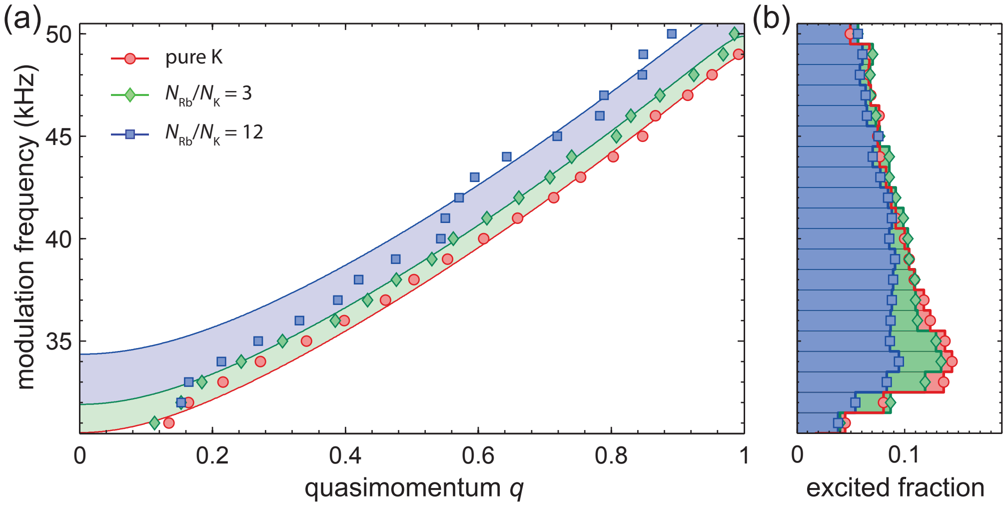

Figure 4.14: Measurement of momentum-resolved excitation spectra in attractive Bose-Fermi mixtures. (a) shows the momentum- and energy-resolved excitation spectrum for pure fermions and two different admixtures of bosonic atoms. The red circles correspond to measurements with $N_\mathrm{K} = 5.7 \times 10^4$, the green diamonds to $N_\mathrm{K} = 5.3 \times 10^4$ and $N_\mathrm{Rb} = 1.56 \times 10^5$, and the blue squares to $N_\mathrm{K} = 2.2 \times 10^4$ and $N_\mathrm{Rb} = 2.63 \times 10^5$. The data was evaluated using the COM-momentum approach, which gives the same results as the other approaches at the investigated lattice depths. Solid lines are fitted dispersion relations using only data for $0.55 < q < 0.85$. (b) shows the number of transferred atoms for each modulation frequency.

This lattice depth has been carefully chosen to minimize the overlap between the second excited band of the bosonic atoms and the investigated second excited band of the fermionic atoms (see Fig. 3.10 for a comparison of both band structures). The third excited band of the bosonic band structure has a finite energetical overlap with the fermionic second band, but being an odd band, it does not allow for a large excitation amplitude at the large lattice depth of $19\,E_\mathrm{r}$. Therefore, the chosen lattice depth avoids the simultaneous excitation of bosonic atoms together with the fermionic atoms, and thus prevents a possible influence on the spectroscopy signal.

Figure 4.14 shows the corresponding measurements. The shift of the band structure is again clearly visible. For the different mixtures, lattice depths of $8.2\,E_\mathrm{r}$ and $9.2\,E_\mathrm{r}$ are fitted using the COM-momentum approach. This is an effective change of the lattice depth of up to $20\,\%$. With a bare fermionic tunneling amplitude of $J/h = 160\,\mathrm{Hz}$ the effective tunneling energies are 138 Hz and 109 Hz. This reduction of the tunneling amplitude of up to $30\,\%$ is in very good agreement with the theoretical values obtained form the data shown in Fig. 4.12, where the larger bosonic particle number excellently agrees with an occupation of three bosons and the lower bosonic particle number suggests an occupation of $\langle n_\mathrm{b} \rangle = 1$.

In the zero-tunneling limit, the ground state of the bosonic atoms in the harmonically trapped lattice system can be calculated [180], resulting in a wedding cake density profile as discussed in section 3.3. In the experiments presented in Fig. 4.14, the lower bosonic particle number results in a maximal bosonic occupancy of two, while for the larger particle number up to three bosons occupy a single lattice site. These numbers are in good agreement with the observed shifts, as discussed above.

The presence of the wedding cake structure is probably the reason for the unexpected structure in the spectroscopy signal especially for large bosonic atom numbers. The additional inhomogeneity due to the wedding cake is much larger than the typical inhomogeneity of the lattice beams, which is typically in the order of only 2% of the lattice depth over the whole Fermi cloud. Different regions of the Fermi cloud therefore experience different effective lattice depths, which might induce the distorted spectroscopy signal. A full theoretical treatment of this situation would require an involved calculation using the full three-dimensional density profiles, which is beyond the scope of this thesis.

An additional evidence for the above explanation is given by the number of transferred atoms in dependence on the excitation energy, as shown in Fig. 4.14(b). Especially for the largest rubidium number, the relative number of excited atoms is reduced at low excitation frequencies. This can be explained as follows. As evident from the theoretical calculations in Fig. 4.12, the minimum excitation energy is increased for larger bosonic occupations. This results directly from the increase of the effective lattice depth. If now fermionic atoms are excited from two regions with different bosonic occupations, only the regions with lower bosonic occupations contribute to the signal at the lower edge of the band. Therefore, also the effectively observed shift in this region is lower than at higher frequencies, where also the atoms from the region with the larger bosonic occupation contribute. The opposite occurs at the upper edge of the band, where mainly the fermions in the region of large bosonic occupations contribute. Since the fitting procedure mainly includes large quasimomenta, the extracted shifts should be closer to the value for the maximal bosonic occupation. In between, the contribution of all different occupations results in a mean value for all regions.

While a comparison of the experimental spectrum with a full theoretical model would require involved calculations, the good agreement between the expected [using (4.13)] and observed shifts is remarkable. Since the description via bond-charge interactions is equivalent to the effective potential, and both approaches result in comparable tunneling shifts, the observed values are also consistent with the bond-charge approach, which allows an interpretation of the reduced tunneling in terms of an extended Hubbard model.

Whether the observed reduced tunneling is consistent with the earlier observed Mott insulator shift for the bosons [23, 24], or if additional effects, such as adiabatic heating, must be included [82, 84], cannot be concluded from the presented data. In particular, a direct comparison of the observed results would require further theoretical work, including all correlations and the full three-dimensional geometry, comparing the fermionic results obtained here, with the related bosonic parameters. Independent of this open questions, the presented results very well constitute the first direct observation of a interaction-induced reduced tunneling amplitude in attractive Bose-Fermi mixtures in particular and, to my best knowledge, in ultracold quantum gases and solid state systems in general.[3]

4.4 CONCLUSION AND OUTLOOK

In conclusion, a versatile spectroscopy method for fermionic atoms in optical lattices has been presented, taking advantage of momentum-selective excitations to higher bands. In this work, the multiband spectroscopy was used for the first fully momentum-resolved investigation of the band structure of ultracold fermions, resulting in textbook-like images of the reduced and extended zone schemes with unprecedented precision. A great advantage of the presented

---

[3] Note, that this is not comparable to the interaction induced tunneling blockade in, e.g., Mott insulating systems, where the effective tunneling amplitude is not reduced, but the tunneling is tuned offresonant by the on-site interactions.

spectroscopy method is, that no additional lasers or optics are required. This allows an easy implementation in any existing optical lattice setup. Therefore, the multiband spectroscopy is promising to become a new standard procedure for the investigation of ultracold fermions in optical lattices.

In particular the method is not restricted to simple cubic lattice geometries as presented here, but is also applicable to more complex lattice geometries [27, 29]. An especially interesting geometry are, e.g., hexagonal lattices [29] with Dirac points in the lowest energy band [53]. Using the presented multiband spectroscopy, these Dirac points should clearly be reveal, paving the way for studies of graphene-like physics with ultracold fermionic atoms [181, 182]. To aim for this regime, a triangular and hexagonal lattice is implemented at the BFM setup as of this writing.

As a direct application of the novel spectroscopy method, attractively interacting Bose-Fermi mixtures in optical lattices were studied in this thesis [23, 24], demonstrating the applicability of the multiband spectroscopy also for interacting systems. The high measurement precision allowed for the observation of a reduced tunneling of the fermionic atoms, explained by an effective interaction-induced potential by the strongly localized bosons. This constitutes the first direct observation of this effective tunneling, which has been subject to many theoretical discussions in the past, connected especially with an earlier observed shift of the bosonic Mott insulator transition in attractive Bose-Fermi mixtures [56, 82–85, 161].

From the perspective of an extended Hubbard model with bond-charge interactions, which is equivalent to the effective potential approach, such interaction induced tunneling processes are not limited to Bose-Fermi mixtures. Similar effects have also been discussed for pure bosonic systems [176, 183] and originally for superconductivity and ferromagnetism in solids [177, 178]. Since the corresponding processes have a very small amplitude in solids, they have not been observed there so far, to my best knowledge. Consequently, the presented results are of high relevance for the study of extended Hubbard models, which have attracted much interest in the field of cold atoms in recent years [15, 184–186]. In particular, they constitute the first experimental observation of interaction induced corrections beyond normalized on-site interaction parameters [162, 187, 188]. Realizing this long sought-after effect from solid state physics, the presented study constitutes a prime example for a quantum simulation using ultracold atoms.

CHAPTER 5

PHOTOCONDUCTIVITY IN HARMONICALLY CONFINED LATTICE SYSTEMS

The close analogy between electrons in solids and ultracold atoms in optical lattices has stimulated many fascinating discoveries over the last decade, using ultracold atoms to emulate condensed matter physics [15, 16, 45]. Equally important, this analogy had a huge impact on the field of ultracold atom research on its own. In fact, many methods for probing and manipulating the quantum degenerate matter have been conceived in direct analogy to well known methods from solid state physics [168, 189], including the idea to use optical lattices to create analogs to solids in the first place [21, 22].

In this chapter I pursue the latter approach and present the first realization of an analog to photoconductivity using ultracold atoms. Photoconductivity occurs in solids, if resonant photons excite electrons from the valence band to the conduction band in an initially insulating system (see sketch in Fig. 5.1). Both, the excited electrons and the remaining holes constitute free charge carriers, rendering the material conductive. When applying an external potential, a photocurrent arises, which can be measured [190, 191].

Today, photoconductivity is the basis for many technological applications, such as photodiodes and photoresistors, but it is also used in fundamental research to probe the properties of novel materials, such as carbon nanotubes [192], semiconductor nanowires [193], and graphene [194, 195]. A particularly fascinating aspect of photoconductivity is, that its multiband character makes it a simultaneous probe for the valence and the conduction band. Amongst other phenomena, it has been observed in many solids that one sort of charge carriers is trapped and does not participate in the current [190]. In other systems, very long lifetimes of the excited electrons have been observed [191, 196, 197], exceeding days.

These examples strikingly show, that photoconductivity is ideally suited to address questions, which are of high relevance also in ultracold matter research. The investigation of hole excitations in the lowest band of an optical lattice provides many information on the many-body ground state in the lattice [198], which is one of the main research fields using ultracold atoms [22, 23, 25–27, 29, 34, 38, 39]. The investigation of higher excited bands in optical lattice has received much interest in recent years, both from the theoretical side [55–60, 62–65, 199–204] as well as from the experimental side [36, 37, 46, 53, 172, 175, 205–210]. Here, the very intriguing possibility of time-reversal symmetry breaking states is a fascinating prospect, which strongly depends on the particular properties of the optical lattice [58, 201, 208].

The experiments presented in this chapter are based on the novel multiband spectroscopy presented in chapter 4 of this thesis. After the creation of particle and hole excitations, the

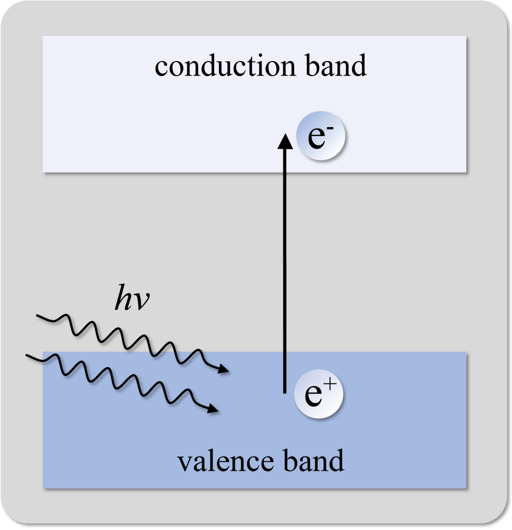

Figure 5.1: Sketch of solid state photoconductivity. A band insulator or semiconductor without free charge carriers is irradiated with light. If the energy $h\nu$ of the light is resonant with the band gap between the completely filled valence band and the empty conduction band, electrons can be excited. This creates negatively charged free charge carriers (electrons) in the conduction band and positively charged free charge carriers (holes) in the valence band, rendering the material conductive.

external trapping potential induces dynamics, in complete analogy to the external potential used in solid state photoconductivity. A coherent time evolution is observed for the particles and the holes, demonstrating the realization of photoconductivity in optical lattices for the first time. The results can be explained quantitatively, using an effective single-particle description for the excitations. Surprisingly, also the hole dynamics, which actually rely on the complex many-body dynamics of all particles in the lowest energy band, can be described precisely. As an alternative approach, a semiclassical approximation is discussed, which allows for an in-depth intuitive understanding of all observed dynamics, by mapping the system onto a classical nonlinear pendulum [47, 211]. This mapping introduces a close analogy of the investigated system to a very general class of systems from various fields, like ultracold bosons in a double-well potential [212], spinor Bose-Einstein condensates [213], semiconductor heterostructures [214] and Josephson junctions [215].

The presented data constitutes the first investigation of the dynamics of fermionic atoms in higher bands of an optical lattice. At the same time, it includes the first observation of the coherent dynamics of holes in momentum space with ultracold fermionic atoms in an optical lattice. Both results constitute a major advance in the understanding of fermionic quantum gases in optical lattice and pave the way towards studies of novel quantum phases, both in the lowest and in excited bands of the optical lattice.

All experimental data presented in this chapter was taken and analyzed together with Jasper S. Krauser and Sören Götze. The numerical calculations using the quantum mechanical approach were performed mainly by myself. All numerical and analytical results using the semiclassical description have been obtained by Alexander Itin and Ludwig Mathey, except for the linearized description (5.11), obtained independently by myself. The results of this chapter are partly published in [4]. The particle excitations of noninteracting systems have partly been discussed in the diploma thesis of Nick Fläschner [116], which was co-supervised by me and

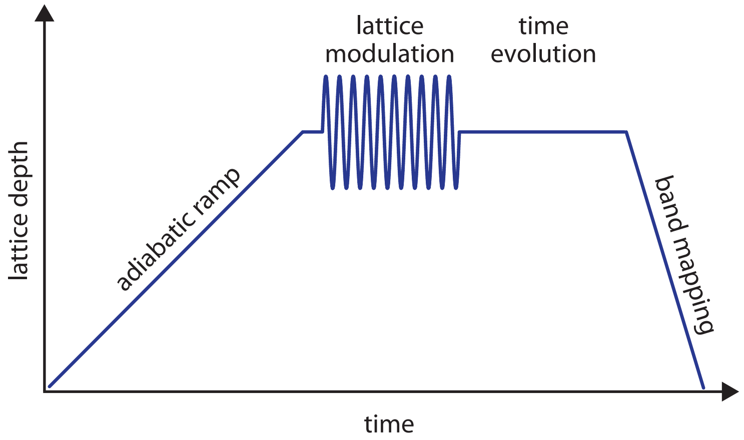

Figure 5.2: Sketch of the experimental sequence for photoconductivity measurements as described in the text.

---

performed at the BFM setup.

5.1 PHOTOCONDUCTIVITY IN ULTRACOLD ATOMS

5.1.1 EXPERIMENTAL REALIZATION

The experimental protocol for photoconductivity measurements in ultracold Fermi gases is based on the multiband spectroscopy from chapter 4 and is sketched in Fig. 5.2. First, the desired quantum gas is produced in the optical dipole trap. In the measurements presented in this chapter, ideal single-component Fermi gases, interacting two-component Fermi gases, and Bose-Fermi mixtures were employed. The general realization of these system is described in chapter 2.

For the non-interacting single-component gases and the Bose-Fermi mixtures, an ultracold Bose-Fermi mixture is produced using sympathetic cooling in the magnetic trap. The mixture is then transferred to the dipole trap remaining the quantum degeneracy.

To produce pure single-component Fermi gases, the ^{87}Rb atoms are removed by a resonant light pulse. Typical atom numbers for the fermionic particles are about 5×10^4 at temperatures of about $0.2\,T_\mathrm{F}$. The typical mean trapping frequencies in this case are between about $2\pi\times40\,\mathrm{Hz}$ and $2\pi\times50\,\mathrm{Hz}$.

For the interacting Fermi-Fermi mixtures, a pure Fermi gas is produced in the magnetic trap, which is than transferred to the dipole trap at a magnetic field of about $3\,\mathrm{G}$. Here, the magnetic field is switched immediately to about $45\,\mathrm{G}$ and a Landau-Zener sweep is used to produce a single-component gas in the $|9/2,-9/2\rangle$ hyperfine state. After that an rf pulse with a rotation angle of $\pi/2$ is applied [see Fig. 2.5(a)], creating a $50/50$ mixture of the hyperfine states $|9/2,-9/2\rangle$ and $|9/2,-7/2\rangle$. The $|9/2,-7/2\rangle$ atoms are transferred to $|9/2,-5/2\rangle$ using a second Landau-Zener sweep. The mixture is subsequently evaporatively cooled by lowering the dipole trap strength exponentially from a mean trapping frequency of about $2\pi\times120\,\mathrm{Hz}$ to about $2\pi\times50\,\mathrm{Hz}$ within $2\,\mathrm{s}$. The final atom numbers are about 5×10^4 per spin component at a temperature of $0.2\,T_\mathrm{F}$.

The prepared mixture has a Feshbach resonance at about $224\,\mathrm{G}$ [152]. To investigate the interaction effects in the mixture, the magnetic field is switched from $45\,\mathrm{G}$ to some desired

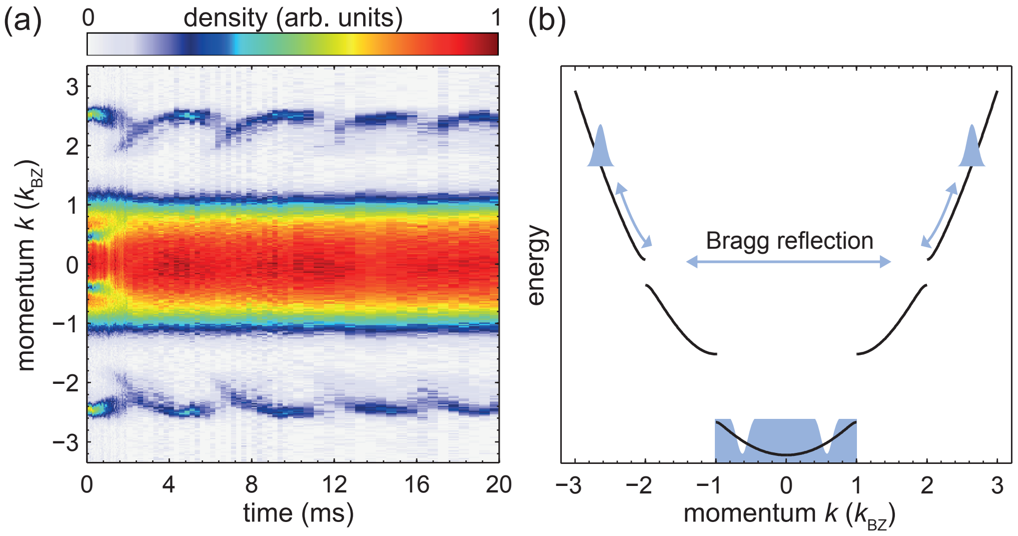

Figure 5.3: Typical photocurrent measurement after excitation to the excited band at $s = 10$ and a trapping frequency $\omega_z = 2\pi \times 50\,\text{Hz}$. (a) Shown are the column densities of the momentum distribution at different times after the excitation. Note the rotation of the image compared to the results in chapter 4. Atoms in the lowest band are represented by the central plateau. The excitations in the upper band clearly oscillate in momentum space. The displayed false color scaling is used in all false color images throughout this chapter, except for the hole distributions. (b) Sketch of the particle dynamics in the extended zone scheme. The atoms are transferred to the second excited band, where they oscillate due to the harmonic confinement. When the excited wave packet reaches the inner boundary of the third Brillouin zone at $q = 0$, it is Bragg reflected to the other side of the extended zone scheme, as observed in the experiment.

value near the Feshbach resonance right after the evaporation with a subsequent waiting time of about 100 ms for the magnetic field to settle. This corresponds to the adjustment of the scattering length between both spin states. For experiments far away from the Feshbach resonance, the background scattering length is about $168.5\,a_B$ (see chapter 6).

After the preparation of the respective atomic ensemble, an optical lattice is adiabatically ramped up linearly within 100 ms. Simultaneously, the trapping frequencies of the system are adjusted as needed, by changing the relative beam powers of the two dipole trap beams. The final trapping frequencies are a combination of the trap and the lattice beams and range between $\omega_z = 2\pi \times 26\,\text{Hz}$ and $2\pi \times 78.5\,\text{Hz}$ in the z-direction and a mean-trapping frequency between $2\pi \times 40\,\text{Hz}$ and $2\pi \times 100\,\text{Hz}$. The trapping frequency in the z-direction is especially important, since all dynamics presented in this chapter have been recorded along this direction.

At the final lattice depth and trapping frequencies, the lattice amplitude is modulated for 1 ms to create the particle and hole excitations. These excitations are eigenstates of the pure lattice Hamiltonian, since the excitation time is much smaller than the inverse trap frequency. Therefore the trap is averaged out in the excitation process (see chapter 4 for a more detailed discussion).

The important contrast to the spectroscopy measurements is, that the band mapping is not performed immediately after the excitation pulse. Instead, the system evolves dynamically before its quasimomentum distribution is probed. During this time, the external trapping potential induces dynamics of the excited particles and the remaining holes. The resulting quasimomentum distribution at different times of the evolution is detected by band mapping and TOF, as described for the multiband spectroscopy measurements.

A typical photocurrent time evolution in a non-interacting gas is shown in Fig. 5.3(a). The particle number is about 5×10^4, the trapping frequency is $2\pi\times50\,$Hz, and the lattice depth is $10\,E_\mathrm{r}$. The lattice modulation has an amplitude of 20% a frequency of 39 kHz, and it was performed for the lattic beam in the z-axis. Since all lattice directions separate, the system only evolves with respect to the z-direction.

The atoms that have been transferred to the excited band exhibit a pronounced oscillation in momentum space, while the holes in the lowest energy band apparently close very fast within the first 2 ms for the specific experimental parameters of Fig. 5.3.

In comparison to the fast closing of the holes, a lifetime of the excitations is observed which exceeds 100 ms. This indicates a slow recombination between the excited particles and holes. Therefore, this cannot explain the observed fast closing of the holes. The lifetime of the excitations is also much longer than the observed oscillation period in the excited band. Since the atoms in the presented measurement are not interacting, the finite lifetime cannot result from interparticle scattering, leading to a relaxation of the excitations to lower bands.

A different possible loss mechanism in this noninteracting system can result from trap losses due to the high excitation energy of the particles in the third band. The trap depths for the presented data are about $2\,h$kHz in the vertical x-direction and $75\,h$kHz in the horizontal directions. Comparing this to the excitation energy of $39\,h$kHz in the horizontal directions, where the oscillations are observed, direct losses from the trap are not possible, since the trap is still considerably higher than the excitation energy. However, every misalignment of the lattice leading to a small oscillation in the vertical x-direction would lead to immediate losses of the excited particles from the trap. In addition, the Gaussian trap potential is not perfectly separable in reality and therefore, the trap itself induces a coupling between the different directions. This coupling is especially important for highly excited states, where the harmonic approximation around the potential minimum (see section 2.3) becomes less reliable. Therefore, a finite lifetime of the excitations in the excited band is to be expected. Since the possible coupling mechanisms are very weak, the lifetime should be much longer than the direct dynamical timescales along the excitation direction, which is in good agreement with the observation.

Coming back to the observed dynamics, let me briefly mention that the oscillatory dynamics of the particles, while induced by the harmonic confinement, have a much faster oscillation frequency than expected for usual dipole trap oscillations. The latter should simply reflect the trap frequency, which would correspond in this case to an oscillation period of 20 ms. In contrast, the observed dynamics have a much shorter period, indicating a more involved explanation, than simple dipole oscillations in the trap. To clarify this behavior, I explain in the following, how these dynamics can be intuitively and theoretically understood. Afterwards, I present a thorough experimental investigation of the observed behavior in dependence on the relevant experimental parameters, such as the lattice depth, the trapping frequency, and the initial quasimomentum.

5.1.2 NUMERICAL MODEL AND ANALYSIS OF THE PHOTOCURRENT

A first qualitative interpretation of the observed excitation dynamics can be obtained by studying the band structure in the optical lattice. In particular, the extended zone scheme is very instructive, as depicted in Fig. 5.3(b). After the excitation pulse, the harmonic confinement leads to an oscillatory dynamics of the atoms in the trap, which is equivalent to an oscillation in momentum space. However, the band dispersion of the lattice hinders the atoms to leave the second excited band since all bands are effectively decoupled concerning the influence of the trap (compare discussion in section 3.1). This leads to a Bragg reflection when the atoms reach the quasimomentum $q = 0$, as depicted in Fig. 5.3(b). In this way, the excited particle are transferred to the other side of the third Brillouin zone as observed in the the data of Fig. 5.3(a). The Bragg reflection skips a part of the usual dipole trap oscillation, which leads to a reduced oscillation period [172].

The above explanation leads to a qualitative understanding of the observed particle dynamics. An equally simple explanation for the hole dynamics is not possible on the basis of the extended zone scheme. To gain more insight into the hole behavior, it is instead necessary to perform a full calculation of the dynamics in the combined lattice and trapping potential. This should also allow for a more quantitative description of the particle dynamics.

I start here with the particle dynamics in the excited band. To obtain a theoretical description of the photocurrent dynamics in a simple model, it is necessary to identify the relevant contributions to the Hamiltonian. First, the measurements are performed with an ideal non-interacting Fermi gas. Second, because of the small amplitude of the excitations, many-body effects due to Pauli blocking can be neglected for the observed dynamics. Therefore, it is reasonable to use a single-particle Hamiltonian for the numerical description.

Note, that the excitation is separable in the different lattice directions in the same way as the potential. In the following, I will only discuss excitations in a single lattice direction, such that a one-dimensional description is sufficient. The full single-particle Hamiltonian for this situation is given by (3.4) as

$$H_{\mathrm{LT}} = \frac{p^2}{2m} + sE_{\mathrm{r}} \sin^2(k_{\mathrm{L}} z) + \frac{1}{2} m \omega_{\mathrm{z}}^2 z^2 \,. \tag{5.1}$$

As discussed in section 3.1, all bands can be treated separately at typical experimental parameters. Further, the oscillatory dynamics for the particles indicate, that the excitations are not localized states at the edge of the system, which would presumably not perform any dynamics. Therefore, the quasimomentum eigenstates $|n, q\rangle$ of the pure lattice and kinetic energy Hamiltonian form a good basis set for the description of the photocurrent dynamics. These are coupled by the harmonic confinement, which eventually induces the observed periodic photocurrent dynamics.

A direct approach on the single-particle dynamics is to calculate the eigenstates of the Hamiltonian (5.1) and based on this, the resulting time evolution of the initial state. The numerical calculation of the eigenstates $|m\rangle$ and eigenenergies E_{m} of (5.1) is straightforward and was already discussed in section 3.1. The quasimomentum time evolution of the initial particle excitation $|p\rangle$ is given by

$$\langle q, n | p(t) \rangle = \sum_{\mathrm{q}', \mathrm{n}', \mathrm{m}} \langle q, n | m \rangle \langle m | q', n' \rangle \langle q', n' | p \rangle \mathrm{e}^{-\mathrm{i} E_{\mathrm{m}} t / \hbar} \,. \tag{5.2}$$

The only unknown parameter is the exact initial form of the excitation $|p\rangle$. Since dynamics can already occur during the excitation process, a full simulation of this time-dependent process is beyond the scope of this work. Instead I follow time-dependent perturbation theory to extract the energy width of the excitation, induced by the 1 ms lattice amplitude modulation pulse [129]. The quasimomentum width is a combined result of the finite energy width of the excitation pulse and the band width of the involved bands. The procedure is described in more detail in appendix A.4. To keep the calculations as simple as possible, the quasimomentum distribution is approximated as a Gaussian, instead of the generally complicated shape. As shown in section 4.1, the lattice amplitude modulation is indeed a coherent process, showing Rabi oscillations in the number of excited particles. Therefore, the created excitations are assumed

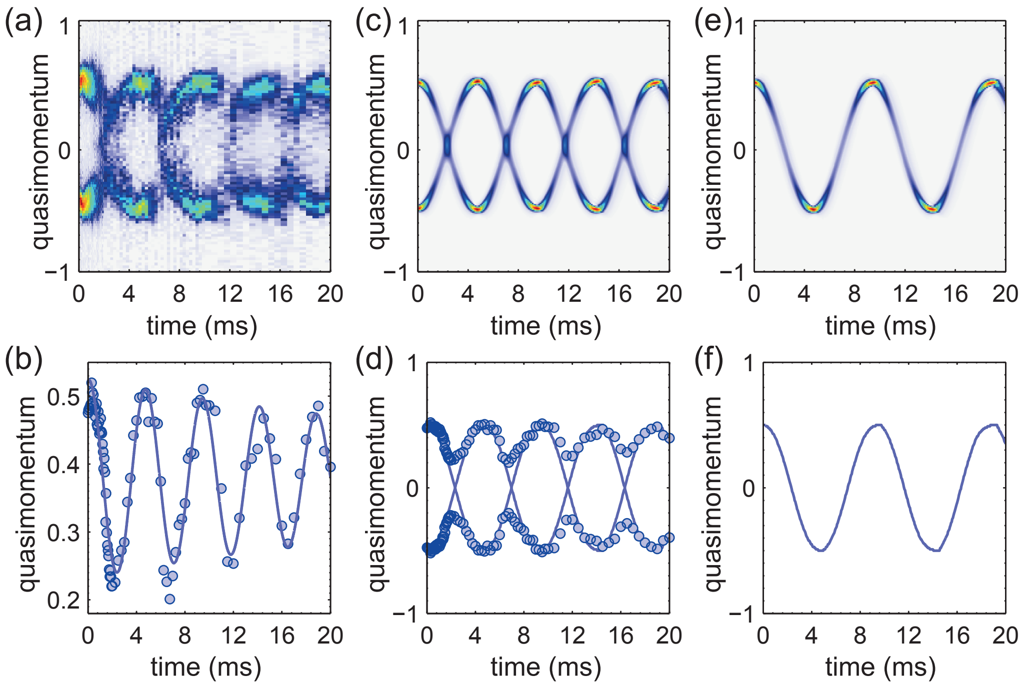

Figure 5.4: Momentum-resolved comparison of the numerical and experimental data for the observed particle dynamics in the excited band. (a) shows the same experimental data as in Fig. 5.3. Here, only the third Brillouin zone is depicted, where all dynamics take place due to the Bragg reflection. (b) Extracted quasimomentum using the difference of both sides of the Brillouin zone. The solid line is fit using an exponentially damped cosine. Note the different scale for the quasimomentum in this image. (c) Numerical results for the parameters of (a). (d) Comparison of the numerical and the experimental data, showing both sides of the Brillouin zone, as in the false color images. The position of the excitation in the theoretical data is obtained by the local maximum of the distribution. (e) Dynamics of a single excitation at positive q_0. The atoms move along the full quasimomentum range from $-q_0$ to q_0, leading to an apparent doubling of the oscillation frequency, if both excitations are considered simultaneously. (f) Extracted position for the numerical calculation as in (e).

---

to be a coherent superposition of quasimomentum eigenstates instead of an incoherent mixture, as characteristic for the full linear response limit. In total the particle excitation is described by a state of the form

$$|p\rangle = \mathcal{N} \sum_{\mathrm{q}} e^{-\frac{1}{2}\left(\frac{q-q_0}{\Delta q}\right)^2} |q\rangle \tag{5.3}$$

with a proper normalization $\mathcal{N}$. For the 1 ms pulse, the energy width of the Gaussian pulse is about 365 Hz, leading to a quasimomentum width of about $\Delta q = 0.022$ for the parameters of the data shown in Fig. 5.3.

Using all these assumptions, the dynamics of the particle excitation can be calculated. Figure 5.4 shows a comparison of the experimental results shown in Fig. 5.3 and the numerical results obtained as described above, which are in excellent agreement. For the calculation 11 bands and 200 quasimomenta within in the first Brillouin zone have been used. The quantitative analysis of the particle dynamics in the photocurrent measurements uses the COM-momentum approach introduced for the multiband spectroscopy in section 4.1. The quasimomentum is extracted at each time step using the center-of-mass of excitations with both, positive and negative quasimomentum. This leads to the extracted data shown in Fig. 5.4(d). To minimize systematical errors due to displacements of the full system, the distance between both excitations is

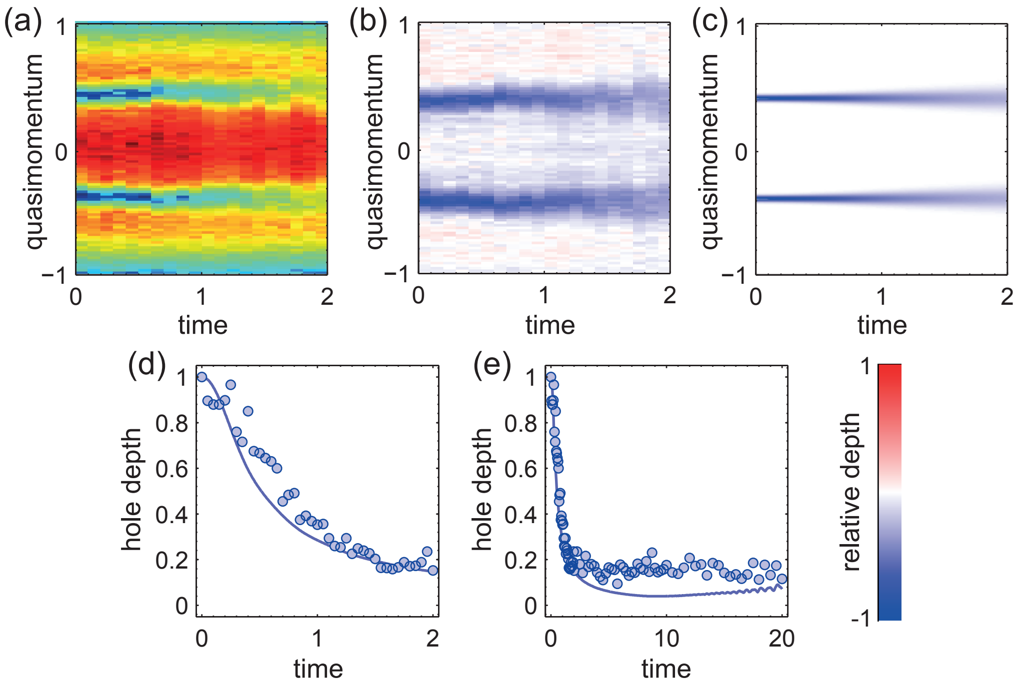

Figure 5.5: Momentum-resolved comparison of the numerical and experimental data for the observed hole dynamics in the lowest band. (a) shows the first 2 ms of the same experimental data set as in Fig. 5.3 and (b) the corresponding differential image. Only the first Brillouin zone is depicted. The displayed false color scaling is used in all false color images of hole distributions in this chapter. (c) Numerical result for the corresponding dynamics without any free parameters. The time evolution of the hole depth is defined as the maximum of the hole distribution in (b) for each time step, normalized to the overall maximum. It is shown for the initial closing in (d) and for longer times in (e) in comparison with the numerical results (solid lines) as described in the text. Note, that the hole depth is depicted positive in the quantitative analysis.

---

evaluated for each time step, leading to the data presented in Fig. 5.4(b). From this data, the oscillation frequency is obtained using a fit with an exponentially damped cosine, revealing an oscillation frequency of 214±4 Hz for the presented data.

The numerical data of Fig. 5.4(c) can be evaluated similarly, leading to the theory results in Fig. 5.4(d). As in the experiment, the initial state in the simulation has two independent excitations at $\pm q_0$. However, the calculations show, that each of the excitations performs oscillations through the full momentum range from $-q_0$ to q_0, as depicted in Figs. 5.4(e) and (f), where the dynamics for only one excitation is shown. The disagreement at small quasimomenta between theory and experiment stems from the COM-momentum evaluation, which is not reliable at small quasimomenta, as discussed in chapter 4.

As the extraction of the oscillation frequency for the experimental data uses quasimomentum differences, the effective observed oscillation frequency is artificially doubled compared to the theoretically predicted oscillation frequency for a single excitation. To account for this, I report in the following only the corrected oscillation frequency of one excitation, obtained by a rescaling of the fitted frequency by a factor of $1/2$, leading to an oscillation frequency of 107±2 Hz for the data shown in Fig. 5.4.

After this successful quantitative description of the particle dynamics in a single-particle picture, it remains open, how to treat the hole dynamics. The holes represent missing particles in the lowest energy band, which is still filled with many other fermions. Though these are not interacting, they feel strong many-body effects due to the Pauli blocking, which hinders the simultaneous occupation of the same spin states. Interestingly, there is a very beautiful description of exactly this situation used in solid state physics. In this approach, holes in an otherwise completely filled band are considered as particles with a negative mass in an otherwise completely empty band [142, 190]. Surprisingly, in the present case this resembles exactly the model used above for the particles in the excited band. The only differences in the Hamiltonian (5.1) are the replacement of the mass by its negative and that the energy dispersion for the lowest band must be used. In this way, the equation (5.2) can also be used to calculate the time evolution for the hole excitation. It is important to note here, that the initial state $|h\rangle$ for the hole excitation has exactly the same quasimomentum distribution as the particle excitation $|p\rangle$. The reason for this is the quasimomentum conservation of the lattice amplitude modulation. Every excited particle must have the same quasimomentum as it had in the lowest energy band before the lattice modulation, equalizing the shapes of both excitations.

For a comparison of the numerical and experimental results, see Fig. 5.5, which again reveals an excellent agreement without any free parameters in the calculation. Note in particular, that no discernible quasimomentum evolution can be observed in the experiment or in the theoretical calculation. At the same time the observed depth of the hole strongly decreases, until the hole nearly vanishes. Note, that the very good agreement of the experimental data and the effective single particle theory is very surprising, regarding the strong approximations made to describe the genuine *many-body* system in the lowest band.

The evaluation of the hole depth in Fig. 5.5 has been performed in the following way. First, a differential image is computed for each time step. For a definition of the differential image, see Fig. 4.2 in chapter 4. To evaluate the hole, first the column density of the differential image is calculated and the hole depth is defined as the maximum of the resulting hole distribution. For the measurement of the hole depth versus time, as shown in Fig. 5.5, all absorption images are normalized to the same total particle number and the hole depths are always reported relative to the maximal value for each individual series of measurements.

From the above discussion a more intuitive insight on the dominant processes regarding the hole dynamics can be obtained. Recall here, that the lattice amplitude modulation creates the same initial state for both excitations, if represented in the quasimomentum basis, and the dynamics can be described by the same effective single-particle theory. Therefore, the explanation for the different behavior must result from the different influence of the external trapping potential on the excited and lowest energy band. The main difference is, that due to the different band widths, the states in the lowest energy band are much stronger localized than in the excited band (see section 3.1). The stronger spatial localization also reduces the localization of the eigenstates in quasimomentum, which means, that the full eigenstates of the combined potential do not resemble the original quasimomentum eigenstates very well anymore. This probably leads to a fast dephasing of the hole excitation in momentum space.

In summary, the simulations reproduce the observed dynamics shown in Fig. 5.3 very well. Surprisingly, the single-particle description still works for the hole excitation using an particle-hole mapping from solid state theory, resulting in a completely different dynamics compared to the particle excitation. The qualitative behavior of the particle excitation can also be explained in an intuitive explanation using the extended zone scheme of the optical lattice. For the hole excitations, another interpretation has been found, where the fast closing arises from the strong localization of the eigenstates in the lowest band.

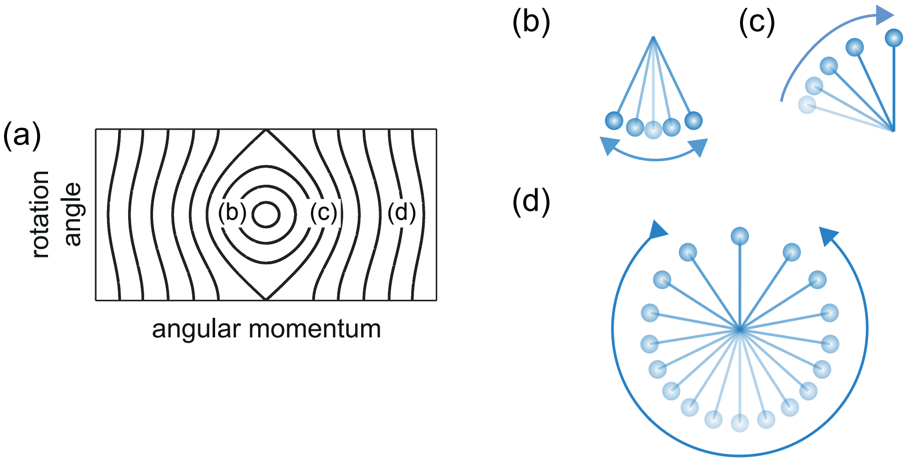

Figure 5.6: (a) Phase space of the nonlinear pendulum with (b) closed trajectories showing periodic oscillations around the equilibrium position, (c) a separatrix, where the pendulum asymptotically approaches the inverted unstable equilibrium position and (d) open trajectories, leading to periodic oscillations with nearly constant angular momentum and moving through all possible rotation angles of the pendulum.

5.2 SEMICLASSICAL PHASE SPACE DESCRIPTION

The intuitive understanding of the dynamics developed above can be extended by using a semiclassical approximation of the harmonically confined lattice system [10, 47, 211]. This approach allows for a very elegant representation of the full system in the form of a semiclassical phase space, where the properties of the different bands are highlighted, which eventually lead to the unlike dynamics of the particle and hole excitations. A particularly interesting aspect of this approximation is, that the investigated system maps directly onto the classical nonlinear pendulum [211], which allows for an especially lucid explanation for the oscillation frequencies of the excited particles, as discussed later.

In general, the semiclassical approximation is based on a mapping of the Hamilton operator (5.1) onto a scalar-valued Hamilton function $\mathcal{H}(z, q)$ that determines the semiclassical dynamics via the Hamilton equations of motion [216]

$$\partial_t z = \partial_q \mathcal{H}\,, \tag{5.4}$$

$$\partial_t q = -\partial_z \mathcal{H}\,. \tag{5.5}$$

Here, position and quasimomentum are the proper conjugate variables [47].

The semiclassical approximation for the present system treats every band independently, which is justified for all experimental parameters, as discussed earlier. Based on this, the kinetic energy and lattice potential are replaced by the corresponding lattice momentum dispersion $E_{\mathrm{q}}^{\mathrm{n}}$ in the Hamiltonian (5.1). As a next step, the quasimomentum q and the position operator z are treated as classical numbers. For convenience, both variables are typically taken to be dimensionless, where $z \to z/(\lambda_{\mathrm{L}}/2)$. This defines a phase space for each band, spanned by the the spatial coordinate z and the quasimomentum q. The general form of the resulting Hamilton function is [47]

$$\mathcal{H}(z, q) = E_{\mathrm{q}}^{\mathrm{n}} + \frac{\nu}{2} z^2\,, \tag{5.6}$$

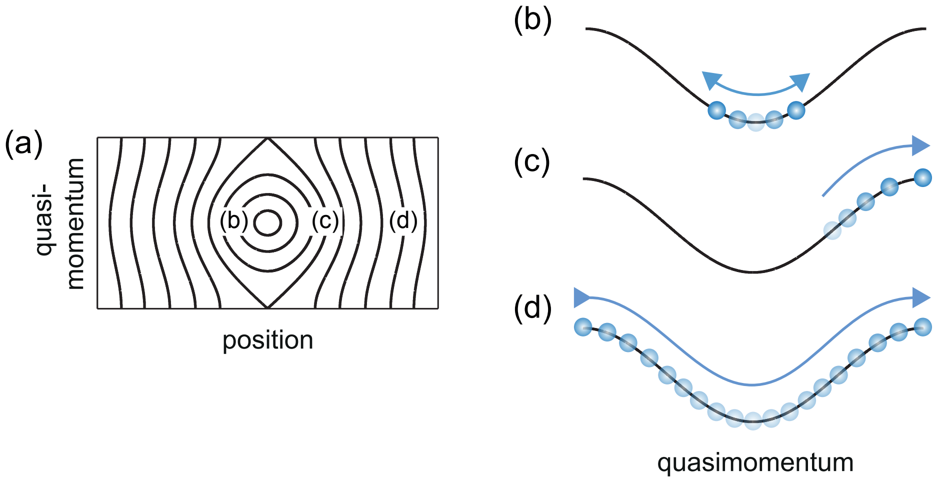

Figure 5.7: Phase space of an optical lattice with harmonic confinement. (a) Phase space diagram for the lowest energy band of an optical lattice with harmonic confinement. (b) Quasimomentum dynamics corresponding to closed trajectories, leading to oscillations in the quasimomentum. (c) Dynamics on the separatrix, asymptotically approaching the unstable equilibrium configuration at $q = 1$. (d) Bloch oscillation-like dynamics for open trajectories. The atoms cross the whole Brillouin zone and re-enter it at the other site, performing a periodic motion.

---

where $\nu = m\omega_z^2(\lambda_L/2)^2$.

The essential properties of (5.6) are most clearly visible in the particularly interesting case of the tight-binding approximation. Here, the band dispersion has the cosine form (3.9) and the Hamilton function becomes [211]

$$\mathcal{H}(z,q) = -2J\cos(\pi q) + \frac{\nu}{2}z^2 \,. \tag{5.7}$$

Note, that this Hamilton function is identical to that of the nonlinear pendulum, where momentum and position are interchanged.

5.2.1 THE NONLINEAR PENDULUM ANALOGY

To visualize the behavior of the nonlinear pendulum and the corresponding ultracold atom system, it is convenient to introduce the semiclassical phase space diagram, which is shown in Fig. 5.6. The solid lines depict equal energy surfaces of the Hamilton function $\mathcal{H}$, which constitute the phase space trajectories for any dynamical evolution. The system shows two qualitatively different regions. At small angles and small angular momenta, the system exhibits closed trajectories, which correspond to a small amplitude oscillation of the pendulum near the harmonic limit. At large angular momenta, the nonlinear pendulum rotates completely and has open trajectories. Between the two different regimes, there is a so-called separatrix. It corresponds to the situation, where the pendulum asymptotically approaches the unstable equilibrium such that the tip of the pendulum points completely upwards. Therefore, the oscillation frequency of the pendulum effectively reaches zero at the separatrix.

The correspondence to the optical lattice system is straightforward. It is important that momentum and position are interchanged from the real nonlinear pendulum (see Fig. 5.7) [211]. The closed trajectories correspond to oscillations of the atoms through the lattice, due to the harmonic trapping potential. The open trajectories correspond to Bloch oscillations in Wannier

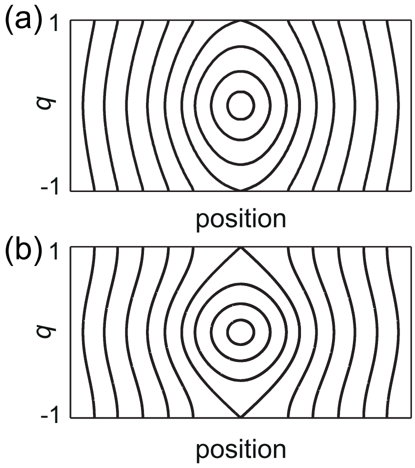

Figure 5.8: Phase space of the second excited band. (a) Calculation of the phase space for the second excited band for $s = 10$. It includes the same qualitative features as the tight-binding solution shown in (b) and leads to the same dynamical regimes.

---

stark ladders [143, 217]. Finally, the separatrix corresponds to a state, where the unstable equilibrium corresponds to $z = 0$ and $q = 1$. Due to the flat form of the dispersion and the minimum of the trap energy at this point, the state has no velocity ($\partial_t z = 0$) and no acceleration ($\partial_t q = 0$) and therefore shows no dynamics. If the system is prepared at another point on the separatrix, it reaches the equilibrium point asymptotically and again the oscillation frequency vanishes.

If the tight-binding approximation is not valid, the momentum dependent part of semiclassical Hamilton function becomes in general $E^{\mathrm{n}}_{\mathrm{q}}$. This dispersion has the same essential features as in tight binding with a parabolic form around $q = 0$, and a vanishing gradient at $q = 1$, leading to the same regions in the phase space. Being relevant for the performed experiments, an exemplary phase space for the second excited band is shown in Fig. 5.8 for $s = 10$. In the nonlinear pendulum analogy, this situation corresponds to a nonlinear pendulum with a slightly deformed potential compared to (5.7).

5.2.2 GROUND STATE AND EXCITATIONS ON THE PHASE SPACE

As mentioned above, all dynamics on the semiclassical phase space are bound to equal energy trajectories. Therefore, a constant phase space distribution along one of these lines is a time independent state, resembling an eigenstate of the Hamiltonian in the quantum mechanical description, as sketched in Fig. 5.9. This observation gives a strong analogy of the different regimes in the semiclassical description to the quantum mechanical results from section 3.1. States within in the separatrix are delocalized in spatial and quasimomentum coordinates, representing the quantum mechanical eigenstates at energies within the band of the optical lattice. States outside the separatrix are localized only to a small region in real space and therefore correspond to the localized states in the band gap of the pure lattice. The separatrix marks the equal energy trajectory coinciding with the band width ΔE of the energy band. Therefore, the semiclassical description is fully consistent with the numerically obtained results for the inhomogeneous lattice system. There, the localized states due to the harmonic confinement also appear exactly above the band edge.

The $T = 0$ ground state of a Fermi gas in the combined periodic and harmonic potential can

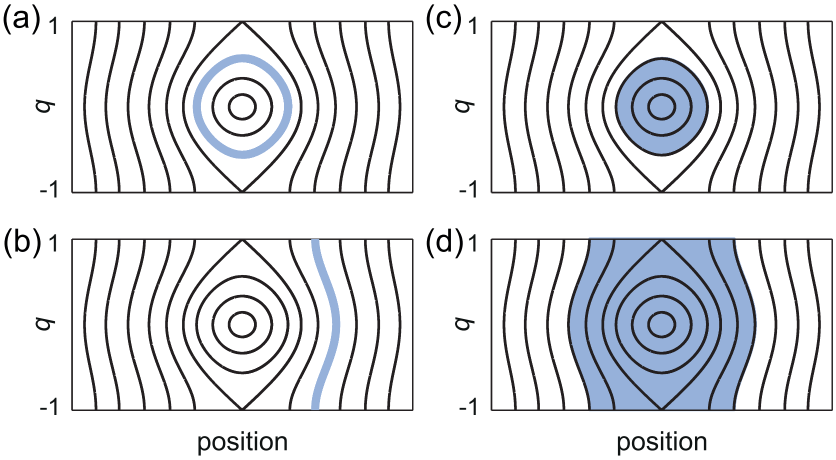

Figure 5.9: Representation of atoms on the semiclassical phase space. (a) shows a single classical stationary state corresponding to a quantum mechanical eigenstate in the center of the trap. (b) Classical stationary state corresponding to a localized state at the edge of the trap. (c) Metallic many-body ground state in the phase space representation. No localized states are occupied. The Fermi energy lies below the separatrix. (d) Band insulating ground state in the phase-space representation, where many localized states are occupied and the Fermi energy lies above the separatrix.

---

be described in the semiclassical approximation by a constant distribution, filling up all equal energy surfaces up to the Fermi energy, leading to a semiclassical distribution function $W(z,q)$. The spatial and the momentum distribution are given by the integral over the correspondingly other direction

$$n(z) = \int dq W(z,q)\,, \tag{5.8}$$

$$n(q) = \int dz W(z,q)\,. \tag{5.9}$$

In a more technical sense, the distribution can be calculated as the Wigner function of the single-particle density matrix of the full many-body state [218, 219]. A similar approach for interacting fermions in a harmonic trap is presented in chapter 7, where this correspondence is discussed in more detail. Figure 5.9 shows the phase-space distribution for one metallic and one band insulating state exemplarily. The separatrix marks the transition from metallic to insulating states.

In the photoconductivity measurements described above, the particle and hole excitations are created starting from an initial band insulator. As discussed in section 5.1, the excitations are well described by a coherent Gaussian wave packet with a finite momentum width, determined by the finite amplitude modulation pulse time and the band dispersions of the coupled bands. The semiclassical distribution function of this state can be calculated using the above mentioned Wigner transform. For a Gaussian state with a momentum width Δq, the Wigner transform results in a phase-space distribution function, that is also Gaussian in the spatial domain, with an inverse width $\Delta z = 1/\Delta q$. As in the quantum mechanical calculation, particle and hole excitations have the same semiclassical distribution function $W_{\mathrm{p/h}}(z,q)$. See [4] for a more in-depth discussion of the Wigner function for the excitations.

A sketch of both excitations, starting from an initial band insulator, is shown in Fig. 5.10. Due to the different band width of the excited and lowest energy band the particle and hole

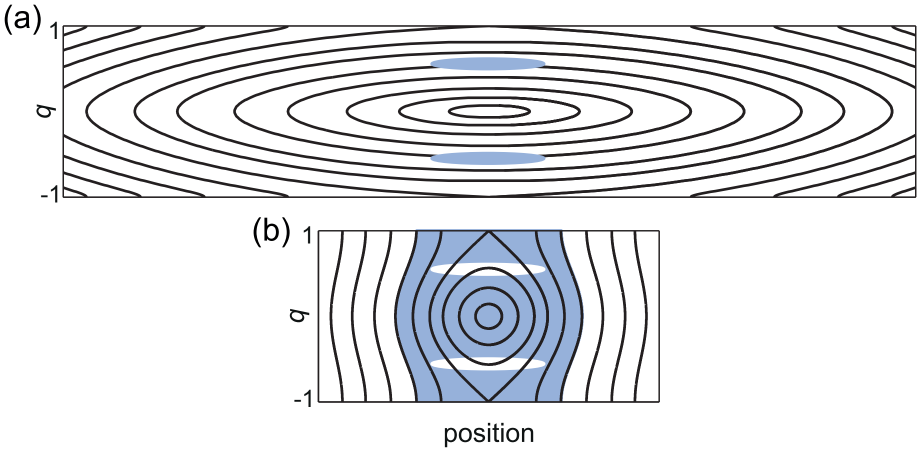

Figure 5.10: Sketch of the particle and hole excitations on the semiclassical phase space for (a) the second excited band and (b) the lowest energy band in a lattice of $10\,E_\mathrm{r}$. The lattice amplitude modulation removes a Gaussian wave packet from the band insulating state in the lowest band and shifts the atoms into the second excited band, where they occupy the same phase-space coordinates. The phase space of the excited band is much wider in the spatial direction, which stems from the larger bandwidth of the excited band compared to the lowest band.

excitations have very different compositions of equal energy trajectories, although they have the same absolute distribution functions. While the particle excitation is located at approximately one single trajectory, the hole excitation is distributed over many different trajectories with different oscillation frequencies. This very fact leads to the pronounced difference of the particle and hole dynamics as observed in the experiment and in the numerical simulations.

5.3 HIGHER-BAND DYNAMICS OF EXCITED PARTICLES

In this section, I concentrate on the particle photocurrent, which exhibits an oscillatory behavior in the excited band. The hole dynamics are comprehensively discussed in the next section. From the semiclassical description, various important deductions about the dynamical evolution can be made. On the one hand, the systems resembles a nonlinear pendulum and thus, the dynamics are expected to depend on the initial quasimomentum. On the other hand, the strength of the nonlinearity is connected to the band structure, and thus the dynamics should depend on the lattice depth. Naturally, also the strength of the harmonic confinement, which induces the dynamics initially, has an influence on the oscillation frequency. The trapping frequency and lattice depth can easily be tuned experimentally by varying the intensity of the corresponding laser beams. A full quasimomentum resolution is provided by the employed excitation method using lattice amplitude modulation on an initial band insulator. In this way all important dependencies can be studied in the experiment.

In a first measurement, the trapping frequency was varied at a fixed lattice depth and equal initial quasimomenta. The results are shown in Fig. 5.11(a) and (b). A linear dependence of the oscillation frequency on the trapping frequency is observed. In a second set of experiments, the photocurrent frequency was studied in dependence on the lattice depth and initial quasimomentum, as shown in Fig. 5.11(c). As expected, the oscillation frequency does strongly depend on both parameters. With increasing lattice depth, the oscillations become slower. They also

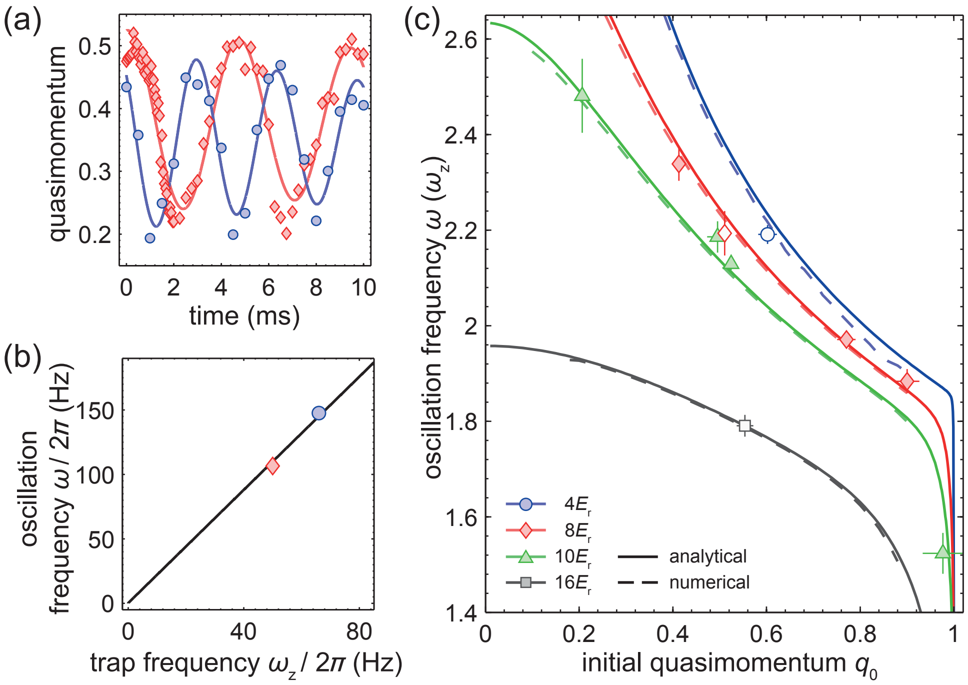

Figure 5.11: Measurement of the particle-photocurrent in dependence on lattice depth, quasimomentum, and trapping frequency. (a) Exemplary oscillation measurements of the particles in the excited band at $10\,E_\mathrm{r}$ and $q_0 = 0.5$ for two different trapping frequencies $\omega_\mathrm{z} = 2\pi \times 66\,\mathrm{Hz}$ (circles) and $\omega_\mathrm{z} = 2\pi \times 50\,\mathrm{Hz}$ (diamonds). Solid lines are fits to the data. Extracted oscillation frequencies are $\omega = 2\pi \times (148 \pm 5)\,\mathrm{Hz}$ (circles) and $\omega = 2\pi \times (107 \pm 2)\,\mathrm{Hz}$ (diamonds). (b) Oscillation frequency ω in dependence on ω_z. The solid line is a linear fit with the assumption, that no dynamics take place at $\omega_\mathrm{z} = 0$. The data indicates a linear dependence of ω on the trapping frequency ω_z, which perfectly agrees with the results of (5.10) of the semiclassical analysis. All errorbars are fit errors showing one standard deviation. (c) Results for the variation of quasimomentum and lattice depth. Filled symbols represent measurements with non-interacting mixtures. Open symbols show data with interacting binary spin mixture of $|9, 2, -9/2\rangle$ and $|9, 2, -5/2\rangle$ at a background scattering length of $a = 168.5\,a_\mathrm{B}$. Solid lines show the results of (5.10). Dashed lines show numerical calculations using (5.2).

slow down with increasing quasimomentum.

Figure 5.11 additionally shows numerical data and the results of an analytical calculation in the semiclassical approximation as described below. Both fit excellent to the data and are fully consistent with each other. Small deviations can be observed between both models, which are only significant at very small lattice depths. As the numerical calculation becomes unstable at very large and small momenta, the results are only shown for central momenta. Hence, a comparison of the models near the separatrix is not possible. Inspecting the experimental and semiclassical data in more detail shows a sharp decrease of the oscillation frequency near $q = 1$. This is a result of the separatrix in the semiclassical phase space. The observation of this frequency drop clearly demonstrates the very good description of the system using the semiclassical approximation.

Note, that the preparation of states outside the separatrix is not possible in the excited band. Since the inner region of oscillating trajectories has a much larger spatial extend in excited band compared to the lowest energy band, all excitations are strictly confined to the oscillating region. Therefore, no Bloch oscillation like dynamics have been observed in the experiments. Some data shown in Fig. 5.11 was taken using interacting binary mixtures at a scattering length

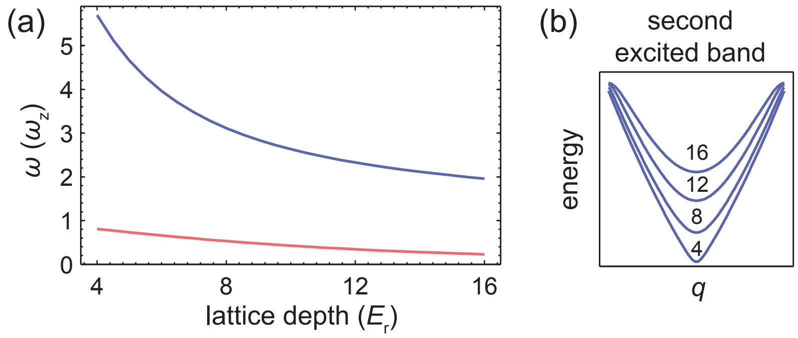

Figure 5.12: Calculation of the photocurrent frequency in dependence on the lattice depth for small quasimomenta. (a) Oscillation frequency in dependence on the lattice depth, obtained using (5.11) as the effective momentum dispersion. The dynamics get slower for larger lattice depths, arising from the reduced curvature as shown in (b), where the second excited band is depicted for $s = 4, 8, 12, 16$ in the reduced zone scheme. The blue solid line in (a) depicts the second excited band. In comparison, the result for the hole dynamics is shown in red, as discussed in the text.

---

of $168.5\,a_{\mathrm{B}}$. The results do not deviate from the single-particle calculations. This is due to the low density of particles in the excited band, which suppresses interaction effects that can alter the dynamics.

The semiclassical calculations were performed by Alexander Itin and Ludwig Mathey. Therefore, I only give a short motivation of the analytical treatment, which allows for the elegant description leading to the results of Fig. 5.11. A complete derivation can be found in [4]. As discussed in section 5.2, the excited particles are well localized in the phase space of the upper band, and occupy approximately only one single equal-energy trajectory. This is a result of the excitation process in combination with the different bandwidths of the lowest and the excited energy band. Hence, the excited particles can be modeled in good approximation as a single point in phase space instead of using the full Gaussian phase space distribution. The excitation has a freely tunable initial quasimomentum q_0 and is always centered at $z = 0$. Using these points as the initial coordinates of the excitations, the total energy is given only by the kinetic energy $E^2_{\mathrm{q}_0}$, while the spatial energy vanishes at $z = 0$.[1] The Hamilton equations of motion (5.4) and (5.5) can be solved for these initial conditions by inserting (5.6) and exploiting the energy conservation in the dynamical evolution. The calculation yields

$$\omega(q_0) = \omega_{\mathrm{z}} \frac{\pi}{2} \left(\int_0^{q_0} dq \sqrt{\frac{E_{\mathrm{r}}}{E^2_{q_0} - E^2_q}} \right)^{-1} , \tag{5.10}$$

which directly confirms the linear dependence of ω on ω_{z}, which was found also experimentally and numerically. Also the lattice depth and quasimomentum dependencies are perfectly described by (5.10), as seen in Fig. 5.11 in comparison with the experimental and numerical data.

While the quasimomentum dependence is a direct consequence of the nonlinear pendulum behavior, the influence of the lattice depth can be most clearly described in the limit of excitations with small initial quasimomenta. In this case, the band dispersion can be approximated

---

[1] Since all experimental data is taken for $n = 2$, I show all calculations explicitly for this case. However, the same is true for all other bands n that are sufficiently isolated, where only the appropriate band dispersion E^n_{q} must be used.

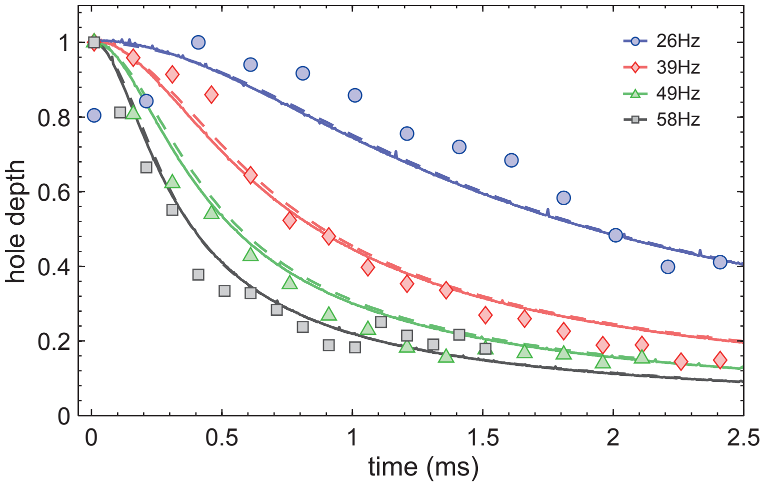

Figure 5.13: Measurement of the hole-closing dynamics. Time evolution of hole depth relative to the maximum depth at $10\,E_{\mathrm{r}}$ and $q_0 = 0.5$ for different trapping frequencies $\omega_z/2\pi$ as indicated. The particle number is about 1×10^5 at a temperature of about $0.2\,T_{\mathrm{F}}$. Solid lines are semiclassical simulations as described in the text, performed and kindly provided by Alexander Itin. The dashed lines show the full numerical calculations for the holes.

harmonically as

$$E^2_{\mathrm{q}} \approx \frac{q^2}{2m'}\,, \tag{5.11}$$

where m' is the effective mass of the atoms at $q = 0$, given by the inverse curvature of the excited band $m' = (d^2E^2_q/dq^2|_{q=0})^{-1}$. Inserting (5.11) into (5.6) leads to the Hamilton function of a harmonic oscillator, where the oscillation frequency is independent of the initial quasimomentum and is given by $\omega = \sqrt{m/m'}\omega_{\mathrm{z}}$ with the bare mass m of ^{40}K. A calculation of ω in dependence on the lattice depth using the above approximation is shown in Fig. 5.12. The effective mass increases with the lattice depth, since the curvature decreases correspondingly. This leads to a decrease of ω as observed in the experiment. The decrease of the oscillation frequency for all higher quasimomenta is a direct consequence of the result for small q, since all oscillating trajectories pass through $q = 0$, where the oscillation is slowed down due to the increased effective mass.

The presented data represents the first study of ultracold fermions in excited bands of an optical lattices. The investigation of the fundamental properties of the excited particles constitutes an important step towards the realization of fermionic many-body systems in higher bands.

5.4 HOLE DYNAMICS IN THE LOWEST ENERGY BAND

I now turn to the hole dynamics in the lowest energy band. Note here again, that the holes show no evidence for dynamical evolution during their closing time, both in experiment and in theory. The explanation for this is closely related to the above result (5.11) for the particle dynamics. There it is argued, that the increased effective mass slows down the oscillation with increasing lattice depth. The same should happen for the holes, since they evolve on a similar phase space than the particles. Indeed, calculating the curvature of the lowest energy band in comparison to the second excited band results in a much larger effective mass for

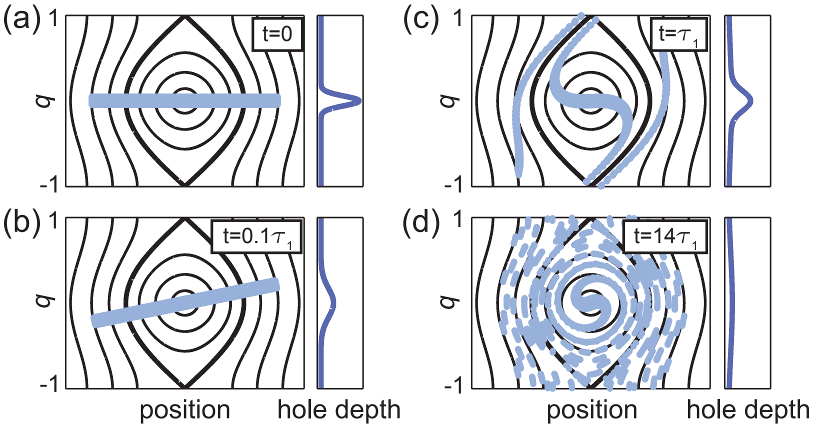

Figure 5.14: Sketch of the hole-closing dynamics in the semiclassical phase space. (a) Initial phase space distribution of a hole at $q_0 = 0$ together with its quasimomentum distribution $n(q)$. (b) Phase space distribution after a short time during the hole closing. The hole basically rotates in the phase space with a constant shape. The momentum distribution becomes significantly flatter due to the rotation. (c) Phase space distribution after a full rotation period τ_1. A rephasing of the hole depth occurs. (d) After many rotations, the hole distribution is completely distorted and no rephasings are possible. This is due to the nonlinear pendulum behavior of the system, where all trajectories have slightly different rotation frequencies.

---

the holes. The oscillation frequency of the holes around $q = 0$ is also shown in Fig. 5.12 in comparison to the particle result, revealing a suppression of the hole frequency by about one order of magnitude. Due to this strong slow-down of the momentum dynamics of the holes, I concentrate in the following only on the hole-closing dynamics, which appear on a much faster timescale, effectively obscuring any oscillatory dynamics.

The fast closing dynamics in the order of a few ms are consistent with numerical simulations. To isolate the relevant processes, additional measurements were performed for different trapping frequencies. The results are shown in Fig. 5.13. It is clearly visible, that the holes close faster with increasing trapping frequencies. Figure 5.13 shows also full numerical calculations and simulations in the semiclassical approximation, both in very good agreement with each other and the experiment. As for the numerical calculations shown in Fig. 5.5, a Gaussian wave packet of particles with a negative mass is used in the semiclassical simulation.

The intuitive explanation for the hole closing obtained from the numerical approach can be extended using the semiclassical description. The main mechanism for the hole-closing dynamics is illustrated in Fig. 5.14. The hole stretches over many different equal energy trajectories and thus does not show a simple rotation along one of them, as observed for the excited particles. However, for short times after the initial excitation, the hole distribution basically rotates and does not significantly alter its shape. This rotation looks like a closing of the hole, since the measured hole depth is determined by the projection of the distribution onto the quasimomentum axis. This is drastically reduced by the rotation, if the initial distribution is very elongated. Consequently, the apparent closing of the holes does not destroy the character of the excitation, but changes only its alignment in the phase space.

In addition to the hole-closing dynamics, Fig. 5.14 shows that the system can exhibit revivals of the hole depth in principle. While such a revival is not visible in the data of Fig. 5.3, I discuss the experimental observation of this phenomenon in a suitably chosen parameter regime later. For the moment I restrict the discussion to the initial closing, which can be described in

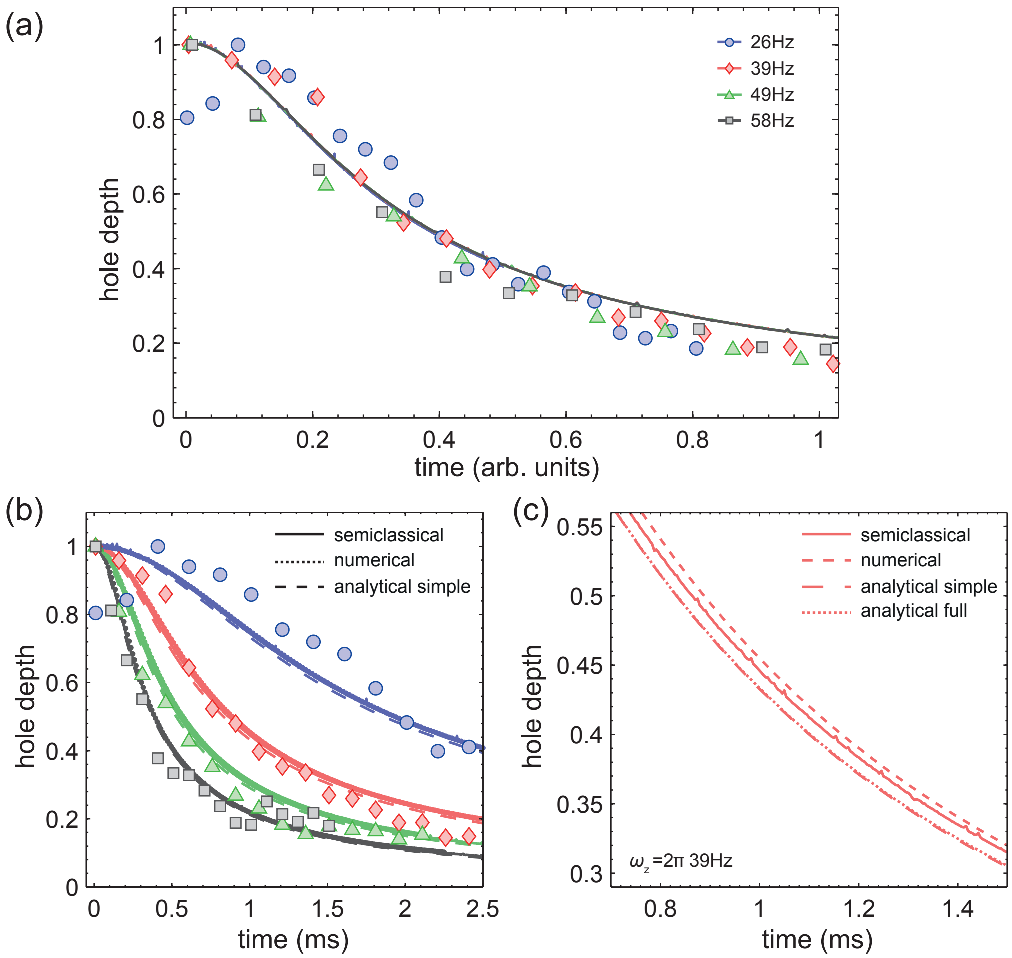

Figure 5.15: Comparison of analytical and numerical results for the hole-closing dynamics with the experiment. (a) Rescaled hole-closing data with the square of the trapping frequency $t \to t \times \omega_z^2$. Solid lines show the semiclassical simulation from Fig. 5.13, kindly provided by Alexander Itin. Due to the perfect scaling behavior of the theoretical results, the different curves are not discernible. (b) Same data as in Fig. 5.13. The different lines represent the three different calculations, namely the semiclassical simulation (solid line), a numerical calculation (dotted line) and the analytical result (5.13). (c) Comparison of the three calculations from (b) and the full analytical result (5.12) for $\omega_z = 2\pi \times 39\,\text{Hz}$ in more detail. Note in particular the perfect agreement between both analytical results, justifying the simplification in (5.13).

---

an analytical expression treating the short time limit only. The calculations were again performed by Alexander Itin and Ludwig Mathey and are motivated shortly below. For more details, see [4]. To obtain the analytical expression, first the equations of motion are linearized, which corresponds to a harmonic oscillator limit. A full rotation of this oscillator has a period of $\tau_1 = h/\sqrt{2J\nu}$, which determines the validity of the short time approximation as $t \ll \tau_1$. Solving the linearized equations of motion for the Gaussian initial state up to second order in time and projecting the result onto the quasimomentum axis leads to a time evolution of the maximal hole depth, which is

$$D(t) = \frac{D(t=0)}{\sqrt{1+(t/T)^2}} \exp\left(-\left(\frac{t}{\tau_2}\right)^2 \frac{(t/T)^2}{1+(t/T)^2}\right) . \tag{5.12}$$

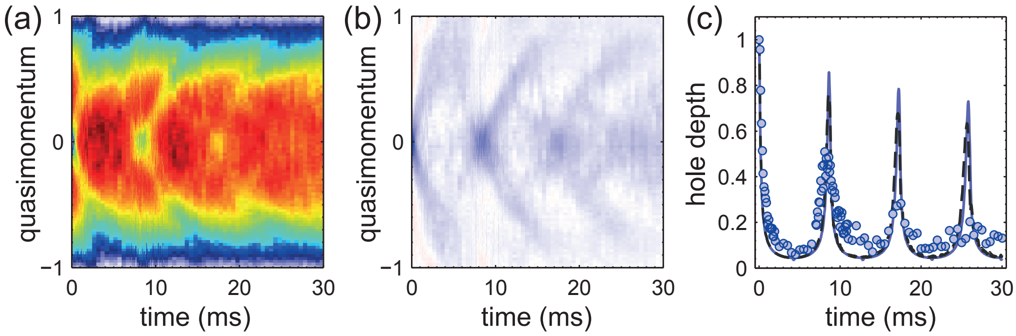

Figure 5.16: Observation of coherent hole revivals at shallow lattices. The experimental data shows a clear rephasing of a hole excitation for long evolution times at $2\,E_\mathrm{r}$, $q_0 = 0.0$ and $\omega_\mathrm{z} = 2\pi \times 63\,\mathrm{Hz}$. The particle number is about 1×10^5 and the temperature is $0.2\,T_\mathrm{F}$. (a) Momentum resolved data, where only the first Brillouin zone is depicted. (b) Differential image of the data from (a). Here three rephasing can be observed. (c) Comparison of experimental and theoretical data for the extracted hole depth. The solid line is a semiclassical simulation, kindly provided by Alexander Itin. The dashed line shows a full numerical simulation.

Here, two additional timescales are introduced, namely $\tau_2 = \hbar\Delta z/\pi J \sin^2(\pi q_0)$ and $T = \hbar\pi^2\Delta q^2/\nu$, which govern the dynamics in the short time limit. τ_2 sets the timescale for changes of the spatial distribution. It is essentially given by the spatial width Δz of the wave packet divided by the tunneling energy J in the lattice. Thereby, the relative change of the spatial distribution due to the phase space rotation decreases with increasing Δz, while an increase in J leads to a faster rotation. In a quantum mechanical description, the spatial redistribution in the lattice increases with increasing tunneling amplitude J. On the other hand, an already spatially extended state has less relative change in the distribution than an initially very compressed state, assuming a simple diffusion of the particle.

A similar analysis for T reveals, that it governs the change of the momentum distribution. The momentum width Δq appears in the same way as Δz before, and the harmonic confinement ν, which couples the quasimomentum states in the lattice, takes the role of the tunneling amplitude J in the spatial domain. In the experiment very elongated states are used, where $\Delta z \gg \Delta q$ and thus $\tau_2 \gg T$. Since the measurements are performed in the momentum domain, the spatial redistribution is irrelevant and (5.12) can be simplified for times $t \ll \tau_2$ to

$$D(t) = \frac{D(t=0)}{\sqrt{1+(t/T)^2}}\,. \tag{5.13}$$

Equation (5.13) shows two important properties of the holes. First, they are stabilized for broader wave packets. Second, the hole-closing time is inversely proportional to the square of the trapping frequency $T \propto 1/\omega_\mathrm{z}^2$. A comparison with the experimental timescales shows, that very stable holes with closing times in the order of 10 ms can be achieved even at moderately low trapping frequencies of about 10 Hz, which is easily realized experimentally. To study the validity of the scaling behavior predicted by (5.13), the experimental data and the semiclassical simulations shown in Fig. 5.13 are rescaled by T, as shown in Fig. 5.15(a). All four data sets perfectly reduce to one single curve, as expected from the analytical result. The absolute agreement of (5.13) with the numerical and experimental data is demonstrated in Fig. 5.15(b) and (c), where also both approximations, (5.12) and (5.13), are compared. All approaches show very good agreement with each other and the data, demonstrating the applicability of the simple analytical result (5.12) to describe the hole-closing dynamics over a wide range of parameters.

As shown above, the closing of the hole can be described very good by a simple rotation of the hole in the phase space, which does not involve any distortion of the hole distribution itself. For longer times, these distortions are introduced by the nonlinear structure of the Hamilton function, leading to different oscillation frequencies within the separatrix and a completely different, Bloch oscillation like, behavior outside. The numerical and semiclassical simulations suggest, however, that for carefully chosen parameters the hole distribution does not change its shape drastically during a few rotations, leading to revivals of the hole depth in momentum space. At longer times these revivals are eventually damped out due to the finite nonlinearity of the system.

The main prerequisite for a pronounced hole revival is to create a hole that has mainly contributions in the phase space region within the separatrix. All corresponding states have a rotational dynamical behavior, allowing for a rotation of the hole in the first place. This situation is favored for shallow lattices, where the extension of the inner region is larger than for deep lattices, due to the increased bandwidth. It is also favorable to work with a state at $q = 0$, where the extension of this inner region is maximal. At very shallow lattices with $s \leq 3$ also the band dispersion starts to deviate from the pure tight-binding result, showing a more harmonic form with decreasing lattice depth. This also favors the global rotation by minimizing the nonlinear behavior at small q. Figure 5.16 shows a measurement specifically addressing this parameter regime. It indeed reveals the coherent hole revivals in very good agreement with the theoretical prediction. Recall from Fig. 5.5 that for strongly nonlinear systems, as realized in deeper lattices, measurements show no discernible revivals in agreement with the numerical calculations.

The presented results constitute the first observation of coherent dynamics of holes in momentum space using ultracold atoms in optical lattices. While this type of excitations is very common in solid state physics [142], its investigation in ultracold matter has been not possible up to now.

5.5 INFLUENCE OF INTERACTIONS

For Fermi-Fermi and Bose-Fermi mixtures, interparticle interactions lead to an additional coupling between quasimomentum states. Here I present measurements, which explore the influence of interactions on the dynamics of particle and hole excitations. Starting with the excited particles, it was already shown in Fig. 5.11, that moderate interactions in a binary Fermi-Fermi mixture do not influence the oscillation frequency within the experimental resolution. To test the behavior at different interaction strength, one can tune the interspecies scattering length in a wide range, using a Feshbach resonances. In the present case, the spin mixture $m = -9/2$ and $m = -5/2$ has been used, which has a Feshbach resonance at 224 G [152].

A measurement of the excitation lifetime for different scattering lengths is shown in Fig. 5.17. It is found, that the excitations are lost very quickly from the excited band already at moderate interactions, corresponding to the background scattering length. Reducing the scattering length leads to an increase of the lifetime. All observed lifetimes are much lower than the result for the noninteracting gases, however. An independent measurement reveals, that the total particle loss from the trap does not depend on the interaction strength used in the presented measurements. Therefore, the observed lifetime must be limited by interband transitions. No increase of particles could be detected in the first excited band within the experimental resolu-

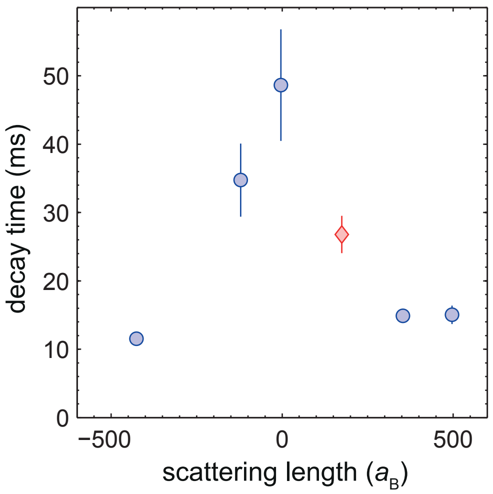

Figure 5.17: Recombination time of particle and hole excitations in interacting Fermi gases. Shown is the experimentally observed $1/e$ lifetime of particles in the second excited band as a function of the scattering length. About 7×10^4 particles are confined to a three-dimensional lattice of $8\,E_r$ with total trapping frequencies of about $2\pi\times(63, 68, 68)$ Hz. The modulation frequency is 38 kHz. The data at the background scattering length (red diamond) was taken far away from the Feshbach resonance near zero magnetic field, showing that the reduced lifetime cannot be explained simply by losses due to the Feshbach resonance.

tion. This is limited by the band mapping quality at the band edge to the lowest energy band, such that particle might accumulate at large quasimomenta in the first excited band, which cannot be discerned from particles in the lowest band. Assuming a decay of the particles to the lowest band, the observed lifetime of the excited particles can be regarded as a measure for particle-hole recombination in analogy to solid state photoconductivity [190], where the particles fill up empty states in conduction band, which eventually becomes insulating again.

Decay of particles from the excited spatial states has been studied already with bosonic atoms [207, 220, 221]. In these studies the scattering properties of the particles were fixed and only changes in the density allowed for the tuning of the decay channels. In these studies different processes were found that lead to the decay of particles. An important difference to the earlier studies on this topic is the nearly isotropic geometry of the investigated system of Fig. 5.17, concerning both, trapping frequencies and lattice depths. Therefore, most effects observed in the earlier experiments, which rely on the strong asymmetry of the potential, are excluded for the present experiments.

Due to the influence of gravity, the trap depths of the Gaussian potential are not isotropic but are given by about $(8, 190, 190)\,h$kHz. Since the total particle decay from the trap does not depend on the scattering length, however, losses along the vertical direction can be excluded as a possible explanation for the decreased lifetime. Since the energy of the excited particles, determined by the excitation energy of $38\,h$kHz, must be conserved by the loss process, the remaining possible process is the deexcitation to localized states at the edge of the system. The energy of these states is given approximately by the local trapping potential, which exceeds the excitation energy by a factor of 5 in the horizontal directions. To investigate this process in more detail, a dipole trap with variable trapping depths in the horizontal direction would be necessary at otherwise similar parameters. This could be achieved using anticonfining blue-detuned beams in addition to the red-detuned trap beams. This combination would allow to

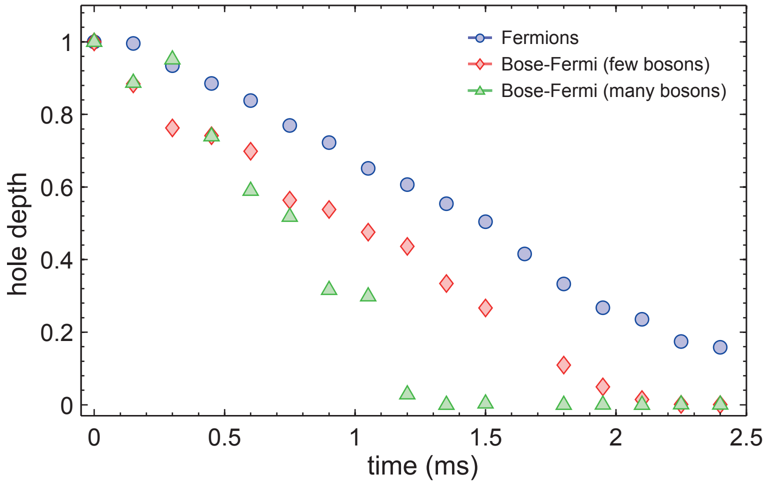

Figure 5.18: Hole-closing dynamics in attractive Bose-Fermi mixtures in a three-dimensional lattice of $2.5\,E_\mathrm{r}$. Measurement of the hole-closing dynamics for noninteracting fermions and two mixtures with increasing bosonic particle number. This data is not evaluated using the differential image method, since no offset image exists. The hole depth was determined by a double Gaussian fit, one Gaussian for the background and one for the hole at $q = 0$. This leads to the systematic drop to zero of the hole depth at large times.

---

shape the potential freely and to adjust the trap parameters accordingly.

A possible application of the interaction depended losses is the characterization of the zero-crossing of Feshbach resonances, complementary to existing approaches such as the study of Bloch oscillation damping [222] or the diffusion dynamics in optical lattices. [52].

For the investigation of the behavior of holes in interacting mixtures, only few measurements were performed during this work. To give a short outlook on possible directions of investigations, I present the corresponding data here. For binary Fermi-Fermi mixtures the hole-closing dynamics were measured in a shallow three-dimensional lattice of $4\,E_\mathrm{r}$. No discernible influence of interaction strength on the closing time has been observed between $200\,a_\mathrm{B}$ and $500\,a_\mathrm{B}$. Note here, that the additional harmonic confinement due to the lattice beams reduces the bare hole-closing time quadratically. Therefore, measurements at larger lattice depths suffer from the fast closing of the holes that conceals any interaction effects. In a system with reduced trapping frequencies, which can be obtained using a blue detuned lattice, interaction effects might be observable. In particular, a different excitation dynamics might be expected for a band insulating and the Mott insulating ground states. The former has a hole excitation spectrum, which is basically identical to the noninteracting case, while the excitation spectrum of the latter is strongly interaction dependent. The dynamics of the hole excitation should therefore strongly differ in both cases, allowing to distinguish between both situations.

Complementary to the investigation of interaction effects in Fermi-Fermi mixtures, Bose-Fermi mixtures have been studied. In these systems, no Pauli blocking is present for the bosons and therefore, the hole in the fermionic gas can couple via interactions to many momentum degrees of freedom introduced by the bosonic component. The closing dynamics for this case were studied for two different admixtures of bosonic atoms in addition to the fermionic cloud. The results are shown in Fig. 5.18. A clear reduction of the hole lifetime is observed with an increased bosonic admixture. These results are consistent with the observation of Bose-induced equilibration of a displaced Fermi cloud in an one-dimensional lattice [223], where the interaction with the bosons allows for a release of the fermionic atoms from localized states. This mechanism might allow for a better characterization of interspecies Feshbach resonances, but also forms an analog to the coupling of hole excitations to phonons from usual solid state physics. The phonons are here replaced by the Bogoliubov excitations of the Bose-Einstein condensate or by the bosons themselves.

5.6 CONCLUSION AND OUTLOOK

To summarize, the first realization of an analog to photoconductivity using ultracold atoms has been reported in this chapter. The multiband character of the excitation process allowed for the simultaneous investigation of particle and hole excitations in ideal Fermi gases as well as interacting Fermi-Fermi and Bose-Fermi mixtures.

The observation of the particle excitations in the second excited band constitutes the first study of ultracold fermions in higher bands of an optical lattice, exceeding merely the preparation of such states [46, 53]. Regarding the huge interest in higher-band physics with ultracold atoms in recent years, the presented study is of high importance for the realization of such systems, revealing the strong influence of the harmonic confinement in the excited bands as well as a fast decay to lower bands at moderate interactions already.

At the same time, the presented photoconductivity measurements provide the first momentum-resolved study of holes in an optical lattice. In this context, a coherent dynamics has been observed, in close analogy to hole currents in conventional solid state systems. Hole currents are very common in conventional solids [142, 190], however, the observation of similar effects in ultracold atom systems was restricted to strongly interacting bosons [198] so far. The observation of this effect in genuinely fermionic systems represents a novel analogy between solid state physics and ultracold atoms, leading to a deeper understanding of the nature of ultracold fermionic quantum gases.

The observed dynamics can be understood in terms of effective single-particle descriptions, which is especially surprising for the hole excitations that are actually missing particles in the otherwise completely filled valence band. The full quantum state in the lowest band is, as a matter of fact, a many-body state composed of all remaining particles. A deep insight in the behavior of the hole excitation is provided by noting, that the essential ingredient for the theoretical description of the hole is in exact analogy to holes in usual solids. This further affirms the strong similarity between the investigated quantum system and real solids.

The presented studies can be extended in many fascinating directions. A natural next step is a systematic investigation of interaction effects on the photocurrent dynamics. In the theoretical description, this corresponds to a Drude-model for the excited particles, where the remaining background atoms in the lowest band simulate the immobile ions, leading to a damping of the particle oscillations [224]. This extension would deepen the analogy between the optical lattice and conventional solids even further.

Another exciting proposal exploiting multiband physics is the realization of excitons in optical lattice systems, being bound states of particle and hole excitations [57]. These particle-like excitations are bosonic and attractively interacting. Therefore, they are expected to condense in the lattice similar to Cooper pairs in the BCS limit.

Finally, a very intriguing possibility is the creation and investigation of hole excitations at the Dirac points of a hexagonal lattice. Such hole excitations would have a dispersion relation resembling the relativistic Dirac equation for massless particles, which is at the heart of the many fascinating properties of graphene [181, 182].

CHAPTER 6

MULTICOMPONENT FERMI GASES IN OPTICAL LATTICES

Interparticle interactions play a major role for the properties of many-body systems. This is true from the classical regime, where thermalization processes can only occur with finite interactions, to the quantum regime, where they are relevant for conduction properties of solids, including even superconductivity [142].

Interacting quantum systems in periodic potentials, such as electrons in solids, are often described via Hubbard models [144], including only short range interactions, and constituting one of the simplest realization of interacting many-body systems. Whereas Hubbard models are only approximations for electrons in solids, which actually interact via long-ranged Coulomb forces, the scattering processes in ultracold atomic gases are typically very short ranged [151]. This allows for the nearly perfect realization of Hubbard models [15, 21], and many interesting phenomena have been investigated in this context during the last decade [15, 16, 45]. A particularly fascinating aspect is the realization of strongly correlated ground state phases, such as the Mott insulator [22, 25, 26].

Conventional Hubbard models are typically restricted to one bosonic [225] or two fermionic [144] spins. With ultracold matter, an extension of these systems is possible, using multiple components that are provided by the internal hyperfine states of the atoms [67, 73, 74, 86–98, 226, 227]. This leads to completely novel phenomena in optical lattices [27, 228–230]. Especially for fermionic atoms, many efforts have been made in recent years, to understand the properties of such high-spin gases with $f > 1/2$ in optical lattices [2, 51, 101, 103–113].

The understanding of the microscopic interaction processes in high-spin Fermi gases is of major importance for a controlled investigation of the rich spectrum of phenomena proposed. In this spirit, the interaction properties of multicomponent Fermi gases in optical lattices are studied in this chapter, using ^{40}K, which provides a high spin of up to $f = 9/2$. ^{40}K has very favorable spin-dependent scattering lengths in order to observe spin-dependent effects. This allowed for the first realization of coherent spin-changing collisions with ultracold fermionic atoms during this work. In particular, the first observation of higher-order spin-exchange is reported in this context (for a sketch of different spin-changing collision, see Fig. 6.1).

Spin-changing collisions can also be used for the investigation of the interacting ground states in the lattice system. A spin-resolved determination of the double occupancy in fermionic lattice gases is presented [231], which has potential applications for both, conventional two-component systems [25, 232] or novel high-spin lattice models [51]. Especially the spin resolution should enable the detection of unconventional ground state phases in such high-spin

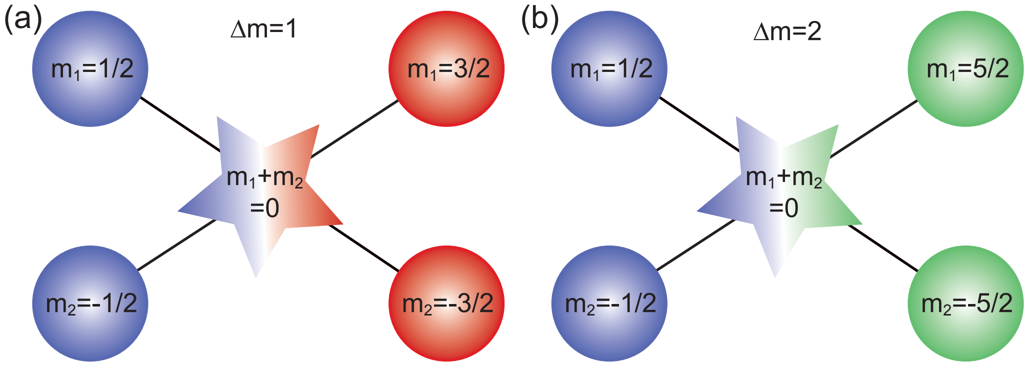

Figure 6.1: Sketch of spin-changing collisions. (a) Two particles collide and change their internal spin configuration from $|1/2\rangle|-1/2\rangle$ to $|3/2\rangle|-3/2\rangle$. The spin exchange for each particle is $\Delta m = 1$. While the individual spins are changed, the total magnetization remains constant. (b) Higher-order spin-changing collision, where the internal spin configuration is changed from $|1/2\rangle|-1/2\rangle$ to $|5/2\rangle|-5/2\rangle$. The corresponding spin exchange for each particle is $\Delta m = 2$.

---

systems [101, 105, 111, 113, 233].

Finally, I propose the realization of a novel phase crossover between two strongly correlated phases. These are the Mott insulator at strong elastic interactions [25, 26] and a novel insulating phase at strong inelastic interactions, induced by the quantum Zeno effect [31, 54, 234, 235]. To study the crossover, a novel Feshbach resonance in ^{40}K can be used, which allows for a continuous tuning of the elastic and inelastic two-body collisions. Since the recent discovery of the quantum Zeno insulator, the underlying mechanisms have been found to be relevant in context of many different quantum gas systems [54, 234, 235] and beyond [236].

All experimental data presented in this chapter was taken and analyzed together with Jasper S. Krauser. The numerical and analytical results have been obtained mainly by myself, except for the coupled channel calculations providing the scattering lengths and loss rates in Tab. 6.1 and in section 6.4, kindly provided by T. Hanna and L. Cook.

The results of this chapter have been partly published in [5]. A more detailed description of the experimental study on spin-changing collisions will be given in thesis of Jasper S. Krauser [114].

6.1 SCATTERING PROPERTIES OF THE HIGH-SPIN FERMION ^{40}K

In this section, the interaction Hamiltonian for a spinor quantum gas is derived [86]. In particular, I concentrate on the properties of the fermionic isotope ^{40}K, for which the scattering lengths in the $f = 9/2$ hyperfine ground state manifold are derived. For pure s-wave interactions, and using a set of general assumption, such as rotational symmetry and particle exchange symmetry, the interaction Hamiltonian H_S can be constructed, using only a very small number of species-dependent parameters. Based on the general form of the interaction, I derive the exact background scattering lengths of ^{40}K, employing numerical results from molecular coupled channel calculations, kindly provided by T. Hanna and L. Cook [237].

6.1.1 INTERACTION HAMILTONIAN FOR SPINOR ATOMS

Experiments with spinor quantum gases are usually performed at small magnetic fields, where the atoms have a well defined total spin f and a magnetization m (see section 2.2) [89]. In this regime, the characteristic scattering properties of spinor quantum gases can be derived using few constraints on the full interaction Hamiltonian [86].
In the following, I assume

I *S-wave scattering:* Ultracold atoms only interact via s-wave collisions, corresponding to a relative angular momentum $L = 0$ between both atoms.

II *Rotational symmetry:* The interaction is rotationally symmetric and the inner structure of the atoms is neglected. This is a good approximation for alkali atoms, where dipolar and higher-order interactions are very small [238–240].

III *Fixed atomic spin f:* Both atoms have the same total spin $f = f_1 = f_2$, before and after the collision. In principle also collisions which change the atomic spin f are possible. These are excluded here and are discussed separately in section 6.3.

IV *Indistinguishable particles:* All atoms are of the same species and isotope and are thus indistinguishable. This leads to different symmetry restrictions for bosonic and fermionic particles.

The spatial part of the interaction is fully determined by assumption I, which states, that the atoms only interact via *s-wave scattering*, which is the typical case for ultracold atoms. The standard description of s-wave scattering employs the δ-function approximation, where the spatial part of the interaction is [16, 151]

$$\frac{4\pi\hbar^2}{m}\delta(\vec{r}_1 - \vec{r}_2)\,. \tag{6.1}$$

The δ-function is only non-vanishing, if both particles are at the same position ($\vec{r}_1 = \vec{r}_2$), and therefore constitutes an effective contact interaction with an angular momentum $L = 0$.

To describe the spin part of the interaction Hamiltonian, I proceed with assumption II, which states that the full interaction has a genuine *rotational symmetry*. In quantum mechanics, a rotationally symmetric operator H commutes with the total spin operator $\vec{F}^2$ and it conserves the total magnetization M of the system. Therefore, its eigenstates can be ordered by the corresponding quantum numbers F and M as the eigenstates of the total spin operator

$$\vec{F}^2|F, M\rangle = F(F+1)|F, M\rangle\,. \tag{6.2}$$

Since s-wave interactions have a vanishing spatial angular momentum $L = 0$, the total spin of the interacting particles is only provided by the internal spins f_1 and f_2. The spin operator is thus given by $\vec{F} = \vec{f}_1 + \vec{f}_2$ and the total magnetization is the sum of both single-particle magnetizations $M = m_1 + m_2$. The spin part of the Hamiltonian can be written in terms of the total-spin eigenstates $|F, M\rangle$ as a sum of spin channels in the form

$$\sum_{\mathrm{F=0}}^{F_{\max}} \sum_{\mathrm{M=-F}}^{\mathrm{F}} a_{\mathrm{F}}^{\mathrm{M}} |F, M\rangle\langle F, M|\,, \tag{6.3}$$

where the total spin and total magnetization are conserved. In principle, the different F and M-conserving channels can have different amplitudes, defined by corresponding scattering lengths $a_{\mathrm{F}}^{\mathrm{M}}$. Since the interaction must be rotationally symmetric, the scattering must be the same for all channels with the same quantum number F. However, it may differ for channels with different F. Combining all of the above, the most general Hamiltonian for the interaction of two ultracold high-spin atoms is

$$H_{\mathrm{S}} = \frac{4\pi\hbar^2}{m}\delta(\vec{r}_1 - \vec{r}_2) \sum_{\mathrm{F}=0}^{F_{\max}} \sum_{\mathrm{M}=-\mathrm{F}}^{\mathrm{F}} a_{\mathrm{F}} |F, M\rangle\langle F, M| \,, \tag{6.4}$$

with the scattering lengths a_{F}, being only dependent on the total spin F.

Following assumption III, for two particles with a *fixed atomic spin* f, this Hamiltonian contains spin channels with $F = 0, 1, 2, \ldots, 2f$, which also conserve the total spin $f = f_1 = f_2$ of both particles.

Employing assumption IV, that the collisions are between *indistinguishable particles*, an additional particle-exchange symmetry of the total two-particle wave function is required. It must be antisymmetric for fermions and symmetric for bosons. S-wave scattering requires a symmetric spatial wave function, since both particles must be at the same position to interact. Consequently, the spinor part of the wave function is restricted to be antisymmetric (symmetric) for fermions (bosons) for the interacting channels, which must be incorporated into the Hamiltonian (6.4).

The simplest example for this situation are fermions with $f = 1/2$. Two of these atoms can form total spins of $F = 0$ and $F = 1$. The corresponding states are the singlet state

$$|\,F{=}0, M{=}0\rangle = \sqrt{1/2}\Big(|\,1/2\rangle_1|-1/2\rangle_2 - |-1/2\rangle_1|\,1/2\rangle_2\Big) \tag{6.5}$$

for $F = 0$ and the triplet states

$$|\,F{=}1, M{=}0\rangle = \sqrt{1/2}\Big(|\,1/2\rangle_1|-1/2\rangle_2 + |-1/2\rangle_1|\,1/2\rangle_2\Big)\,, \tag{6.6}$$

$$|\,F{=}1, M{=}1\rangle = |\,1/2\rangle_1|\,1/2\rangle_2\,, \tag{6.7}$$

$$|\,F{=}1, M{=}-1\rangle = |-1/2\rangle_1|-1/2\rangle_2 \tag{6.8}$$

for $F = 1$. The singlet $F = 0$ channel is antisymmetric in the spinor wave function. The triplet $F = 1$ states are symmetric. Therefore, only fermions in the singlet state can interact via s-wave interactions. This example can be extended for larger spins and it turns out that for both, fermions and bosons, only the even total spins $F = 0, 2, 4, \ldots$ have the correct symmetrization, required for s-wave interactions. This reduces the number of spin channels and thus the number of independent scattering lengths in (6.4) by a factor of 2.

The Hamiltonian (6.4) describes the scattering properties of spinor atoms in the natural total spin basis $|F, M\rangle$. However, this basis set is not the usual observation basis in the experiment, where the Stern-Gerlach separation essentially allows for the detection of the single-particle magnetizations m. The corresponding basis for two particles with fixed atomic magnetizations is given by the symmetric ("+", bosons) and antisymmetric ("−", fermions) two-particle spin states

$$|m_1; m_2\rangle = \sqrt{\frac{1}{2}}\Big(|m_1\rangle_1|m_2\rangle_2 \pm |m_2\rangle_1|m_1\rangle_2\Big)\,. \tag{6.9}$$

Note, that the states $|m_1; m_2\rangle$ form a complete basis for all spin states of interacting atom pairs. To formulate the Hamiltonian in the observation basis, a basis transformation from the total spin basis $|F,M\rangle$ to the magnetization basis $|m_1;m_2\rangle$ is necessary, given by the coefficients

$$\begin{aligned} c^{\mathrm{F},\mathrm{M}}_{\mathrm{m_1},\mathrm{m_2}} &= \langle F,M|m_1;m_2\rangle \\ &= \sqrt{\frac{1}{2}}\Big(\langle F,M|m_1\rangle_1|m_2\rangle_2 \pm \langle F,M|m_2\rangle_1|m_1\rangle_2\Big) \\ &= \sqrt{\frac{1}{2}}\Big(c^{\mathrm{f,f,F}}_{\mathrm{m_1,m_2,M}} \pm c^{\mathrm{f,f,F}}_{\mathrm{m_2,m_1,M}}\Big)\,, \end{aligned} \tag{6.10}$$

where in the last row the Clebsch-Gordan coefficients for the coupling of two spins $|f,m_1\rangle$ and $|f,m_2\rangle$ to one spin $|F,M\rangle$ are used [241].

The resulting Hamiltonian is

$$H_{\mathrm{S}} = \frac{4\pi\hbar^2}{m}\delta(\vec{r}_1-\vec{r}_2)\sum_{\mathrm{m_1+m_2=m_3+m_4}} a_{\mathrm{m_1m_2m_3m_4}}|m_3;m_4\rangle\langle m_1;m_2|\,, \tag{6.11}$$

where the sum is restricted to states with $m_1+m_2=m_3+m_4$, ensuring the conservation of total magnetization. The magnetization-dependent scattering lengths $a_{\mathrm{m_1m_2m_3m_4}}$ can be calculated from the total-spin dependent scattering lengths a_{F} via

$$a_{\mathrm{m_1m_2m_3m_4}} = \sum_{\mathrm{F}=0}^{F_{\max}}\sum_{\mathrm{M}=-\mathrm{F}}^{\mathrm{F}} a_{\mathrm{F}}c^{\mathrm{F},\mathrm{M}}_{\mathrm{m_1},\mathrm{m_2}}c^{\mathrm{F},\mathrm{M}}_{\mathrm{m_3},\mathrm{m_4}}\,. \tag{6.12}$$

Processes with $m_1,m_2\neq m_3,m_4$ are called spin-changing collisions. For fermionic atoms, the antisymmetrization of the spinor wave function includes Pauli blocking, ensuring that before and after the collision also $m_1\neq m_2$ and $m_3\neq m_4$. Spin-changing collisions are only present in high-spin systems [86–88, 103]. They have been extensively studied experimentally using bosonic atoms, but have not been investigated in ultracold fermions until now.

To understand the connection of spin-changing collisions with the F-dependent scattering lengths a_{F}, consider two fermionic atoms with $f\geq 3/2$ in the initial spin configuration

$$|1/2;-1/2\rangle = \sum_{\mathrm{F}} c^{F,\ 0}_{\frac{1}{2},-\frac{1}{2}}\,|F,0\rangle\,, \tag{6.13}$$

which has $M=0$ and can therefore be written as a combination of eigenstates $|F,0\rangle$ of the interaction Hamiltonian (6.4). Using the Hamiltonian (6.4), each state $|F,0\rangle$ has an F-dependent eigenenergy $\mathcal{E}_{\mathrm{F}}$, which is proportional to the F-dependent scattering length $\mathcal{E}_{\mathrm{F}}\propto a_{\mathrm{F}}$. Therefore, each of the different F-channels acquires a different phase in the time evolution.

$$e^{-\mathrm{i}H_{\mathrm{S}}t/\hbar}|1/2;-1/2\rangle = \sum_{\mathrm{F}} c^{F,\ 0}_{\frac{1}{2},-\frac{1}{2}}\,e^{-\mathrm{i}\mathcal{E}_{\mathrm{F}}t/\hbar}|F,0\rangle\,, \tag{6.14}$$

The time-evolved state on the right hand side of (6.14) is in general a new combination of states $|F,0\rangle$. Projecting it onto the two-particle states $|m_1;m_2\rangle$, it can include any state combination with $M=0$, e.g., $|3/2;-3/2\rangle$ or $|5/2;-5/2\rangle$, depending on the exact scattering lengths a_{F} and the spin f of the colliding atoms. Thus, the spin-changing collisions directly emerge from the *scattering-length differences* of the multiple F-channels. Therefore, in the case of equal scattering lengths a_{F}, as realized in $SU(N)$ symmetric systems like ytterbium or strontium, no spin-changing collisions occur.

Spin-conserving channel	Abbreviation of channel	Scattering length at $B=1\,\mathrm{G}$ (a_B)
$\|1/2;-1/2\rangle\langle 1/2;-1/2\|$	ef	151.6211
$\|3/2;-3/2\rangle\langle 3/2;-3/2\|$	dg	155.6224
$\|5/2;-5/2\rangle\langle 5/2;-5/2\|$	ch	156.2764
$\|7/2;-7/2\rangle\langle 7/2;-7/2\|$	bi	154.2121
$\|9/2;-9/2\rangle\langle 9/2;-9/2\|$	aj	145.7684
$\|9/2;-1/2\rangle\langle 9/2;-1/2\|$	ej	165.8722
$\|9/2;-3/2\rangle\langle 9/2;-3/2\|$	dj	164.3502
$\|9/2;-5/2\rangle\langle 9/2;-5/2\|$	cj	161.6432
$\|9/2;-7/2\rangle\langle 9/2;-7/2\|$	bj	156.9478

Table 6.1: Scattering lengths of ^{40}K in $f = 9/2$. The values are kindly provided by T. Hanna and L. Cook (see text for details). The abbreviations a,. . . ,j correspond to $-9/2,\ldots,9/2$ for later reference.

Total-F channel	Channels used for calculation	Calculated scattering length (a_B)
a_8	bj,cj,dj,ej	168.53
a_6	bj,cj,dj,ej	166.00
a_4	bj,cj,dj,ej	161.11
a_2	bj,cj,dj,ej	147.83
a_0	bj,cj,dj,ej,aj	119.92
a_0	bj,cj,dj,ej,bi	120.40
a_0	bj,cj,dj,ej,ch	120.16
a_0	bj,cj,dj,ej,dg	119.72
a_0	bj,cj,dj,ej,ef	119.93

Table 6.2: Scattering lengths calculated for channels with constant total spin F. Calculations are performed with the linear equation system (6.12). The different combinations for calculating a_0 show the consistency of the calculations.

Spin-changing channel	Calculated scattering length (a_B)
$\|3/2;-3/2\rangle\langle 1/2;-1/2\|$	13.40
$\|5/2;-5/2\rangle\langle 3/2;-3/2\|$	10.86
$\|5/2;-5/2\rangle\langle 1/2;-1/2\|$	8.78
$\|7/2;\ \ 5/2\rangle\langle 9/2;\ \ 3/2\|$	1.16
$\|7/2;\ \ 3/2\rangle\langle 9/2;\ \ 1/2\|$	1.24

Table 6.3: Examples for spin-changing scattering lengths. Note the large variation of the absolute strengths and in particular the large value in the third row, which shows a spin-changing channel with a magnetization change of $\Delta m = 2$.

6.1.2 BACKGROUND SCATTERING LENGTHS OF ^{40}K

All reported experiments in this chapter are performed using ^{40}K. I concentrate in the following exclusively on this case. In particular, I consider the energetically lowest $f = 9/2$ hyperfine manifold, where all possible total-spin channels are $F = 0, \ldots, 9$. As discussed above, the antisymmetry of the total wave function reduces the possible scattering channels to the five even spin channels $F = 0, 2, 4, 6, 8$ with corresponding scattering lengths a_{F}. The ground state and excitation properties of the spinor gas sensitively depend on the actual differences between these scattering lengths, and therefore a precise knowledge of them is extremely important for their detailed understanding. To determine the scattering lengths, the results of molecular coupled-channel calculations for spin-conserving scattering processes [237] have been used. These calculations were performed by T. Hanna and L. Cook to describe Feshbach resonances in ^{40}K, as discussed in more detail in section 6.4. From their provided data, the scattering lengths for nine different spin-conserving channels have been extracted, as shown in Tab. 6.1.

The linear equation system (6.12) relates the magnetization-dependent and total-spin dependent scattering lengths. It can be solved for the a_{F}. Using the data from Tab. 6.1 for the spin-conserving scattering rates results in the total spin-dependent scattering lengths shown in Tab. 6.2.

Note here, that only five independent parameters a_{F} determine the full scattering matrix. From the coupled-channel calculations nine values have been extracted for the spin-conserving channels, however. Thus, the linear equation system (6.12) is overdetermined, allowing for different combinations of input parameters to determine the five independent a_{F}. This can be used to check the calculated scattering lengths for consistency. The results of this additional calculations are also reported in Tab. 6.2, showing an excellent consistency for all calculations of the $F = 0$ scattering length a_0, which was independently calculated from different sets of input parameters. The small deviations between the calculated scattering lengths are probably due to errors in the coupled-channel calculations, for which the numerical uncertainties are not known, however. For all further calculations in this thesis, the scattering lengths from the first five rows of Tab. 6.2 are used.

The scattering lengths in Tab. 6.2 have some notable properties. First, there is a relatively large difference between the maximum and minimum *total-spin dependent* scattering lengths in the order of 40%. This is very large compared to ^{23}Na, where the difference is about 5% and ^{87}Rb, where the difference ranges between 1% and 7% [93, 242]. Similar values have been found for bosonic ^{52}Cr [243], where also differences in the order of $40\,\%$ have been reported [244].

The strongly different scattering properties lead to very large *spin-changing* scattering lengths $a_{\mathrm{m_1 m_2 m_3 m_4}}$, which are proportional to the differences of the individual a_{F} channels [86, 245]. This should induce spin-changing collisions with large amplitudes and on timescales much faster than observed in ^{23}Na or ^{87}Rb. Table 6.3 shows the scattering lengths for some exemplary spin-changing collisions channels. In comparison, typical values for both, ^{87}Rb and ^{23}Na, are about $1\,a_{\mathrm{B}}$ [93, 242, 245]. These examples demonstrate the wide range of spin-changing parameters possible with ^{40}K. In particular, much larger values as rubidium and sodium can be achieved. Note in particular the large value for the spin-changing scattering length from $|1/2, -1/2\rangle$ to $|5/2, -5/2\rangle$, that includes a change of the single-particle magnetizations of $\Delta m = 2$. Collisions of this kind have not been observed before, mainly because the spin-changing scattering lengths are too small to observe the corresponding dynamics on experimental time scales. This has been especially noted for ^{87}Rb [242], where stable $f = 2$ condensate are possible . For chromium, which has a high spin of $f = 3$, also no higher-order

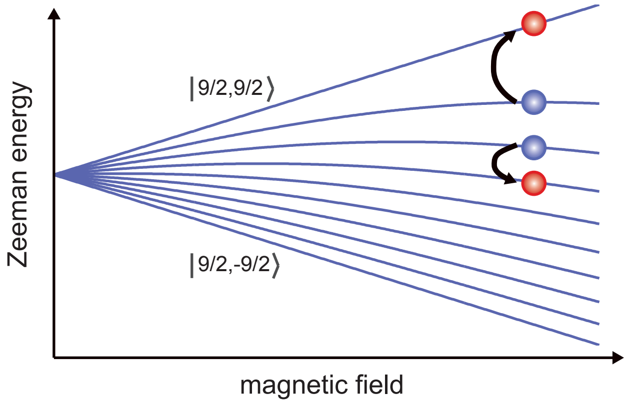

Figure 6.2: Sketch of a spin-changing collision at finite magnetic fields. Shown is a spin-changing collision in the $f = 9/2$ manifold of ^{40}K. The change of the internal spin state changes the total magnetic Zeeman energy of the system.

spin-changing processes have been reported so far [230]. Here, strong demagnetization processes, induced by the large dipole moment, hinder the investigation of high-spin systems with many spin states involved [229].

Note also, that the scattering lengths for different *spin-conserving* channels in ^{40}K differ on the order of $20\,a_\mathrm{B}$, as shown in Tab. 6.1. Since spin-changing collisions change the instantaneous spin configuration, this interaction energy difference leads to a detuning of the involved levels, which strongly affects the resulting dynamics.

Finally, a_0 is the lowest F-dependent scattering length with more than 20%, or about $27\,a_\mathrm{B}$, difference to the next higher scattering length. Therefore, the ground state of this system at $M = 0$ should be of spin-singlet ($F = 0$) character, minimizing the total interaction energy.

In conclusion, ^{40}K is very much suited for the investigation of spin-changing collisions and has the potential to realize complex magnetic ground state phases of fermionic high-spin systems.

6.2 TWO-PARTICLE SPIN DYNAMICS IN OPTICAL LATTICES

In this section, I discuss the extension of the interaction Hamiltonian derived in the preceding section to fully describe the spin-changing dynamics of two ^{40}K atoms. Since the dynamics include a change of the spin occupation, it is necessary to include the internal energy of the different spin states, which depends on the external magnetic field [89]. Therefore, I derive first the corresponding Zeeman Hamiltonian and afterwards discuss the realization of pure two-particle dynamics using deep optical lattices, where all sites are basically independent on the timescales of the spin-changing collisions. Finally, I present data of a proof-of-principle experiment for fermionic spin-changing collisions in good agreement with the numerical results using all five scattering lengths calculated above.

6.2.1 THE ZEEMAN ENERGY

In the presence of a magnetic offset field the energy of the different spin components changes depending on their magnetization, due to the Zeeman effect [246]. If an atom pair undergoes

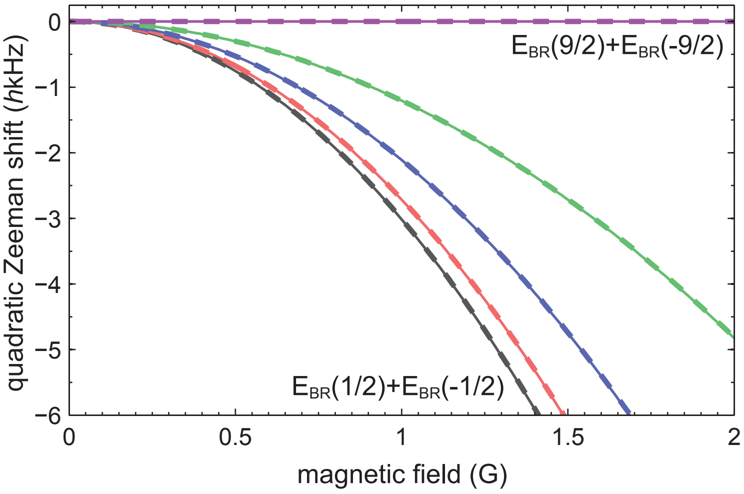

Figure 6.3: Zeeman energy for various spin mixtures with $M = 0$, namely $|1/2;-1/2\rangle$ (black), $|3/2;-3/2\rangle$ (red), $|5/2;-5/2\rangle$ (blue), $|7/2;-7/2\rangle$ (green), and $|9/2;-9/2\rangle$ (purple). All energies are depicted in difference to the offset energy at $B = 0$. Solid lines are calculated using equation (2.1). Dashed lines are calculated using equation (6.17), showing no discernible difference to the full Zeeman energy (2.1) .

spin-changing collisions, the atoms change their individual magnetizations and therefore their Zeeman energies as sketched in Fig. 6.2. Therefore, the Zeeman energy due to the magnetic field influences the spin-changing dynamics of particle pairs and can be used to tune them accordingly.

The full dependence of the internal Zeeman energy on the magnetic field is given by the Breit-Rabi formula (2.1) as discussed in section 2.2. However, as shown below, spin-changing collisions only appear at very low magnetic fields. To understand the basic properties of the magnetic field dependent Zeeman energy in this regime, one can perform a series expansion of (2.1) in the magnetic field B. The lowest order contribution of the Zeeman energy is provided by the linear Zeeman shift [129]

$$E_1(m, B) = \frac{g_J \mu_B}{9} m B \tag{6.15}$$

of a single atom. For spin-changing collisions only the combined energy of a colliding pair is relevant. The linear Zeeman energy for two particles adds up to

$$E_1(m_1, m_2, B) = \frac{g_J \mu_B}{9}(m_1 + m_2)B = \frac{g_J \mu_B}{9} M B\,, \tag{6.16}$$

where the total magnetization M enters the equation. Since spin-changing collisions conserve the total magnetization M, also the linear Zeeman energy is conserved during in this process. Therefore, it leads only to constant energy offset and can be neglected in the description of spin-changing collisions.

Due to the conservation of the lowest order of the Zeeman energy, higher-order contributions dominate the spin-changing dynamics. The second-order contribution to the energy difference between different spin states is the so-called quadratic Zeeman effect [89, 247], which is proportional to the square of the magnetizations and the magnetic field as

$$E_2(m_1, m_2, B) = -\frac{2^3 \mu_B^2}{9^3 A_{\text{hfs}}}(m_1^2 + m_2^2)B^2 = -q(m_1^2 + m_2^2)B^2\,. \tag{6.17}$$

Here, the abbreviation $q=\frac{2^3\mu_\mathrm{B}^2}{9^3 A_\mathrm{hfs}}$ is introduced. The value of (6.17) is not conserved in a spin-changing collision and thus must be included in the spin-changing dynamics Hamiltonian. The Zeeman energies of all spin mixtures with $M=0$ are shown in Fig. 6.3 in the relevant magnetic field region for spin-changing collisions, calculated using (2.1) and (6.17), which shows that the latter is an excellent approximation.

The Hamiltonian corresponding to the Zeeman energy of two particles can be most easily written in terms of the $|m_1;m_2\rangle$ basis as

$$H_\mathrm{B} = \sum_{\mathrm{m_1,m_2}} (E_\mathrm{BR}(m_1,B)+E_\mathrm{BR}(m_2,B))|m_1;m_2\rangle\langle m_1;m_2| \tag{6.18}$$

$$\approx \sum_{\mathrm{m_1,m_2}} \quad -q(m_1^2+m_2^2)B^2 \quad |m_1;m_2\rangle\langle m_1;m_2|\,. \tag{6.19}$$

In the following, the full Zeeman Hamiltonian (6.18) is used in all numerical calculations, while the approximate form (6.19) is used for all analytical results to illustrates the important physical dependencies.

6.2.2 SPINOR-HUBBARD HAMILTONIAN

In the experiments presented in this chapter, the high-spin fermionic ^{40}K atoms are confined to a deep optical lattice. This situation can be most conveniently described by a Hubbard model similar as for the two-component case (3.15) in section 3.2. As usual, the kinetic and the lattice potential lead to a spin-independent tunneling term

$$H_\mathrm{J} = -J\sum_\mathrm{m}\sum_{\mathrm{<ij>}} a^\dagger_\mathrm{i,m}a_\mathrm{j,m}\,. \tag{6.20}$$

The interaction includes all spin-dependent scattering lengths, translating into spin-dependent interaction parameters

$$U_\mathrm{m_1m_2m_3m_4} = \frac{4\pi\hbar^2}{m}a_\mathrm{m_1m_2m_3m_4}\int dx|w^\mathrm{x}(x)|^4\int dy|w^\mathrm{y}(y)|^4\int dz|w^\mathrm{z}(z)|^4\,, \tag{6.21}$$

where particles on the same lattice site occupy the same spatial wave function, resulting in a genuinely symmetric spatial and antisymmetric spinor part. The interaction Hamiltonian becomes

$$H_\mathrm{S} = \sum_{\mathrm{m_1+m_2=m_3+m_4}}\sum_\mathrm{i} U_\mathrm{m_1m_2m_3m_4}a^\dagger_\mathrm{i,m_3}a^\dagger_\mathrm{i,m_4}a_\mathrm{i,m_2}a_\mathrm{i,m_1}\,, \tag{6.22}$$

accordingly. The Zeeman energy takes the form of a single-particle operator

$$H_\mathrm{B} = -qB^2\sum_\mathrm{m} m^2\sum_i a^\dagger_\mathrm{i,m}a_\mathrm{i,m}\,, \tag{6.23}$$

resulting in a spin-dependent energy offset. The full Hamiltonian is given by

$$H_\mathrm{SHM} = H_\mathrm{J}+H_\mathrm{S}+H_\mathrm{B}\,. \tag{6.24}$$

For all measurements presented in this chapter, a lattice depth of $20-30\,E_\mathrm{r}$ is used, providing a tunneling energy in the order of $J/h\approx 2-12\,\mathrm{Hz}$. This is much smaller than both, the spin-conserving and the typical spin-changing scattering rates $U_\mathrm{m_1m_2m_3m_4}/h$, which are about

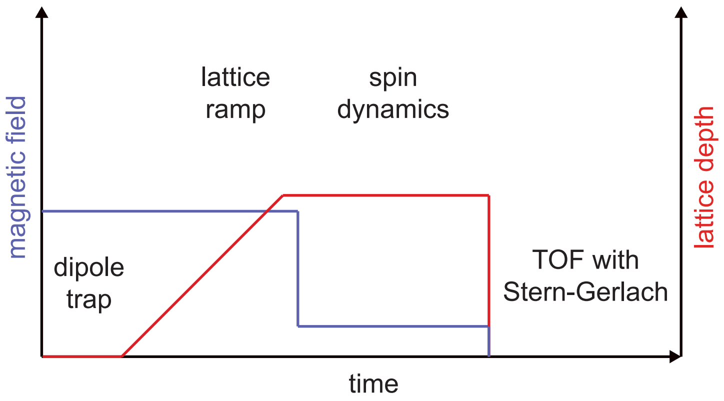

Figure 6.4: Sketch of the experimental sequence to study spin-changing dynamics.

$3-4\,\mathrm{kHz}$ and $300-400\,\mathrm{Hz}$, for these parameters. Therefore, a vanishing tunneling rate ($J = 0$) can be assumed to understand the most relevant interaction processes involved.

For singly occupied sites, this approximation removes all possible couplings in the Hamiltonian (6.24). For doubly occupied site, the internal Zeeman energy and the spin-dependent interaction energy dominate the system properties [87, 228, 248]. These can be split into three important contributions. First, the *Zeeman energy* introduces a spin-dependent energy shift. Second, a similar shift is introduced by the *spin-conserving interaction* channels, which change up to 20% for different spin configurations. Third, the *spin-changing collisions* couples different spin configurations.

At large magnetic fields, the Zeeman energy offset dominates all other energy scales. Due to energy conservation, the spin-changing collisions are suppressed in this regime and the initial two-particle state $|m_1; m_2\rangle$ is stable. At low magnetic fields, where the Zeeman energy offset is in the same order as the spin-conserving interaction offsets, an energy transfer between these two quantities is possible, when a spin-changing collision leads to a transfer between two different spin configurations. In this regime, complex spin dynamics are possible.

6.2.3 EXPERIMENTAL REALIZATION OF SPIN-CHANGING COLLISIONS WITH TWO PARTICLES

The experimental sequence to study the two-particle spin dynamics is sketched in Fig. 6.4. First, an ultracold mixture of two spin components in the optical dipole trap is prepared, as described in section 2.1. After the evaporation, the atoms are held at a large magnetic field, such that the spin-changing collisions are suppressed. An optical lattice is switched on adiabatically, creating a band insulator with two atoms per site in the center of the trap. The initial preparation of a two-component mixture ensures a maximal double occupancy of two particles per site, realizing the band insulating ground state at large particle numbers. This is a clear advantage compared to the bosonic systems, where a Mott insulator can be used to create doubly occupied sites for the study of two-particle spin-changing collisions [228]. However, due to the absence of Pauli blocking, an increase in the particle number leads to triple occupancy or even higher values, which distort the global signal [231] .

After the preparation of the band insulator, the spin-changing dynamics are initialized by a quench of the magnetic field to a lower value, where the difference in quadratic Zeeman energy

Two-particle states coupled via spin-changing collisions	M	Number of levels	scattering lengths involved
$\|9/2;\ \ 7/2\rangle$	8	1	a_8
$\|9/2;\ \ 5/2\rangle$	7	1	a_8
$\|9/2;\ \ 3/2\rangle$, $\|7/2;\ \ 5/2\rangle$	6	2	a_6, a_8
$\|9/2;\ \ 1/2\rangle$, $\|7/2;\ \ 3/2\rangle$	5	2	a_6, a_8
$\|9/2;-1/2\rangle$, $\|7/2;\ \ 1/2\rangle$, $\|5/2;\ \ 3/2\rangle$	4	3	a_4, a_6, a_8
$\|9/2;-3/2\rangle$, $\|7/2;-1/2\rangle$, $\|5/2;\ \ 1/2\rangle$	3	3	a_4, a_6, a_8
$\|9/2;-5/2\rangle$, $\|7/2;-3/2\rangle$, $\|5/2;-1/2\rangle$, $\|3/2;\ \ 1/2\rangle$	2	4	a_2, a_4, a_6, a_8
$\|9/2;-7/2\rangle$, $\|7/2;-5/2\rangle$, $\|5/2;-3/2\rangle$, $\|3/2;-1/2\rangle$	1	4	a_2, a_4, a_6, a_8
$\|9/2;-9/2\rangle$, $\|7/2;-7/2\rangle$, $\|5/2;-5/2\rangle$, $\|3/2;-3/2\rangle$, $\|1/2;-1/2\rangle$	0	5	a_0, a_2, a_4, a_6, a_8

Table 6.4: Spin-changing collision subspaces for two interacting ^{40}K atoms. Only subspaces with positive or zero magnetization are shown. Equivalent subspaces with negative magnetization exist, where all single-particle magnetizations are negative compared to the displayed cases.

---

and the difference of spin-conserving interactions are in the same order of magnitude.

After the quench, the system is not in an eigenstate of the Hamiltonian, but in a combination of the new eigenstates. The quench leads to oscillatory dynamics with frequencies corresponding to the energy differences between the occupied eigenstates. Since all doubly occupied sites have the same initial state, which is a direct consequence of the initial band insulator, all atom pairs show the same time evolution, allowing for a detection of the individual dynamics using a global measurement. In this case, the relevant observable is the occupation of the two-particle states $|m_1; m_2\rangle$, which can be directly inferred from the occupation of all single-particle magnetization states $|m\rangle$. This spin composition is probed using a $500\,\mu$s band-mapping procedure, followed by a Stern-Gerlach separation of the spin components during time-of-flight, and absorption imaging. The band mapping is advantageous, since it reduces the size of the single spin distributions to the size of the first Brillouin zone. In this way, the spin states can be separated more easily by the Stern-Gerlach procedure during TOF.

The described procedure allows for the preparation and study of the spin dynamics of an array of completely equal atom pairs. The total number of interacting two-particle states $|m_1; m_2\rangle$ in the $f = 9/2$ hyperfine manifold is 45. However, the restrictions by magnetization conservation and Pauli blocking limit the number of two-particle states coupled via spin-changing collisions considerably. Table 6.4 shows all subspaces in which two ^{40}K atoms can evolve under the influence of spin-changing collisions. As displayed, the largest possible subspace is the $M = 0$ manifold with five two-particle states involved in the dynamics. The scattering lengths for this subspace can be calculated from the theoretical values for all five a_F and are given by

$$\begin{pmatrix} 145.77 & 11.18 & -6.48 & 4.50 & -3.69 \\ 11.18 & 154.12 & 10.19 & -6.99 & 5.83 \\ -6.48 & 10.19 & 156.23 & 10.86 & -8.78 \\ 4.50 & -6.99 & 10.86 & 155.66 & 13.40 \\ -3.69 & 5.83 & -8.78 & 13.40 & 151.62 \end{pmatrix} a_\mathrm{B}\,, \tag{6.25}$$

where the top row and first column denote the two-particle state $|9/2; -9/2\rangle$ and the bottom row and last column the two-particle state $|1/2; -1/2\rangle$. This scattering matrix shows, that the $M = 0$ subspace is particularly suited for the investigation of involved spin-changing dynamics. All states are strongly coupled. Especially the scattering lengths for collisions with magnetization transfer of $\Delta m \geq 2$ are in the same order as the usual $\Delta m = 1$ collisions. There is no simple analytical solution for the five-level system, where all states are strongly coupled. However, the numerical diagonalization of such a five-level system is very simple and can be performed numerically exact.

For the particular investigation of the $M = 0$ subspace, a band insulator of a binary $|1/2\rangle|-1/2\rangle$ mixture is prepared at about $45\,\mathrm{G}$. The experimental parameters for the preparation are as follows (see section 2.1 for a general description of the quantum gas preparation). A single-component Fermi gas of about 2×10^6 spin polarized fermions in the state $|9/2, 9/2\rangle$ is transferred to the dipole trap. Using the dipole trap setup 2, the trapping frequencies are about $2\pi\times(50, 100, 200)\,\mathrm{Hz}$ and the trap depths are about $200\,h\mathrm{kHz}$ (vertical) to $300\,h\mathrm{kHz}$ (horizontally). Using a $10\,\mathrm{ms}$ Landau-Zener sweep at about $45\,\mathrm{G}$, a single component gas in the state $|9/2, 1/2\rangle$ is produced. A subsequent rf-pulse creates an equal superposition of the states $|9/2, 1/2\rangle$ and $|9/2, -1/2\rangle$ (from here on, these states are simply called $|1/2\rangle$ and $|-1/2\rangle$). By lowering the trap depth, the mixture is evaporatively cooled to quantum degeneracy within $2\,\mathrm{s}$, ending up with 4×10^5 atoms at $0.15-0.25\,T_\mathrm{F}$. To increase the double occupancy in the afterwards created band insulator, the trapping frequencies are typically increased to about $2\pi\times(125, 41, 32)\,\mathrm{Hz}$ by increasing the dipole trap power.

During the evaporation in the dipole trap losses due to Feshbach resonances prevent an efficient evaporation for many magnetic fields. For the $|1/2\rangle|-1/2\rangle$ mixture, in particular magnetic fields around $45\,\mathrm{G}$ and below $15\,\mathrm{G}$ allow for a stable evaporation. A details analysis of the evaporation process for this initial state, as well as further initial states will be presented in the thesis of Jasper Krauser [114]. The particular observed Feshbach resonances for the $|1/2\rangle|-1/2\rangle$ mixture can also be found in the diploma thesis by Nick Fläschner [116], prepared at the BFM setup, and co-supervised by me.

Finally, a three-dimensional optical lattice is ramped up linearly over $100\,\mathrm{ms}$ to typically $s = 20 - 30$. During this ramp, the magnetic field was fixed to about $7\,\mathrm{G}$, effectively preventing any spin-changing collisions during the lattice ramp. In the ramp process, the atoms adiabatically follow in the ground state of the system. Thus, every pair of atoms ends up in an antisymmetrized two-particle spin state $|1/2; -1/2\rangle$.

Typical measurements at two different magnetic fields after a quench from $7\,\mathrm{G}$ are shown in Fig. 6.5. Both measurements clearly show coherent oscillatory dynamics of the spin populations, coupling all spin states available. These measurements demonstrate the possibility of spin-changing collisions with fermionic atoms for the first time. At the high magnetic field, basically one single frequency is observed within the experimental resolution, indicating the contribution of only two eigenstates. At the small magnetic field, the time evolution shows pronounced beat notes in the oscillatory signal. The beat notes are a clear signature of multiple frequencies and therefore of multiple eigenstates involved in the spin-changing dynamics, in contrast to the single frequency at large magnetic fields. Especially the large occupation of the $m = \pm 9/2$ components is remarkable.

In order to compare the experimental data with the developed two-particle theory, using the calculated scattering lengths (6.25) and the Zeeman energy, the five-dimensional Hamiltonian $H_\mathrm{S} + H_\mathrm{B}$ is solved numerically. The resulting eigenenergies and eigenstates are used to calculate the spin-changing dynamics of two particles from the initial state $|1/2; -1/2\rangle$. The two-particle calculations of the spin-oscillation dynamics are depicted in Fig. 6.6, using the exact parameters as for the measurements shown in Fig. 6.5 The results show a good agreement

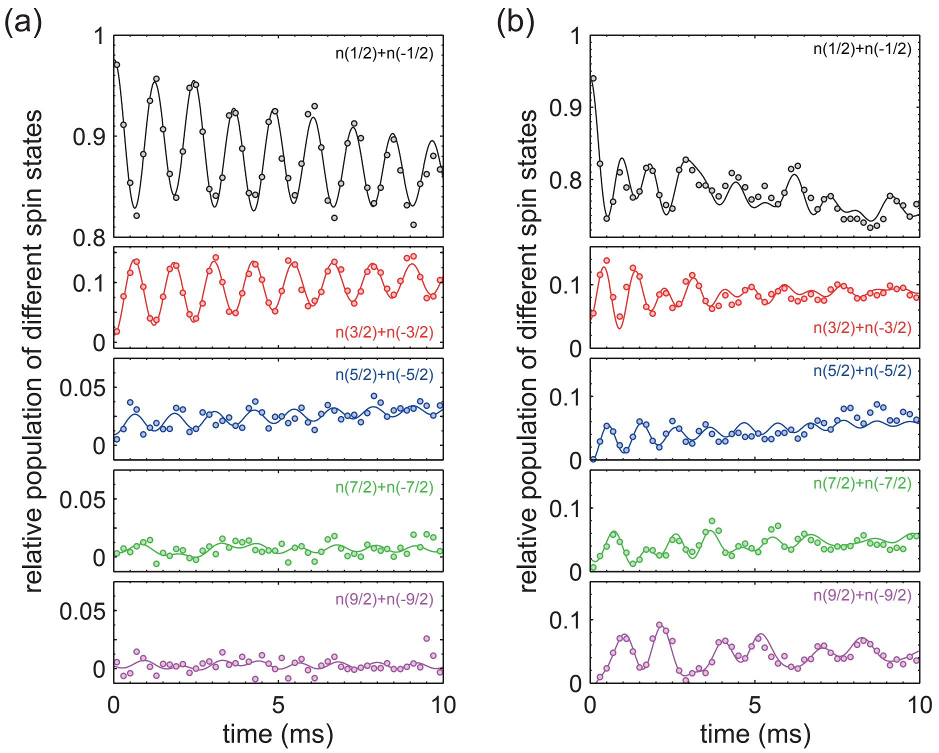

Figure 6.5: Measurement of coherent spin oscillations with five two-particle states involved. Plotted are the observed sums of the relative populations $n(m) + n(-m)$ of different spin states $|m\rangle$ as a function of time, corresponding to the populations of the two-particle states $|m; -m\rangle$. Solid lines are fits with the sum of several damped cosine oscillations and serve as guides to the eye. (a) The lattice depth is $25\,E_\mathrm{r}$ and the magnetic field is $B = 1.01\,\mathrm{G}$. All five two-particle states are involved in the oscillations, which have only one common frequency anyway. This indicates the coupling of mainly two eigenstates of the full two-particle Hamiltonian. (b) Data for the same parameters as in (a), except for the magnetic field, which is $B = 0.10\,\mathrm{G}$. Pronounced beat notes appear in the signal, indicating the contribution of multiple eigenstates.

---

with the experimental data.

Finite deviations between both results can be attributed to the following effects. First, the absolute amplitude in the calculation is much larger than the observed amplitude. Recall, that the band insulator is only realized in the center of the system due to the inhomogeneous filling in the trap. The remaining atoms are distributed on singly occupied sites at the edge of the system, and do not exhibit any spin-changing dynamics. Hence, they lead to a constant background of $|1/2\rangle$ and $|-1/2\rangle$ atoms. Second, there is a slow damping of the experimentally observed oscillations. This results from the finite tunneling amplitude of $5\,\mathrm{Hz}$. Finally, there is a deviation due to the magnetic field switching procedure. Since the quench of the magnetic field is not instantaneous, finite phase changes between the different spin states are introduced.

Despite these small deviations, the similarity between the experimental and theoretical results is quite astounding, confirming a very precise determination of the F-depended scattering lengths in the preceding section. Especially the agreement at low magnetic fields is remarkable, where all five levels, and therefore many different interaction parameters, are involved. In this regime, the large rates for spin-changing collisions with $\Delta m \geq 2$ are expected to contribute significantly. To verify this, the same calculations have been performed as for the results shown

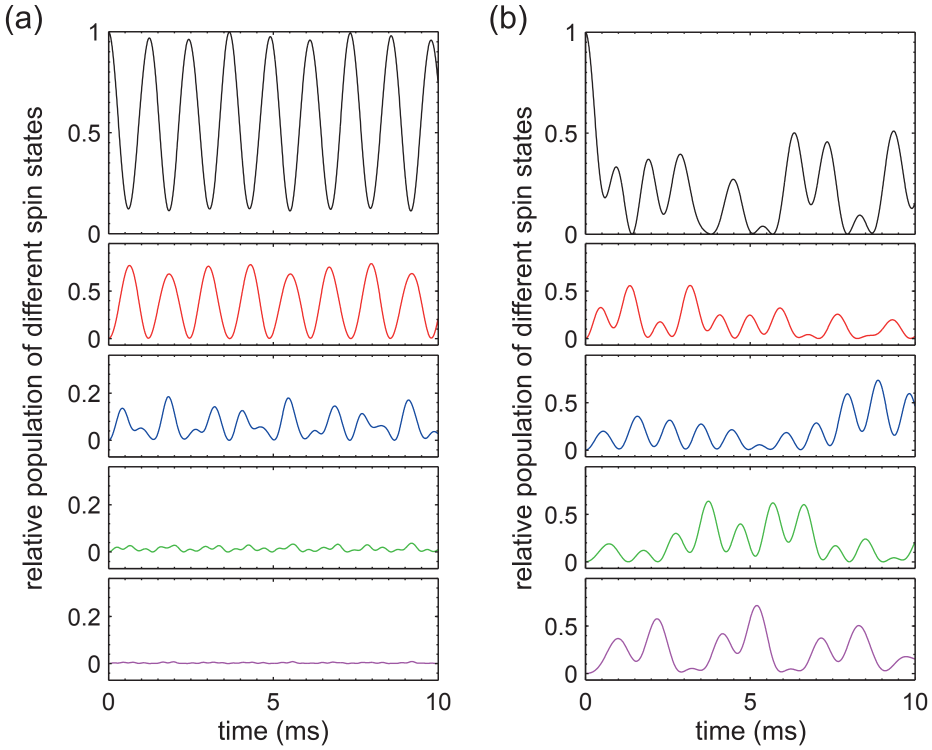

Figure 6.6: Theoretical calculations for the two-particle spin-changing dynamics in the five-level system. (a) Calculation for the same parameters as in the experiment of Fig. 6.5(a). (b) Calculation for the same parameters as in the experiment of Fig. 6.5(b).

---

in Fig. 6.6, now excluding scattering lengths that lead to the higher-magnetization exchanges. Figure 6.7 shows the results, where different numbers of processes are neglected. The calculations reveal that the dynamics at the larger magnetic fields does not change its fundamental behavior, if higher-order spin-changing collisions are neglected. The oscillation still includes mainly one frequency component, but only the absolute frequency changes. This difference could in principle also be a result of slightly wrong scattering lengths or an inaccurate magnetic field calibration. Therefore, the large field dynamics does not allow for a clear identification of higher-order spin-changing collisions.

In contrast, at the low magnetic fields the results without collisions corresponding to $\Delta m \geq 2$ are also qualitatively different from the experimental data and the full calculation. The dynamics of $m = \pm 9/2$ shows especially pronounced beating dynamics, which are very well reproduced by the full simulation. Neglecting more and more scattering channels changes this beat feature considerably. The combination of both observations, the good agreement between the full calculation and the change of the qualitative behavior, if higher-order scattering processes are neglected, gives strong evidence for the influence of $\Delta m \geq 2$ collisions on the observed dynamics. This is in contrast to results for $f = 2$ in ^{87}Rb, where such processes can safely be neglected to explain the experimental results [92, 242]. Moreover, to my best knowledge no experimentally evidence for spin-changing collisions with $\Delta m \geq 2$ has been reported elsewhere [230].

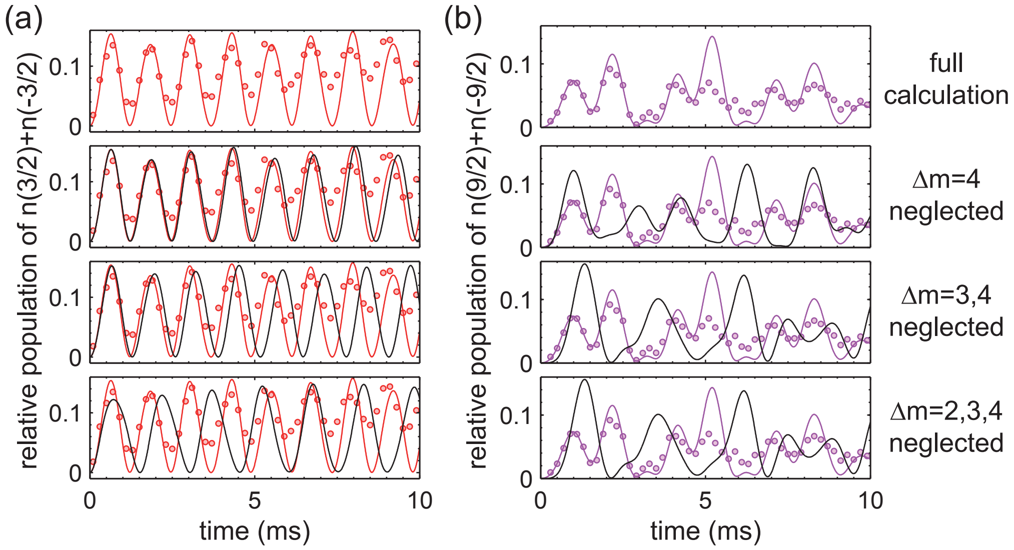

Figure 6.7: Theoretical calculation of the spin-changing dynamics neglecting different spin-changing channels in comparison with exemplary experimental data. Oscillation dynamics for (a) the higher and (b) the lower magnetic field. Shown are exemplary spin states $|\pm 3/2\rangle$ and $|\pm 9/2\rangle$ from the measurements shown in Fig. 6.5. The first row shows a comparison between the experimental and numerical results using the full scattering lengths matrix (6.25) in the calculation. The numerically calculated amplitudes are scaled by a factor of 0.2 to fit the experimental amplitudes, according for the number of doubly occupied sites in the experiment. In the second to fourth row, different higher-order spin-changing processes are neglected in the calculations. These results are depicted by the black solid lines, while the colored lines depicts the result for the full scattering matrix from the first row for comparison. Going downwards from the second row, the channels with $\Delta m = 4$, $\Delta m = 3,4$, and $\Delta m = 2,3,4$ are neglected.

6.3 DETECTION OF DOUBLE OCCUPANCY VIA SPIN-CHANGING COLLISIONS

In the measurements presented above, a two-component band insulator is prepared initially. At this stage, the system is described by the conventional $s = 1/2$ Hubbard model (3.15), whose ground state phases are the band insulator (unity filling), the Mott insulator (half filling), and a metallic phase (inconsumerate filling) [154]. To distinguish these different phases, the number of doubly occupied sites is an especially useful observable [25], which is also a useful quantity in many other contexts [38, 61, 188, 231, 232, 249].

In the literature, several approaches to measure double occupancy are reported, [25, 188, 231, 250]. Among them are spin-changing collisions in a deep optical lattice, which has been used for bosons to distinguish different Mott shells [231]. An alternative approach are f-changing collisions, where one or both components are transferred to the $f = 7/2$ manifold. Any interacting pair is subsequently lost from the sample, since the internal excitation energy of 1.3 GHz is inelastically converted to kinetic energy.

6.3.1 m-CHANGING COLLISIONS

In deep optical lattices all sites evolve independently, such that the total amplitude of coherent spin-changing collisions is proportional to the double occupancy of the system. This observ-

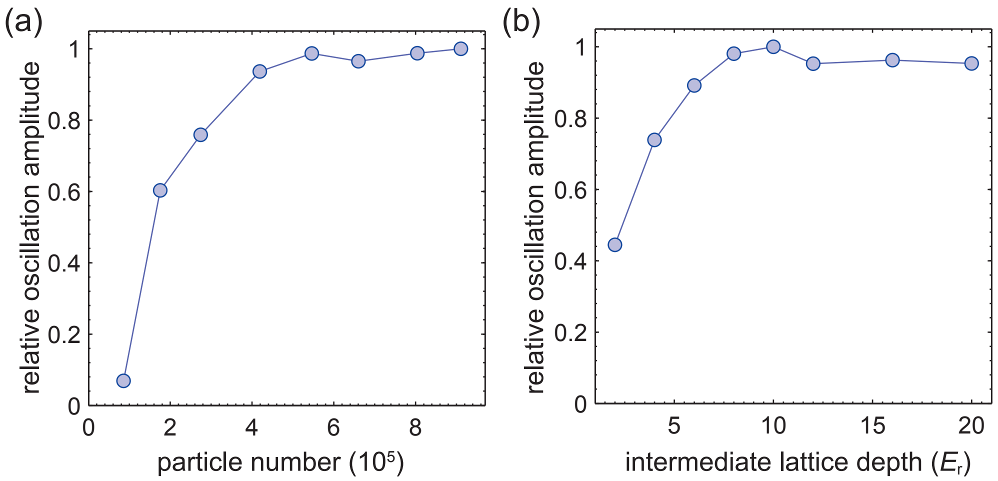

Figure 6.8: Double-occupancy measurement in a three dimensional lattice for different particle numbers and lattice depths using spin-changing collisions. Experimental data is connected by solid lines as a guide to the eye. (a) Shown is the amplitude of the spin-changing collisions in dependence of the particle number for different evaporation procedures. The signal is proportional to the double occupancy in the system. The lattice depth is $s = 20$. (b) Same signal as in (a), now in dependence of the lattice depth after a linear 100 ms lattice ramp, followed by a 5 ms lattice ramp to a depth of $s = 20$. The final ramp ensures equal conditions for the spin-changing collisions, but does not induce any change the double occupancy or the band population. The particle number in (b) is 2.4×10^5. The trapping frequencies without the lattice are about $2\pi \times (125, 41, 32)$ Hz for both measurements.

---

able allows for a very precise determination of the relative change of the double occupancy [231]. Therefore, a vanishing double occupancy can be effectively detected. Comparing the observed oscillation amplitude to the theoretically calculated amplitude, as shown in Fig. 6.7, allows in principle also for a detection of the absolute double occupancy. However, since this method includes the assumption that all experimental parameters are known precisely for the calculation, this determination of the absolute double occupancy is prone to systematical errors.

Figure 6.8(a) shows a measurement of the spin-changing collision amplitude in dependence on the initial particle number. The lattice depth is $20\,E_\mathrm{r}$, corresponding to a value of about $J/h = 12$Hz and $U/J \approx 250$, where the system is either in a Mott insulating or a band insulating ground state, depending on the total particle number. At large particle numbers, a finite double occupancy is observed, which indicates a band insulating core in the center of the trap. At the lowest particle number, the double occupancy drops to nearly zero, indicating a Mott insulting state in the center [154], where only singly occupied sites exist. The absolute double occupancy at the largest particle numbers can be estimated to be about 20 %, if the absolute spin-changing collision amplitude is compared to the theoretical expectation. Combining this with the relative values reported in Fig. 6.8(a), the lowest detected double occupancy is below 2 %, which is the detection threshold in the reported measurement. To unambiguously determine the state of the system additional measurements of the excitation spectrum [25] or of the compressibility [26] of the system are required, but the vanishing double occupancy is already a very promising sign, that the Mott insulating state has been reached. Using lower initial trapping frequencies would allow for an even larger regime of particle numbers in the Mott insulating state.

To investigate the influence of the lattice parameters on the double occupancy, a further measurement was performed as shown in Fig. 6.8(b). Here, the relative double occupancy was measured in dependence on the final lattice depth. A rise of the double occupancy with in-

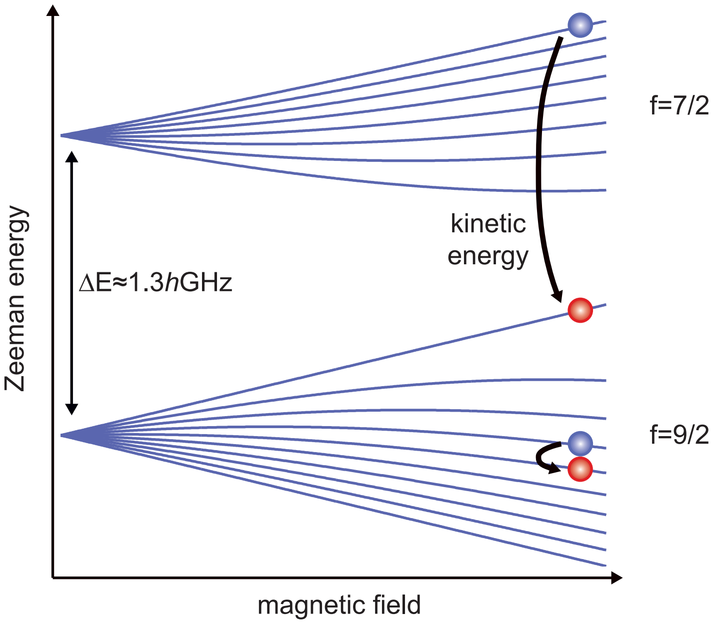

Figure 6.9: Sketch of f-changing collisions in ^{40}K. If one atom is excited to the $f = 7/2$ hyperfine manifold, collisions can lead to an inelastic decay to the energetically lower $f = 9/2$ manifold. The released kinetic energy is much larger than any other energy scale in the system. Thereby, the two colliding atoms are lost from the sample.

creasing lattice depth is observed for small absolute lattice depths. This is due to the increased harmonic confinement introduced by the lattice beams. For lattice depths beyond $s = 10$ the double occupancy reaches a plateau, while the harmonic confinement is still getting stronger. This can be explained by a combination of multiple effects. First, at large lattice depths the tunneling energy J becomes very small, which prevents an adiabatic redistribution during the lattice ramp [251]. Second, around the band insulating core a Mott insulating ring develops at large lattice depths [154], which is expected to appear above $10\,E_\mathrm{r}$. This ring suppresses further redistribution towards doubly occupied sites in the center by slowing down mass transport considerably [252]. An increase of the total double occupancy could be achieved by a further increase of the trapping frequency before ramping up the optical lattice, or by using Feshbach resonances to reduce the interparticle interaction, which shifts the appearance of the Mott insulating ring to higher lattice depths.

6.3.2 f-CHANGING COLLISIONS

An alternative method for the detection of double occupancy are inelastic f-changing collisions, which lead to fast losses of all doubly occupied sites. A sketch of the basic process in ^{40}K is shown in Fig. 6.9. During a collision of two atoms with at least one in the excited $f = 7/2$ manifold, this atom can change its spin to $f = 9/2$, while the total spin F of both atoms is conserved. This process releases an energy of about $1.3\,$GHz, corresponding to the splitting between the two hyperfine manifolds. The energy is converted to kinetic energy in the process, leading to inelastic collisions. Since the converted energy is much larger than any other energy scale in the system, such a collision leads to an instantaneous loss of the colliding atoms.

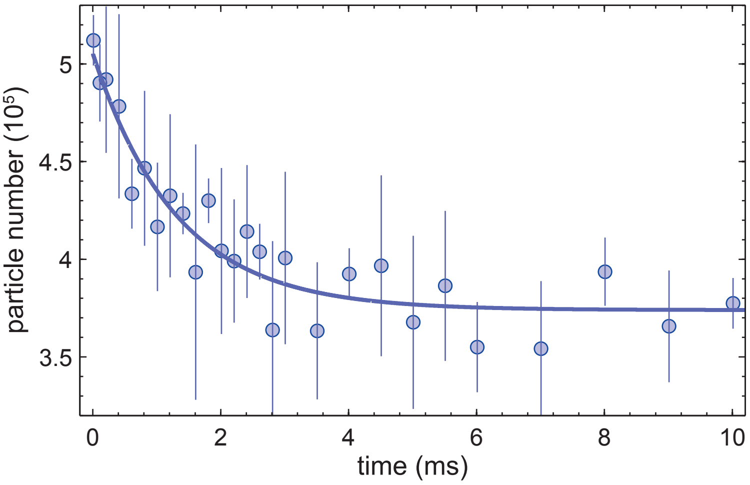

Figure 6.10: Double-occupancy measurement using losses due to f-changing collisions from the state $|9/2,7/2\rangle|7/2,3/2\rangle$. The experimental data shows the particle number in the state $|9/2,7/2\rangle$ for different times after the preparation of the $|7/2,3/2\rangle$ atoms using a mw pulse. The solid line is an exponentially decaying fit to the data, allowing for a constant offset in the particle number. The difference between the initial and the offset particle number determines the double occupancy of the system, as described in the text.

Confining the atoms to a deep optical lattice, collisions are only possible between atoms on initially doubly occupied sites for times shorter than the typical tunneling time h/J. In this regime, the inelastic f-changing collisions lead to a fast loss of all atoms on doubly occupied sites. This provides a direct measure of the total double occupancy of the system, by measuring the total particle number loss. For this, the atoms are prepared in two interacting states in the $f=9/2$ manifold. After their transfer to the deep optical lattice one or both components are excited to the $f=7/2$ manifold using microwave radiation, as described in section 2.2.

Figure 6.10 shows a typical measurement starting from the initial state $|9/2,7/2\rangle|9/2,3/2\rangle$, where the $|9/2,3/2\rangle$ component is transferred to $|7/2,3/2\rangle$. The initial state is prepared very similar to the $|9/2,1/2\rangle|9/2,-1/2\rangle$ mixture in section 6.2, again requiring to take care of losses due to Feshbach resonances in the evaporation [114]. The final magnetic field in the optical lattice is 3 G and the lattice depth is 30 E_r. The trapping frequencies without the lattice are about $2\pi\times(125,41,32)$ Hz. The data shows a fast decrease of the atom number during the first 5 ms. Fitting an exponential decay to the data gives a lifetime of about 1.3 ms, corresponding to a loss rate of $\Gamma\approx 2\pi\times 770$ Hz, equivalent to a two-body loss coefficient $\gamma\approx 2\pi\times 4.8\times 10^{-18}\,\mathrm{m}^3/\mathrm{s}$. Comparing this to a typical interaction energy of $U/\hbar\approx 2\pi\times 4$ kHz the loss rate is a factor of about five smaller. This shows, that the decay is in the same order as the typical f-conserving but m-changing collisions (see (6.25)). This is actually expected, since both processes arise from the same underlying scattering processes [151]. Note here, that the exact background for the collisions with mixed f cannot be calculated directly from the reported a_F. However, the data for other alkali atoms, such as ^{87}Rb [155], shows that the typical scattering lengths for such mixed-f collisions are very similar to the equal-f collisions (see section 6.1). Therefore, using a typical value from the $f=9/2$ manifold is well justified as an approximation for the elastic scattering rate.

The lattice depth in the data from Fig. 6.10 is $s=30$, resulting in a tunneling rate of about $J/h=2$ Hz, much slower than the observed particle decay time. This allows to assume independent lattice sites during the observation time for the data shown in Fig. 6.10. Hence, the double occupancy can be directly determined from the particle number decrease. This is supported by the observed plateau of remaining atoms after the fast initial particle loss. The plateau corresponds to all atoms on singly occupied sites, which need to tunnel before being lost from the sample due to inelastic collisions. The timescales for this is the tunneling time $h/J = 500\,\mathrm{ms}$, being much longer than the observed decay time.

Using the number of lost atoms, a double occupancy of about $26\,\%$ is observed for the initial particle number of about 5.2×10^5. The presented method can in principle overestimate the total double occupancy, since other processes that potentially lead to atom loss could increase the double occupancy signal. Further, fluctuations of the total particle number lead to noisy signals, which requires repeated measurements for averaging. In the data reported in Fig. 6.10, three individual measurements were performed and averaged for each time step. A quick estimate of the double occupancy can be obtained by measuring only the loss after $5\,\mathrm{ms}$, which coincides with the fitted value within the uncertainty. The maximal double occupancy measured with the presented method was $40\,\%$, at a total particle number of 6.4×10^5 and otherwise identical parameters as for the measurement shown in Fig. 6.10.

In addition to the above mentioned loss channel $|9/2, 7/2\rangle|7/2, 3/2\rangle$, also the loss rates for $|7/2, 7/2\rangle|9/2, 3/2\rangle$ and $|7/2, 7/2\rangle|7/2, 3/2\rangle$ have been measured, resulting in $64\,\mathrm{Hz}$ and $1.8\,\mathrm{kHz}$, respectively. These values are equivalent to two-body loss coefficients $\gamma \approx 2\pi \times 4.0 \times 10^{-19}\,\mathrm{m}^3/\mathrm{s}$ and $2\pi \times 1.1 \times 10^{-17}\,\mathrm{m}^3/\mathrm{s}$. This shows a clear stabilization for the $|9/2, 3/2\rangle$ $|7/2, 7/2\rangle$ mixture by an order of magnitude. The strength of the inelastic collisions is only in the order of about $1-2\,\%$ of the usual background interaction for this mixture. While this is still an order of magnitude larger than the very small loss rate for mixtures of $f = 1$ and $f = 2$ in ^{87}Rb [120, 253], the possibility of such small loss rates might already enable an efficient production and investigation of such mixed-f mixtures in ^{40}K for future applications. Since the observed loss rates strongly depend on the precise mixture, varying almost about two orders of magnitude already for the three reported mixtures, a more detailed investigation might reveal even lower loss rates for other mixtures.

Finally, let me point out that the detection of double occupancy using f-changing collisions can be extended to investigate spinor gases with more than two components. In particular, it allows for a spin-resolved detection of double occupancy in these systems. Each spin state can be transferred to the excited $f = 7/2$ manifold independently. Measuring the relative loss in all other spin states gives a direct measure for the number of doubly occupied sites containing the transferred state and each of the other states. Repeating this measurement for each spin state, the full distribution of different doubly occupancies can be obtained. This might have potential applications in the detection of unconventional phases or superexchange dynamics in high-spin Fermi gases [2, 111, 113, 233].

6.4 PHASE CROSSOVER FROM A MOTT TO A QUANTUM ZENO INSULATOR

In the preceding section, I discussed losses due to inelastic two-body collisions in an optical lattice. Assuming collisions exclusively between atoms on doubly occupied sites and including only short-time dynamics, this gives an estimate for the double occupancy in the initial state. However, for longer times, also inelastic collisions between atoms from initially singly occupied sites must be included. For this, at least one of the atoms needs to tunnel to the neighboring well. This happens in the order of the tunneling time h/J.

If the system has additionally strong elastic collisions with $U \gg J$, being in the Mott insulating phase, the tunneling is further suppressed by the interaction gap. In this regime superexchange processes dominate the tunneling, which have an amplitude of $2J^2/U \ll J$ [15]. This is the case for all measurements described in section 6.3. Consequently, the effective loss rate for atoms that are initially prepared on singly occupied sites is further reduced by this interaction blockade.

In the following, I discuss the effective decay rate in optical lattice systems with inelastic and elastic interactions. A thorough theoretical description of this situation can be found in [234, 235], and the following discussion is meant as a short review of the most important concepts and results. As a central result, the effective loss rate is decreased in both, the regime of dominating elastic interactions ($U \gg \hbar\Gamma$) and in the regime of dominating inelastic interactions ($U \ll \hbar\Gamma$). The latter has been attributed to the quantum Zeno effect [54, 254–256] and has already been observed for molecular quantum gases [31, 54, 234]. However, the transition between both regimes has not been observed experimentally, so far.

Such a study would allow for the observation of a novel crossover from the strongly correlated Mott insulating state [25, 26] to the strongly correlated quantum Zeno induced state [31, 54]. This constitutes a completely novel approach on the investigation of strongly correlated systems. In particular, since the particle number is not conserved, the system is an open quantum system, which have gained a lot of interest in the context of ultracold atoms in recent years (see, e.g., [257] and citations therein).

I propose here, how to use ultracold ^{40}K atoms for the experimental study of this crossover, from the usual Mott insulating regime with suppressed losses, to the quantum-Zeno regime. For this, a novel Feshbach resonance of ^{40}K can be applied that provides strong inelastic two-body losses in combination with very small elastic interactions.

The effective loss rate Γ_{eff} from an initially purely singly occupied lattice can be calculated by introducing the bare inelastic collision rate Γ as an imaginary term in the total scattering amplitude

$$U_{\text{t}} = U + \mathbb{i}\frac{\hbar\Gamma}{2} = \upsilon\left(g + \mathbb{i}\frac{\hbar\gamma}{2}\right) . \tag{6.26}$$

Here, υ is the total integral over the Wannier functions in the definition (3.14) of U. Assuming a tunneling rate much lower than both U and Γ, the existence of a doubly occupied site can be integrated out of the Hilbert space, as sketched in Fig. 6.11. For the interaction term U, this corresponds to the usual description of superexchange in the hardcore limit, where no doubly occupied sites can be dynamically created [15]. For the loss term Γ, the tunneling induced realization of a doubly occupied site leads to a fast loss of both particles, such that the double occupancy can be regarded as a transitory state between two singly occupied sites and two empty sites.

In a double-well, as sketched in Fig. 6.11, the resulting Hilbert space has only two states. The corresponding Hamiltonian

$$H = \begin{pmatrix} 0 & J \\ J & U - \mathbb{i}\hbar\Gamma/2 \end{pmatrix} \tag{6.27}$$

is not hermitian, however, which is due to the imaginary interaction term. Nevertheless, the Hamiltonian 6.27 allows for a calculation of the effective decay rate. In the regime of strong interactions $[(\hbar\Gamma, U) \gg J]$ the effective loss rate can be evaluated as [235]

$$\Gamma_{\text{eff}} = \frac{8J^2}{\hbar^2\Gamma}\left(\frac{1}{1 + (2U/\hbar\Gamma)^2}\right) . \tag{6.28}$$

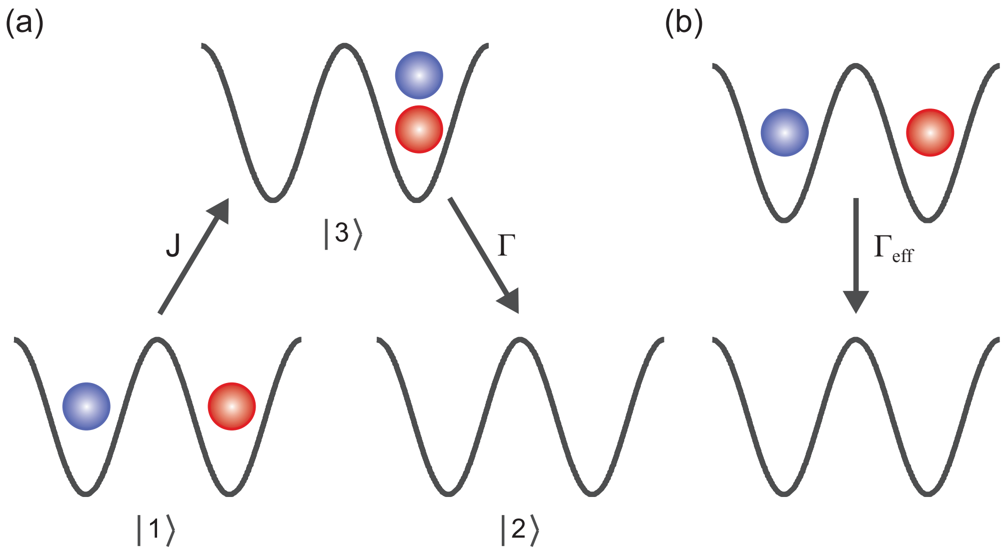

Figure 6.11: Sketch of the Hilbert space reduction for strong inelastic interactions. (a) Bare states $|1\rangle$, $|2\rangle$ and $|3\rangle$ for a double well system with half filling. $|1\rangle$ and $|3\rangle$ are coupled via a tunneling event, while $|2\rangle$ and $|3\rangle$ are coupled via a loss process. (b) Effective two-level system after the integration over state $|3\rangle$. The imaginary interaction term drives a system initially prepared in the state $|1\rangle$ slowly into the vacuum state $|2\rangle$ with an effective rate Γ_{eff}.

Figure 6.12 shows the effective loss rate (6.28) as a function of the ratio $\hbar\Gamma/U$. At small and large $\hbar\Gamma/U$, the loss is suppressed, while it is maximal for similar interaction strengths $\hbar\Gamma/U \approx 2$. To understand the peculiar behavior of (6.28), a closer examination of the limiting cases is very instructive.

First, in the usual case of small losses and strong elastic interactions $(U \gg \hbar\Gamma)$, corresponding to a Mott insulator, the effective loss rate simplifies to [235]

$$\Gamma_{\mathrm{eff}}^{U\gg\hbar\Gamma} = \frac{2J^2}{\hbar U}\frac{\hbar\Gamma}{U}\,. \tag{6.29}$$

This result reveals the interaction induced tunneling blockade, as discussed at the beginning of the section. Inelastic collisions between the atoms are inhibited by the correlations created by the dominating elastic interactions. Therefore, the loss rate is basically multiplied by the typical tunneling amplitude $2J^2/U$ of the dominating superexchange collisions.

The second relevant limit is the opposite situation with strong losses $\hbar\Gamma \gg U$. Here, the effective loss rate becomes [235]

$$\Gamma_{\mathrm{eff}}^{\hbar\Gamma\gg U} = \frac{8J^2}{\hbar^2\Gamma}\,, \tag{6.30}$$

which is inversely proportional to the bare loss rate Γ. This intriguing result shows, that the physical loss of particles is indeed reduced for an increased strength of inelastic interactions. This suppression of losses due to a dissipative channel is in fact a realization of the quantum Zeno effect [54], where the repeated measurement of a system hinders its time evolution and stabilizes the system in its present state [254–256]. Whether or not the two atoms are lost from the system can be regarded as a measurement, since the system is projected onto different states for both results. Thus, the mere possibility of this loss suppresses the actual tunneling process that would induce the inelastic collisions [54]. Therefore, the system stabilizes in a configuration of maximally one particle per site. This can only be achieved by information exchange

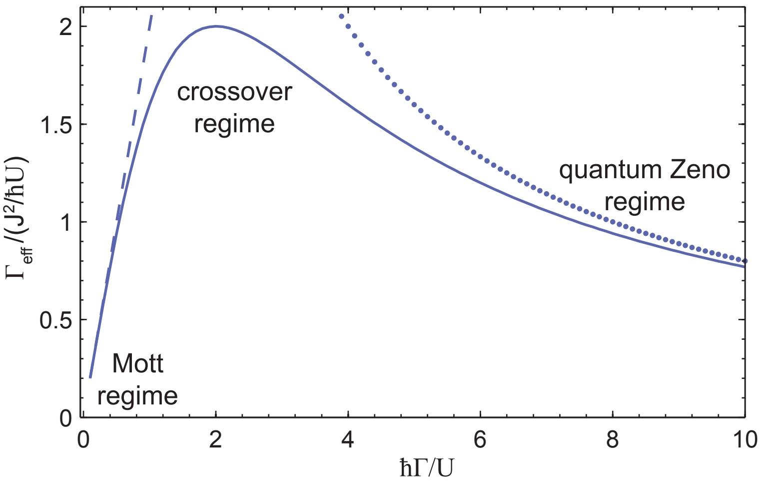

Figure 6.12: Effective loss rate with strong inelastic and elastic interactions as calculated with (6.28). For both limiting cases $U \gg \hbar\Gamma$ and $\hbar\Gamma \gg U$, the effective loss rate is reduced, while at similar strengths $\hbar\Gamma/U = 2$ there is a maximum. The dashed line is the approximate result of (6.29), demonstrating the linear behavior of Γ_{eff} at small Γ. The dotted line is the approximate result of (6.30), showing a clear $\Gamma_{\text{eff}} \propto 1/\Gamma$ behavior at large Γ.

between the different lattice sites, realized through virtual exchange processes. Therefore, the configuration with suppressed losses corresponds to a highly correlated state. In the previous realizations of this regime [31, 54] the loss rate behavior has been measured as a function of the tunneling energy and the inelastic interaction strength, in both cases, however, with a fixed ratio $\hbar\Gamma/U$.

To investigate the crossover between the limiting cases discussed above, a degenerate quantum system with tunable elastic and inelastic interactions is required, where the ratio $\hbar\Gamma/U$ can be freely adjusted. This can be achieved using a novel Feshbach resonance in a two-component mixture of ^{40}K atoms, which has been identified during this thesis. It allows for the very controlled tuning of $\hbar\Gamma/U$ over many orders of magnitude with high precision and covers the full parameter regime from (6.29) to (6.30). Figure 6.13 shows a loss measurement for the relevant mixture of the spin states $|9/2, 9/2\rangle$ and $|9/2, -5/2\rangle$. In comparison, the results for the inelastic and elastic collisions from a coupled channel calculation are shown, kindly provided by T. Hanna and L. Cook [237]. Both, experiment and theory show two clear maxima of the particle loss rate within the investigated magnetic field range. Inspecting the calculations of the s-wave scattering length, the loss maxima can be attributed to s-wave Feshbach resonances [237].

For the presented resonances the elastic scattering rate does not reach negative values, but is only reduced by about two orders of magnitude. Since the resonance at 63 G is much broader, it is easier to control the scattering length in this region. Therefore I concentrate on this resonance in the following. Quantifying the interaction strength in terms of scattering lengths, the lowest value at 66 G is about $1.5\,a_{\text{B}}$, while the maximal value is about $230\,a_{\text{B}}$ at about 60 G. The background scattering length is about $161\,a_{\text{B}}$. Since small scattering lengths around $a \approx 1.5\,a_{\text{B}}$ are reached at the minimum of the elastic scattering rate in dependence on the magnetic field, a very controlled preparation of this regime should be possible. Note, that in this regime the inelastic scattering rate is up to two orders of magnitude higher than the elastic scattering rate.

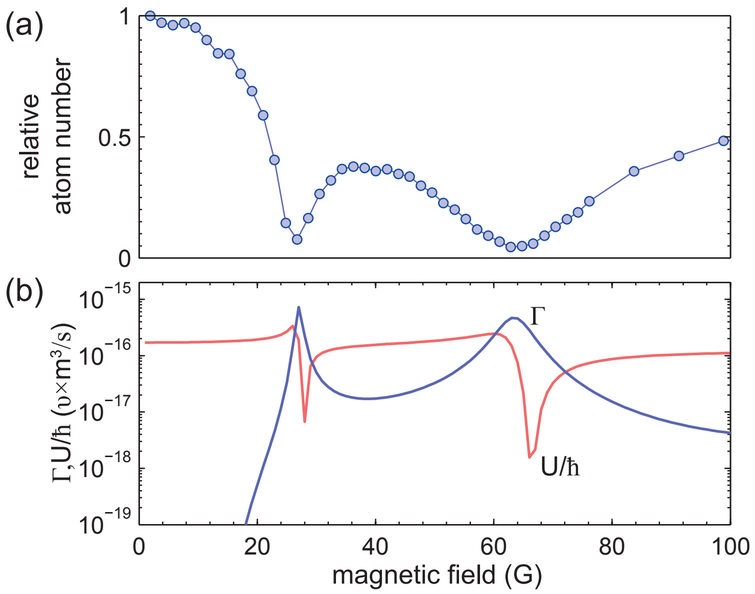

Figure 6.13: Loss measurement of an s-wave Feshbach resonance in the states $|9/2, 9/2\rangle$ and $|9/2, -5/2\rangle$. (a) The system is initially prepared in the mixture $|9/2, 9/2\rangle|9/2, 7/2\rangle$ in the optical dipole trap. The $|9/2, 7/2\rangle$ state is then transferred to $|9/2, -5/2\rangle$ using rf-sweeps at about $45\,$G. Subsequently, the magnetic field is ramped to its final value and after a waiting time of $100\,$ms, the magnetic field and all trapping potentials are switched off and the remaining particle number is detected after TOF. The data shows two clear loss features, where especially the second at approximately $63\,$G is very strong and broad. (b) Theoretical calculation of the scattering parameter $U/\hbar$ and the two-body loss rate Γ (see (6.26) for the definition of ν). The calculations show two Feshbach resonances in accordance with the experimentally observed loss maxima. They additionally reveal, that the loss rate strongly exceeds the elastic interaction in these regions. The theoretical calculations have been performed and kindly provided by T. Hanna and L. Cook.

For the region between $64\,$G and $92\,$G, the ratio $\hbar\Gamma/U$ can be tuned over several orders of magnitude from approximately 0.05 to 182. The corresponding effective loss rates as calculated from (6.28) are shown in Fig. 6.14. These results show, that the full regime from the very stable Mott insulator to the quantum Zeno induced regime can be reached, allowing for a investigation of the full crossover. Choosing suitable lattice parameters, the reduction of losses with increasing inelastic collisions can be unambiguously connected to the quantum Zeno effect-induced localization. Using a tunneling energy, such that a Mott insulator is realized for the background scattering length of $161\,a_\mathrm{B}$, but not around the reduced scattering length of $1{-}20\,a_\mathrm{B}$, which are conveniently realized from $65{-}69\,$G, the loss reduction in this regime cannot be attributed to the Mott insulating state. Reducing the lattice depth even further, or switching of the lattice entirely should realize a strongly correlated gas of “fermionized” two-component fermions [258, 259], created by the strong inelastic collisions [31, 234, 236]

The loss rates for the different ratios $\hbar\Gamma/U$ serve as a direct measure for the system behavior. Additional probes of the transition at different interaction ratios are the excitation spectrum [25] and the compressibility [26] of the system, which allow for a direct determination of its insulating properties.

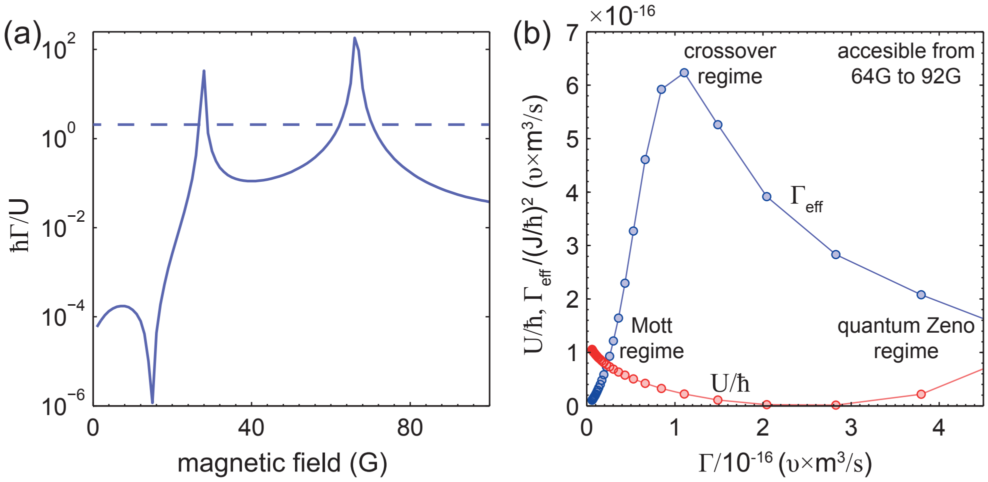

Figure 6.14: Tuning the effective loss rate using a lossy Feshbach resonance in the states $|9/2, 9/2\rangle$ and $|9/2, -5/2\rangle$. (a) Ratio $\hbar\Gamma/U$ in dependence on the magnetic field from the same numerical data as in Fig. 6.13(b). The dashed line shows $\hbar\Gamma/U = 2$, where the effective loss rate is maximal. For all higher values of $\hbar\Gamma/U$, the effective loss rate should be suppressed due to the quantum Zeno effect. (b) Effective loss rate Γ_{eff} and U in dependence on Γ for the region between 64 G and 92 G. The resolution of the calculation is 1 G, and the individual values are depicted by circles. The solid lines connect the numerical results as a guide to the eye. A clear reduction of the effective loss rate at strong inelastic and weak elastic collisions, as well as at low inelastic and strong elastic interactions is observed for the investigated Feshbach resonance. This demonstrates the possibility to tune between the quantum Zeno regime and the conventional Mott insulating regime over a broad range of parameters and with high resolution.

6.5 SUMMARY AND OUTLOOK

In this chapter, I discussed the interaction properties of unconventional fermionic lattice systems. I started with the discussion of the full background scattering properties of ^{40}K in the lowest ground state manifold. Together with ^{6}Li, ^{40}K is the working horse for the investigation of ultracold Fermi gases. An important difference between the two species is the high spin of the latter, which allows for the realization of completely novel spinor-many-body systems [98–102]. The excitation properties in these novel systems strongly depend on the exact scattering properties, which makes a detailed knowledge inevitable for the investigation.

A proof-of-principle experiment is presented, realizing the coherent spin-changing collisions in a fermionic high-spin system, using independent pairs of atoms prepared in a deep optical lattice. These results constitute the first study of the spin-excitation properties of high-spin Fermi gases. A comparison with a full quantum mechanical model, using the theoretically determined scattering lengths, reveals, that these spinor dynamics strongly depend on higher-order spin-changing processes with $\Delta m \geq 2$. Such processes have not been observed so far in other high-spin quantum gases [230, 242] and constitute a new class of magnetic exchange interactions, strongly affecting the system properties.

In addition, a spin-resolved measurement technique for the double occupancy in ultracold Fermi gases has been presented. The double occupancy is one of the most important observables for the characterization of strongly correlated ground state phases [25, 51]. Therefore, its spin-resolve detection will be a powerful tool in future studies of high-spin lattice systems.

The presented results allow for a deep insight into the interaction properties of high-spin

Fermi gases and pave the way for the investigation of novel quantum phases of ultracold fermions in optical lattice [51, 101, 104–113], including spatial degrees of freedom. Indeed, a first result in this direction has already been presented in the original publication [5], where a new form of melting of a band insulator has been observed, using spin-changing collisions.

A different direction to investigate high-spin Fermi gases are harmonically trapped systems without any lattice potential. First results concerning spin waves in this regime are presented in chapter 7 and a corresponding outlook on the related topics will be given there.

Finally, the realization of a novel phase crossover was discussed, connecting two strongly correlated states, driven by elastic collisions (Mott insulator, [25, 26]) or inelastic collisions (quantum Zeno insulator, [31, 54, 234, 235]). This allows for a completely novel approach on the investigation of the strongly correlated regime. In particular, the crossover takes place in an open quantum system, where the particle number is not conserved. The study of such open quantum systems with ultracold atoms has gained a lot of interest in recent years (see, e.g., [257] and citations therein).

Beyond that, the properties in the quantum Zeno regime can be used to measure the two-particle correlation function of the particular quantum state [31, 54, 234]. Therefore, a quench from the Mott to the quantum Zeno regime should allow for the measurement of the correlation function for the Mott insulating state. This is only possible in tunable system as discussed here. By that, particle ordering in strongly correlated many-body systems, like antiferromagnetism [260–263] or frustration in triangular lattices [264, 265], could be investigated.

CHAPTER 7

SPIN WAVES IN SPINOR FERMI GASES

Spinor quantum gases with $f > 1/2$ are a very vital field in ultracold atom research. Many theoretical and experimental studies have been performed on this topic since the advent of Bose-Einstein condensation, revealing novel magnetic properties, collective spinor excitations, spontaneous pattern formation, and many more fascinating results [67, 86–97, 226, 227]. The systems under investigation have been mainly limited to bosonic quantum gases, however. This changed in recent years, where an increasing number of theory proposals explores the rich physics of fermionic high-spin systems [98–102], going hand in hand with a growing, but still limited, number of experimental realizations of these complex systems [50, 73, 74]. A very intriguing prospect of fermionic high-spin systems are collective excitations, which are rare in fermionic systems because of Pauli blocking, but benefit from the additional internal degrees of freedom.

In this chapter, I concentrate on the novel properties of high-spin Fermi gases in spin-independent harmonic traps. There, the fermionic atoms are only weakly interacting and the typical interaction energy is much smaller than the average kinetic energy. For conventional two-component gases, it has been demonstrated that spin waves are the dominating low energy excitations in this regime [266–274]. They are characterized by a periodic counterflow spin current at constant total density. At stronger interactions, spin waves are suppressed and domain formation dominates [91, 275], which corresponds to itinerant ferromagnetism for fermionic quantum gases [276–279].

Concentrating on the weakly interacting regime, the goal of this chapter is to investigate the influence of the high spin on the spin-wave excitations. In order to identify the most fundamental high-spin effects, a four-component subspace of the full $f = 9/2$ hyperfine manifold of ^{40}K is used. This realizes an effective spin $3/2$ quantum gas. Since $f = 3/2$ is the simplest possible realization of a high-spin Fermi gas, this case is heavily studied in theory (see, e.g., [280] and references therein) and constitutes a model system for all higher spins.

The physical origin of spin waves in cold gases is the so-called identical spin rotation effect (ISRE), which results from an interference effect in the scattering of indistinguishable particles [281]. The ISRE was first described in the context of seminal experiments studying collective spin-wave excitation in hydrogen and helium [281–285], which are closely related to the spin waves observed in the ultracold regime [268]. The system can be equivalently described using a semiclassical mean-field theory (SMFT) [268]. Two-component systems can be conveniently described in this approach using the well known spin vector description [269, 273]. For higher spins, this is not sufficient and an extended description must be employed using higher-order irreducible spherical tensors [286]. These novel degrees of freedom contain the additional effects introduced by the high spin.

The multicomponent spin waves have been investigated for a large set of parameters, ranging from the linear to the nonlinear regime, and also for different initial states. For a comparison with the experimental results the SMFT has been extended to Fermi gases with high spins by Ulrich Ebling, supervised by Andre Eckardt and Maciej Lewenstein, and the results have been kindly provided (for results on spin waves in bosonic atoms with high spin, see [286, 287]). An excellent agreement is found between theory and experiment, demonstrating the comprehensive understanding and control of high-spin Fermi gases, which paves the way for further studies of these system.

All experimental data presented this chapter was taken and analyzed together with Jasper S. Krauser. The semiclassical model has been worked out by Ulrich Ebling, who kindly provided the numerical data based thereon. The representation of the results in the irreducible spherical tensor representation and the linearized description have been worked out and implemented together with Ulrich Ebling.

The results of this chapter have been partly published in [3].

7.1 IDENTICAL SPIN ROTATION EFFECT

The investigation of weakly interacting dilute gases requires a reconsideration of the basic two-body interaction process, discussed in section 6.1 for Fermi gases with arbitrary spin. As discussed in the following, the leading-order interaction term in the weakly interacting regime is the ISRE. It affects only indistinguishable particles with internal spin [281]. While scattering theory usually treats the interaction of particles in the basis set of orthogonal spin states $|m\rangle$, $|m'\rangle$ with $\langle m'|m\rangle = 0$, the ISRE is related to coherent superpositions of different spin states, allowing for interference effects. The full derivation of the ISRE is beyond the scope of this thesis and can be found in [268, 281]. In the following, I give only a short review of the results therein.

The main statement of the discussion in [268, 281] is best introduced in terms of the single-particle density matrix (SPDM), which is a generalized description of quantum mechanical states containing all single-particle information. Consider for simplicity one atom with two internal spin degrees of freedom, $|1/2\rangle$ and $|-1/2\rangle$. The most general state of such an atom is

$$|\varphi\rangle = c_+|1/2\rangle + c_-|-1/2\rangle = |c_+|e^{\mathbb{i}\theta_+}|1/2\rangle + |c_-|e^{\mathbb{i}\theta_-}|-1/2\rangle\,. \tag{7.1}$$

Such states are called *pure states*, where the atom is in a coherent superposition of both spins. The SPDM of the most general state (7.1) is defined as

$$\rho_\phi = |\varphi\rangle\langle\varphi| = \begin{pmatrix} |c_+|^2 & c_+c_-^* \\ c_+^*c_- & |c_-|^2 \end{pmatrix} = \begin{pmatrix} n_+ & n_{+-} \\ n_{+-}^* & n_- \end{pmatrix}\,. \tag{7.2}$$

Equation (7.2) shows, that the diagonal elements of the density matrix contain the populations $n_\pm$ of the spin states $|\pm 1/2\rangle$. The trace of ρ_ϕ is always unity, reflecting the normalization of the wave function (7.1). The offdiagonal elements n_{+-} contain the relative phase of the superposition and are therefore called coherences. For a pure state as in (7.2), the absolute value of the coherences is directly related to the occupations, leading to the relation

$$n_{+-} = \sqrt{|c_+c_-|}e^{\mathbb{i}(\theta_+-\theta_-)}\,. \tag{7.3}$$

This shows, that the SPDM (7.2) contains all information of the state (7.1).[1]

However, not every SPDM can be written in the form (7.2). The SPDM representation rather allows for the description of a different class of physical systems, that cannot be represented by a pure state as (7.1). For these states the relation (7.3) is not fulfilled and it serves only as an upper bound for the coherence amplitude. The most prominent example is the state

$$\rho_{\text{inc}} = \begin{pmatrix} 0.5 & 0 \\ 0 & 0.5 \end{pmatrix}, \tag{7.4}$$

which exhibits no coherences between the two magnetizations $|\pm 1/2\rangle$. Such a state is called an incoherent state and corresponds to a classical mixture, where no interference is possible. Note, that the concept of a density matrix is equally valid for external degrees of freedom or for many-body systems, where the latter can be described by a density matrix using many-body Fock states as a basis set.

For the derivation of the ISRE, I consider here two indistinguishable fermionic atoms with two internal degrees of freedom, following reference [268, 281]. The initial state is taken to be completely uncorrelated. The particles have the spin density matrices ρ_1 and ρ_2 and opposite momentum states $|\vec{p}\rangle_1$ and $|-\vec{p}\rangle_2$. In the SPDM representation this relates to the two-particle state

$$\rho_\Phi = \mathcal{A}\left\{|\vec{p}\rangle\langle\vec{p}|_1\rho_1 \otimes |-\vec{p}\rangle\langle-\vec{p}|_2\rho_2\right\}, \tag{7.5}$$

where the brackets $\mathcal{A}\{\dots\}$ indicate a proper antisymmetrization incooperating the fermionic character of the atoms.

The ISRE is an interaction phenomenon. Therefore, one needs to inspect the scattering process of the two atoms in (7.5). For a two-component Fermi gas the spin is conserved during a collision process. Therefore, the interaction does only influence the external degrees of freedom and a spin exchange is only possible via interference due to the indistinguishability of the atoms. A scattering process is usually analyzed in scattering theory by the so-called S-matrix, which describes a process, where the two scattering particles are initially far away from each and are detected again far away from each other after the scattering process. For a scattering of two identical fermions the spatial part of the S-matrix takes the form

$$\langle\vec{q}|\langle-\vec{q}|S|\vec{p}\rangle|-\vec{p}\rangle = \delta(\vec{p}-\vec{q}) - \mathbb{i}\pi\frac{m}{\hbar^2 k}T(\vec{q},\vec{p}), \tag{7.6}$$

where $|\vec{p}| = |\vec{q}|$ is required by energy conservation and $k = |\vec{p}|/\hbar$. The T-matrix is used here, which contains the scattered part of the particles [129].

In this context of ultracold atoms, using a pseudo-potential approach with scattering length a, the T-matrix becomes independent of the scattering direction and can be calculated in the Born approximation [129, 151] as

$$T(\vec{q},\vec{p}) = T(k) = \frac{4\pi\hbar^2}{m}\left(a - a^2\mathbb{i}k + O(a^3)\right) \tag{7.7}$$

up to second order in the scattering length. It is necessary to include the imaginary second-order term here, in order to comply to first order with the optical theorem [129, 268], which is used below.

Using the s-matrix, scattering processes in the state (7.5), are described by

$$\rho_{\text{scat}} = S^\dagger\rho_\Phi S\,. \tag{7.8}$$

---

[1] The SPDM (7.2) does not contain the global phase of (7.1), which is irrelevant for the quantum mechanical description and contains no additional information about the state.

This process includes scattering in all three spatial dimensions. A distinguished direction is given by forward scattering, where the atoms do not change their momentum. For distinguishable particles, without any antisymmetrization, the forward scattering ($\vec{q}=\vec{p}$) leads to a change in the density matrix given by

$$\rho_{\text{dis}} \propto \frac{8\pi^3 m}{\hbar^2 k} \Im\left(T(k)\right) \rho_1 \,, \tag{7.9}$$

where $\Im\left(T(k)\right)$ denotes the imaginary part of the T-matrix in the forward direction. Any particle, which is scattered, is removed from the forward direction, leaving the unscattered atoms as the remaining fraction. In accordance with the optical theorem [288], the total scattering crosssection σ_{dis} of (7.9) is proportional to the imaginary part of the T-matrix. Inserting the Born approximation (7.7) yields the well known result $\sigma_{\text{dis}} = 4\pi a^2$. Note here again, that this result is only obtained consistently, keeping the second order of the Born approximation in (7.7).

For indistinguishable fermions the result is modified and the ISRE shows up in this process. The total scattering amplitude for this case is given by

$$\rho_{\text{ind}} \propto \frac{8\pi^3 m}{\hbar^2 k} \left(\Im\left(T(k)\right) \rho_1 - \frac{1}{2} \Im\left(T(k)\right) \{\rho_1, \rho_2\} - \mathbb{i}\frac{1}{2} \Re\left(T(k)\right) [\rho_1, \rho_2] \right) . \tag{7.10}$$

The additional terms in (7.10) account for interference effects between unscattered and backscattered atoms in the scattering process, resulting from the indistinguishability of the particles. The backscattered atoms result from collision processes, where the atoms exchange exactly their momenta and subsequently move opposite to their original direction $\vec{q} = -\vec{p}$. When the particles are indistinguishable, this process cannot be distinguished from the original forward scattering in (7.9). The corrections due to the interference contains products of the SPDMs of the two colliding particles, where one term depends on their anticommutator and one term on their commutator.

The total crosssections of the interference terms depend on the imaginary part and on the real part of the T-matrix, respectively. They can be calculated to be $\sigma_{\text{ind}} = 4\pi a^2$ for the anticommutator term and $\tau_{\text{ind}} = 4\pi a/k$ for the commutator term. As the latter depends on the real part of the T-matrix, it arises in lower order than the other terms and should therefore play a dominant role in the scattering process, especially at small scattering lengths, where the lowest order Born approximation is the leading term. Its inverse dependence on the scattering momentum also reveals, that the commutator term is especially dominant for low densities, where small relative scattering momenta are typical. The commutator term in (7.10) is called the ISRE [281] and according to the above discussion dominates the interaction in the low density (small momenta) and weak interaction (small scattering length) regime.

Finally, it is very instructive to evaluate the spin dependence of the correction terms more closely, to understand which kind of initial states (7.5) are subject to them. Inspecting these terms in detail shows the following. First, if both fermions have the same spin state, the commutator vanishes, while the anticommutator cancels exactly the original scattering term (7.9). Due to Pauli blocking no interactions are possible at all, resulting from the indistinguishability of the atoms. Second, if both fermions have orthogonal spin states, both the anticommutator and the commutator vanish. This shows, that indistinguishable atoms in orthogonal polarizations scatter in the same way as distinguishable particles. No interference is possible for orthogonal states, similar to the case of orthogonally polarized photons. Third, for any completely incoherent state the commutator vanishes, since these states can be represented as a sum of pure orthogonal states. These special cases show, why no influence of the ISRE has been observed on the spin dynamics in chapter 6, where only orthogonally polarized states have been used.

In summary, in order to realize a system, where the ISRE is present, it is necessary to create particles with different, non-commuting SPDMs. For this, the introduction of coherences to the system is necessary, since for all pure and mixed states the ISRE vanishes as discussed above. The ISRE, while discussed here and in [281] only for two-component systems, should equally well dominate the physics of spinor Fermi gases in the weakly interacting regime. In this case, the interactions also include spin-dependent processes leading to, e.g., spin-changing collisions and require to include higher-order spin tensors for a complete description. Still, the fundamental excitations introduced by the ISRE should be spin waves, as in the two-component case.

7.2 HARMONICALLY CONFINED SPINOR FERMIONS

In this section, I discuss the physical system examined and the experimental procedure for spin waves in spinor Fermi gases. The system consists of an ultracold gas of ^{40}K atoms in the $f = 9/2$ hyperfine manifold, confined to a spin-independent optical dipole trap. Trapping frequencies are approximately $\omega_{(\mathrm{x,y,z})} = 2\pi \times (70, 74, 12)$ Hz with an aspect ratio of about 6. The corresponding trap depths are around 6 hkHz (vertically) and 90 hkHz (horizontally). The full system is described by the many-body Hamiltonian [289]

$$H = \int dr^3 \left[\sum_{\mathrm{ij}} \psi_{\mathrm{i}}^\dagger(\vec{r}) h_{\mathrm{ij}}(\vec{r}) \psi_{\mathrm{j}}(\vec{r}) + \sum_{\mathrm{ijkl}} \frac{g_{\mathrm{ijkl}}}{2} \psi_{\mathrm{i}}^\dagger(\vec{r}) \psi_{\mathrm{k}}^\dagger(\vec{r}) \psi_{\mathrm{l}}(\vec{r}) \psi_{\mathrm{j}}(\vec{r}) \right] , \tag{7.11}$$

where the kinetic energy and the external harmonic potential are included in the single-particle part

$$h_{\mathrm{ij}}(\vec{r}) = \left[-\frac{\hbar^2}{2m} \left(\partial_x^2 + \partial_y^2 + \partial_z^2 \right) + \frac{m}{2} \left(\omega_{\mathrm{x}}^2 x^2 + \omega_{\mathrm{y}}^2 y^2 + \omega_{\mathrm{z}}^2 z^2 \right) \right] \delta_{\mathrm{ij}} \, . \tag{7.12}$$

The Hamiltonian (7.11) includes an interaction term, which is characterized by the parameter $g_{\mathrm{ijkl}} = \frac{4\pi\hbar^2}{m} a_{\mathrm{ijkl}}$ using the spin-dependent s-wave scattering lengths as derived in section 6.1 for ^{40}K. The Hamiltonian is written in terms of the fermionic field operators $\psi_{\mathrm{i}}\,(x)$ ($\psi_{\mathrm{i}}^\dagger(x)$), which annihilate (create) a fermion at position x with magnetization i and obey the usual fermionic anticommutation relations.

In the elongated dipole trap, the interacting two-component mixture of the spin states $|1/2\rangle$ and $|-1/2\rangle$ is evaporatively cooled to temperatures of approximately $0.25\, T_{\mathrm{F}}$ and total particle numbers of about $N = 3.5 \times 10^5$. For the preparation of the initial $|1/2\rangle|-1/2\rangle$ mixture prior to the evaporation see chapter 6. Recall, that in such a mixture of two orthogonal spin states, the ISRE vanishes. It is very instructive for the following, to discuss, how this situation of many particles can be described in a SPDM picture. The realized fermionic quantum gas is a genuine many-body system. Assuming the system initially in the quantum mechanical ground state $|\Psi\rangle$, it can alternatively be described by the many-body density matrix $\rho_\Psi = |\Psi\rangle\langle\Psi|$, which contains all many-body correlations. However, as shown in the previous section, the only information necessary for the description of the ISRE are of single-particle nature, not relying on any many-body correlations in the initial state apart from the indistinguishability of the atoms. All single-particle information is encoded in the SPDM, as discussed in the preceding section.

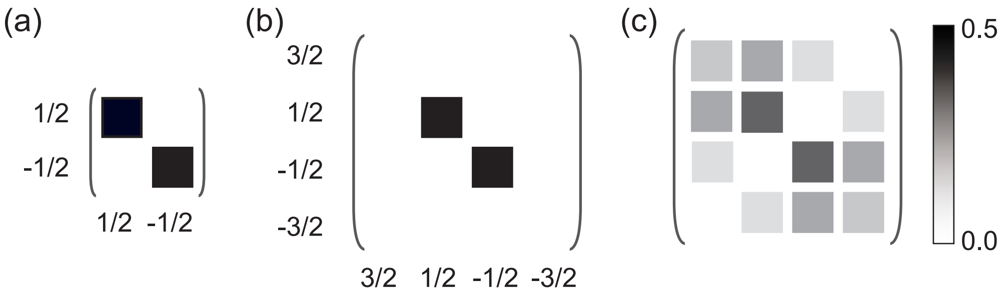

Figure 7.1: Single-particle density matrix in spin space. The shading represents the amplitude of the entries. The phase of the coherences is not captured in this representation. (a) Incoherent state for two internal degrees of freedom ($f=1/2$). (b) Same state as in (a), if the system has four spin degrees of freedom ($f=3/2$). (c) Rf rotation of (b), as discussed in appendix A.3, representing a coherent admixture of the states $|\pm 3/2\rangle$.

For a many-body system as described here, the SPDM can obviously not be defined as in (7.2). Instead, it is defined as the expectation value of all single-particle operators in a given representation with respect to the state of the system [273]. Using the field operator representation, the SPDM becomes

$$n_{\mathrm{ij}}(\vec{r},\vec{r}') = \left\langle \psi_{\mathrm{i}}^{\dagger}(\vec{r})\psi_{\mathrm{j}}(\vec{r}')\right\rangle_{\Psi} , \tag{7.13}$$

where the parentheses $\langle \ldots \rangle_{\Psi}$ denote the expectation value using the current many-body density matrix ρ_{Ψ} of the system. Equation (7.13) yields the definition (7.2), if $|\Psi\rangle$ describes only a single particle, and is therefore a reasonable generalization of the SPDM.

Applying (7.13) to the initial interacting two-component mixture, one obtains the SPDM

$$n(\vec{r},\vec{r}') = \tilde{n}(\vec{r},\vec{r}') \begin{pmatrix} 0.5 & 0 \\ 0 & 0.5 \end{pmatrix} , \tag{7.14}$$

where $\tilde{n}(\vec{r},\vec{r}')$ is the spatial density matrix of the gas including the spatial distribution $n(\vec{r}) = \tilde{n}(\vec{r},\vec{r})$ and the spatial correlations $\tilde{n}(\vec{r},\vec{r}' \neq \vec{r})$. The spin degrees of freedom are in a mixed state, corresponding to an *incoherent superposition* with respect to the *single-particle degrees of freedom*. As discussed in section 7.1, such a state is not subject to the ISRE, since it can be written as a superposition of orthogonal spin states. For a visualization of the SPDM in spin space, see Fig. 7.1(a).

To investigate spin waves in the spinor Fermi gas, which are driven by the ISRE, it is necessary to introduce single-particle spin coherences to the system. In addition, it is necessary that different particles have SPDMs that do not commute, such that the ISRE term acquires a finite value. To achieve this, a procedure was used, similar to earlier investigations of spin wave phenomena in $s=1/2$ [266, 269, 274]. The initially incoherent mixture is rotated in spin space using an rf pulse at low magnetic field, leading to an equal coupling between all pairs of spin states (see section 2.2). As shown in Fig. 2.6, this leads to a coherent admixture of the additional spin components $|\pm 3/2\rangle$, $|\pm 5/2\rangle$ and so forth. For the measurements presented in this chapter, the pulse area is chosen typically below 0.2π, corresponding to the regime where only the states $|\pm 1/2\rangle$ and $|\pm 3/2\rangle$ are populated. For this reason, the SDPM is restricted to this subspace in the following, corresponding to a pseudo $f=3/2$ spinor system. Figures 7.1(b) and (c) show the initial and the rotated SPDM for the typical initial state used in most of

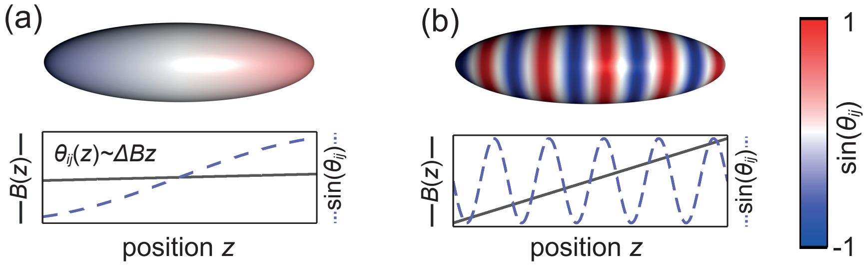

Figure 7.2: Sketch of the initial phase spiral for different magnetic field gradients. Shown is the relative phase θ_{ij} of the superposition of different spin states. Exemplary pictures of the phase change across the atomic cloud for (a) a small gradient of about $0.5\,\mathrm{G}$ and (b) a large gradient of about $5.0\,\mathrm{G}$ for the typical experimental parameters.

the following experiments. The pulse area for this state is about 0.145π, leading to populations of about $\rho_{\pm\frac{1}{2}} = 0.37$, $\rho_{\pm\frac{3}{2}} = 0.12$, and below 0.01 for all the higher spin states that are excluded from the discussion in the following. Another preparation scheme at larger magnetic fields has also been employed to investigate spin waves in imbalanced mixtures. This scheme is discussed below in direct connection with the corresponding measurements.

The rf pulse is homogeneous over the whole sample, such that the SPDMs of all particles commute. Hence, the state is still not subject to the ISRE. Therefore, in the second step, a spatially varying phase must be created in the coherences over the atomic cloud, such that the SPDMs for different positions do not commute anymore. In combination with the trap dynamics, which mixes particles from different positions, this leads to a non-vanishing ISRE and induces the spin waves [266, 269, 274]. The phase profile is imprinted using a magnetic gradient field switched on for a short time. In general a finite magnetic field strength B leads to a rotation of the phase of the coherences between different hyperfine states in the density matrix, due to the difference in internal Zeeman energy of both states. To first order this phase difference is proportional to the magnetic field strength and to the magnetization difference. The phase evolution follows the linear Zeeman energy as in (6.15)

$$n_{\mathrm{ij}}(\vec{r},\vec{r}') = |n_{\mathrm{ij}}(\vec{r},\vec{r}')| e^{-\mathrm{i} g_J \mu_{\mathrm{B}} (i-j) B t / 9\hbar} \,. \tag{7.15}$$

For a homogeneous magnetic field, the SPDM changes homogeneous over the whole sample and therefore the system stays in the same overall spin configuration, where the phase change can be gauged out.

By applying a magnetic field gradient to the sample for a finite time T, a spatially varying phase can be imprinted on the atomic distribution (see Fig. 7.2). Assuming a weak linear gradient field $B_{\mathrm{G}}(z) = \Delta B z$ in the linear Zeeman regime, the phase change also depends linearly on the position:

$$\theta_{\mathrm{ij}}(z) = \theta_{\mathrm{i}}(z) - \theta_{\mathrm{j}}(z) \propto (i-j)\Delta B z T \,. \tag{7.16}$$

This process creates different SPDMs at different positions in the trap, which do not commute with each other. As mentioned above, the following trap dynamics lead to mixing of particles from different positions, allowing the ISRE to influence the system and to induce the sought-for spin waves.

Since the spin waves constitute counterflow spin oscillations of the different spin states, they must be recorded spin-resolved. As discussed in section 2.1, the low trapping frequency in z-direction together with the Stern-Gerlach separation do not allow for a sufficient TOF to

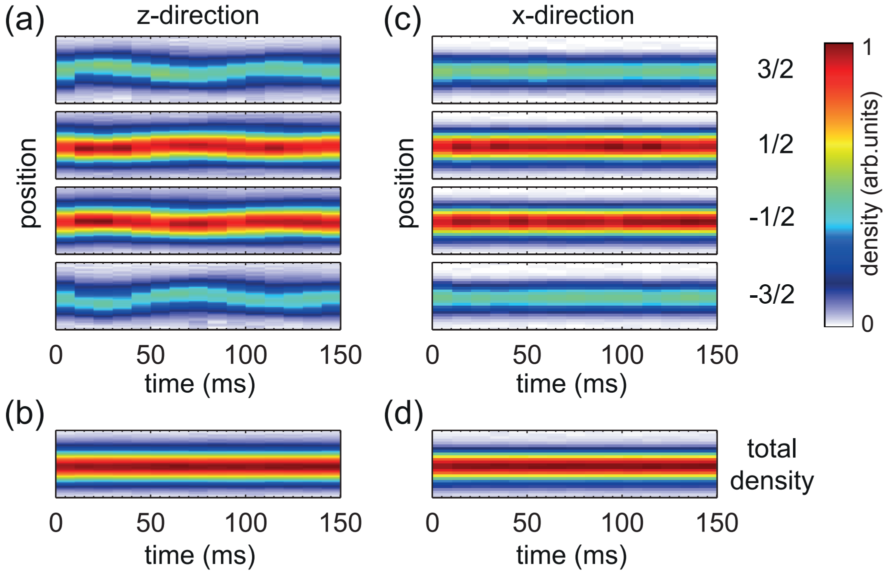

Figure 7.3: *In situ* measurement of spin waves in a pseudo $f = 3/2$ Fermi gas. (a) depicts the time evolution of the $|3/2\rangle$ to the $|-3/2\rangle$ component after a 10 ms magnetic field gradient pulse of $\Delta B = 3.4$ G/m along the z-direction. The particle number is $N = 1.8 \times 10^5$ and the temperature is $0.3\,T_\mathrm{F}$. Shown are the column densities along the z-direction at different times after the excitation. All four components oscillate in the excitation direction with a common frequency. The common oscillation frequency of all four components is about 10 Hz. (b) shows the total density of the system in the x-direction, remaining constant for all times, indicating the counterflow character of the spin wave. (c) and (d) show the corresponding results for the perpendicular x-direction. No oscillations of the different spin components are observable at all, proving the effective one-dimensional character of the excitation.

---

detect the momentum distribution properly, but rather a mixture of spatial and momentum degrees of freedom. As dipole oscillations are invariant under the Fourier transformation, which is introduced by the TOF, this method still allows for the detection of spin waves in the spatial dipole mode, while all higher spatial modes effectively average out. As shown below, the dipole oscillations, corresponding to oscillations of the atomic cloud in the trap, are the dominating spatial dynamics in the presented experiments and therefore the TOF method conserves the most important information faithfully.

An alternative detection method is *in-situ* absorption imaging, as also discussed in section 2.1. This allows for the direct detection of the spatial dynamics of all spin components. Since each component must be detected separately in a single experimental run this method increases the measurement time by a factor of 4 and even more for larger spins. Therefore, most of the measurements have been performed using a 18.5 ms TOF, revealing only the dominating spatial dipole oscillations, and only few measurements were performed using *in-situ* imaging to study certain aspects in the high-spin regime.

A typical *in situ* measurement of a spin wave in a four component, i.e. pseudo $f = 3/2$, system is shown in Fig. 7.3. The preparation of the coherent superposition is performed at 1.01 G, where the maximal difference between the transitions in the $f = 9/2$ manifold is 1.23 kHz. The rf pulse has a length of 20 μs, corresponding to a width of about 50 kHz, much broader than the transition differences, allowing for the simultaneous coupling of all spin states. As mentioned above, the pulse area is about 0.145π, creating population in the $m = \pm 3/2$ states only, resulting in an effective pseudo-spin $3/2$ system.

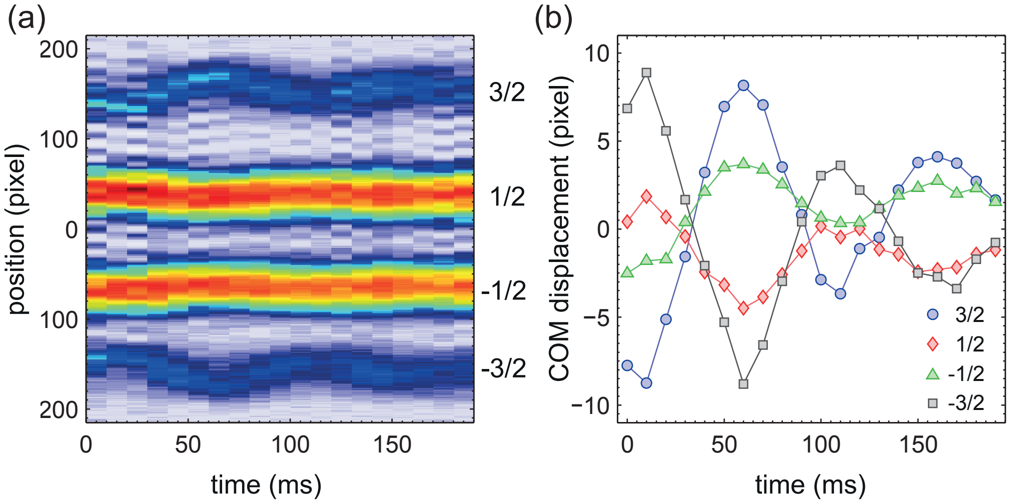

Figure 7.4: Typical spin wave observed after TOF of 18.5 ms for a magnetic field gradient of 3 G/m, a particle number of $N = 3.8\times10^5$ and a temperature of $0.25\,T_\mathrm{F}$. (a) Momentum resolved data for all four spin components. (b) Oscillation of the center-of-mass of all four components versus time. Solid lines connect the data as a guide to the eye.

The magnetic field gradient is aligned with the weak trapping direction, where $\omega_\mathrm{z} = 2\pi\times 12\,\mathrm{Hz}$. The results clearly show an oscillatory behavior in the z-direction, while the perpendicular directions are not affected. The observed oscillation frequency is about 10 Hz, which is in the order of the trapping frequency. This results in an energetical detuning of excitations in the different directions that prevents the coupling of the spin-wave excitation to the perpendicular directions. Starting from a directed magnetic field gradient in one direction, the system develops an effectively one-dimensional spin-wave excitation. The measurement presented in Fig. 7.3 also confirms the counterflow character of the spin-wave excitation, since the total density is constant during the whole evolution time. An indication of the complex spinor structure of the observed spin wave is given by the alternating oscillation direction of neighboring spin components. This behavior is a clear evidence for novel tensorial degrees of freedom, not present in conventional two-component systems as explained in section 7.4.

A typical data set for the detection after TOF is shown in Fig. 7.4. The preparation is completely identical to the *in situ* detection measurement. The results show, that the inversed oscillation direction is clearly observable also after TOF. The inverted oscillation directions are a result of an inverted magnetic field gradient in both measurements, effectively reversing the spin wave amplitude for each component.

7.3 MEAN-FIELD APPROXIMATION

Before turning to a detailed investigation of the spin-wave properties in dependence of the the excitation amplitude and the initial state, I discuss here a theoretical description for these systems, which allows for a deeper understanding of the spin wave dynamics.

Since the experiments are performed in a weakly interacting, low-density regime, a mean-field description of the system is a natural choice. In previous investigation of spin waves and related phenomena, the experimental results could be well described in a semiclassical mean-field theory (SMFT) based on a collisionless Boltzmann-equation [267, 268, 281]. In particular, the SMFT has been successfully applied to weakly interacting bosonic and fermionic systems with two-components [267, 268, 271, 272] and has been extended to $f = 1$ spinor bosons recently [286, 287]. In the spirit of this previous work, Ulrich Ebling, Andre Eckardt, and Maciej Lewenstein extended the SMFT to spinor Fermi gases [3]. In the following I give a short review of the derivation of this model. Later, I concentrate on its interpretation in terms of spherical tensor operators and discuss a linearized description. Finally, a comparison of experimental results with numerical calculations using this model, kindly provided by Ulrich Ebling, reveals an excellent agreement.

Recall, that the experiments have been carried out in an elongated dipole trap with an aspect ratio of about 6. For a fermionic quantum gas, this geometry does not allow for a complete one-dimensional description in general. However, since the spin-wave energy is in the order of the trapping frequency the coupling to transverse modes is strongly energetically inhibited, already for an aspect ration of 6, as evident from Fig. 7.3. Therefore, the transverse dimensions can be integrated out in the mean-field description, leading to effective one-dimensional equations of motion. These are the same as obtained from a pure one-dimensional treatment with appropriately normalized interaction parameters [289]. In the following, I discuss only the one-dimensional system for simplicity, while the normalized parameters have been used for all numerical calculations presented in this chapter.

The development of the SMFT contains several approximations [268, 273]:

I *Heisenberg equation of motion:* first, the time evolution of the SPDM must be defined in terms of the Heisenberg equation of motion.

II *Single-particle description:* the set of equations is reduced to a single-particle level, where all many-body correlations are neglected in the interaction part.

III *Wigner transformation:* a Wigner transformation is applied, creating a description in a semiclassical phase space of position z and momentum p.

IV *Truncated gradient expansion:* the equations of motion are simplified using a truncated gradient expansion to linear order.

I discuss these points step by step, following [268, 273]. The SPDM has been introduced above in (7.13). Following step I its Heisenberg equations of motion are given by [273]

$$\mathbb{i}\hbar\partial_t n_{\mathrm{ij}}(z,z') = \left\langle \left[\psi_{\mathrm{i}}^{\dagger}(z)\psi_{\mathrm{j}}(z'), H\right]\right\rangle \tag{7.17}$$

with a one-dimensional version of the Hamiltonian (7.11). This equation contains the full quantum dynamics of the system, which is reflected in the fact, that the right hand side of (7.17) contains terms of the form

$$\left\langle \psi_{\mathrm{i}}^{\dagger}(z)\psi_{\mathrm{j}}^{\dagger}(z)\psi_{\mathrm{k}}(z)\psi_{\mathrm{l}}(z)\right\rangle . \tag{7.18}$$

These terms are not part of the SPDM, but are rather included in the two-particle density matrix. Via these terms, (7.17) describes the influence of many-particle correlations onto the dynamics of the SPDM.

To obtain a full single-particle description as stated in step II, it is necessary to approximate the full equations of motion further, by reducing terms of the form (7.18) to products of SPDM elements as

$$\left\langle \psi_{\mathrm{i}}^{\dagger}\psi_{\mathrm{j}}^{\dagger}\psi_{\mathrm{k}}\psi_{\mathrm{l}}\right\rangle \approx \underbrace{\left\langle \psi_{\mathrm{i}}^{\dagger}\psi_{\mathrm{l}}\right\rangle \left\langle \psi_{\mathrm{j}}^{\dagger}\psi_{\mathrm{k}}\right\rangle}_{n_{\mathrm{il}}n_{\mathrm{jk}}} - \underbrace{\left\langle \psi_{\mathrm{i}}^{\dagger}\psi_{\mathrm{k}}\right\rangle \left\langle \psi_{\mathrm{j}}^{\dagger}\psi_{\mathrm{l}}\right\rangle}_{n_{\mathrm{ik}}n_{\mathrm{jl}}}, \tag{7.19}$$

where the minus sign reflects the fermionic anticommutator relations of the field operators. This substitution is a Hartree-Fock approximation, which is suitable for weak interactions and corresponds to neglecting many-particle correlations entirely [268, 273]. From the point of view of section 7.1, this approximation corresponds to a consideration of only forward scattering events described by (7.10) [268].

Inserting the decomposition (7.19) into (7.17) leads to equations of motion for the $n_{\mathrm{ij}}(z, z')$, which only depend on themselves. This creates a fully self-consistent single-particle description[2]

$$\mathrm{i}\hbar\partial_t n(z, z') = \left[n(z, z'), h(z)\right] + \left[n(z, z'), h^{\mathrm{mf}}(x)\right], \tag{7.20}$$

where the single-particle Hamiltonian $h(z)$ is only defined in one dimension, similar to the three-dimensional (7.12) and the mean-field potential resulting from the decomposed interaction term is given as

$$h_{\mathrm{ij}}^{\mathrm{mf}}(z) = \sum_{\mathrm{kl}} \left(g_{\mathrm{klji}} - g_{\mathrm{kijl}}\right) n_{\mathrm{kl}}(z, z). \tag{7.21}$$

In the effective single-particle equations of motion (7.20), the SPDM enters quadratically in the interaction term. Therefore, the self-consistent dynamics are governed by a nonlinear set of differential equations.

Inspecting equation (7.20), it appears to be highly nonlocal, since the SPDM is defined at two different positions simultaneously, including spatial correlations in this way. This unusual behavior can be elucidated by performing a Wigner transformation, as noted in step III, which leads to a description in a phase space of independent spatial and momentum variables z and p, similar to the description of particle and hole dynamics in chapter 5. The transformation is performed by applying [273]

$$W_{\mathrm{ij}}(z, p) = \frac{1}{2\pi\hbar} \int dy e^{-\mathrm{i}z'p/\hbar} n_{\mathrm{ij}}(z - z'/2, z + z'/2), \tag{7.22}$$

on the SPDM, projecting the spatial correlations onto the momentum variable p.

Applying the transformation onto the mean-field potential results in

$$V_{\mathrm{ij}}^{\mathrm{mf}}(z) = \int dp \sum_{\mathrm{kl}} \left(g_{\mathrm{klji}} - g_{\mathrm{kijl}}\right) W_{\mathrm{kl}}(z, p), \tag{7.23}$$

which depends only on the spatial distribution of the Wigner distribution, while an integral is performed to average over the momentum direction.

The equations of motion (7.21) transform to a complicated infinite series of gradient terms, acting on the potential and the mean-field term [273]. Truncating this series at a finite gradient order is a semiclassical approximation, excluding highly oscillating Wigner functions, and simplifies the equations of motion considerably. The truncation is performed to linear order, according to step IV. This describes the harmonic trapping exactly but neglects higher-order

---

[2] Note, that the commutators have to be applied with care in (7.20). They correctly describe the spin indices, however, since $h(z)$ is a differential operator, it always needs to be applied from the left onto $n(z, z')$.

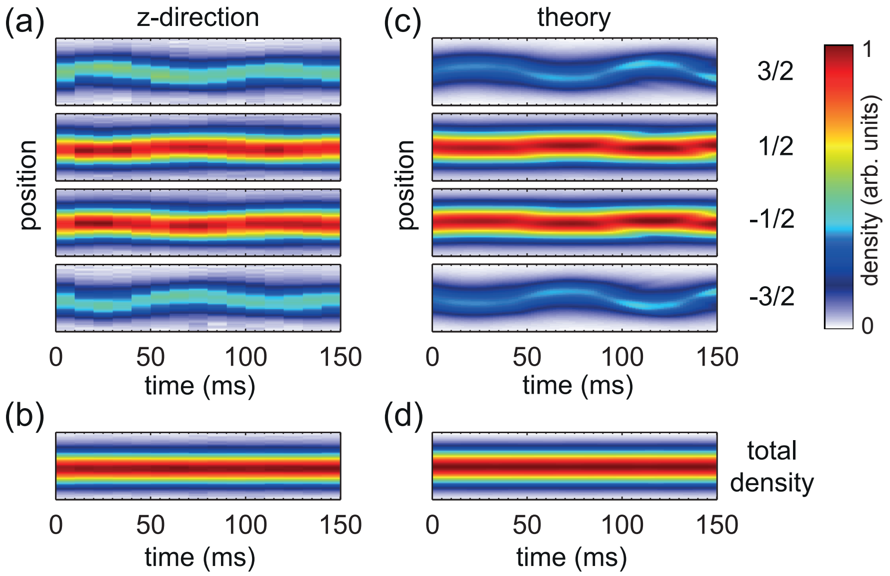

Figure 7.5: Comparison of theory and experiment for an *in situ* spin wave in a pseudo $f = 3/2$ Fermi gas. (a) and (b) depict the same data as (a) and (b) in Fig. 7.3. (c) and (d) show the corresponding results from the numerical calculation using (7.24), revealing an excellent agreement between theory and experiment. The calculations have been performed and the results were kindly provided by Ulrich Ebling.

---

mean-field terms. The truncated equations of motion read [273]

$$\begin{aligned}\partial_t W(z,p) = &\left(-\frac{p}{m}\partial_z + m\omega_z^2 z\partial_p\right) W(z,p)\\ &+ \frac{1}{\mathrm{i}\hbar}[W(z,p), V^{\mathrm{mf}}(z)]\\ &+ \frac{1}{2}\left\{\partial_p W(z,p), \partial_x V^{\mathrm{mf}}(z)\right\} .\end{aligned} \tag{7.24}$$

The first line of the right hand side in (7.24) corresponds to the single-particle part $h(z)$ of the Hamiltonian H. The commutator in the second line denotes the lowest-order interaction term from the gradient expansion, which is equivalent to the ISRE discussed in section 7.1, and is also given by the commutator term in (7.10) [268]. It dominates the interaction, if single-particle coherences allow for interference effects in the interaction process. The third line contains the first order interaction term from the gradient expansion and corresponds to the sum of the distinguishable interaction term (7.9) and the anticommutator in (7.10). Comparing the absolute values of the different terms for the typical parameter used in the presented experiments, the anticommutator is an order of magnitude smaller than the ISRE term. However, it is the dominating interaction term, if orthogonal states are prepared, such that no interference is possible.

The semiclassical equations of motion (7.24) describe the dynamics of the spinor Fermi gas. For a simulation of the observed spin waves, it is additionally necessary to define the initial state properly. Note, that the initial state prior the magnetic field gradient can be separated into spatial and spin degrees of freedom as $W(z,p) = f(z,p)\rho$. The spin part of the Wigner function can is described by a SPDM ρ, as discussed in section 7.2. The spatial part is a distribution function on the semiclassical phase space. For weak interactions, it can be approximated by

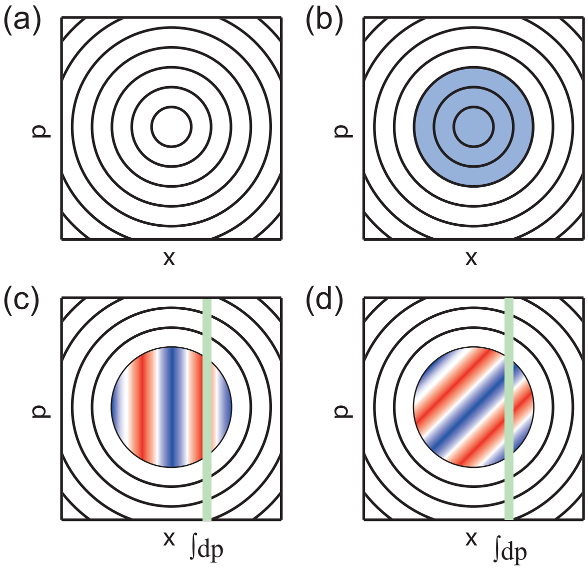

Figure 7.6: Phase space dynamics of the initial phase spiral. (a) Semiclassical phase space for a harmonically confined system. The quadratic momentum and position dependence of the kinetic and potential energy lead to concentric circles representing equal energy trajectories. (b) The initial state at $T = 0$ can be represented by a flat distribution with unity filling up to the Fermi energy. (c) The magnetic field gradient breaks the rotational symmetry of the initial state on the semiclassical phase space, by introducing a phase spiral along the spatial direction. The green shading depicts the integral of the momentum in the calculation of the mean-field potential. (d) The trap dynamics rotate the phase-space distribution. Thereby, the phase spiral is rotated with respect to the position axis and the mean-field potential acquires information about the phase distribution at neighboring positions.

the Thomas-Fermi distribution $f_{\mathrm{TF}}(\vec{r},\vec{p})$ of a non-interacting Fermi gas (see, e.g., [10, 118] and appendix A.2). At a total atom number N, each component consists of $N/2$ atoms and forms an independent Thomas-Fermi distribution. Therefore, the total density is given by twice the density $n_{\mathrm{TF}}(\vec{r}) = \int d^3p f_{\mathrm{TF}}(\vec{r},\vec{p})$ of a Thomas-Fermi distribution with $N/2$ atoms. Integrating over the two perpendicular spatial dimensions gives the correct initial Wigner function $W(z,p)$ in the one-dimensional description with a density $n(z) = \int dp f(z,p)$.

Using this initial state together with the proper SPDM in spin space, the experimentally observed dynamics, presented in Fig. 7.3, can be numerically simulated. The resulting dynamics are shown in Fig. 7.5, in comparison with the experimental data, demonstrating an excellent agreement.

The numerical calculations show, that the anticommutator term in the third row of the equations of motion (7.24) has only a very weak influence on the observed dynamics. The leading terms creating the observed spin waves are the ISRE term and the harmonic trap. This is expected, since the anticommutator term is much weaker than the ISRE for the parameter regime used in the experiment. While the anitcommutator term is kept in all further numerical results, it is neglected in the following for clarity in all analytical calculations.

The description of the Fermi gas in the Wigner function representation developed above is strongly connected to the semiclassical description of the harmonically confined lattice system in chapter 5. For the non-mean field terms, a similar phase space can be introduced using the variables z and p. Since no optical lattice is used in the present case, the equal energy trajectories in the harmonically confined system are simply concentric circles as depicted in Fig. 7.6 [273]. The initial state can be described as for the lattice system simply by a unity occupation up to the equal energy trajectory, corresponding to the Fermi energy. For this state, the commutator in (7.24) simply vanishes, since the mean-field interaction $V^{\mathrm{mf}}(z)$, which is obtained by integrating over the Wigner function in momentum space, is simply proportional to the local Wigner function $W(z,p)$, which has no relevant momentum structure.

If the magnetic field gradient is applied on the system, the resulting phase spiral breaks the position-momentum symmetry of the initial state. However, also in this state the commutator vanishes, since no momentum structure is present in the Wigner function and the mean field is still proportional to it at each position. Only the subsequent trap dynamics changes this situation, where the phase spiral is rotated with respect to the integration axis, breaking the direct proportionality between $V^{\mathrm{mf}}(z)$ and $W(z,p)$ for all momenta and positions. Thereby, the commutator in (7.24) becomes non-vanishing and the ISRE interactions affect the dynamics. The subsequent influence of the interaction leads to the spatial separation of the different spin states, creating a spin wave in the occupations of the density matrix.

7.4 SPIN-WAVE PROPERTIES

Figure 7.5 demonstrates, that the mean-field description introduced in the preceding section allows for a quantitative description of spinor Fermi gases. In this section, I compare experimental and theoretical results on spin waves in these systems for a wide range of parameters, from the linear to the nonlinear regime and for different initial states. To obtain an intuitive understanding of the underlying processes I introduce an alternative basis set, which conserves the rotational symmetry of the interaction.

7.4.1 THE SPHERICAL TENSOR DESCRIPTION AND NONLINEAR MODE COUPLING

While the mean-field equations of motion allow for a quantitatively correct description of the observed spin waves shown in Fig. 7.5, their representation in the form of (7.24) does not allow for an intuitive understanding of the novel features generated by the high spin of $f=3/2$ in the experiments. For this, it is beneficial to introduce another basis set for the description of the spin degree of freedom, which captures the intrinsic symmetries of the Hamiltonian (7.11) and therefore of the equations of motion (7.24). This should simplify the equations of motion (7.24) by emphasizing the dominating processes and couplings.

As discussed in section 6.1, the interaction of high spin-Fermi gases is rotationally symmetric in spin space. The same is true for the kinetic energy and the dipole trap potential in (7.11). Therefore, the minimal symmetry of the equations of motion (7.24) is this rotational symmetry. The natural basis for rotationally symmetric systems are the irreducible spherical tensors $T_{\mathrm{l}}^{\mathrm{m}}$ [129]. They are ordered by a total spin index $l=0,1,2,\ldots$, and a magnetization index $m=-l,\ldots,l$. Under rotation only tensors with the same total spin l and different m are mixed with each other, while there is no coupling between tensors with different l. The most well known examples of irreducible spherical tensors are the spherical harmonics $Y_{\mathrm{l}}^{\mathrm{m}}$ for spatial degrees of freedom. For internal spins, the unity matrix corresponds to the scalar tensor T_0^0. Another common example are the Pauli matrices for $f=1/2$, which constitute the spin vector $S=(\sigma_{\mathrm{x}},\sigma_{\mathrm{y}},\sigma_{\mathrm{z}})$ that corresponds to the three components of the $l=1$ tensor T_1^{m}.

A particle with spin $1/2$ is described by a two-by-two SPDM. The four operators T_0^0 and T_1^{m} are sufficient to describe all possible spin configurations in the form

$$\rho_{1/2}=\begin{pmatrix} c_0+c_{\mathrm{z}} & c_{\mathrm{x}}-\mathbb{i}c_{\mathrm{y}} \\ c_{\mathrm{x}}+\mathbb{i}c_{\mathrm{y}} & c_0-c_{\mathrm{z}} \end{pmatrix}=\underbrace{c_0\mathbb{1}}_{\text{scalar}}+\underbrace{c_{\mathrm{x}}\sigma_{\mathrm{x}}+c_{\mathrm{y}}\sigma_{\mathrm{y}}+c_{\mathrm{z}}\sigma_{\mathrm{z}}}_{\text{vector}}\,. \tag{7.25}$$

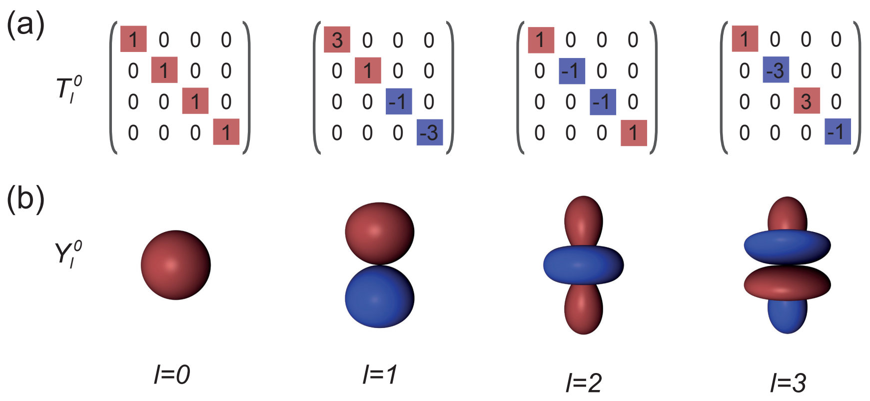

Figure 7.7: Irreducible spherical tensors for $f = 3/2$. (a) shows the tensors T_l^0 for $l = 0, 1, 2, 3$ in a $f = 3/2$ spin system. For comparison, (b) shows the spherical harmonics Y_l^0 depicted by equal potential orbits for positive (red) and negative (blue) values. The similar structure of both representations is clearly visible, being a direct consequence of the identical rotational properties.

The representation of the full density matrix with only the identity and the spin vector is no longer possible for systems with higher spins, which are discussed in this thesis. For these systems, higher-order tensors are required [129, 290]. For the particular case of $f = 3/2$, which is described by a four-by-four SPDM, the five nematic tensors T_2^m and the seven octupole tensors T_3^m must be included in the description. This results in a total of 16 basis elements and a decomposition of the SPDM in the form

$$\rho_{3/2} = \underbrace{c_0 T_0^0}_{\text{scalar}} + \underbrace{\sum_{\mathrm{m}=-1}^{1} c_1^\mathrm{m} T_1^m}_{\text{vector}} + \underbrace{\sum_{\mathrm{m}=-2}^{2} c_2^\mathrm{m} T_2^m}_{\text{nematic}} + \underbrace{\sum_{\mathrm{m}=-3}^{3} c_3^\mathrm{m} T_3^m}_{\text{octupole}} \,, \tag{7.26}$$

where the spherical tensors are normalized as

$$\mathrm{Tr}\left(T_\mathrm{l}^\mathrm{m} T_\mathrm{k}^\mathrm{n}\right) = \delta_\mathrm{lk}\delta_\mathrm{mn} \,. \tag{7.27}$$

Figure 7.7 shows the $m = 0$ components of the tensor basis for $f = 3/2$, corresponding to the diagonal terms of the SPDM and thus to the observable densities of the four spin components. A list of all tensors can be found in appendix A.5. In particular, the tensor T_0^0 accounts for the total density of the system and the tensor T_1^0 is proportional to the total magnetization. The tensors T_2^0 and T_3^0 are measures for the extended spin degrees of freedom imposed by the high spin. These nematic and octupole tensors are not present in conventional spin $1/2$ systems, as shown by (7.25). The tensors components with $m \neq 0$ correspond to the offdiagonal terms of the SPDM, that is, to the coherences.

The *in situ* measurements and numerical simulations in the spin-component basis, presented originally in Figs. 7.3 and 7.5, can be translated to the irreducible spherical tensor-basis. For given column density distributions $n_\mathrm{m}(z)$ the spatial distribution of the T_l^0 tensors can be calculated as

$$\left\langle T_\mathrm{l}^0(z)\right\rangle = \sum_{\mathrm{m}=-3/2}^{3/2} n_\mathrm{m}(z)\left(T_\mathrm{l}^0\right)_\mathrm{mm} \tag{7.28}$$

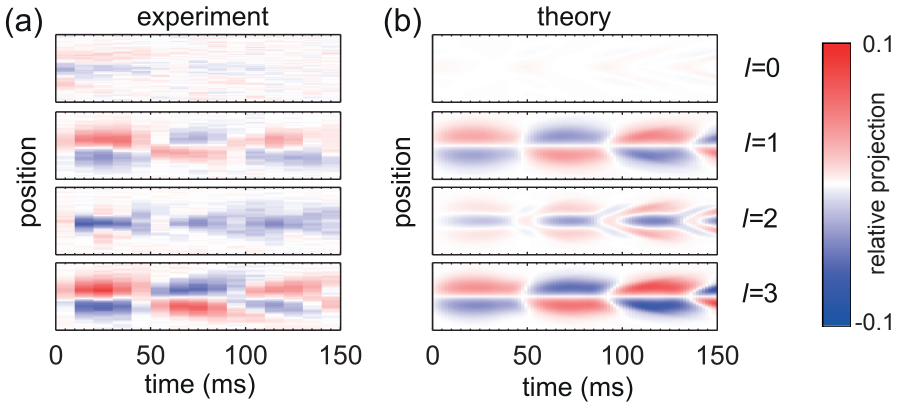

Figure 7.8: *In situ* spin-wave dynamics in the irreducible spherical tensor representation. (a) depicts the absolute variation of the tensors T_0^0 to T_3^0 from the initial state for the same data as in Fig. 7.3(a). T_0^0 corresponds to the total density, which is basically constant within the experimental resolution and shows no variations over time. T_1^0 and T_3^0 show clear dipole oscillations in the trap, while T_2^0 exhibits dominantly breathing dynamics. (b) shows the corresponding tensors from the numerical calculation already shown in Fig. 7.3(c), in very good agreement with the experiment. The projection amplitude is reported relative to the maximum of the total density of the system.

---

for each time step. Starting at $t = 0$ the initial state is exclusively composed of scalar and nematic components. This can be seen as follows: The initial incoherent superposition of $|1/2\rangle$ and $|-1/2\rangle$ is a pure superposition of T_0^0 and T_2^0 as

$$\begin{pmatrix} 0 & 0 & 0 & 0 \\ 0 & 0.5 & 0 & 0 \\ 0 & 0 & 0.5 & 0 \\ 0 & 0 & 0 & 0 \end{pmatrix} = \frac{1}{2} \underbrace{\begin{pmatrix} 0.5 & 0 & 0 & 0 \\ 0 & 0.5 & 0 & 0 \\ 0 & 0 & 0.5 & 0 \\ 0 & 0 & 0 & 0.5 \end{pmatrix}}_{T_0^0} + \frac{1}{2} \underbrace{\begin{pmatrix} -0.5 & 0 & 0 & 0 \\ 0 & 0.5 & 0 & 0 \\ 0 & 0 & 0.5 & 0 \\ 0 & 0 & 0 & -0.5 \end{pmatrix}}_{T_2^0}, \tag{7.29}$$

while the initial density $n(z)$, which is the same for both spin states, gives a smooth spatial envelope. This state is subsequently rotated in spin space using a resonant rf pulse. By definition, tensor components with different l do not mix during such a rotation. Therefore, the resulting state with single-particle coherences does also contain only the unique $l = 0$ tensor, describing the total density, and tensor components with $l = 2$. Since the rf-pulse is much faster than all spatial dynamics, the spatial envelope of the rotated state is the same common density distribution $n(z)$ as initially.

Figure 7.8 shows the dynamics of the initial nematic state in the irreducible spherical tensor basis. It is again visible, that the total density described by T_0^0 is constant for all times. The situation for the other three tensors is more complicated. The vector and the octupole component show essentially a dipole mode behavior, consistent with the oscillatory dynamics of the center-of-mass for all four spin components, shown in Fig. 7.3. In contrast, the nematic component shows clear breathing mode dynamics. This behavior is hidden in the spin component representation used in section 7.3. The complete absence of dipole oscillations in this component combined with the dominating coupling to the next higher spatial mode is very peculiar and suggests the presence of nonlinear mode coupling.

The numerical results evaluated in irreducible spherical tensor-basis show exactly the same

Spin index l	Combinations (l', l'')
0	
1	$(1,1)$, $(2,2)$, $(3,3)$
2	$(1,2)$, $(2,1)$, $(2,3)$, $(3,2)$
3	$(1,3)$, $(3,1)$, $(2,2)$, $(3,3)$

Table 7.1: Spin combinations (l', l'') that contribute directly to the time derivative of l in the semiclassical equations of motion (7.33).

behavior as the experimental data (see Fig. 7.8). Therefore, the intriguing difference of the spatial dynamics for different tensor components should be intuitively explainable within the equations of motion (7.24). For this, the spin parts of the Wigner function $W_{\rm ij}(z,p)$ and of the mean-field potential $V_{\rm ij}(z)$ must be rewritten in terms of the tensor basis. For the Wigner function this corresponds to a simple basis transformation

$$W_{\rm l}^{\rm m}(z,p) = \mathrm{Tr}\left(T_{\rm l}^{\rm m} W(z,p)\right) , \tag{7.30}$$

and the total Wigner function is given by

$$W(z,p) = \sum_{\rm l=0}^{3} \sum_{\rm m=-l}^{\rm l} W_{\rm l}^{\rm m}(z,p) T_{\rm l}^{\rm m} . \tag{7.31}$$

To transform the mean-field potential, the representation (7.30) must be inserted into (7.23), where the interaction tensor is applied onto the Wigner function. Remember, that the interaction is rotationally symmetric and therefore does not mix any tensors with different l, such that the mean-field components take the form

$$V_{\rm l}^{\rm m}(z,p) = \alpha_l \int dp W_{\rm l}^{\rm m}(z,p) , \tag{7.32}$$

with l-dependent scattering parameters α_l. As for the full two-particle interaction in section 6.1, the rotationally invariant interaction cannot depend on the magnetization of the state and therefore, the α_l cannot depend on the index m.

Inserting (7.30) and (7.32) into the mean-field equations of motion (7.24) and taking the equations of motion for each tensor component leads to[3]

$$\begin{aligned} \partial_t W_{\rm l}^{\rm m}(z,p) = & \left(-\frac{p}{m}\partial_z + m\omega_{\rm z}^2 z \partial_p\right) W_l^m(z,p) \\ & + \frac{1}{i\hbar} \sum_{l'l''} \sum_{m'm''} \alpha_{l''} \int dq W_{l''}^{m''}(z,q) W_{l'}^{m'}(z,p) \mathrm{Tr}\left(T_l^m \left[T_{l'}^{m'}, T_{l''}^{m''}\right]\right) . \end{aligned} \tag{7.33}$$

The symmetry properties of the interaction are encoded in the trace operation over three tensors in (7.33). Omitting the m-index, all combinations of total spins l' and l'', that contribute to the time evolution of the different l-components, are depicted in Tab. 7.1.

Certain combinations are forbidden by the addition rules for tensor operators, such as $l = 3$ and $l' = l'' = 1$. This is due to the Wigner-Eckart theorem [129] and corresponds to the usual

---

[3] Note, that the anticommutator term is neglected here, as discussed above, since it does not induce any qualitative and only very small quantitative changes.

addition rule for spins, that $|l'-l''| \leq l \leq |l'+l''|$. Other combinations are forbidden by time-reversal symmetry. As a general statement, irreducible spherical operators with even (odd) l also have an even (odd) parity under time reversal. In addition, the time derivative on the left hand side of (7.33) has an odd parity under time reversal. Since both sides of the equations of motion must have the same time-reversal parity, this restrict the possible scattering channels. Applying both restrictions on the scattering term in (7.33) leads to the same results as calculated from the trace in (7.33).

Inserting the results of Tab. 7.1 into (7.33), still omitting the m-index for simplicity, leads to the symbolic equations of motion

$$\begin{aligned}
\partial_t W_0 &\cong \partial_0 W_0\,,\\
\partial_t W_1 &\cong \partial_0 W_1 + \frac{1}{\mathbb{i}\hbar}\big([W_1,V_1]+[W_2,V_2]+[W_3,V_3]\big)\,,\\
\partial_t W_2 &\cong \partial_0 W_2 + \frac{1}{\mathbb{i}\hbar}\big([W_2,V_1+V_3]+[W_1+W_3,V_2]\big)\,,\\
\partial_t W_3 &\cong \partial_0 W_3 + \frac{1}{\mathbb{i}\hbar}\big([W_3,V_1]+[W_1,V_3]+[W_2,V_2]+[W_3,V_3]\big),
\end{aligned} \tag{7.34}$$

with the abbreviation $\partial_0 = (-p/m\partial_z + m\omega_z^2 z\partial_p)$.

From (7.34) one can easily understand the different behavior of the spin tensors in the dynamics shown in Fig. 7.8. Bear in mind, that the initial state for the observed dynamics is composed only of scalar $l=0$ and nematic $l=2$ components.

The time evolution of the scalar component in (7.34) depends only on itself. As the scalar component, representing the total density of the system, is given by the identity matrix and has no additional components, representing coherences, it is not affected by the phase spiral imprinted by the magnetic field. Therefore, the scalar component should not show any dynamics due to the spin-wave preparation as performed in the experiment. Note here, that the anticommutator term in (7.24) couples the $l=0$ component to the other components, possibly leading to small breathing dynamics of the total density in principle. Weak breathing dynamics in the $l=0$ component are indeed observable in the theoretical data shown in Fig. 7.8, however, the experimental resolution does not allow for a clear verification of the effect.

The equations of motion (7.34) also show, that the scalar component does not influence the dynamics of any other component via the commutator term of the interaction. As a result of this decoupling of the W_0 component, the dynamics are initially driven by the nematic component W_2 only. This results in a completely nematic mean-field V_2, due to the rotation symmetry of the interaction [see (7.32)]. Inspecting (7.34), the time derivative of the vector and octupole components W_1 and W_3 depend on a commutator of the form $[W_2,V_2]$ and therefore spin waves in these components are driven by the initial spin configuration. Since the excitation procedure via the magnetic field gradient creates a linear phase twist, this leads to dipole oscillations as visible in Fig. 7.8.

The equation of motion of the nematic component W_2 itself does not include a term of the form $[W_2,V_2]$, as would be necessary to support spin waves with the employed initial state. The absence of this term is a result of the time-reversal symmetry in the equations of motion. The observed spin-wave amplitude in the nematic component are therefore a higher-order effect, induced by interactions between the lowest-order spin waves in the vector and octupole components with the background. This nonlinear mode coupling leads to the breathing mode of the dynamics in the $l=2$ component.

Higher spatial modes can also be excited in two-component spin waves, using quadratic magnetic fields [266] or via nonlinear excitations as in the present case [291]. For the latter

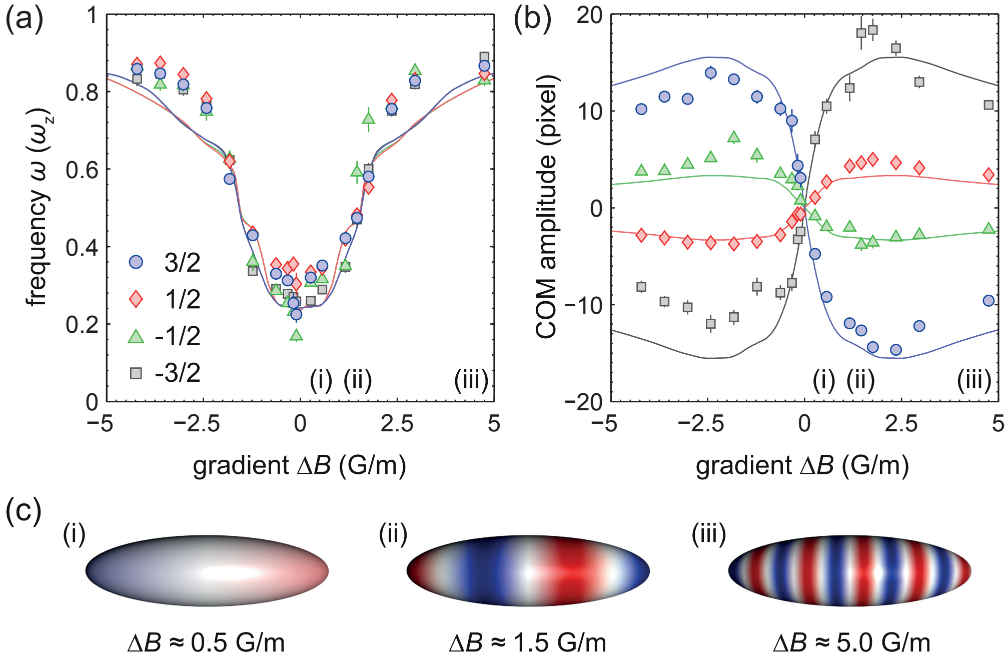

Figure 7.9: (a) Frequency and (b) oscillation amplitude of spin waves excited with different magnetic field gradients, recorded after a TOF of 18.5 ms. The particle numbers are $N = 3.8\times10^5$ and the temperature is $0.25\,T_\mathrm{F}$. Negative amplitudes denote an inverted initial direction. Experimental values are obtained as in Fig. 7.4 by fitting an exponentially damped cosine oscillation to the center-of-mass of each component. All error bars solely correspond to fit errors, representing one standard deviation. Solid lines are numerical data for each component showing the maximum of the first oscillation period, kindly provided by Ulrich Ebling. Since the experimental amplitudes are taken after TOF and the numerical amplitudes have been calculated *in situ*, both are rescaled onto each other by a global factor. (c) Sketch of the phase windings across the atom cloud for different gradient pulses, as indicated by the labels (i)-(iii) in (a) and (b).

case, the nonlinear mode coupling has only been observed indirectly via an amplitude dependence of the spin wave frequency. The direct observation of the higher spatial modes is difficult in this case, since all spatial modes have the same spin tensor $l = 1$. The linear decoupling of the nematic component in the presented high-spin system circumvents this and enables the direct observation of the mode coupling (Fig. 7.8).

7.4.2 NONLINEAR SPIN WAVES: DENSITY DEPENDENCE AND LINEARIZED DESCRIPTION

In the preceding section, I addressed the effect of nonlinear mode coupling on the spin-wave decomposition at large excitation amplitudes. In a different set of experiments, the amplitude and frequency behavior of the system was investigated in dependence on the initial phase gradient and on the density of the Fermi gas. The dynamics have been recorded after TOF for these measurements.

Figure 7.9 shows the results for multiple measurements similar to the data shown in Fig. 7.4, tuning the initial magnetic field gradient strength. This corresponds to a change of the initial phases θ_ij in the SPDM, while the initial coherence amplitudes $|W_\mathrm{ij}|$ are kept constant. The center-of-mass oscillations, as shown in Fig. 7.4, are fitted by exponentially decaying cosines, allowing for a determination of the oscillation amplitude and frequency. The numerical calculations reported in Fig. 7.9 are in good agreement with the experimental results. For small gradients, the frequency is amplitude independent and the amplitude rises approximately linearly with the gradient strength. At intermediate gradients, the system shows a strongly nonlinear behavior, driven by nonlinear mode coupling, as discussed above, which results in an amplitude-dependent oscillation frequency. This behavior has also been observed for spin waves in $f = 1/2$ Bose gases [291]. For large gradients, the frequency approaches the trapping frequency and is again only weakly dependent on the excitation amplitude.

The limiting regimes of small and large gradients can be understood on different grounds. I start here with the regime of small gradients. It corresponds to a weakly excited system, where only small spin-wave amplitudes are present and nonlinear mode coupling can be neglected. Consequently, the equations of motion can be linearized to describe the spin-wave dynamics in this regime. This ansatz is consistent with the observation, that the spin-wave amplitude rises linearly with the gradient field strength. It also matches with the amplitude independence of the frequency, which is expected in the linear regime. The resulting linearized spin waves are the fundamental low energy excitations of the system.

The linearization has been performed together with Ulrich Ebling using the method of moments [267], taking into account only spatial dipole oscillations, and is discussed in more detail in [3]. It results in an equation for the spin composition of the dipole spin-wave excitation given by

$$(\omega^2 - \omega_z^2)\delta\rho = 2\omega\omega_{\mathrm{mf}}\,[\rho, \delta\rho]\ , \tag{7.35}$$

where ω is the spin-wave frequency, determined by this equation, and ω_{mf} corresponds to the mean-field interaction strength given by

$$\omega_{\mathrm{mf}} = \frac{g}{2\hbar\langle p^2\rangle}\int dz \int dp\, p^2 f(z,p) n(z) \tag{7.36}$$

with

$$\langle p^2\rangle = \int dz \int dp\, p^2 f(z,p)\,. \tag{7.37}$$

For simplicity it is assumed in (7.35), that all scattering lengths $a_0, a_2, \ldots, a_8$ in ${}^{40}K$ are equal, taking their mean value $152\,a_{\mathrm{B}}$, which leads to a mean scattering parameter g in (7.36). The SPDM ρ is given by the initial state without any magnetic field gradient applied. The small perturbation $\delta\rho$ is the sought-after spin configuration, which constitutes the linearized spin-wave excitation. Solving (7.35) for $\delta\rho$ and ω corresponds to calculating an eigenvector of the commutator with the initial density matrix ρ according to

$$[\rho, \delta\rho] = \lambda\delta\rho \tag{7.38}$$

with the eigenvalue λ.

For the initial state used in the experiment the trivial eigenvalue $\lambda = 0$ and the eigenvalue $\lambda = 0.5$ are found. In the trivial case of $\lambda = 0$, the excitation is not influenced by the interaction and commutes with the mean-field term. The total oscillation frequency from (7.35) is in this case the trapping frequency $\omega = \omega_z$. In the other case, the excitation is interaction driven, and solving (7.35) leads to an oscillation frequency of

$$\omega = -\omega_{\mathrm{mf}} + \sqrt{\omega_{\mathrm{mf}}^2 + \omega_z^2}\,. \tag{7.39}$$

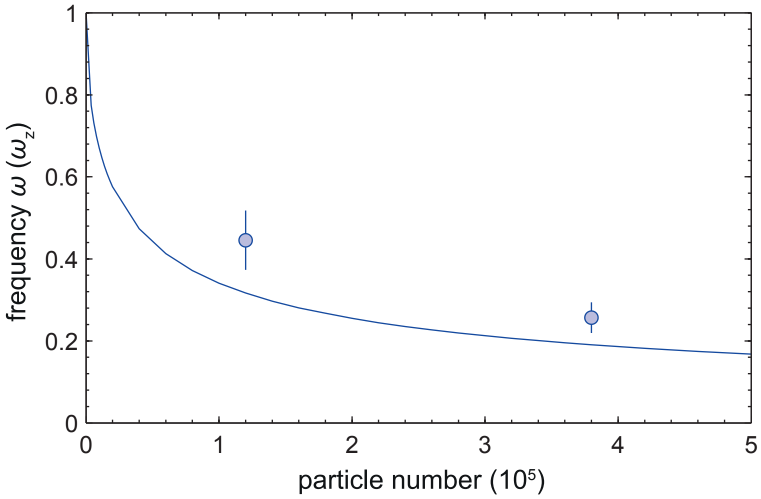

Figure 7.10: Spin-wave frequency for small magnetic field gradients in comparison with the linearized description (solid line) at different particle numbers. The calculation was performed using (7.39) with (7.36) for the different particle numbers. The errorbars show the standard deviation for the average over all four spin components.

The eigenvector solution corresponding to the frequency (7.39) is given by linear combination of the vector and octupole tensor only. This directly confirms the linear decoupling as discussed in connection with (7.34).

The spin-wave frequency in the low-gradient regime has been extracted for two measurements at different densities and is compare to the theoretical prediction in Fig. 7.10. The experimental results differ from the calculated results in the absolute value, but show the same trend as the calculation. Two main sources could lead to the disagreement between experiment and theory: First, the mean scattering parameter g used in (7.36) might change the result. However, the relative error introduced by this does not exceed 5% of the total interaction stength and is therefore considerably smaller than the observed shift. Second, the assumption of completely linear spin waves might not be correct. Possibly, the total interaction is already strong enough to excite higher spatial modes also at low gradients. Since the full theory reproduces the excitation frequency at small gradients very well, all other sources, like errors in the extraction of experimental parameters, can be excluded.

For large gradients, the frequency slowly approaches the trapping frequency. Numerical simulations show, that in this regime the phase spiral is averaged out dynamically on timescales much shorter than $2\pi/\omega_z$ [273], such that the mean-field potential no longer affects the subsequent oscillation. The interactions are so strong, that the original rotating phase spiral is destroyed quickly and the following random phase distribution averages the integral in the mean-field definition to zero for all later times.

7.4.3 CONTROLLING THE SPIN-WAVE DECOMPOSITION

Until here, all presented measurements have been performed with the same initial state prior to the application of the magnetic field gradient, which initializes the spin-wave dynamics. However, the versatile state preparation techniques for high-spin Fermi gases developed in this thesis allow for a full control over the SPDM, both for the occupations and the coherences.

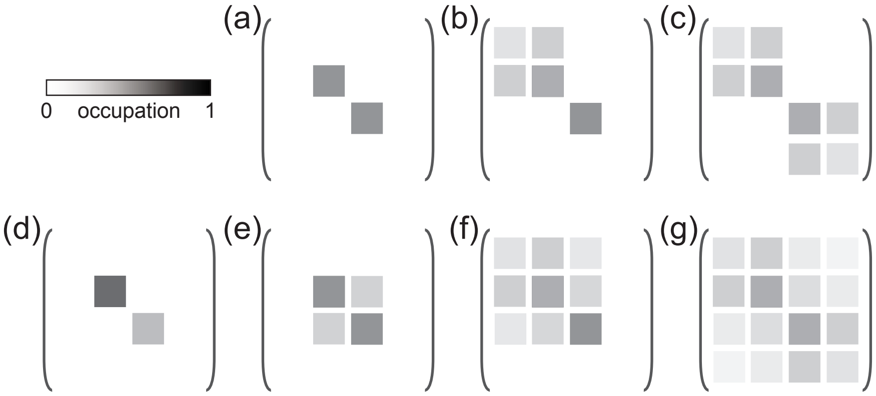

Figure 7.11: Sketch of the coherence preparation in the SPDM. The preparation for two different initial states with equal spin state occupations is shown. (a)-(c) show the preparation from an initially fully balanced incoherent state, while (d)-(g) show the preparation from an initially imbalanced incoherent state.

Therefore, also the multipole decomposition of the initial state can be fully controlled, which in turn affects the spin-wave characteristics via the l-dependent scattering processes in (7.34). In order to investigate the initial state dependence, a further set of experiments has been performed, where the initial state has been engineered, such that the population of all four spin components $|W_{\mathrm{ii}}|$ remains the same as in all experiments above, but the initial coherence amplitudes $|W_{\mathrm{ij}}|$ are changed. This investigation is complementary to the results shown in Fig. 7.9, where the phase θ_{ij} of the coherence was changed by using different gradient strengths, while the coherence amplitudes were kept constant.

A sketch of the preparation procedure is shown in Fig. 7.11. Note here, that the following experiments have been performed at larger magnetic fields of $11.8\,\mathrm{G}$, where the minimal transition difference between two pairs of states in the $f = 9/2$ manifold is about $20\,\mathrm{kHz}$. Using $200\,\mu\mathrm{s}$ rf pulses, corresponding to pulse widths of about $5\,\mathrm{kHz}$, all transitions between pairs of states $\{|m\rangle|m'\rangle\}$ can be addressed individually in this regime.

In a first step, a two-component mixture of the magnetization states $|1/2\rangle$ and $|-1/2\rangle$ is evaporatively prepared, corresponding to an incoherent superposition as before. In contrast to the measurements above, however, this incoherent mixture is not necessarily balanced. This allows the tuning of the coherences of the initial state for the spin-wave dynamics.

The preparation of coherences in an initially balanced mixture is shown in Fig. 7.11(a) to (c). After the incoherent mixture is created via evaporation, two rf pulses are performed, coupling the transitions from $|1/2\rangle$ to $|3/2\rangle$ and from $|-1/2\rangle$ and $|-3/2\rangle$ individually. The complete symmetry of the final state, as depicted in Fig. 7.11(c), shows, that the resulting state does not depend on the order of the pulses. The state created via this procedure is chosen such, that the relative occupations of the $|\pm1/2\rangle$ to the $|\pm3/2\rangle$ states is identical to the measurements performed at lower magnetic fields, presented earlier in this chapter.

To tune the spin waves, this preparation scheme is extended by one step. For this, instead of a completely balanced mixture, imbalanced mixtures of $|\pm1/2\rangle$ are evaporatively cooled initially. The particle numbers and temperatures achieved in this procedure are about the same as for the balanced mixture.

To end up with the same occupations after the full preparation procedure, an additional rf pulse is applied to the imbalanced mixture before the two other preparation pulses, as shown in

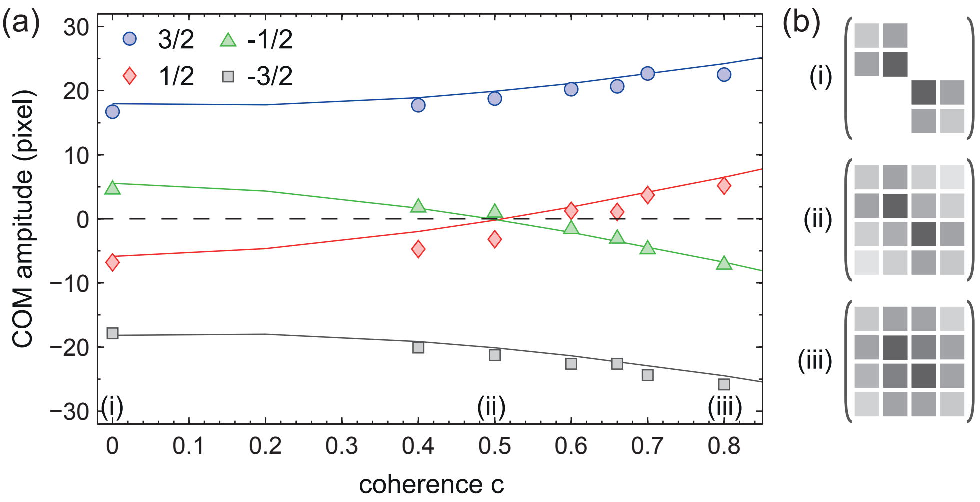

Figure 7.12: (a) Spatial oscillation amplitude of spin-wave excitations for different initial coherences at $\Delta B = 3.6\,\mathrm{G/m}$. The particle number is 3.6×10^5 and the typical temperature is about $0.2\,T_\mathrm{F}$. Solid lines show the initial spin-wave amplitude extracted from numerical calculations, kindly provided by Ulrich Ebling. The experimental amplitudes, which are taken after TOF, and the numerical amplitudes, calculated *in situ*, are rescaled onto each other by a global factor. (b) Typical SPDMs for different coherences c, as indicate by the labels (i)-(iii) in (a).

Fig. 7.11(d)-(g). The resulting state has equal populations in $|{\pm}1/2\rangle$, but also a finite coherence amplitude $\left|\rho'_{\frac{1}{2}-\frac{1}{2}}\right|$ between them. The value of this coherence depends on the initial imbalance. For a completely balanced mixture, it is zero, while for an initial single-component gas, it reaches its maximal value of 0.5.

More quantitatively, the size of the coherence $\rho'_{\frac{1}{2}-\frac{1}{2}}$ after the first rotation is proportional to the initial imbalance as

$$\left|\rho'_{\frac{1}{2}-\frac{1}{2}}\right| = \frac{1}{2}\left(\rho^\mathrm{I}_{\frac{1}{2}\frac{1}{2}} - \rho^\mathrm{I}_{-\frac{1}{2}-\frac{1}{2}}\right) , \tag{7.40}$$

where $\rho^\mathrm{I}_\mathrm{m,m}$ are the initial populations directly after the evaporation. The two additional rotations now do not only couple the occupations of the $|\pm 1/2\rangle$ states to the $|\pm 3/2\rangle$ states, but also their coherence amplitude, creating mutual coherences between all four states.

The coherence $\rho_{1/2-1/2}$ on the resulting state is a measure for the change of the spin-wave parameters due to the different preparation procedure. The ratio between this coherence and the occupation of the $|\pm 1/2\rangle$ states is an especially suggestive quantity, since it is strongly connected to the preparation scheme. Indeed, it is identical to the initial imbalance

$$c = \left|\frac{\rho_{\frac{1}{2}-\frac{1}{2}}}{\rho_{\frac{1}{2}\frac{1}{2}}}\right| = \rho^\mathrm{I}_{\frac{1}{2}\frac{1}{2}} - \rho^\mathrm{I}_{-\frac{1}{2}-\frac{1}{2}} . \tag{7.41}$$

Thus, the coherence amplitude can be easily changed in the presented preparation scheme, by tuning the initial imbalance in the evaporation. This procedure further extends the control over the multicomponent quantum gases, beyond the case of balanced mixtures. It demonstrates once again the unprecedented control achieved over the internal degrees of freedom of spinor Fermi gases in this work.

Figure 7.12 shows the experimentally determined oscillation amplitudes for different initial coherences in the spin-component representation. A comparison of experimental and numerical

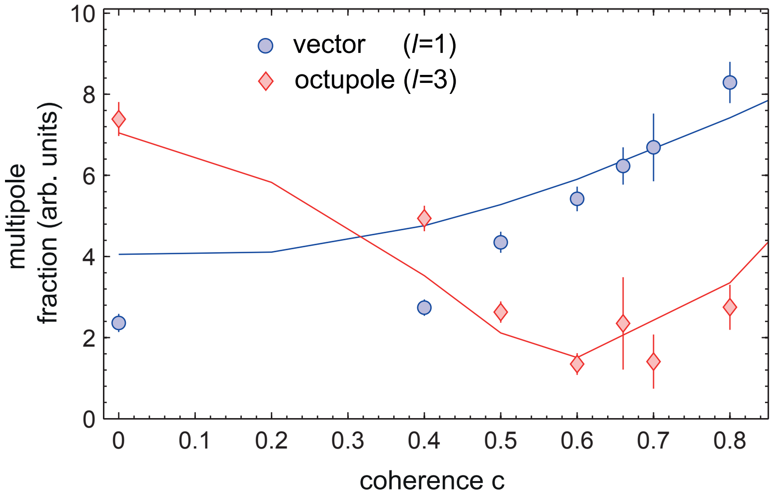

Figure 7.13: Vector and octupole fraction of spin-wave excitations for different initial coherences for the same data as in Fig. 7.12. Results are obtained as described in the text. Solid lines show the initial spin-wave amplitude extracted from numerical calculations, kindly provided by Ulrich Ebling. The experimental amplitudes, which are taken after TOF, and the numerical amplitudes, calculated *in situ*, are rescaled onto each other by a global factor. All error bars solely correspond to fit errors, representing one standard deviation.

data shows a very good agreement. An inspection of the oscillation amplitude reveals, that at the normalized coherence $c \approx 0.5$ the system changes its qualitative behavior, where the $|1/2\rangle$ and $|-1/2\rangle$ components interchange their oscillation direction. For large coherences c, the different spin states oscillate proportional to their magnetization sign, where the positive spins $|1/2\rangle$ and $|3/2\rangle$ have a positive and $|-1/2\rangle$ and $|-3/2\rangle$ have an initially negative oscillations direction. For $c < 0.5$, neighboring spin states have opposite oscillation directions.

The observed behavior in the spin-component representation can be recast into the irreducible tensor notation. Using this basis set, the dynamical properties at small and large coherences are easily elucidated. The magnetization dependent oscillation direction, as observed at large c, clearly indicates a spin-vector dominated spin-wave dynamics. For the opposite case of staggered oscillation amplitudes, realized at small c, the dominating spin-wave constituent is the octupole tensor T_3^0. Figure 7.13 shows an evaluation of the vector and octupole fraction for the same measurements as in Fig. 7.12. The results clearly support the above statement, that the spin wave changes its characteristic from octupole to vector dominated with increasing coherence c. Again the numerical calculations describe the engineered spin waves well.

From the above considerations, the octupole component shows a surprising behavior. While it behaves as expected for small and intermediate coherences, it shows an anew increase at large coherences, which is also captured by the numerical calculations, however. This apparently contradicts the increased vector character of the oscillations as observed in the spin component basis in Fig. 7.12. To resolve this contradiction, it is necessary to discuss the extraction procedure for the vector and octupole fraction in more detail.

The vector and octupole dynamics are obtained in the same way as for the in situ measurements [see (7.28)]. The only difference is that in the present measurements the Stern-Gerlach separation leads to displacement of the four spin components. This is compensated by an independent measurement of the positions of the atomic clouds at rest. By this, similar images as in

Fig. 7.8 are obtained for the different tensor components. To obtain a measure for the relative strength of the different tensor components, the absolute value of the tensor distributions for each time step is taken and the sum over the spatial coordinate leads to a single amplitude for each spin component for each time step. The resulting oscillatory dynamics of this value are fitted by an exponentially damped cosine to extract the oscillation amplitude for each tensor component, which is reported in Fig. 7.13.

Using this definition of the tensor fraction, the anew increase of the octupole amplitude at large c can be explained, as the spatial sum over the absolute value of the tensor distribution does not distinguish between different spatial excitations. The integral ads up all structures induced by higher-order spatial modes in the wave function, which can eventually dominate the results for the tensor fraction. In contrast, the center-of-mass oscillation amplitude can be unaffected from such structures in the density distribution resulting. Therefore, the observed increase is a result of the nonlinear mode coupling, as discussed above.

7.5 SUMMARY AND OUTLOOK

In conclusion, I have presented a thorough investigation of collective spin-wave excitations in a weakly interacting spinor Fermi gas. These results constitute the first experimental investigation of collective many-body dynamics of high-spin fermions. They also demonstrate the excellent control obtained on these systems, including the preparation and study of imbalanced Fermi gases.

The spin-wave dynamics is studied for a large set of parameters, ranging from the linear to the nonlinear regime. An intuitive description of the multicomponent spin waves on the basis of irreducible spherical tensors is worked out. Together with an especially adapted in-situ detection for multiple spin components, it allowed for the direct observation of nonlinear mode coupling at large excitation amplitudes. Beyond that, the excellent control over the initial spin composition achieved in this thesis allowed for a tuning of the spin-wave decomposition in a wide range of parameters. The experimental results are compared to numerical calculations using a semiclassical mean-field theory for high-spin Fermi gases, developed by Ulrich Ebling. The experimental results are very accurately described by this method for all investigated parameters, validating the theoretical approach for the description of the quantum degenerate regime.

The presented results pave the way towards novel schemes for spintronics in ultracold atomic gases, using the intrinsic high spin as a valuable resource [270]. The unprecedented control over the spinor Fermi gas also enables the study of different collective excitations, driven, e.g., by spin-changing collisions, as extensively studied in bosonic gases [89, 90, 92, 93, 292]. However, the existence and nature of such collective excitations purely in spin space is not *a priori* obvious for fermionic atoms and has not been observed until now. Studies of this topic are performed as of this writing at the BFM setup and will be discussed in [1, 114]. For the investigation of ground states in such high-spin systems, the tensor basis is especially suited, since it preserves the rotational symmetry of the interaction. In particular, for $s = 3/2$ systems, an extended interaction symmetry has been predicted [101, 280], which should result in a degeneracy of the vector and the octupole tensor interaction, which should be observable in this representation.

Many theoretical investigations on multicomponent systems aim for pairing in attractively interacting Fermi gases [98–102]. This is not directly possible in ^{40}K, using multiple components. However, using an optical lattice, an effectively attractive interaction for *all* spin components could be realized [293], using negative temperatures, recently observed for bosonic atoms [294]. In combination with the excellent control over the ^{40}K spinor gas, this might give access to intriguing regimes of paired states with high spin.

APPENDIX A

ADDITIONAL CALCULATIONS

This appendix contains some additional detailed information on calculations performed in the main part of the thesis.

A.1 FUNDAMENTAL CONSTANTS

common name	abbreviation	value
Speed of light	c	$2.99792458\times10^{8}\,\mathrm{m}\cdot\mathrm{s}^{-1}$
Vacuum permittivity	ϵ_0	$8.8541878\times10^{-12}\,\mathrm{F}\cdot\mathrm{m}^{-1}$
Elementary charge	e	$1.6021773\times10^{-19}\,\mathrm{C}$
Planck constant	h	$6.6260755\times10^{-34}\,\mathrm{J}\cdot\mathrm{s}$
Planck constant (reduced)	$\hbar$	$1.0545887\times10^{-34}\,\mathrm{J}\cdot\mathrm{s}$
Electron mass	m_e	$9.1093897\times10^{-31}\,\mathrm{kg}$
Boltzmann constant	k_B	$1.380658\times10^{-23}\,\mathrm{J}\cdot\mathrm{K}^{-1}$
Atomic mass unit	u	$1.6605387\times10^{-27}\,\mathrm{kg}$
Gravity of Earth (Hamburg)	g	$9.813749\,\mathrm{m}\cdot\mathrm{s}^{-2}$
Bohr radius	a_B	$5.2917721\times10^{-11}\,\mathrm{m}$
Bohr magneton	μ_B	$9.27400915\times10^{-24}\,\mathrm{J}\cdot\mathrm{T}^{-1}$

Table A.1: Fundamental constants in the International System of Units [295], as used in this thesis. The atomic properties of ^{87}Rb and ^{40}K as used in all calculations can be found in [126] and [134] and in the references therein.

A.2 HARMONICALLY TRAPPED FERMI GASES

The Fermi energy of a harmonically trapped Fermi gas is [10, 124]

$$E_\mathrm{F} = \hbar(6\omega_\mathrm{x}\omega_\mathrm{y}\omega_\mathrm{z}N)^{1/3}\,, \tag{A.1}$$

where N is the particle number. With the Fermi energy, the Fermi temperature is given by $T_\mathrm{F} = E_\mathrm{F}/k_\mathrm{B}$.

The Thomas-Fermi distribution of a trapped Fermi gas in a general potential V at finite temperature T is [10, 124]

$$f_{\mathrm{TF}}(\vec{r},\vec{p}) = \frac{1}{(2\pi\hbar)^3}\left(\mathrm{Exp}\left[\frac{1}{k_{\mathrm{B}}T}\left\{\frac{p_{\mathrm{x}}^2+p_{\mathrm{y}}^2+p_{\mathrm{z}}^2}{2m}+V(\vec{r})-\mu\right\}\right]+1\right)^{-1}, \tag{A.2}$$

with the chemical potential μ, which coincides with the Fermi energy at zero temperature.

A.3 MULTICOMPONENT SPIN TRANSFER

As shown in chapter 2, very short rf pulses can be used to couple all spin states of a single hyperfine manifold with spin f, if the magnetic field is sufficiently low. For the theoretical description of this situation it is important, that rf radiation can only couple states with a magnetization difference $\Delta m = 1$. Since all spin states are coupled equally, the resulting transformation in spin space must be rotationally symmetric. Otherwise, different spin states would be distinguished by the process. The operators, which exactly induces this, a rotationally invariant change of the magnetization by ± 1, are the well known angular momentum operators $S_\pm$ for a given spin f. Together with S_0, they form the usual angular momentum algebra [129]. Since the rf pulse couples transitions in both directions, $\Delta m = \pm 1$, the correct operator acting on the atomic spin configuration must be given by

$$H = S_+ + e^{\mathrm{i}\phi} S_-\,, \tag{A.3}$$

where the phase ϕ is in general unknown, but also irrelevant, due tot he total rotation symmetry of the system. Therefore, it can be chosen without loss of generality to be $\phi = 0$ and the resulting rotation operator is

$$H = S_+ + S_- = 2S_{\mathrm{x}}\,, \tag{A.4}$$

being the spin-operator in the x-direction. A finite rotation of the spin state $|m\rangle$ of a single atom in the fully couped hyperfine manifold is therefore described by

$$|\theta\rangle = e^{-\mathrm{i}S_{\mathrm{x}}\theta/2}|m\rangle\,. \tag{A.5}$$

Here the θ is the rotation angle shown in the abscissa in Fig. 2.6. The factor of two is required in the exponent, such that a full rotation, coming back to the initial state, is obtained at an angle $\theta = 2\pi$.

As discussed in chapter 7, the initial state in Fig. 2.6 is not a pure state, but an incoherent state, if only single-particle information are considered. This can be described by a SPDM ρ. The generalization of (A.5) to SDPMs is straightforward and is obtained in the usual way by

$$\rho_\theta = e^{-\mathrm{i}S_{\mathrm{x}}\theta/2}\rho e^{\mathrm{i}S_{\mathrm{x}}\theta/2}\,. \tag{A.6}$$

A.4 MODELING OF PARTICLE AND HOLE EXCITATIONS

To model the observed dynamics in the photoconductivity measurements of chapter 5, it is necessary to define a proper initial state for the dynamics. In the experiment, the ideal situation of a single particle excitation with a sharp momentum is not perfectly realized. Instead, the 1 ms lattice amplitude modulation pulse has a finite energy resolution, which consequently induces a finite momentum width of the excitations.

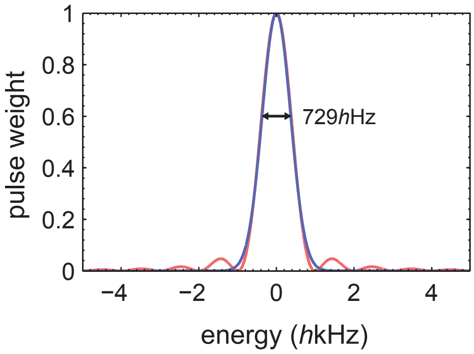

Figure A.1: Energy-shape of the lattice amplitude modulation pulse. The pulse of 1 ms lattice amplitude modulation induces a the usual sinc-response with additional maxima in the wings (red). A Gaussian distribution is fitted to the main peak of the sinc, leading to a total width at $e^{-1/2}$ amplitude of 729 Hz (blue).

Since a full simulation of the time-dependent excitation process is beyond the scope of this work, I follow a time-dependent perturbation theory approach. The excitation is created by a 1 ms square pulse of lattice amplitude modulation. The corresponding energy-shape is given by the usual sinc response [129]

$$S(\nu) \propto \left(\frac{1}{\nu_0 - \nu}\right)^2 \sin(\nu_0 - \nu)^2 \tag{A.7}$$

This form is relatively complicated with additional peaks in the wings. To keep the simulations as simple as possible, a Gaussian

$$G(\nu) \propto \mathrm{Exp}\left[-\frac{1}{2}\left(\frac{\nu_0 - \nu}{\Delta\nu}\right)^2\right] \tag{A.8}$$

is fitted to the energy response leading to a total width at $e^{-1/2}$ amplitude of $2\Delta\nu = 729$ Hz. The quality of this fit is depicted in Fig. A.1.

From the Gaussian energy distribution, the quasimomentum distribution of the excitation is obtained. For this, the energy difference between the two coupled bands is calculated for a homogeneous lattice. Using the local slope at the center of the excitation, a linearly dependence between quasimomentum and the excitation energy is assumed. This preserves the Gaussian form of the distribution, and results in (5.3), as used to simulate the experiment. The assumption of a linear slope does only work properly in the center of the band, between $q = 0$ and 1, where the dispersion doe not become flat. This might be the reason, why the numerical simulations do not properly work for very high and very low quasimomenta as noted in connection with Fig. 5.11.

A.5 TENSOR COMPONENTS FOR THE DESCRIPTION OF $f = 3/2$

In chapter 7, spin waves in an $f = 3/2$ Fermi gas are studied, using a basis set of irreducible spherical tensor operators [129]. This basis set is in general very well suited for the description of systems with rotationally invariant interactions, as realized in ultracold quantum gases.

For the specific case of $f = 3/2$, the basis set contains 16 elements, which can be grouped into four tensors with a effective spins $l = 0, 1, 2, 3$, each containing $2l + 1$ components. They are conveniently denoted by $T_{\mathrm{l}}^{\mathrm{m}}$. Under rotations, the different tensors do not mix, but only their individual components.

In this appendix, I denote all 16 components as they are used throughout this thesis. Thereby, the basis elements are assumed to be orthonormal with respect to the trace operation as

$$\mathrm{Tr}\left(T_{\mathrm{l}}^{\mathrm{m}} T_{\mathrm{k}}^{\mathrm{n}}\right) = \delta_{lk}\delta_{\mathrm{mn}}\,. \tag{A.9}$$

With this normalization, the scalar tensor component is given by [3]

$$T_0^0 = \frac{1}{2}\mathbb{1} = \frac{1}{2}\begin{pmatrix} 1 & 0 & 0 & 0 \\ 0 & 1 & 0 & 0 \\ 0 & 0 & 1 & 0 \\ 0 & 0 & 0 & 1 \end{pmatrix}, \tag{A.10}$$

the vector components are

$$T_1^0 = \sqrt{\tfrac{1}{5}} S_{\mathrm{z}} = \begin{pmatrix} \frac{3}{2} & 0 & 0 & 0 \\ 0 & \frac{1}{2} & 0 & 0 \\ 0 & 0 & -\frac{1}{2} & 0 \\ 0 & 0 & 0 & -\frac{3}{2} \end{pmatrix}, \tag{A.11}$$

$$T_1^1 = \sqrt{\tfrac{1}{5}} S_{\mathrm{x}} = \begin{pmatrix} 0 & \sqrt{\frac{3}{4}} & 0 & 0 \\ \sqrt{\frac{3}{4}} & 0 & 1 & 0 \\ 0 & 1 & 0 & \sqrt{\frac{3}{4}} \\ 0 & 0 & \sqrt{\frac{3}{4}} & 0 \end{pmatrix}, \tag{A.12}$$

$$T_1^2 = \sqrt{\tfrac{1}{5}} S_{\mathrm{y}} = \mathbb{i} \begin{pmatrix} 0 & -\sqrt{\frac{3}{4}} & 0 & 0 \\ \sqrt{\frac{3}{4}} & 0 & -1 & 0 \\ 0 & 1 & 0 & -\sqrt{\frac{3}{4}} \\ 0 & 0 & \sqrt{\frac{3}{4}} & 0 \end{pmatrix}, \tag{A.13}$$

the quadrupole components are given by

$$T_2^0 = \tfrac{1}{2}\left(S_z^2 - \tfrac{5}{4}\mathbb{1}\right), \tag{A.14}$$

$$T_2^1 = \tfrac{1}{2\sqrt{3}}\left(S_x^2 - S_y^2\right), \tag{A.15}$$

$$T_2^2 = \tfrac{1}{2\sqrt{3}}\left(S_x S_y + S_y S_x\right), \tag{A.16}$$

$$T_2^3 = \tfrac{1}{2\sqrt{3}}\left(S_z S_x + S_x S_z\right), \tag{A.17}$$

$$T_2^4 = \tfrac{1}{2\sqrt{3}}\left(S_y S_z + S_z S_y\right), \tag{A.18}$$

and the octupole components are

$$T_3^0 = \frac{\sqrt{5}}{3}\left(S_z^3 - \frac{41}{20}S_z\right), \tag{A.19}$$

$$T_3^1 = \frac{\sqrt{5}}{3}\left(S_x^3 - \frac{41}{20}S_x\right), \tag{A.20}$$

$$T_3^2 = \frac{\sqrt{5}}{3}\left(S_y^3 - \frac{41}{20}S_y\right), \tag{A.21}$$

$$T_3^3 = \frac{1}{2\sqrt{3}}\left\{S_x, S_y^2 - S_z^2\right\}, \tag{A.22}$$

$$T_3^4 = \frac{1}{2\sqrt{3}}\left\{S_y, S_z^2 - S_x^2\right\}, \tag{A.23}$$

$$T_3^5 = \frac{1}{2\sqrt{3}}\left\{S_z, S_x^2 - S_y^2\right\}, \tag{A.24}$$

$$T_3^6 = \frac{1}{\sqrt{3}}\left(S_x S_y S_z + S_z S_y S_x\right), \tag{A.25}$$

where $\{.,.\}$ denotes again the anticommutator.

BIBLIOGRAPHY

[1] J. S. Krauser, U. Ebling, N. Fläschner, J. Heinze, K. Sengstock, M. Lewenstein, A. Eckardt and C. Becker: "Giant Spin Oscillations in an Ultracold Fermi Sea", Science **343**, 157–160 (2014).

[2] O. Jürgensen, J. Heinze and D.-S. Lühmann: "Large-amplitude superexchange of high-spin fermions in optical lattices", New Journal of Physics **15**, 113017 (2013).

[3] J. Heinze, J. S. Krauser, N. Fläschner, K. Sengstock, C. Becker, U. Ebling, A. Eckardt and M. Lewenstein: "Engineering Spin Waves in a High-Spin Ultracold Fermi Gas", Phys. Rev. Lett. **110**, 250402 (2013).

[4] J. Heinze, J. S. Krauser, N. Fläschner, B. Hundt, S. Götze, A. P. Itin, L. Mathey, K. Sengstock and C. Becker: "Intrinsic Photoconductivity of Ultracold Fermions in Optical Lattices", Phys. Rev. Lett. **110**, 085302 (2013).

[5] J. S. Krauser, J. Heinze, N. Fläschner, S. Götze, O. Jürgensen, D.-S. Lühmann, C. Becker and K. Sengstock: "Coherent multi-flavour spin dynamics in a fermionic quantum gas", Nat. Phys. **8**, 813–818 (2012).

[6] J. Heinze, S. Götze, J. S. Krauser, B. Hundt, N. Fläschner, D.-S. Lühmann, C. Becker and K. Sengstock: "Multiband Spectroscopy of Ultracold Fermions: Observation of Reduced Tunneling in Attractive Bose-Fermi Mixtures", Phys. Rev. Lett. **107**, 135303 (2011).

[7] U. Bissbort, S. Götze, Y. Li, J. Heinze, J. S. Krauser, M. Weinberg, C. Becker, K. Sengstock and W. Hofstetter: "Detecting the Amplitude Mode of Strongly Interacting Lattice Bosons by Bragg Scattering", Phys. Rev. Lett. **106**, 205303 (2011).

[8] J. C. Maxwell: "On the dynamical theory of gases", Philos. Trans. Roy. Soc. Lond. for the year 1867 **CLVII**, 49–88 (1868).

[9] S. Weinberg: *The Quantum Theory of Fields*, Cambridge University Press (2005).

[10] L. Pitaevskii and S. Stringari: *Bose-Einstein Condensation*, Oxford University Press (2002).

[11] M. H. Anderson, J. R. Ensher, M. R. Matthews, C. E. Wieman and E. A. Cornell: "Observation of Bose-Einstein Condensation in a Dilute Atomic Vapor", Science **269**, 198–201 (1995).

[12] C. C. Bradley, C. A. Sackett, J. J. Tollett and R. G. Hulet: "Evidence of Bose-Einstein Condensation in an Atomic Gas with Attractive Interactions", Phys. Rev. Lett. **75**, 1687–1690 (1995).

[13] K. B. Davis, M. O. Mewes, M. R. Andrews, N. J. van Druten, D. S. Durfee, D. M. Kurn and W. Ketterle: "Bose-Einstein Condensation in a Gas of Sodium Atoms", Phys. Rev. Lett. **75**, 3969–3973 (1995).

[14] B. DeMarco and D. S. Jin: "Onset of Fermi Degeneracy in a Trapped Atomic Gas", Science **285**, 1703–1706 (1999).

[15] M. Lewenstein, A. Sanpera, V. Ahufinger, B. Damski, A. Sen(De) and U. Sen: "Ultracold atomic gases in optical lattices: mimicking condensed matter physics and beyond", Advances in Physics **56**, 243–379 (2007).

[16] I. Bloch, J. Dalibard and W. Zwerger: "Many-body physics with ultracold gases", Rev. Mod. Phys. **80**, 885–964 (2008).

[17] C. A. Regal, M. Greiner and D. S. Jin: "Observation of Resonance Condensation of Fermionic Atom Pairs", Phys. Rev. Lett. **92**, 040403 (2004).

[18] C. Chin, M. Bartenstein, A. Altmeyer, S. Riedl, S. Jochim, J. H. Denschlag and R. Grimm: "Observation of the Pairing Gap in a Strongly Interacting Fermi Gas", Science **305**, 1128–1130 (2004).

[19] G. B. Partridge, K. E. Strecker, R. I. Kamar, M. W. Jack and R. G. Hulet: "Molecular Probe of Pairing in the BEC-BCS Crossover", Phys. Rev. Lett. **95**, 020404 (2005).

[20] M. W. Zwierlein, J. R. Abo-Shaeer, A. Schirotzek, C. H. Schunck and W. Ketterle: "Vortices and superfluidity in a strongly interacting Fermi gas", Nature **435**, 1047–1051 (2005).

[21] D. Jaksch, C. Bruder, J. I. Cirac, C. W. Gardiner and P. Zoller: "Cold Bosonic Atoms in Optical Lattices", Phys. Rev. Lett. **81**, 3108–3111 (1998).

[22] M. Greiner, O. Mandel, T. Esslinger, T. W. Hänsch and I. Bloch: "Quantum phase transition from a superfluid to a Mott insulator in a gas of ultracold atoms", Nature **415**, 39–44 (2002).

[23] S. Ospelkaus, C. Ospelkaus, O. Wille, M. Succo, P. Ernst, K. Sengstock and K. Bongs: "Localization of Bosonic Atoms by Fermionic Impurities in a Three-Dimensional Optical Lattice", Phys. Rev. Lett. **96**, 180403 (2006).

[24] K. Günter, T. Stöferle, H. Moritz, M. Köhl and T. Esslinger: "Bose-Fermi Mixtures in a Three-Dimensional Optical Lattice", Phys. Rev. Lett. **96**, 180402 (2006).

[25] R. Jördens, N. Strohmaier, K. Günter, H. Moritz and T. Esslinger: "A Mott insulator of fermionic atoms in an optical lattice", Nature **455**, 204–207 (2008).

[26] U. Schneider, L. Hackermüller, S. Will, T. Best, I. Bloch, T. A. Costi, R. W. Helmes, D. Rasch and A. Rosch: "Metallic and Insulating Phases of Repulsively Interacting Fermions in a 3D Optical Lattice", Science **322**, 1520–1525 (2008).

[27] C. Becker, P. Soltan-Panahi, J. Kronjäger, S. Dörscher, K. Bongs and K. Sengstock: "Ultracold quantum gases in triangular optical lattices", New J. Phys. **12**, 065025 (2010).

[28] S. Sugawa, K. Inaba, S. Taie, R. Yamazaki, M. Yamashita and Y. Takahashi: "Interaction and filling-induced quantum phases of dual Mott insulators of bosons and fermions", Nat. Phys. **7**, 642–648 (2011).

[29] P. Soltan-Panahi, J. Struck, P. Hauke, A. Bick, W. Plenkers, G. Meineke, C. Becker, P. Windpassinger, M. Lewenstein and K. Sengstock: "Multi-component quantum gases in spin-dependent hexagonal lattices", Nat. Phys. **7**, 434–440 (2011).

[30] T. Kinoshita, T. Wenger and D. S. Weiss: "Observation of a One-Dimensional Tonks-Girardeau Gas", Science **305**, 1125–1128 (2004).

[31] N. Syassen, D. M. Bauer, M. Lettner, T. Volz, D. Dietze, J. J. García-Ripoll, J. I. Cirac, G. Rempe and S. Dürr: "Strong Dissipation Inhibits Losses and Induces Correlations in Cold Molecular Gases", Science **320**, 1329–1331 (2008).

[32] K. Baumann, C. Guerlin, F. Brennecke and T. Esslinger: "Dicke quantum phase transition with a superfluid gas in an optical cavity", Nature **464**, 1301–1306 (2010).

[33] H. Ott, E. de Mirandes, F. Ferlaino, G. Roati, V. Türck, G. Modugno and M. Inguscio: "Radio Frequency Selective Addressing of Localized Atoms in a Periodic Potential", Phys. Rev. Lett. **93**, 120407 (2004).

[34] T. Stöferle, H. Moritz, C. Schori, M. Köhl and T. Esslinger: "Transition from a Strongly Interacting 1D Superfluid to a Mott Insulator", Phys. Rev. Lett. **92**, 130403 (2004).

[35] D. Clément, N. Fabbri, L. Fallani, C. Fort and M. Inguscio: "Exploring Correlated 1D Bose Gases from the Superfluid to the Mott-Insulator State by Inelastic Light Scattering", Phys. Rev. Lett. **102**, 155301 (2009).

[36] P. T. Ernst, S. Götze, J. S. Krauser, K. Pyka, D.-S. Lühmann, D. Pfannkuche and K. Sengstock: "Probing superfluids in optical lattices by momentum-resolved Bragg spectroscopy", Nat. Phys. **6**, 56–61 (2010).

[37] N. Fabbri, S. D. Huber, D. Clément, L. Fallani, C. Fort, M. Inguscio and E. Altman: "Quasiparticle Dynamics in a Bose Insulator Probed by Interband Bragg Spectroscopy", Phys. Rev. Lett. **109**, 055301 (2012).

[38] J. Simon, W. S. Bakr, R. Ma, M. E. Tai, P. M. Preiss and M. Greiner: "Quantum simulation of antiferromagnetic spin chains in an optical lattice", Nature **472**, 307–312 (2011).

[39] J. Struck, C. Ölschläger, R. Le Targat, P. Soltan-Panahi, A. Eckardt, M. Lewenstein, P. Windpassinger and K. Sengstock: "Quantum Simulation of Frustrated Classical Magnetism in Triangular Optical Lattices", Science **333**, 996–999 (2011).

[40] D. Greif, T. Uehlinger, G. Jotzu, L. Tarruell and T. Esslinger: "Short-Range Quantum Magnetism of Ultracold Fermions in an Optical Lattice", Science **340**, 1307–1310 (2013).

[41] M. Aidelsburger, M. Atala, S. Nascimbène, S. Trotzky, Y.-A. Chen and I. Bloch: "Experimental Realization of Strong Effective Magnetic Fields in an Optical Lattice", Phys. Rev. Lett. **107**, 255301 (2011).

[42] K. Jiménez-García, L. J. LeBlanc, R. A. Williams, M. C. Beeler, A. R. Perry and I. B. Spielman: "Peierls Substitution in an Engineered Lattice Potential", Phys. Rev. Lett. **108**, 225303 (2012).

[43] J. Struck, C. Ölschläger, M. Weinberg, P. Hauke, J. Simonet, A. Eckardt, M. Lewenstein, K. Sengstock and P. Windpassinger: "Tunable Gauge Potential for Neutral and Spinless Particles in Driven Optical Lattices", Phys. Rev. Lett. **108**, 225304 (2012).

[44] L. W. Cheuk, A. T. Sommer, Z. Hadzibabic, T. Yefsah, W. S. Bakr and M. W. Zwierlein: "Spin-Injection Spectroscopy of a Spin-Orbit Coupled Fermi Gas", Phys. Rev. Lett. **109**, 095302 (2012).

[45] I. Bloch, J. Dalibard and S. Nascimbéne: "Quantum simulations with ultracold quantum gases", Nat. Phys. **8**, 267–276 (2011).

[46] M. Köhl, H. Moritz, T. Stöferle, K. Günter and T. Esslinger: "Fermionic Atoms in a Three Dimensional Optical Lattice: Observing Fermi Surfaces, Dynamics, and Interactions", Phys. Rev. Lett. **94**, 080403 (2005).

[47] L. Pezzè, L. Pitaevskii, A. Smerzi, S. Stringari, G. Modugno, E. de Mirandes, F. Ferlaino, H. Ott, G. Roati and M. Inguscio: "Insulating Behavior of a Trapped Ideal Fermi Gas", Phys. Rev. Lett. **93**, 120401 (2004).

[48] J. K. Chin, D. E. Miller, Y. Liu, C. Stan, W. Setiawan, C. Sanner, K. Xu and W. Ketterle: "Evidence for superfluidity of ultracold fermions in an optical lattice", Nature **443**, 961–964 (2006).

[49] T. Rom, T. Best, D. van Oosten, U. Schneider, S. Fölling, B. Paredes and I. Bloch: "Free fermion antibunching in a degenerate atomic Fermi gas released from an optical lattice", Nature **444**, 733–736 (2006).

[50] S. Taie, Y. Takasu, S. Sugawa, R. Yamazaki, T. Tsujimoto, R. Murakami and Y. Takahashi: "Realization of a $\mathrm{SU}(2) \times \mathrm{SU}(6)$ System of Fermions in a Cold Atomic Gas", Phys. Rev. Lett. **105**, 190401 (2010).

[51] S. Taie, R. Yamazaki, S. Sugawa and Y. Takahashi: "An $\mathrm{SU}(6)$ Mott insulator of an atomic Fermi gas realized by large-spin Pomeranchuk cooling", Nat. Phys. **8**, 825–830 (2012).

[52] U. Schneider, L. Hackermüller, J. P. Ronzheimer, S. Will, S. Braun, T. Best, I. Bloch, E. Demler, S. Mandt, D. Rasch and A. Rosch: "Fermionic transport and out-of-equilibrium dynamics in a homogeneous Hubbard model with ultracold atoms", Nat. Phys. **8**, 213–218 (2012).

[53] L. Tarruell, D. Greif, T. Uehlinger, G. Jotzu and T. Esslinger: "Creating, moving and merging Dirac points with a Fermi gas in a tunable honeycomb lattice", Nature **483**, 302–305 (2012).

[54] B. Yan, S. A. Moses, B. Gadway, J. P. Covey, K. R. A. Hazzard, A. M. Rey, D. S. Jin and J. Ye: "Realizing a lattice spin model with polar molecules", arXiv:1305.5598 (2013).

[55] C. Wu, D. Bergman, L. Balents and S. Das Sarma: "Flat Bands and Wigner Crystallization in the Honeycomb Optical Lattice", Phys. Rev. Lett. **99**, 070401 (2007).

[56] D.-S. Lühmann, K. Bongs, K. Sengstock and D. Pfannkuche: "Self-Trapping of Bosons and Fermions in Optical Lattices", Phys. Rev. Lett. **101**, 050402 (2008).

[57] A. Kantian, A. J. Daley, P. Törmä and P. Zoller: "Atomic lattice excitons: from condensates to crystals", New J. Phys. **9**, 407 (2007).

[58] K. Sun, W. V. Liu, A. Hemmerich and S. Das Sarma: "Topological semimetal in a fermionic optical lattice", Nat. Phys. **8**, 67–70 (2012).

[59] M. Iskin and C. A. R. Sá de Melo: "Two-band superfluidity from the BCS to the BEC limit", Phys. Rev. B **74**, 144517 (2006).

[60] R. B. Diener and T.-L. Ho: "Fermions in Optical Lattices Swept across Feshbach Resonances", Phys. Rev. Lett. **96**, 010402 (2006).

[61] M. Köhl: "Thermometry of fermionic atoms in an optical lattice", Phys. Rev. A **73**, 031601 (2006).

[62] A. F. Ho: "Fermions in optical lattices near a Feshbach resonance: From band insulator to Mott insulator", Phys. Rev. A **73**, 061601 (2006).

[63] H. G. Katzgraber, A. Esposito and M. Troyer: "Ramping fermions in optical lattices across a Feshbach resonance", Phys. Rev. A **74**, 043602 (2006).

[64] J.-P. Martikainen, E. Lundh and T. Paananen: "Interband physics in an ultracold Fermi gas in an optical lattice", Phys. Rev. A **78**, 023607 (2008).

[65] T. Higashiyama, K. Inaba and S.-I. Suga: "Superfluid-insulator transition of two-band fermionic atom systems in optical lattices", Journal of Physics: Conference Series **150**, 032098 (2009).

[66] D. S. Hall, M. R. Matthews, J. R. Ensher, C. E. Wieman and E. A. Cornell: "Dynamics of Component Separation in a Binary Mixture of Bose-Einstein Condensates", Phys. Rev. Lett. **81**, 1539–1542 (1998).

[67] J. Stenger, S. Inouye, D. M. Stamper-Kurn, H.-J. Miesner, A. P. Chikkatur and W. Ketterle: "Spin domains in ground-state Bose-Einstein condensates", Nature **396**, 345–348 (1998).

[68] A. G. Truscott, K. E. Strecker, W. I. McAlexander, G. B. Partridge and R. G. Hulet: "Observation of Fermi Pressure in a Gas of Trapped Atoms", Science **291**, 2570–2572 (2001).

[69] F. Schreck, L. Khaykovich, K. L. Corwin, G. Ferrari, T. Bourdel, J. Cubizolles and C. Salomon: "Quasipure Bose-Einstein Condensate Immersed in a Fermi Sea", Phys. Rev. Lett. **87**, 080403 (2001).

[70] Z. Hadzibabic, C. A. Stan, K. Dieckmann, S. Gupta, M. W. Zwierlein, A. Görlitz and W. Ketterle: "Two-Species Mixture of Quantum Degenerate Bose and Fermi Gases", Phys. Rev. Lett. **88**, 160401 (2002).

[71] G. Roati, F. Riboli, G. Modugno and M. Inguscio: "Fermi-Bose Quantum Degenerate ^{40}K-^{87}Rb Mixture with Attractive Interaction", Phys. Rev. Lett. **89**, 150403 (2002).

[72] G. Modugno, M. Modugno, F. Riboli, G. Roati and M. Inguscio: "Two Atomic Species Superfluid", Phys. Rev. Lett. **89**, 190404 (2002).

[73] T. Lompe, T. B. Ottenstein, F. Serwane, A. N. Wenz, G. Zürn and S. Jochim: "Radio-Frequency Association of Efimov Trimers", Science **330**, 940–944 (2010).

[74] S. Stellmer, R. Grimm and F. Schreck: "Detection and manipulation of nuclear spin states in fermionic strontium", Phys. Rev. A **84**, 043611 (2011).

[75] C. Ospelkaus, S. Ospelkaus, K. Sengstock and K. Bongs: "Interaction-Driven Dynamics of ^{40}K-^{87}Rb Fermion-Boson Gas Mixtures in the Large-Particle-Number Limit", Phys. Rev. Lett. **96**, 020401 (2006).

[76] T. Best, S. Will, U. Schneider, L. Hackermüller, D. van Oosten, I. Bloch and D.-S. Lühmann: "Role of Interactions in ^{87}Rb-^{40}**K** Bose-Fermi Mixtures in a 3D Optical Lattice", Phys. Rev. Lett. **102**, 030408 (2009).

[77] R. Roth and K. Burnett: "Quantum phases of atomic boson-fermion mixtures in optical lattices", Phys. Rev. A **69**, 021601 (2004).

[78] F. Illuminati and A. Albus: "High-Temperature Atomic Superfluidity in Lattice Bose-Fermi Mixtures", Phys. Rev. Lett. **93**, 090406 (2004).

[79] L. Mathey, D.-W. Wang, W. Hofstetter, M. D. Lukin and E. Demler: "Luttinger Liquid of Polarons in One-Dimensional Boson-Fermion Mixtures", Phys. Rev. Lett. **93**, 120404 (2004).

[80] D.-W. Wang, M. D. Lukin and E. Demler: "Engineering superfluidity in Bose-Fermi mixtures of ultracold atoms", Phys. Rev. A **72**, 051604 (2005).

[81] L. Pollet, M. Troyer, K. Van Houcke and S. M. A. Rombouts: "Phase Diagram of Bose-Fermi Mixtures in One-Dimensional Optical Lattices", Phys. Rev. Lett. **96**, 190402 (2006).

[82] M. Cramer, S. Ospelkaus, C. Ospelkaus, K. Bongs, K. Sengstock and J. Eisert: "Do Mixtures of Bosonic and Fermionic Atoms Adiabatically Heat Up in Optical Lattices?", Phys. Rev. Lett. **100**, 140409 (2008).

[83] A. Mering and M. Fleischhauer: "Multiband and nonlinear hopping corrections to the three-dimensional Bose-Fermi-Hubbard model", Phys. Rev. A **83**, 063630 (2011).

[84] M. Snoek, I. Titvinidze, I. Bloch and W. Hofstetter: "Effect of Interactions on Harmonically Confined Bose-Fermi Mixtures in Optical Lattices", Phys. Rev. Lett. **106**, 155301 (2011).

[85] O. Jürgensen, K. Sengstock and D.-S. Lühmann: "Density-induced processes in quantum gas mixtures in optical lattices", Phys. Rev. A **86**, 043623 (2012).

[86] T.-L. Ho: "Spinor Bose Condensates in Optical Traps", Phys. Rev. Lett. **81**, 742–745 (1998).

[87] C. K. Law, H. Pu and N. P. Bigelow: "Quantum Spins Mixing in Spinor Bose-Einstein Condensates", Phys. Rev. Lett. **81**, 5257–5261 (1998).

[88] T. Ohmi and K. Machida: "Bose-Einstein Condensation with Internal Degrees of Freedom in Alkali Atom Gases", J. Phys. Soc. Jpn. **67**, 1822–1825 (1998).

[89] H. Schmaljohann, M. Erhard, J. Kronjäger, M. Kottke, S. van Staa, L. Cacciapuoti, J. J. Arlt, K. Bongs and K. Sengstock: "Dynamics of $F = 2$ Spinor Bose-Einstein Condensates", Phys. Rev. Lett. **92**, 040402 (2004).

[90] M.-S. Chang, Q. Qin, W. Zhang, L. You and M. S. Chapman: "Coherent spinor dynamics in a spin-1 Bose condensate", Nat. Phys. **1**, 111–116 (2005).

[91] L. E. Sadler, J. M. Higbie, S. R. Leslie, M. Vengalattore and D. M. Stamper-Kurn: "Spontaneous symmetry breaking in a quenched ferromagnetic spinor Bose-Einstein condensate", Nature **443**, 312–315 (2006).

[92] J. Kronjäger, C. Becker, P. Navez, K. Bongs and K. Sengstock: "Magnetically Tuned Spin Dynamics Resonance", Phys. Rev. Lett. **97**, 110404 (2006).

[93] A. T. Black, E. Gomez, L. D. Turner, S. Jung and P. D. Lett: "Spinor Dynamics in an Antiferromagnetic Spin-1 Condensate", Phys. Rev. Lett. **99**, 070403 (2007).

[94] J. Kronjäger, C. Becker, P. Soltan-Panahi, K. Bongs and K. Sengstock: "Spontaneous Pattern Formation in an Antiferromagnetic Quantum Gas", Phys. Rev. Lett. **105**, 090402 (2010).

[95] C. Klempt, O. Topic, G. Gebreyesus, M. Scherer, T. Henninger, P. Hyllus, W. Ertmer, L. Santos and J. J. Arlt: "Parametric Amplification of Vacuum Fluctuations in a Spinor Condensate", Phys. Rev. Lett. **104**, 195303 (2010).

[96] B. Lücke, M. Scherer, J. Kruse, L. Pezzé, F. Deuretzbacher, P. Hyllus, O. Topic, J. Peise, W. Ertmer, J. Arlt, L. Santos, A. Smerzi and C. Klempt: "Twin Matter Waves for Interferometry Beyond the Classical Limit", Science **334**, 773–776 (2011).

[97] C. Gross, E. Strobel, H. Nicklas, T. Zibold, N. Bar-Gill, G. Kurizki and M. K. Oberthaler: "Atomic homodyne detection of continuous-variable entangled twin-atom states", Nature **480**, 219–223 (2011).

[98] Y. Dong and H. Pu: "Spin mixing in spinor Fermi gases", Phys. Rev. A **87**, 043610 (2013).

[99] P. Lecheminant, E. Boulat and P. Azaria: "Confinement and Superfluidity in One-Dimensional Degenerate Fermionic Cold Atoms", Phys. Rev. Lett. **95**, 240402 (2005).

[100] C. Wu: "Competing Orders in One-Dimensional Spin-$3/2$ Fermionic Systems", Phys. Rev. Lett. **95**, 266404 (2005).

[101] C. Wu, J.-p. Hu and S.-c. Zhang: "Exact SO(5) Symmetry in the Spin-3/2 Fermionic System", Phys. Rev. Lett. **91**, 186402 (2003).

[102] A. Rapp, G. Zaránd, C. Honerkamp and W. Hofstetter: "Color Superfluidity and "Baryon" Formation in Ultracold Fermions", Phys. Rev. Lett. **98**, 160405 (2007).

[103] N. Bornemann, P. Hyllus and L. Santos: "Resonant Spin-Changing Collisions in Spinor Fermi Gases", Phys. Rev. Lett. **100**, 205302 (2008).

[104] H.-H. Tu, G.-M. Zhang and L. Yu: "Spin-quadrupole ordering of spin-$\frac{3}{2}$ ultracold fermionic atoms in optical lattices in the one-band Hubbard model", Phys. Rev. B **74**, 174404 (2006).

[105] K. Rodríguez, A. Argüelles, M. Colomé-Tatché, T. Vekua and L. Santos: "Mott-Insulator Phases of Spin-3/2 Fermions in the Presence of Quadratic Zeeman Coupling", Phys. Rev. Lett. **105**, 050402 (2010).

[106] C. Honerkamp and W. Hofstetter: "Ultracold Fermions and the SU(N) Hubbard Model", Phys. Rev. Lett. **92**, 170403 (2004).

[107] M. Hermele, V. Gurarie and A. M. Rey: "Mott Insulators of Ultracold Fermionic Alkaline Earth Atoms: Underconstrained Magnetism and Chiral Spin Liquid", Phys. Rev. Lett. **103**, 135301 (2009).

[108] M. A. Cazalilla, A. F. Ho and M. Ueda: "Ultracold gases of ytterbium: ferromagnetism and Mott states in an SU(6) Fermi system", New J. Phys. **11**, 103033 (2009).

[109] A. V. Gorshkov, M. Hermele, V. Gurarie, C. Xu, P. S. Julienne, J. Ye, P. Zoller, E. Demler, M. D. Lukin and A. M. Rey: "Two-orbital SU(N) magnetism with ultracold alkaline-earth atoms", Nat. Phys. **6**, 289–295 (2010).

[110] M. Colomé-Tatché, C. Klempt, L. Santos and T. Vekua: "Adiabatic spin cooling using high-spin Fermi gases", New J. Phys. **13**, 113021 (2011).

[111] J. Jaramillo, S. Greschner and T. Vekua: "Magnetic field induced band insulator to Mott insulator transformations in 4-component alkali fermions at half-filling", arXiv:1305.0894 (2013).

[112] Z. Cai, H.-H. Hung, L. Wang, D. Zheng and C. Wu: "Pomeranchuk Cooling of SU($2N$) Ultracold Fermions in Optical Lattices", Phys. Rev. Lett. **110**, 220401 (2013).

[113] K. Inaba and S.-I. Suga: "Superfluid State of Repulsively Interacting Three-Component Fermionic Atoms in Optical Lattices", Phys. Rev. Lett. **108**, 255301 (2012).

[114] J. S. Krauser: Ph.D. thesis, to be published.

[115] S. Götze: Ph.D. thesis, to be published.

[116] N. Fläschner: "Higher Lattice Orbital Dynamics and Feshbach Resonances in Ultracold ^{40}K", Master's thesis (2011).

[117] S. Ospelkaus-Schwarzer: "Quantum Degenerate Fermi-Bose Mixtures of ^{40}K and ^{87}Rb in 3D Optical Lattices", Ph.D. thesis (2006).

[118] C. Ospelkaus: “Fermi-Bose mixtures - From mean-field interactions to ultracold chemistry”, Ph.D. thesis (2006).

[119] W. Ketterle, K. B. Davis, M. A. Joffe, A. Martin and D. E. Pritchard: “High densities of cold atoms in a *dark* spontaneous-force optical trap”, Phys. Rev. Lett. **70**, 2253–2256 (1993).

[120] C. J. Myatt, E. A. Burt, R. W. Ghrist, E. A. Cornell and C. E. Wieman: “Production of Two Overlapping Bose-Einstein Condensates by Sympathetic Cooling”, Phys. Rev. Lett. **78**, 586–589 (1997).

[121] N. Masuhara, J. M. Doyle, J. C. Sandberg, D. Kleppner, T. J. Greytak, H. F. Hess and G. P. Kochanski: “Evaporative Cooling of Spin-Polarized Atomic Hydrogen”, Phys. Rev. Lett. **61**, 935–938 (1988).

[122] W. Ketterle, D. Durfee and D. Stamper-Kurn: “Making, probing and understanding Bose-Einstein condensates”, in M. Inguscio, S. Stringari and C. Wieman (editors), “Bose-Einstein condensation in atomic gases, Proceedings of the International School of Physics "Enrico Fermi", Course CXL”, IOS Press, Amsterdam (1999).

[123] B. DeMarco, S. B. Papp and D. S. Jin: “Pauli Blocking of Collisions in a Quantum Degenerate Atomic Fermi Gas”, Phys. Rev. Lett. **86**, 5409–5412 (2001).

[124] B. DeMarco: “Quantum Behavior of an Atomic Fermi Gas”, Ph.D. thesis (1996).

[125] T. Weber, J. Herbig, M. Mark, H.-C. Nägerl and R. Grimm: “Bose-Einstein Condensation of Cesium”, Science **299**, 232–235 (2003).

[126] D. A. Steck: “Rubidium 87 D Line Data”, (2010).

[127] J. Kronjäger: “Coherent Dynamics of Spinor Bose-Einstein Condensates”, Ph.D. thesis (2007).

[128] C. Becker: “Multi component Bose-Einstein condensates From mean field physics to strong correlations”, Ph.D. thesis (2008).

[129] J. J. Sakurai: *Modern Quantum Mechanics*, Addison-Wesley Publishing Company, Inc., revised edition (1994).

[130] G. Breit and I. I. Rabi: “Measurement of Nuclear Spin”, Phys. Rev. **38**, 2082–2083 (1931).

[131] C. Zener: “Non-Adiabatic Crossing of Energy Levels”, Proceedings of the Royal Society of London. Series A **137**, 696–702 (1932).

[132] H. J. Metcalf and P. van der Straten: *Laser Cooling and Trapping,*, Springer (Heidelberg), 2nd edition (2002).

[133] R. Grimm, M. Weidemüller and Y. B. Ovchinnikov: “Optical Dipole Traps for Neutral Atoms”, in B. Bederson and H. Walther (editors), “Advances In Atomic, Molecular, and Optical Physics”, volume 42 of *Advances In Atomic, Molecular, and Optical Physics*, pages 95–170, Academic Press (2000).

[134] T. Tiecke: “Properties of Potassium”, (2010).

[135] A. L. Gaunt, T. F. Schmidutz, I. Gotlibovych, R. P. Smith and Z. Hadzibabic: “Bose-Einstein Condensation of Atoms in a Uniform Potential”, Phys. Rev. Lett. **110**, 200406 (2013).

[136] S. A. Self: “Focusing of spherical Gaussian beams”, Applied Optics **22**, 658–661 (1983).

[137] P.-A. Pantel, D. Davesne, S. Chiacchiera and M. Urban: “Trap anharmonicity and sloshing mode of a Fermi gas”, Phys. Rev. A **86**, 023635 (2012).

[138] P. Verkerk, B. Lounis, C. Salomon, C. Cohen-Tannoudji, J.-Y. Courtois and G. Grynberg: “Dynamics and spatial order of cold cesium atoms in a periodic optical potential”, Phys. Rev. Lett. **68**, 3861–3864 (1992).

[139] P. S. Jessen, C. Gerz, P. D. Lett, W. D. Phillips, S. L. Rolston, R. J. C. Spreeuw and C. I. Westbrook: “Observation of quantized motion of Rb atoms in an optical field”, Phys. Rev. Lett. **69**, 49–52 (1992).

[140] A. Hemmerich, C. Zimmermann and T. W. Hänsch: “Sub-kHz Rayleigh Resonance in a Cubic Atomic Crystal”, Europhys. Lett. **22**, 89 (1993).

[141] M. Weinberg: “Observation of the Amplitude Mode in Strongly Correlated Bose-Einstein Condensates”, Master’s thesis (2010).

[142] C. Kittel: *Introduction to Solid State Physics*, Wiley, New York, 8th edition (2004).

[143] S. R. Wilkinson, C. F. Bharucha, K. W. Madison, Q. Niu and M. G. Raizen: “Observation of Atomic Wannier-Stark Ladders in an Accelerating Optical Potential”, Phys. Rev. Lett. **76**, 4512–4515 (1996).

[144] J. Hubbard: “Electron Correlations in Narrow Energy Bands”, Proceedings of the Royal Society of London. Series A. Mathematical and Physical Sciences **276**, 238–257 (1963).

[145] D. Jaksch and P. Zoller: “The cold atom Hubbard toolbox”, Annals of Physics **315**, 52 – 79 (2005).

[146] G. H. Wannier: “The Structure of Electronic Excitation Levels in Insulating Crystals”, Phys. Rev. **52**, 191–197 (1937).

[147] B. DeMarco, J. L. Bohn, J. P. Burke, M. Holland and D. S. Jin: “Measurement of p-Wave Threshold Law Using Evaporatively Cooled Fermionic Atoms”, Phys. Rev. Lett. **82**, 4208–4211 (1999).

[148] F. Schwabel: *Advanced Quantum Mechanics*, Springer (Heidelberg), 4th edition (2008).

[149] M. Greiner, I. Bloch, O. Mandel, T. W. Hänsch and T. Esslinger: “Exploring Phase Coherence in a 2D Lattice of Bose-Einstein Condensates”, Phys. Rev. Lett. **87**, 160405 (2001).

[150] D. McKay, M. White and B. DeMarco: “Lattice thermodynamics for ultracold atoms”, Phys. Rev. A **79**, 063605 (2009).

[151] J. Weiner, V. S. Bagnato, S. Zilio and P. S. Julienne: "Experiments and theory in cold and ultracold collisions", Rev. Mod. Phys. **71**, 1–85 (1999).

[152] C. A. Regal and D. S. Jin: "Measurement of Positive and Negative Scattering Lengths in a Fermi Gas of Atoms", Phys. Rev. Lett. **90**, 230404 (2003).

[153] W. Hofstetter, J. I. Cirac, P. Zoller, E. Demler and M. D. Lukin: "High-Temperature Superfluidity of Fermionic Atoms in Optical Lattices", Phys. Rev. Lett. **89**, 220407 (2002).

[154] M. Rigol, A. Muramatsu, G. G. Batrouni and R. T. Scalettar: "Local Quantum Criticality in Confined Fermions on Optical Lattices", Phys. Rev. Lett. **91**, 130403 (2003).

[155] M. Egorov, B. Opanchuk, P. Drummond, B. V. Hall, P. Hannaford and A. I. Sidorov: "Measurement of s-wave scattering lengths in a two-component Bose-Einstein condensate", Phys. Rev. A **87**, 053614 (2013).

[156] G. K. Campbell, J. Mun, M. Boyd, P. Medley, A. E. Leanhardt, L. G. Marcassa, D. E. Pritchard and W. Ketterle: "Imaging the Mott Insulator Shells by Using Atomic Clock Shifts", Science **313**, 649–652 (2006).

[157] S. Fölling, A. Widera, T. Müller, F. Gerbier and I. Bloch: "Formation of Spatial Shell Structure in the Superfluid to Mott Insulator Transition", Phys. Rev. Lett. **97**, 060403 (2006).

[158] A. Albus, F. Illuminati and J. Eisert: "Mixtures of bosonic and fermionic atoms in optical lattices", Phys. Rev. A **68**, 023606 (2003).

[159] F. Ferlaino, C. D'Errico, G. Roati, M. Zaccanti, M. Inguscio, G. Modugno and A. Simoni: "Feshbach spectroscopy of a K-Rb atomic mixture", Phys. Rev. A **73**, 040702 (2006).

[160] F. Ferlaino, C. D'Errico, G. Roati, M. Zaccanti, M. Inguscio, G. Modugno and A. Simoni: "Erratum: Feshbach spectroscopy of a K-Rb atomic mixture [Phys. Rev. A 73, 040702 (2006)]", Phys. Rev. A **74**, 039903 (2006).

[161] L. Pollet, C. Kollath, U. Schollwöck and M. Troyer: "Mixture of bosonic and spin-polarized fermionic atoms in an optical lattice", Phys. Rev. A **77**, 023608 (2008).

[162] S. Will, T. Best, S. Braun, U. Schneider and I. Bloch: "Coherent Interaction of a Single Fermion with a Small Bosonic Field", Phys. Rev. Lett. **106**, 115305 (2011).

[163] J. Stenger, S. Inouye, A. P. Chikkatur, D. M. Stamper-Kurn, D. E. Pritchard and W. Ketterle: "Bragg Spectroscopy of a Bose-Einstein Condensate", Phys. Rev. Lett. **82**, 4569–4573 (1999).

[164] N. Fabbri, D. Clément, L. Fallani, C. Fort, M. Modugno, K. M. R. van der Stam and M. Inguscio: "Excitations of Bose-Einstein condensates in a one-dimensional periodic potential", Phys. Rev. A **79**, 043623 (2009).

[165] C. Marzok, B. Deh, S. Slama, C. Zimmermann and P. W. Courteille: "*In situ* Ramsey interferometry and diffraction echo with an atomic Fermi gas", Phys. Rev. A **78**, 021602 (2008).

[166] S. B. Papp, J. M. Pino, R. J. Wild, S. Ronen, C. E. Wieman, D. S. Jin and E. A. Cornell: "Bragg Spectroscopy of a Strongly Interacting ^{85}Rb Bose-Einstein Condensate", Phys. Rev. Lett. **101**, 135301 (2008).

[167] G. Veeravalli, E. Kuhnle, P. Dyke and C. J. Vale: "Bragg Spectroscopy of a Strongly Interacting Fermi Gas", Phys. Rev. Lett. **101**, 250403 (2008).

[168] J. T. Stewart, J. P. Gaebler and D. S. Jin: "Using photoemission spectroscopy to probe a strongly interacting Fermi gas", Nature **454**, 744–747 (2008).

[169] S. Friebel, C. D'Andrea, J. Walz, M. Weitz and T. W. Hänsch: "CO_2-laser optical lattice with cold rubidium atoms", Phys. Rev. A **57**, R20–R23 (1998).

[170] G. Roati, W. Jastrzebski, A. Simoni, G. Modugno and M. Inguscio: "Optical trapping of cold fermionic potassium for collisional studies", Phys. Rev. A **63**, 052709 (2001).

[171] R. Jáuregui, N. Poli, G. Roati and G. Modugno: "Anharmonic parametric excitation in optical lattices", Phys. Rev. A **64**, 033403 (2001).

[172] J. F. Sherson, S. J. Park, P. L. Pedersen, N. Winter, M. Gajdacz, S. Mai and J. Arlt: "The pump-probe coupling of matter wave packets to remote lattice states", New J. Phys. **14**, 083013 (2012).

[173] A. Damascelli: "Probing the Electronic Structure of Complex Systems by ARPES", Physica Scripta **2004**, 61 (2004).

[174] B. Hundt: "Momentum-Resolved Optical Lattice Modulation Spectroscopy on Bose-Fermi Mixtures", Master's thesis (2011).

[175] D. Clément, N. Fabbri, L. Fallani, C. Fort and M. Inguscio: "Multi-band spectroscopy of inhomogeneous Mott-insulator states of ultracold bosons", New J. Phys. **11**, 103030 (2009).

[176] D.-S. Lühmann, O. Jürgensen and K. Sengstock: "Multi-orbital and density-induced tunneling of bosons in optical lattices", New J. Phys. **14**, 033021 (2012).

[177] J. Hirsch: "Bond-charge repulsion and hole superconductivity", Physica C: Superconductivity **158**, 326 – 336 (1989).

[178] J. C. Amadon and J. E. Hirsch: "Metallic ferromagnetism in a single-band model: Effect of band filling and Coulomb interactions", Phys. Rev. B **54**, 6364–6375 (1996).

[179] O. Jürgensen: Private communication.

[180] B. DeMarco, C. Lannert, S. Vishveshwara and T.-C. Wei: "Structure and stability of Mott-insulator shells of bosons trapped in an optical lattice", Phys. Rev. A **71**, 063601 (2005).

[181] A. H. Castro Neto, F. Guinea, N. M. R. Peres, K. S. Novoselov and A. K. Geim: "The electronic properties of graphene", Rev. Mod. Phys. **81**, 109–162 (2009).

[182] A. K. Geim and K. S. Novoselov: "The rise of graphene", Nat. Mat. **6**, 183–191 (2007).

[183] U. Bissbort, F. Deuretzbacher and W. Hofstetter: "Effective multibody-induced tunneling and interactions in the Bose-Hubbard model of the lowest dressed band of an optical lattice", Phys. Rev. A **86**, 023617 (2012).

[184] K. Góral, L. Santos and M. Lewenstein: "Quantum Phases of Dipolar Bosons in Optical Lattices", Phys. Rev. Lett. **88**, 170406 (2002).

[185] P. R. Johnson, E. Tiesinga, J. V. Porto and C. J. Williams: "Effective three-body interactions of neutral bosons in optical lattices", New J. Phys. **11**, 093022 (2009).

[186] H. P. Büchler: "Microscopic Derivation of Hubbard Parameters for Cold Atomic Gases", Phys. Rev. Lett. **104**, 090402 (2010).

[187] S. Will, T. Best, U. Schneider, L. Hackermüller, D.-S. Lühmann and I. Bloch: "Time-resolved observation of coherent multi-body interactions in quantum phase revivals", Nature **465**, 197–201 (2010).

[188] M. J. Mark, E. Haller, K. Lauber, J. G. Danzl, A. J. Daley and H.-C. Nägerl: "Precision Measurements on a Tunable Mott Insulator of Ultracold Atoms", Phys. Rev. Lett. **107**, 175301 (2011).

[189] J.-P. Brantut, J. Meineke, D. Stadler, S. Krinner and T. Esslinger: "Conduction of Ultracold Fermions Through a Mesoscopic Channel", Science **337**, 1069–1071 (2012).

[190] R. Bube: *Photoconductivity in Solids*, Wiley, New York (1960).

[191] A. Rose: *Concepts in Photoconductivity and Allied Problems*, Interscience Publishers, John Wiley & Aons, New York (1963).

[192] M. Freitag, J. C. Tsang, A. Bol, D. Yuan, J. Liu and P. Avouris: "Imaging of the Schottky Barriers and Charge Depletion in Carbon Nanotube Transistors", Nano Lett. **7**, 2037–2042 (2007).

[193] Y. Ahn, J. Dunning and J. Park: "Scanning Photocurrent Imaging and Electronic Band Studies in Silicon Nanowire Field Effect Transistors", Nano Lett. **5**, 1367–1370 (2005).

[194] E. J. H. Lee, K. Balasubramanian, R. T. Weitz, M. Burghard and K. Kern: "Contact and edge effects in graphene devices", Nat. Nano. **3**, 486–490 (2008).

[195] M. Freitag, T. Low, F. Xia and P. Avouris: "Photoconductivity of biased graphene", Nat. Photon. **7**, 53–59 (2013).

[196] H. J. Queisser and D. E. Theodorou: "Hall-Effect Analysis of Persistent Photocurrents in n-GaAs Layers", Phys. Rev. Lett. **43**, 401–404 (1979).

[197] A. Tebano, E. Fabbri, D. Pergolesi, G. Balestrino and E. Traversa: "Room-Temperature Giant Persistent Photoconductivity in SrTiO3/LaAlO3 Heterostructures", ACS Nano **6**, 1278–1283 (2012).

[198] M. Endres, M. Cheneau, T. Fukuhara, C. Weitenberg, P. Schauß, C. Gross, L. Mazza, M. C. Banuls, L. Pollet, I. Bloch and S. Kuhr: "Observation of Correlated Particle-Hole Pairs and String Order in Low-Dimensional Mott Insulators", Science **334**, 200–203 (2011).

[199] O. E. Alon, A. I. Streltsov and L. S. Cederbaum: "Zoo of Quantum Phases and Excitations of Cold Bosonic Atoms in Optical Lattices", Phys. Rev. Lett. **95**, 030405 (2005).

[200] A. Isacsson and S. M. Girvin: "Multiflavor bosonic Hubbard models in the first excited Bloch band of an optical lattice", Phys. Rev. A **72**, 053604 (2005).

[201] W. V. Liu and C. Wu: "Atomic matter of nonzero-momentum Bose-Einstein condensation and orbital current order", Phys. Rev. A **74**, 013607 (2006).

[202] C. Xu and M. P. A. Fisher: "Bond algebraic liquid phase in strongly correlated multiflavor cold atom systems", Phys. Rev. B **75**, 104428 (2007).

[203] V. W. Scarola and S. Das Sarma: "Quantum Phases of the Extended Bose-Hubbard Hamiltonian: Possibility of a Supersolid State of Cold Atoms in Optical Lattices", Phys. Rev. Lett. **95**, 033003 (2005).

[204] C. Wu, W. V. Liu, J. Moore and S. Das Sarma: "Quantum Stripe Ordering in Optical Lattices", Phys. Rev. Lett. **97**, 190406 (2006).

[205] E. Peik, M. Ben Dahan, I. Bouchoule, Y. Castin and C. Salomon: "Bloch oscillations of atoms, adiabatic rapid passage, and monokinetic atomic beams", Phys. Rev. A **55**, 2989–3001 (1997).

[206] T. Salger, C. Geckeler, S. Kling and M. Weitz: "Atomic Landau-Zener Tunneling in Fourier-Synthesized Optical Lattices", Phys. Rev. Lett. **99**, 190405 (2007).

[207] T. Müller, S. Fölling, A. Widera and I. Bloch: "State Preparation and Dynamics of Ultracold Atoms in Higher Lattice Orbitals", Phys. Rev. Lett. **99**, 200405 (2007).

[208] G. Wirth, M. Ölschläger and A. Hemmerich: "Evidence for orbital superfluidity in the P-band of a bipartite optical square lattice", Nat. Phys. **7**, 147–153 (2011).

[209] T. Salger, C. Grossert, S. Kling and M. Weitz: "Klein Tunneling of a Quasirelativistic Bose-Einstein Condensate in an Optical Lattice", Phys. Rev. Lett. **107**, 240401 (2011).

[210] P. Soltan-Panahi, D.-S. Lühmann, J. Struck, P. Windpassinger and K. Sengstock: "Quantum phase transition to unconventional multi-orbital superfluidity in optical lattices", Nat. Phys. **8**, 71–75 (2012).

[211] A. R. Kolovsky and H. J. Korsch: "Bloch Oscillations Of Cold Atoms In Optical Lattices", Int. J. Mod. Phys. B **18**, 1235–1260 (2004).

[212] A. Smerzi, S. Fantoni, S. Giovanazzi and S. R. Shenoy: "Quantum Coherent Atomic Tunneling between Two Trapped Bose-Einstein Condensates", Phys. Rev. Lett. **79**, 4950–4953 (1997).

[213] W. Zhang, D. L. Zhou, M.-S. Chang, M. S. Chapman and L. You: "Coherent spin mixing dynamics in a spin-1 atomic condensate", Phys. Rev. A **72**, 013602 (2005).

[214] K. N. Alekseev and F. V. Kusmartsev: "Pendulum limit, chaos and phase-locking in the dynamics of ac-driven semiconductor superlattices", Phys. Lett. A **305**, 281 – 288 (2002).

[215] P. Anderson: “Special effects in superconductivity”, in E. Caianello (editor), “Lectures on the Many-Body Problem 2”, pages 113–136, Academic, New York (1964).

[216] J. V. Jóse and E. J. Saletan: *Classical Dynamics A Contemporary Approach*, Cambridge University Press (1998).

[217] M. Ben Dahan, E. Peik, J. Reichel, Y. Castin and C. Salomon: “Bloch Oscillations of Atoms in an Optical Potential”, Phys. Rev. Lett. **76**, 4508–4511 (1996).

[218] A. Polkovnikov: “Phase space representation of quantum dynamics”, Ann. Phys. **325**, 1790–1852 (2010).

[219] A. P. Itin and P. Törmä: “Dynamics of a many-particle Landau-Zener model: Inverse sweep”, Phys. Rev. A **79**, 055602 (2009).

[220] I. B. Spielman, P. R. Johnson, J. H. Huckans, C. D. Fertig, S. L. Rolston, W. D. Phillips and J. V. Porto: “Collisional deexcitation in a quasi-two-dimensional degenerate bosonic gas”, Phys. Rev. A **73**, 020702 (2006).

[221] R. Bücker, J. Grond, S. Manz, T. Berrada, T. Betz, C. Koller, U. Hohenester, T. Schumm, A. Perrin and J. Schmiedmayer: “Twin-atom beams”, Nat. Phys. **7**, 608–611 (2011).

[222] M. Gustavsson, E. Haller, M. J. Mark, J. G. Danzl, G. Rojas-Kopeinig and H.-C. Nägerl: “Control of Interaction-Induced Dephasing of Bloch Oscillations”, Phys. Rev. Lett. **100**, 080404 (2008).

[223] H. Ott, E. de Mirandes, F. Ferlaino, G. Roati, G. Modugno and M. Inguscio: “Collisionally Induced Transport in Periodic Potentials”, Phys. Rev. Lett. **92**, 160601 (2004).

[224] L. Mathey: Private communication.

[225] M. P. A. Fisher, P. B. Weichman, G. Grinstein and D. S. Fisher: “Boson localization and the superfluid-insulator transition”, Phys. Rev. B **40**, 546–570 (1989).

[226] B. Pasquiou, E. Maréchal, L. Vernac, O. Gorceix and B. Laburthe-Tolra: “Thermodynamics of a Bose-Einstein Condensate with Free Magnetization”, Phys. Rev. Lett. **108**, 045307 (2012).

[227] M. Fattori, T. Koch, S. Goetz, A. Griesmaier, S. Hensler, J. Stuhler and T. Pfau: “Demagnetization cooling of a gas”, Nat. Phys. **2**, 765–768 (2006).

[228] A. Widera, F. Gerbier, S. Fölling, T. Gericke, O. Mandel and I. Bloch: “Coherent Collisional Spin Dynamics in Optical Lattices”, Phys. Rev. Lett. **95**, 190405 (2005).

[229] A. de Paz, A. Chotia, E. Marechal, P. Pedri, L. Vernac, O. Gorceix and B. Laburthe-Tolra: “Resonant demagnetization of a dipolar BEC in a 3D optical lattice”, arXiv:1212.5469 (2012).

[230] A. de Paz, A. Sharma, A. Chotia, E. Marechal, J. Huckans, P. Pedri, L. Santos, O. Gorceix and B. Vernac, L. Laburthe-Tolra: “Non-equilibrium quantum magnetism in a dipolar lattice gas”, arXiv:1306.2754 (2013).

[231] F. Gerbier, S. Fölling, A. Widera, O. Mandel and I. Bloch: "Probing Number Squeezing of Ultracold Atoms across the Superfluid-Mott Insulator Transition", Phys. Rev. Lett. **96**, 090401 (2006).

[232] N. Strohmaier, D. Greif, R. Jördens, L. Tarruell, H. Moritz, T. Esslinger, R. Sensarma, D. Pekker, E. Altman and E. Demler: "Observation of Elastic Doublon Decay in the Fermi-Hubbard Model", Phys. Rev. Lett. **104**, 080401 (2010).

[233] K. Inaba and S.-I. Suga: "Superfluid, Staggered State, And Mott Insulator Of Repulsively Interacting Three-component Fermionic Atoms In Optical Lattices", Mod. Phys. Lett. B **27**, 1330008 (2013).

[234] J. J. García-Ripoll, S. Dürr, N. Syassen, D. M. Bauer, M. Lettner, G. Rempe and J. I. Cirac: "Dissipation-induced hard-core boson gas in an optical lattice", New J. Phys. **11**, 013053 (2009).

[235] J. Simonet: "Optical traps for ultracold metastable Helium atoms", Ph.D. thesis (2011).

[236] M. Kiffner and M. J. Hartmann: "Dissipation-induced Tonks-Girardeau gas of polaritons", Phys. Rev. A **81**, 021806 (2010).

[237] C. Chin, R. Grimm, P. Julienne and E. Tiesinga: "Feshbach resonances in ultracold gases", Rev. Mod. Phys. **82**, 1225–1286 (2010).

[238] M. Vengalattore, S. R. Leslie, J. Guzman and D. M. Stamper-Kurn: "Spontaneously Modulated Spin Textures in a Dipolar Spinor Bose-Einstein Condensate", Phys. Rev. Lett. **100**, 170403 (2008).

[239] J. D. Sau, S. R. Leslie, D. M. Stamper-Kurn and M. L. Cohen: "Theory of domain formation in inhomogeneous ferromagnetic dipolar condensates within the truncated Wigner approximation", Phys. Rev. A **80**, 023622 (2009).

[240] F. Deuretzbacher, G. Gebreyesus, O. Topic, M. Scherer, B. Lücke, W. Ertmer, J. Arlt, C. Klempt and L. Santos: "Parametric amplification of matter waves in dipolar spinor Bose-Einstein condensates", Phys. Rev. A **82**, 053608 (2010).

[241] A. Lindner: *Drehimpluse in der Quantenmechanik*, Teubner Studienbücher (1984).

[242] A. Widera, F. Gerbier, S. Fölling, T. Gericke, O. Mandel and I. Bloch: "Precision measurement of spin-dependent interaction strengths for spin-1 and spin-2 87 Rb atoms", New J. Phys. **8**, 152 (2006).

[243] A. Griesmaier, J. Werner, S. Hensler, J. Stuhler and T. Pfau: "Bose-Einstein Condensation of Chromium", Phys. Rev. Lett. **94**, 160401 (2005).

[244] B. Pasquiou, G. Bismut, Q. Beaufils, A. Crubellier, E. Maréchal, P. Pedri, L. Vernac, O. Gorceix and B. Laburthe-Tolra: "Control of dipolar relaxation in external fields", Phys. Rev. A **81**, 042716 (2010).

[245] M. Koashi and M. Ueda: "Exact Eigenstates and Magnetic Response of Spin-1 and Spin-2 Bose-Einstein Condensates", Phys. Rev. Lett. **84**, 1066–1069 (2000).

[246] P. Zeeman: "Ueber einen Einfluss der Magnetisirung auf die Natur des von einer Substanz emittirten Lichtes", in "Verhandlungen der Physikalischen Gesellschaft zu Berlin", page 127 (1882).

[247] L. I. Schiff and H. Snyder: "Theory of the Quadratic Zeeman Effect", Phys. Rev. **55**, 59–63 (1939).

[248] J. Heinze, F. Deuretzbacher and D. Pfannkuche: "Influence of the particle number on the spin dynamics of ultracold atoms", Phys. Rev. A **82**, 023617 (2010).

[249] R. Jördens, L. Tarruell, D. Greif, T. Uehlinger, N. Strohmaier, H. Moritz, T. Esslinger, L. De Leo, C. Kollath, A. Georges, V. Scarola, L. Pollet, E. Burovski, E. Kozik and M. Troyer: "Quantitative Determination of Temperature in the Approach to Magnetic Order of Ultracold Fermions in an Optical Lattice", Phys. Rev. Lett. **104**, 180401 (2010).

[250] J. P. Ronzheimer, M. Schreiber, S. Braun, S. S. Hodgman, S. Langer, I. P. McCulloch, F. Heidrich-Meisner, I. Bloch and U. Schneider: "Expansion Dynamics of Interacting Bosons in Homogeneous Lattices in One and Two Dimensions", Phys. Rev. Lett. **110**, 205301 (2013).

[251] J. Wernsdorfer, M. Snoek and W. Hofstetter: "Lattice-ramp-induced dynamics in an interacting Bose-Bose mixture", Phys. Rev. A **81**, 043620 (2010).

[252] C.-L. Hung, X. Zhang, N. Gemelke and C. Chin: "Slow Mass Transport and Statistical Evolution of an Atomic Gas across the Superfluid–Mott-Insulator Transition", Phys. Rev. Lett. **104**, 160403 (2010).

[253] P. S. Julienne, F. H. Mies, E. Tiesinga and C. J. Williams: "Collisional Stability of Double Bose Condensates", Phys. Rev. Lett. **78**, 1880–1883 (1997).

[254] B. Misra and E. C. G. Sudarshan: "The Zeno's paradox in quantum theory", J. Math. Phys. **18**, 756–763 (1977).

[255] W. M. Itano, D. J. Heinzen, J. J. Bollinger and D. J. Wineland: "Quantum Zeno effect", Phys. Rev. A **41**, 2295–2300 (1990).

[256] E. W. Streed, J. Mun, M. Boyd, G. K. Campbell, P. Medley, W. Ketterle and D. E. Pritchard: "Continuous and Pulsed Quantum Zeno Effect", Phys. Rev. Lett. **97**, 260402 (2006).

[257] M. Müller, S. Diehl, G. Pupillo and P. Zoller: "Engineered Open Systems and Quantum Simulations with Atoms and Ions", in P. Berman, E. Arimondo and C. Lin (editors), "Advances in Atomic, Molecular, and Optical Physics", volume 61 of *Advances In Atomic, Molecular, and Optical Physics*, pages 1 – 80, Academic Press (2012).

[258] G. Zürn, F. Serwane, T. Lompe, A. N. Wenz, M. G. Ries, J. E. Bohn and S. Jochim: "Fermionization of Two Distinguishable Fermions", Phys. Rev. Lett. **108**, 075303 (2012).

[259] D. Rubeni, A. Foerster and I. Roditi: "Two interacting fermions in a one-dimensional harmonic trap: Matching the Bethe ansatz and variational approaches", Phys. Rev. A **86**, 043619 (2012).

[260] F. Werner, O. Parcollet, A. Georges and S. R. Hassan: "Interaction-Induced Adiabatic Cooling and Antiferromagnetism of Cold Fermions in Optical Lattices", Phys. Rev. Lett. **95**, 056401 (2005).

[261] L. De Leo, C. Kollath, A. Georges, M. Ferrero and O. Parcollet: "Trapping and Cooling Fermionic Atoms into Mott and Néel States", Phys. Rev. Lett. **101**, 210403 (2008).

[262] A. Koetsier, R. A. Duine, I. Bloch and H. T. C. Stoof: "Achieving the Néel state in an optical lattice", Phys. Rev. A **77**, 023623 (2008).

[263] M. Snoek, I. Titvinidze, C. Tõke, K. Byczuk and W. Hofstetter: "Antiferromagnetic order of strongly interacting fermions in a trap: real-space dynamical mean-field analysis", New J. Phys. **10**, 093008 (2008).

[264] G. H. Wannier: "Antiferromagnetism. The Triangular Ising Net", Phys. Rev. **79**, 357–364 (1950).

[265] S. Sachdev: "Quantum magnetism and criticality", Nat. Phys. **4**, 173–185 (2008).

[266] J. M. McGuirk, H. J. Lewandowski, D. M. Harber, T. Nikuni, J. E. Williams and E. A. Cornell: "Spatial Resolution of Spin Waves in an Ultracold Gas", Phys. Rev. Lett. **89**, 090402 (2002).

[267] T. Nikuni, J. E. Williams and C. W. Clark: "Linear spin waves in a trapped Bose gas", Phys. Rev. A **66**, 043411 (2002).

[268] J. N. Fuchs, D. M. Gangardt and F. Laloë: "Large amplitude spin waves in ultra-cold gases", Eur. Phys. J. D **25**, 57–75 (2003).

[269] X. Du, L. Luo, B. Clancy and J. E. Thomas: "Observation of Anomalous Spin Segregation in a Trapped Fermi Gas", Phys. Rev. Lett. **101**, 150401 (2008).

[270] X. Du, Y. Zhang, J. Petricka and J. E. Thomas: "Controlling Spin Current in a Trapped Fermi Gas", Phys. Rev. Lett. **103**, 010401 (2009).

[271] F. Piéchon, J. N. Fuchs and F. Laloë: "Cumulative Identical Spin Rotation Effects in Collisionless Trapped Atomic Gases", Phys. Rev. Lett. **102**, 215301 (2009).

[272] S. S. Natu and E. J. Mueller: "Anomalous spin segregation in a weakly interacting two-component Fermi gas", Phys. Rev. A **79**, 051601 (2009).

[273] U. Ebling, A. Eckardt and M. Lewenstein: "Spin segregation via dynamically induced long-range interactions in a system of ultracold fermions", Phys. Rev. A **84**, 063607 (2011).

[274] M. Koschorreck, D. Pertot, E. Vogt and M. Kohl: "Universal spin dynamics in two-dimensional Fermi gases", Nat. Phys. **9**, 405–409 (2013).

[275] G. J. Conduit and E. Altman: "Dynamical instability of a spin spiral in an interacting Fermi gas as a probe of the Stoner transition", Phys. Rev. A **82**, 043603 (2010).

[276] G.-B. Jo, Y.-R. Lee, J.-H. Choi, C. A. Christensen, T. H. Kim, J. H. Thywissen, D. E. Pritchard and W. Ketterle: "Itinerant Ferromagnetism in a Fermi Gas of Ultracold Atoms", Science **325**, 1521–1524 (2009).

[277] S. Zhang and T.-L. Ho: "Atom loss maximum in ultra-cold Fermi gases", New J. Phys. **13**, 055003 (2011).

[278] D. Pekker, M. Babadi, R. Sensarma, N. Zinner, L. Pollet, M. W. Zwierlein and E. Demler: "Competition between Pairing and Ferromagnetic Instabilities in Ultracold Fermi Gases near Feshbach Resonances", Phys. Rev. Lett. **106**, 050402 (2011).

[279] G. J. Conduit and E. Altman: "Effect of three-body loss on itinerant ferromagnetism in an atomic Fermi gas", Phys. Rev. A **83**, 043618 (2011).

[280] C. Wu: "Hidden Symmetry And Quantum Phases In Spin-3/2 Cold Atomic Systems", Mod. Phys. Lett. B **20**, 1707 (2006).

[281] C. Lhuillier and L. Laloë: "Transport properties in a spin polarized gas, I", J. Phys. France **43**, 197 – 224 (1982).

[282] B. R. Johnson, J. S. Denker, N. Bigelow, L. P. Lévy, J. H. Freed and D. M. Lee: "Observation of Nuclear Spin Waves in Spin-Polarized Atomic Hydrogen Gas", Phys. Rev. Lett. **52**, 1508–1511 (1984).

[283] W. J. Gully and W. J. Mullin: "Observation of Spin Rotation Effects in Polarized ^{3}He-^{4}He Mixtures", Phys. Rev. Lett. **52**, 1810–1813 (1984).

[284] E. P. Bashkin: "Spin waves in polarized paramagnetic gases", JETP Lett. **33**, 8–11 (1981).

[285] L. P. Lévy and A. E. Ruckenstein: "Collective Spin Oscillations in Spin-Polarized Gases: Spin-Polarized Hydrogen", Phys. Rev. Lett. **52**, 1512–1515 (1984).

[286] S. S. Natu and E. J. Mueller: "Spin waves in a spin-1 normal Bose gas", Phys. Rev. A **81**, 053617 (2010).

[287] Y. Endo and T. Nikuni: "Spin-Dynamics of a Trapped Spin-1 Bose Gas above the Bose-Einstein Transition Temperature", J. Low Temp. Phys. **152**, 21–46 (2008).

[288] K. Gottfried and T.-M. Yan: *Quantum Mechanics: Fundamentals*, Springer (Heidelberg) (2003).

[289] U. Ebling: Private communication.

[290] R. Barnett, A. Turner and E. Demler: "Classifying Novel Phases of Spinor Atoms", Phys. Rev. Lett. **97**, 180412 (2006).

[291] J. M. McGuirk and L. F. Zajiczek: "Optical excitation of nonlinear spin waves", New J. Phys. **12**, 103020 (2010).

[292] J. Kronjäger, C. Becker, M. Brinkmann, R. Walser, P. Navez, K. Bongs and K. Sengstock: "Evolution of a spinor condensate: Coherent dynamics, dephasing, and revivals", Phys. Rev. A **72**, 063619 (2005).

[293] N. Tsuji, T. Oka, P. Werner and H. Aoki: "Dynamical Band Flipping in Fermionic Lattice Systems: An ac-Field-Driven Change of the Interaction from Repulsive to Attractive", Phys. Rev. Lett. **106**, 236401 (2011).

[294] S. Braun, J. P. Ronzheimer, M. Schreiber, S. S. Hodgman, T. Rom, I. Bloch and U. Schneider: "Negative Absolute Temperature for Motional Degrees of Freedom", Science **339**, 52–55 (2013).

[295] P. J. Mohr, B. N. Taylor and D. B. Newell: "CODATA recommended values of the fundamental physical constants: 2010", Rev. Mod. Phys. **84**, 1527–1605 (2012).

DANKSAGUNG

Wie fast alle wissenschaftliche Arbeit in der heutigen Zeit ist auch diese Dissertation nicht im stillen Kämmerlein entstanden. Ganz im Gegenteil gibt es eine große Anzahl an Menschen, die mir mit ihrem Wissen, ihrer Hilfe und ihrem Zuspruch einen unermesslichen Beistand geleistet haben, die hier präsentierten Ergebnisse zu realisieren.

Mein größter Dank gilt meinem Doktorvater Klaus Sengstock danken. Sein unermüdliches Nachhaken, Anspornen und Unterstützen hat einen wesentlichen Anteil zu dem Umfang sowie der Qualität der Ergebnisse dieser Dissertation beigetragen. Dies gilt auch für die exzellenten Arbeitsbedingungen, die er mir und allen anderen in seiner Gruppe immer zur Verfügung gestellt hat.

Mein besonderer Dank gilt auch dem Zweitgutachter dieser Arbeit Ludwig Mathey, dem Drittgutachter Joseph H. Thywissen, dem Zweitprüfer der Disputation Andreas Hemmerich und dem Prüfungsausschussvorsitzenden Peter Schmelcher.

Den anderen Mitarbeitern der Arbeitsgruppe, mit denen ich viele schöne Jahre zusammengearbeitet habe, gilt mein nächster Dank. Alle hatten immer ein offenes Ohr füreinander und waren motiviert gemeinsam die Probleme des Einzelnen zu lösen. Besonders zu erwähnen sind hier natürlich meine direkten Mitarbeiter am Bose-Fermi Mischungs-Experiment (in chronologischer Reihenfolge): Philipp T. Ernst, Sören Götze, Jasper S. Krauser, Christoph Becker, Malte Weinberg, Chris Hamner, Bastian Hundt, Nick Fläschner, Maria Langbecker und Dominik Vogel. Ohne diese wären viele der Ergebnisse dieser Arbeit nicht möglich gewesen.

Des weiteren möchte ich mich bei den vielen Kollegen bedanken, mit denen Teilergebnisse dieser Arbeit in Kooperationen entstanden sind (wiederum chronologisch): Ulf Bissbort, Yongqiang Li, Walter Hofstetter, Ole Jürgensen Dirk-Sören Lühmann, Tom Hanna, L. Cook, Alexander Itin, Ludwig Mathey, Ulrich Ebling, Maciej Lewenstein und André Eckardt. Diese tollen Kooperationen haben mir immer wieder vor Augen geführt, wie fruchtbar und unersetzlich der Austausch mit anderen Wissenschaftlern ist.

Da Wissenschaft heutzutage nicht im stillen Kämmerlein abläuft, werden auch Technisches Personal und Verwaltungspersonal benötigt, um den gesamten Universitäts- und Forschungsapparat am Laufen zu halten, sowie spezielle technische Lösungen am Experiment zu realisieren. All diesen am Fachbereich der Physik der Universität Hamburg, dem DESY, sowie im besonderen am ILP und ZOQ Angestellten, mit denen ich im Laufe meiner Promotion gearbeitet habe, möchte ich hier meinen herzlichen Dank aussprechen.

Für das Korrekturlesen von Teilen dieser Arbeit danke ich Jasper S. Krauser, Bastian Hundt, Nick Fläschner, Christoph Becker sowie Gesa Franke.

Mein abschließender Dank gilt allen meinen Freunden, meiner Familie und insbesondere Gesa Franke für ihre unermüdliche Unterstützung und dafür, dass sie alle im Verlauf der Promotion immer für mich da waren.